

~~Removed from Library~~
NASA Technical Memorandum 101663

EVALUATION OF EQUILIBRIUM TURBULENCE FOR A HYPERSONIC BOUNDARY LAYER AT NONADIABATIC WALL CONDITIONS

7N-34

175-13

CINDY W. ALBERTSON

NOVEMBER 1989

NASA LIBRARY
AMES RESEARCH CENTER
MOFFETT FIELD, CALIF.

COPY NO.	
-------------	--

NASA
National Aeronautics and
Space Administration
Langley Research Center
Hampton, Virginia 23665

(NASA-TM-101663) EVALUATION OF
EQUILIBRIUM TURBULENCE FOR A
HYPERSONIC BOUNDARY LAYER AT
NONADIABATIC WALL CONDITIONS M.S.
Thesis - Old Dominion Univ. (NASA)
265 p

N93-72475

Unclass

29/34 0175273

SUMMARY

This paper presents an experimental study to characterize the compressible turbulent boundary layer produced along a flat plate in the NASA Langley 8-Foot High Temperature Tunnel and to determine the test conditions necessary to achieve equilibrium turbulence. In addition, the present study extends the data base for equilibrium compressible turbulent boundary layers over quasi-isothermal walls which are far from the adiabatic wall temperature. The measurements consist of pitot pressure, static pressure, and total temperature distributions in the boundary layer. A flat plate measuring 9.7 feet long and 4.3 feet wide was used for the study to provide a naturally turbulent boundary layer which is suitably thick for probing. In addition, surface measurements consisting of heat transfer and pressure distributions were obtained. The tests were conducted at a nominal free-stream Mach number of 6.5, total temperatures of 2700 and 3300 °R, and angles of attack of 5 and 13 degrees. The corresponding nominal boundary-layer edge Mach numbers were 6.2 and 5.0. The nominal ratios of adiabatic wall temperature to cold wall temperature were 4.4 and 5.4 and the momentum thickness Reynolds numbers at the boundary-layer probe locations ranged from 400 to 7800.

The results of this study indicate that momentum thickness Reynolds numbers of at least 4000 are required to obtain an equilibrium turbulent boundary layer along a flat plate in the Langley 8-Foot High Temperature Tunnel. This evaluation is based primarily on the behavior of shape factors

calculated from the velocity and density distributions which were inferred from the pressure and temperature measurements in the boundary layer. These results are generally supported by comparisons made with the standard incompressible velocity distributions given by Coles using the compressible transformation of van Driest.

TABLE OF CONTENTS

	Page
LIST OF SYMBOLS.....	v
Chapter	
1 INTRODUCTION.....	1
1.1 Background.....	1
1.2 Review of Research Pertaining to Compressible Turbulent Layers in Equilibrium and Near-Equilibrium.....	3
1.3 Purpose.....	8
2 DESCRIPTION OF EXPERIMENT.....	9
2.1 Model.....	9
2.2 Instrumentation.....	12
2.2.1 Surface Pressure Orifices and Coaxial Thermocouples.....	17
2.2.2 Boundary-Layer Rake Assemblies.....	22
2.3 Data Acquisition, Reduction, and Uncertainties.....	36
2.4 Test Facility.....	39
2.5 Test Conditions.....	42
3 RESULTS AND DISCUSSION OF SURFACE AND BOUNDARY-LAYER MEASUREMENTS.....	47
3.1 Surface Pressure Distributions.....	48
3.1.1 Data Repeatability.....	48
3.1.2 Effect of Boundary Layer Rake Assemblies.....	48
3.1.3 Effect of Angle of Attack.....	51
3.1.4 Effect of Free-stream Unit Reynolds Number.....	56
3.2 Surface Heating Rate Distributions.....	58
3.2.1 Effect of Angle of Attack.....	59
3.2.2 Effect of Free-stream Unit Reynolds Number.....	66
3.2.3 Correlation of Heating Rates.....	66

Chapter		Page
3.3	Boundary-Layer Distributions.....	71
3.3.1	Static Pressure Distributions.....	71
3.3.2	Spanwise and Longitudinal Variations.....	76
3.3.3	Effect of Free-Stream Unit Reynolds Number.....	92
3.3.4	Effect of Temperature Ratio.....	105
3.3.5	Correlation of Velocity Power Law Exponent.....	115
3.3.6	Total Temperature Variation with Velocity.....	117
4	ASSESSMENT OF EQUILIBRIUM TURBULENCE.....	127
4.1	Comparison with Coles' Incompressible Profile.....	127
4.2	Shape Factors.....	149
4.3	Correlation of Test Conditions with Momentum Thickness Reynolds Number.....	175
5	CONCLUDING REMARKS.....	179
5.1	Recapitulation.....	179
5.2	Conclusions.....	180
5.3	Recommendations.....	181
	REFERENCES.....	183
	APPENDICES.....	187
A	MODEL THERMAL DISTORTION ESTIMATES.....	187
B	SURFACE ROUGHNESS CALCULATIONS.....	190
C	BOUNDARY-LAYER THERMAL DISTORTION ESTIMATES.....	191
D	SURFACE HEATING RATE ERROR ESTIMATES.....	195
E	TOTAL TEMPERATURE PROBE ERROR ESTIMATES.....	199
F	FREE-STREAM FLOW SURVEYS.....	201
G	SURFACE PRESSURE AND HEAT TRANSFER DATA TABULATION.....	208
H	BOUNDARY-LAYER DATA TABULATION.....	228

LIST OF SYMBOLS

c_f	local skin friction coefficient based on Eckert's reference enthalpy, $2\tau_w / (\rho^* U_e^2)$
c_p	specific heat at constant pressure, Btu/lb _m - °R
C	intercept for logarithmic law, Eq. (8)
e	emissivity
E	thermal expansion coefficient, in./in.-°R
G	Clauser's shape factor, Eq. (17)
h	heat transfer coefficient, Btu/ft. ² -s-°R
H	enthalpy, Btu/lb _m
\bar{H}	distance normal from tunnel axial centerline, in.
k	thermal conductivity, Btu/ft.-s-°R
K	slope for logarithmic law, Eq. (8)
l	thermal bowing length, in., Eq. (22)
L	panel holder length, 116.62 in.
M	Mach number
N	power law exponent , Eq. (5)
p	pressure, psia
Pr^*	Prandtl number, $\mu^* c_p^* / k^*$
q	heat transfer rate, Btu/ft. ² -s
r	roughness height, in., Eq. (25)
R	specific gas constant for methane-air combustion products, 1771 ft. ² /s ² - °R

Re_{∞}	free-stream unit Reynolds number, $\rho_{\infty}U_{\infty}/\mu_{\infty}$, 1/ft.
Re_x	local Reynolds number based on boundary-layer edge temperature, $\rho_e U_e x / \mu_e$
Re^*	local unit Reynolds number based on reference enthalpy, $\rho^* U_e / \mu^*$, 1/ft.
Re_x^*	local Reynolds number, $\rho^* U_e x / \mu^*$
Re_v^*	Reynolds number corresponding to the virtual origin of the turbulent boundary layer, $\rho^* U_e x_v / \mu^*$
$Re_{\delta^*}^*$	displacement thickness Reynolds number, $\rho^* U_e \delta^* / \mu^*$
Re_{θ}^*	momentum thickness Reynolds number, $\rho^* U_e \theta / \mu^*$
St^*	Stanton number, $q / (H_{aw} - H_w) \rho^* U_e$
t	plate thickness, in.
T	temperature, °R
U	velocity, ft./s
\bar{U}	transformed velocity, ft./s, Eq. (10)
U^+	ratio of transformed velocity to shear velocity
U_{τ}	shear velocity, $(\tau_w / \rho_w)^{0.5}$, ft./s
W	plate width, 51.50 in.
x, y, z	coordinates for instrumentation (See Figs. 4 and 9.)
x_v	distance from the leading edge to the origin of turbulence
z^+	nondimensionalized distance measured normal from plate surface, $U_{\tau} z / \nu_w$
α	angle of attack, deg.
β	pressure gradient parameter, $\beta = (\delta^* / \tau_w)(dp/dx)$

δ_M	boundary-layer thickness corresponding to the boundary-layer edge Mach number, in.
δ_T	boundary-layer thickness corresponding to the boundary-layer edge total temperature, in.
δ_U	boundary-layer thickness corresponding to the boundary-layer edge velocity, in.
δ^*	displacement thickness, in., Eq. (15)
δ_H	enthalpy thickness, in., Eq. (19)
Δ	defect thickness, in., Eq. (18)
γ	ratio of specific heats
η	thermal bowing height, in., Eq. (22)
μ	viscosity, lb _m /ft.-s
ν	kinematic viscosity, ft. ² /s
Π	wake parameter, $\Pi = 0.8 (\beta + 0.5)^{0.75}$
θ	momentum thickness, in., Eq. (16)
ρ	density, lb _m /ft. ³
σ	Stefan-Boltzmann constant, 4.761×10^{-13} Btu/ft. ² -s-°R ⁴
τ_w	skin friction, psia
σ_{w-p}	radiation view factor

SUBSCRIPTS

aw	adiabatic wall
c	combustor
e	boundary-layer edge

p	tunnel pod wall
t	total conditions
t2	stagnation condition behind a normal shock
tc	total conditions in the combustor
te	total conditions at the boundary-layer edge
w	wall
∞	free-stream

SUPERSCRIPT

*	condition at Eckert's reference enthalpy, Eq. (2)
---	---

Chapter 1

INTRODUCTION

1.1 Background

Methods of accurately predicting heat transfer for hypersonic vehicles, such as the National Aero-Space Plane (NASP), require a detailed knowledge of the boundary-layer behavior over the vehicle. Due to the flight regime, such boundary layers are expected to be turbulent over much of the vehicle and influenced by large differences between the flow-based adiabatic wall temperature and the actual wall temperature. The predictive capabilities needed to provide design information for such flows have been found to be deficient [1-3]*, particularly for flows involving shock-wave turbulent boundary-layer interactions. These flows are unsteady and difficult to predict with the current knowledge of turbulence [3].

Because of the flow complexity, wind tunnel experiments are needed both to obtain the required design information and to provide test data for numerical prediction validations. To provide a baseline comparison for numerical predictions of shock-wave turbulent boundary-layer flows, the boundary layer ahead of the interaction region should be in turbulent equilibrium. Also, in order for wind tunnel experiments to relate to flight data

*Numbers in [] indicate references.

and numerical predictions, the upstream boundary-layer conditions must be independent of the wind tunnel. This requires an evaluation of the upstream boundary layer to define the conditions required for equilibrium turbulence and to identify any anomalous flow behavior caused by the wind tunnel.

Equilibrium turbulent boundary layers can be described in general as flows which are self-similar. (See Schlichting [4].) This implies that when properly scaled, the dimensionless velocity profiles are independent of distance from the leading edge. Typical mathematical descriptions of these velocity profiles have evolved over several decades and are often based on mixing length concepts. An early discussion on the subject is given by Clauser [5] in his 1954 paper. Clauser suggested that an equilibrium turbulent boundary layer is one in which the velocity profiles plotted in defect coordinates collapse onto a universal curve which is independent of the distance from the leading edge. The equation for this curve is often referred to as the velocity defect equation.

A significant modification to both the velocity defect equation and the velocity equation in wall coordinates was later presented by Coles [6] in a 1956 survey paper. Coles presented a variety of incompressible profiles, plotted primarily in wall coordinates. The data include the effect of adverse and favorable pressure gradients, free-stream turbulence, and departure from two-dimensional flow on boundary-layer profiles. Coles concluded that the profiles can be represented by a linear combination of a logarithmic wall function and a wake function, provided that the Reynolds number is high enough for equilibrium turbulence. In addition, pressure gradients must be modest enough that the boundary layer does not either separate or

relaminarize. Coles also showed that the wake function can be represented by a sinusoidal function.

A later report containing a large amount of incompressible data is the compilation prepared by Coles and Hirst for the 1968 Stanford Conference [7]. This compilation has been particularly useful, not only for evaluating the theories presented at the conference [8], but also as a source of data for correlations. Some of the equilibrium data were used by White [9] to further refine the wake law for flows with pressure gradients. In his 1974 textbook, White presented a correlation between the wake parameter presented by Coles and the pressure gradient parameter. White further refined the definition for an equilibrium turbulent boundary layer by stating that the wake parameter should be a function of the pressure gradient parameter only.

Significant earlier investigations involving compressible turbulent boundary layers and a discussion on how well the wall and wake laws apply to compressible flow are presented in the following section.

1.2 Review of Research Pertaining to Compressible Turbulent Boundary Layers in Equilibrium And Near-Equilibrium

Various experiments in compressible turbulent boundary layers have been conducted over several decades which include mean profile data, in terms of Mach number, velocity, and temperature measurements [10, 11]. However, compressible turbulent data generally lack the quality of incompressible data for a number of reasons. One major factor affecting the

quality of compressible turbulent boundary-layer data is the use of boundary-layer trips. It has been shown by various researchers that the Reynolds number for both the start and end of transition increases with Mach number [12]. As a result, many high speed facilities cannot operate at Reynolds numbers which are high enough to obtain naturally turbulent flow. The required trip height also increases with Mach number, such that at hypersonic speeds, the trip height required for transition near the trips has been found to be at least twice the boundary-layer thickness [13]. The resulting profiles have been shown to be distorted to some degree, even at large distances from the trips [14]. Another difficulty encountered in high Mach number turbulent boundary layer studies is obtaining a boundary layer which is thick enough for probing because many hypersonic facilities lack sufficient length. Largely because of these experimental difficulties, test data for the 1968 Stanford Conference were limited to incompressible flows [15].

In spite of the difficulties, equilibrium and near-equilibrium compressible turbulent boundary layer data of reasonable quality does exist as reported by Fernholz and Finley, who prepared a set of three data compilation reports [10, 11, and 16]. These reports include effects of pressure gradient, roughness, heat transfer, Mach number, and Reynolds number for nominally two-dimensional boundary layers. The purpose of this compilation was primarily to provide a set of test cases for compressible turbulent theories, similar to the compilation of incompressible data prepared by Coles and Hirst [7] for the Stanford Conference. A secondary objective was to summarize what experimental conditions have been covered sufficiently and to identify test conditions which still require experimental data.

The first report of this series [10] consisted primarily of mean profile data tabulations, in terms of Mach number, velocity, and total temperature distributions. Also, some of the listings include heat transfer and skin friction measurements. The Mach number range of the data considered was 3.0 to 7.2 and the ratio of the adiabatic wall temperature to wall temperature ranged from 1.0 to 3.3. The compilation included a mix of data obtained on flat plates and along nozzle walls, each of which has its advantages and disadvantages. Some of the flat plate data were obtained behind trips and therefore may be questionable for the reasons cited previously. However, the flat plate data generally has the advantage of negligible upstream history effects. The authors cited only one nozzle flow experiment in which the development was so gradual that the boundary layer had relaxed fully from the impressed upstream pressure and temperature gradients. In only two other experiments is the upstream history even reasonably well described. Experiments with temperature ratios above 2.0 are rare, particularly flat plate experiments. The authors note only two such studies with a temperature ratio above 2.0. The limited amount of data at relatively large temperature ratios is a result of the limited number of wind tunnel facilities which can operate at high temperatures.

The second report [11] is primarily a commentary by Fernholz and Finley on the data compiled in the first report. The authors' most significant conclusion was that for the range of data investigated, the wall and wake laws established by incompressible studies can be applied to compressible turbulent boundary layers. However, the effects of Mach number and temperature ratio must be taken into account in order to correlate the data with the incompressible relations. The authors state that a reasonably good

correlation can be obtained using the compressible transformation of van Driest [17]. The authors further state that the constants which appear in the incompressible laws are unaltered by the effect of Mach number, Reynolds number, and temperature ratio. This is a significant finding because some earlier researchers had concluded that the wall and wake laws may not be applicable to hypersonic flows [18, 19], particularly those flows involving significant heat transfer. Fernholz and Finley state that the reason why the van Driest transformation works reasonably well is described by "Morkovin's Hypothesis" [20, 21]. This hypothesis states that the basic structure of turbulence is unaltered by compressibility, provided that the ratio of the density fluctuations to mean density is small. Therefore, the primary factors to be taken into account in a compressible transformation are Mach number and the ratio of adiabatic wall temperature to wall temperature. The van Driest transformation does, however, break down if there are strong gradients of pressure and temperature at the wall. This is due, at least in part, to a breakdown in the Crocco-Busemann relationship between temperature and velocity [22, 23] used by van Driest in deriving the transformation.

A secondary conclusion stated by Fernholz and Finley is that the transformed data generally show more scatter in the intercept for the logarithmic law of the wall than do incompressible data. Furthermore, the wake strength, defined as the maximum difference between the velocity measured in the wake and the velocity given by the logarithmic law normalized by the shear velocity, shows scatter as high as 20 percent. The scatter in the logarithmic law intercept is apparent particularly in the data with heat transfer. Because the skin friction coefficient is used directly in the correlation, the scatter may be due to difficulties in obtaining accurate skin

friction measurements in high speed flow. For flows involving heat transfer, obtaining accurate skin friction data is hampered by the difficulty of keeping the sensing element at the same temperature as the surrounding wall, to avoid additional errors.

The third report [16] of the series consisted primarily of measured turbulent shear and normal stresses in compressible turbulent boundary layers. Some of the data were obtained directly using hot wire, laser doppler, and electron beam techniques. The direct measurements of these quantities tend to show significant scatter, and for this reason, Fernholz and Finley stated that the data are best regarded as qualitative. However, the authors did conclude that these measurements generally support the trends found in incompressible data. In addition, indirect measurements of turbulent shear stresses, inferred from mean velocity profile measurements, are included in the compilation and show more consistent trends. In their discussion of these data, Fernholz and Finley cited the 1974 survey paper by Sandborn [24]. Sandborn concluded that for adiabatic, zero pressure gradient boundary layers up to Mach 7, there is no significant effect of Reynolds or Mach number on the turbulent shear stress distributions. Therefore this class of boundary layers can be well represented by the incompressible distribution originally measured by Klebanoff [25] using a hot wire anemometer. This is in agreement with Morkovin's hypothesis, which was discussed earlier. The effect of heat transfer was investigated later by Watson [26], who inferred turbulent shear stresses from his velocity profile measurements for ratios of adiabatic wall temperature to wall temperature up to 2.6 at Mach 10. The turbulent shear stresses have the same trend as the incompressible measurements, but are generally higher for the outer 70 percent of the

boundary layer. Whether this discrepancy is a sign that the incompressible model is beginning to break down is difficult to judge because Watson's velocity profiles show good correlation with the established incompressible profiles.

Based on the literature surveyed, the incompressible descriptions of equilibrium turbulent boundary layers should be applicable to the present compressible study where the van Driest transformation is employed. However, it should be noted that the temperature ratio for the present study ranges from 4.4 to 5.6, which is considerably higher than other compressible studies found in the literature, particularly for the flat plate studies.

1.3 Purpose

The primary purpose of the present investigation was to characterize the compressible turbulent boundary layer on a flat plate in the NASA Langley Research Center 8-Foot High Temperature Tunnel. These measurements will help to define the flow conditions necessary to achieve equilibrium turbulent boundary layers for future shock boundary-layer interaction studies. In addition, the present study extends the current data base for equilibrium compressible turbulent boundary layers to ratios of adiabatic wall temperature to wall temperature up to 5.6.

Chapter 2

DESCRIPTION OF EXPERIMENT

2.1 Model

The model used for the present study was an instrumented flat plate. The plate was made of Nickel 200 and was mounted on the panel holder, a generalized test apparatus for the NASA Langley 8-Foot High Temperature Tunnel (8' HTT). A photograph of the model installed in the 8' HTT test section is shown in Fig. 1 and a sketch showing plate mounting details is presented in Fig. 2. The plate measured 51.50 x 107.26 x 0.38 inches and covered the top surface of the panel holder completely. The plate was attached to the panel holder using one fixed attachment near the leading edge and 48 sliding attachments to allow for in-plane thermal expansion.

Nickel 200 was chosen as the plate material to minimize the temperature gradient through the plate and the attendant thermal distortion during exposure to the high temperature stream. Estimates of maximum distortion at peak heating conditions, presented in Appendix A, indicate that the surface should bow no more than 0.014 inches over a distance of 15.4 inches, the maximum distance between attachments. Surface waviness, measured at room temperature conditions using a straight edge and a feeler gage, varied by no more than ± 0.02 inches over a minimum distance of 24 inches. The surface roughness of the plate was less than 32 μ inches rms. The surface roughness levels are well within the criteria for a hydraulically

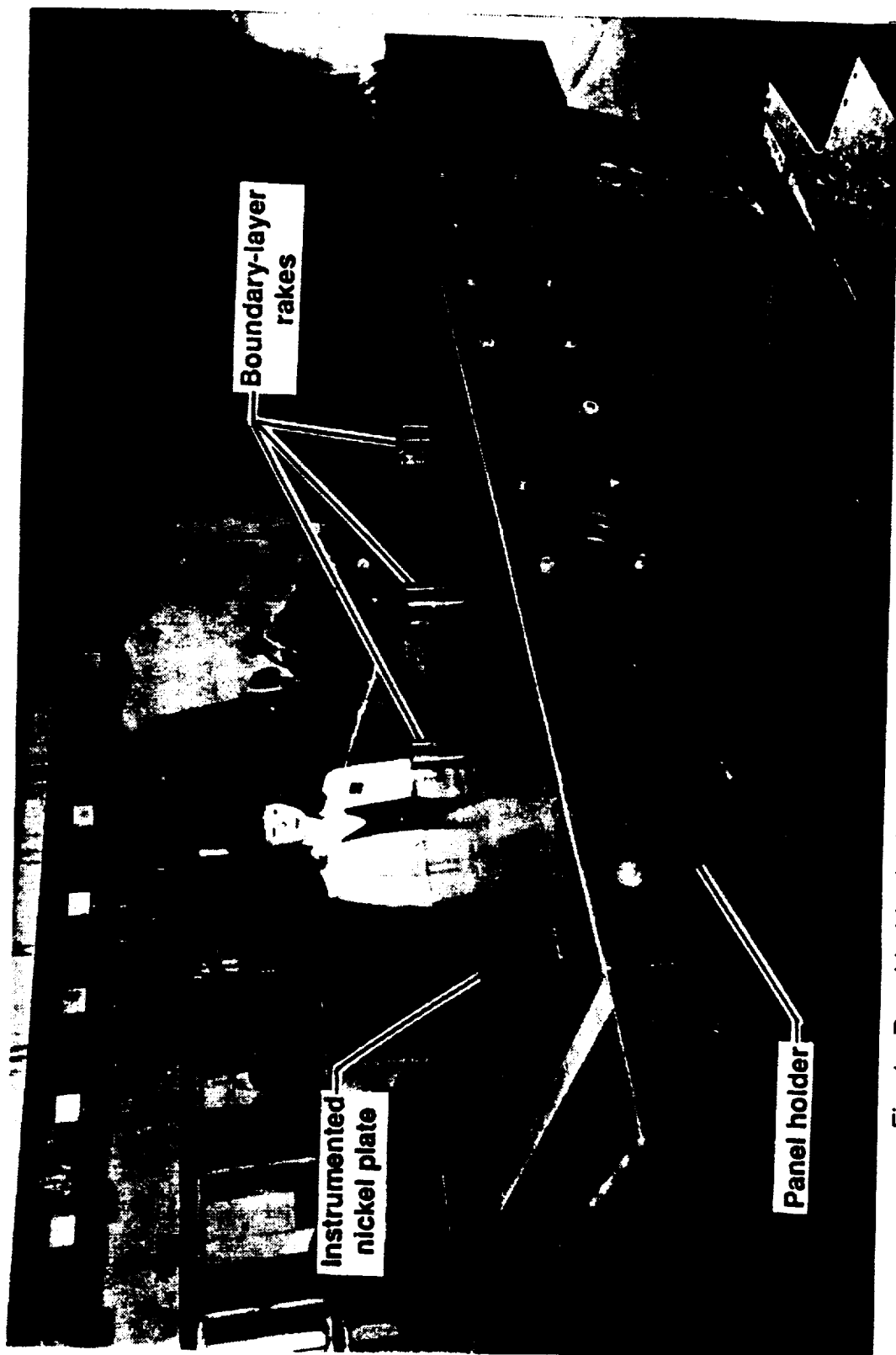
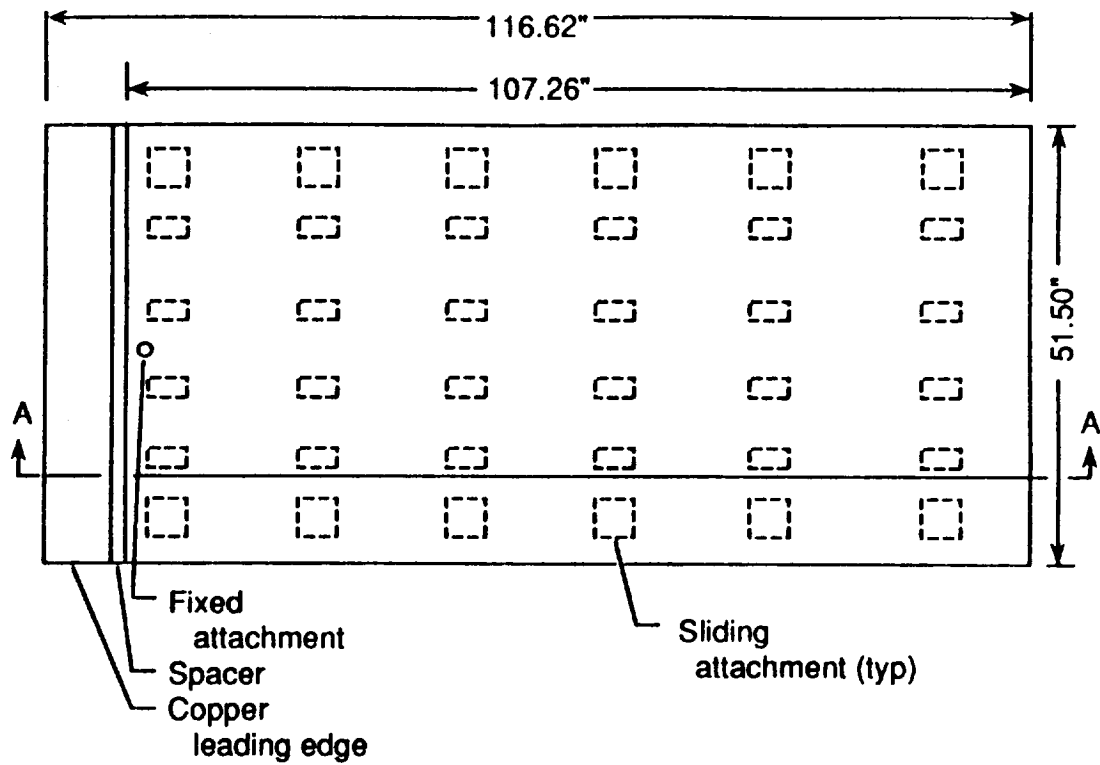
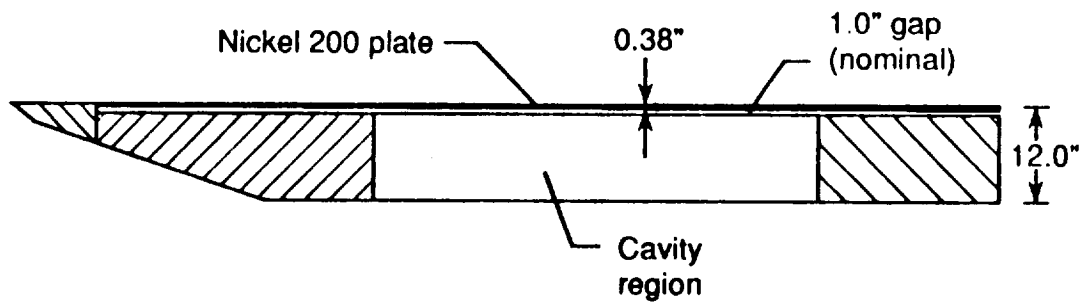


Fig. 1. Panel holder in the NASA Langley 8-foot High Temperature Tunnel test chamber.



a) Top view



b) Section A-A

Fig. 2. Mounting details for instrumented Nickel 200 plate.

smooth wall given by Schlichting [4] for the worst case test condition, as shown in Appendix B. A gap of approximately one inch existed between the plate and the panel holder to allow space for instrumentation. In the cavity region of the panel holder, a space of approximately 12 inches in height was provided for additional instrumentation. The overall length of the model was 116.62 inches with the leading edge assembly attached to the panel holder, as shown in Fig. 2.

Details of the leading edge assembly are shown in Fig. 3. The assembly was designed to accommodate a boundary-layer trip plate. However, for the present study, a spacer was installed in place of a trip to obtain natural transition to turbulent flow. The leading edge was made of solid copper to reduce thermal gradients. The leading edge radius was 0.015 inches. The steps in the junction regions of the leading edge and over the surface of the nickel plate resulting from machining inaccuracies were no greater than 0.001 inches high and were all rearward facing. Gaps were no greater than 0.0005 inches.

2.2 Instrumentation

The surface of the plate was equipped with pressure orifices, coaxial thermocouples, and boundary-layer rake assemblies. An instrumentation layout of the test plate is shown schematically in Fig. 4. The spatial locations of the pressure orifices and full scale values for each gage are given in Table 1. Boundary-layer rake assemblies, consisting of pitot pressure, static pressure, and total temperature probes were used to survey the boundary layer at various locations on the plate. Survey locations are indicated in Fig. 4,

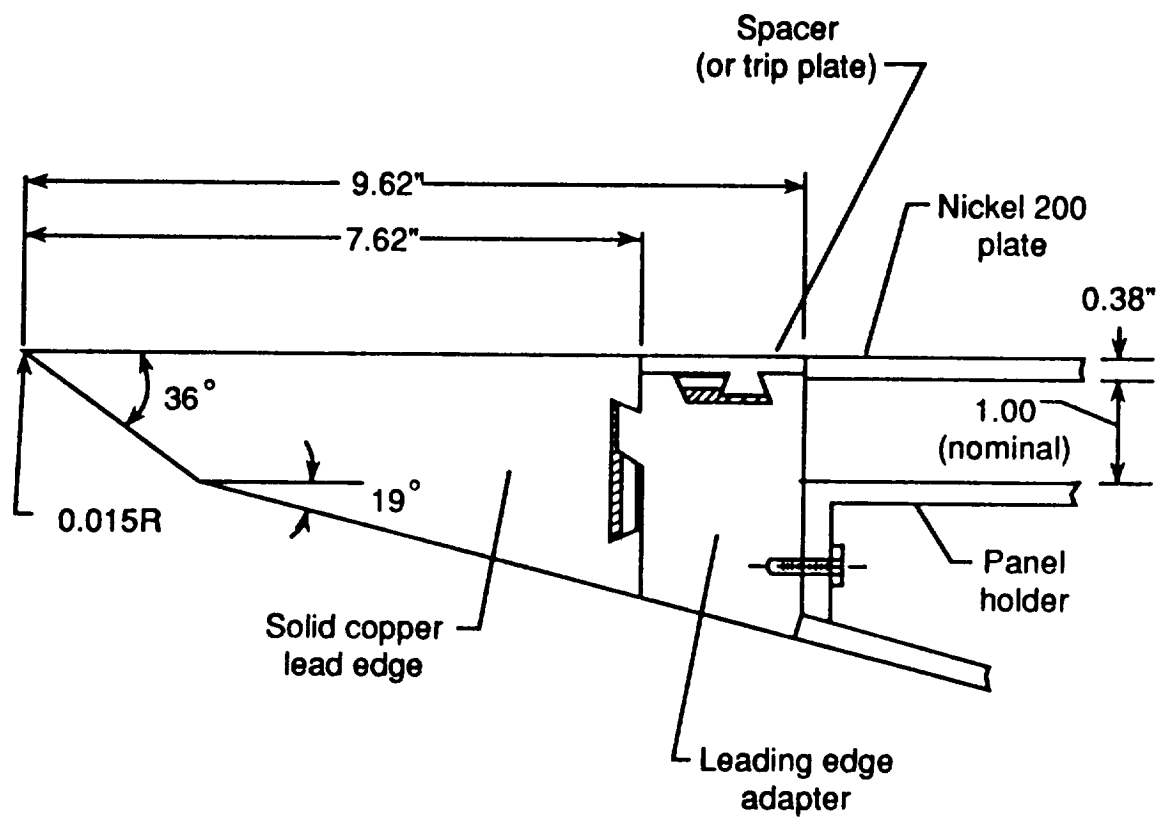
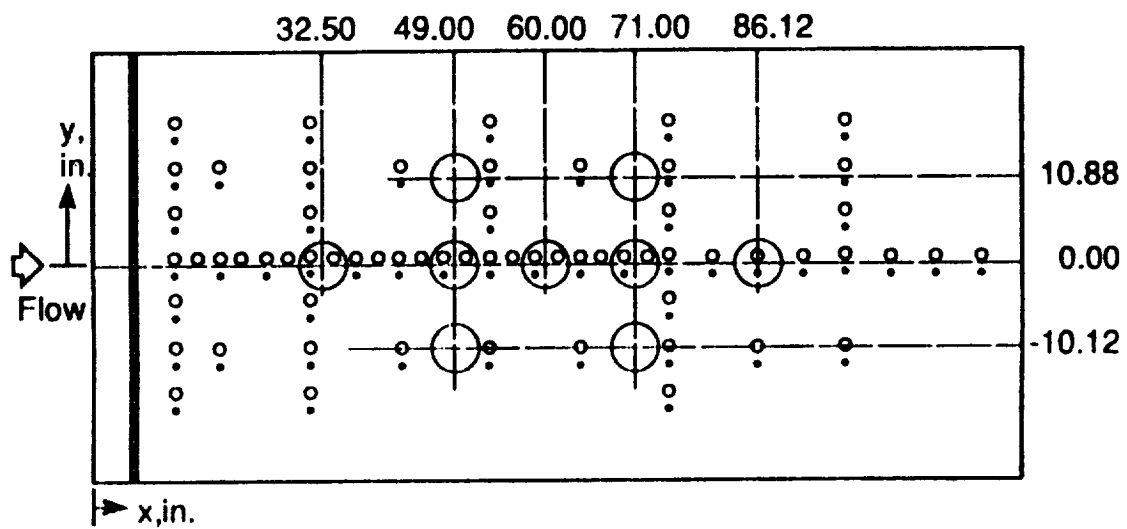


Fig. 3. Details of panel holder leading edge assembly.



- Pressure orifice location
- Coaxial thermocouple location
- Rake assembly location

Fig. 4. Schematic of instrumentation layout.

Table 1 Surface Instrumentation Locations

Designation	<u>Coaxial thermocouple</u>		<u>Pressure tap</u>	gage range, psia
	x, inch	y, inch	y, inch	
1	14.62	-16.62	-17.62	5
2	31.12	-15.62	-17.62	5
3	75.12	-15.62	-17.62	5
4	14.62	-10.12	-12.12	3
5	20.12	-10.12	-12.12	3
6	31.12	-10.12	-12.12	3
7	42.12	-10.12	-12.12	5
8	53.12	-10.12	-12.12	3
9	64.12	-10.12	-12.12	3
10	75.12	-10.12	-12.12	5
11	86.12	-10.12	-12.12	3
12	97.12	-10.12	-12.12	3
13	14.62	-4.62	-6.62	3
14	31.12	-4.62	-6.62	3
15	75.12	-4.62	-6.62	5
16	14.62	0.88	-1.12	5
17	17.38	0.88	-----	-
18	20.12	0.88	-1.12	5
19	22.88	0.88	-----	-
20	25.62	0.88	-1.12	5
21	28.38	0.88	-----	-
22	31.12	0.88	-1.12	5
23	33.88	0.88	-----	-
24	36.62	0.88	-1.12	5
25	39.38	0.88	-----	-
26	42.12	0.88	-1.12	5
27	44.88	0.88	-----	-
28	47.62	0.88	-----	5
29	50.38	0.88	-----	-
30	53.12	0.88	-1.12	5
31	55.88	0.88	-----	-
32	58.62	0.88	-1.12	5
33	61.38	0.88	-----	-
34	64.12	0.88	-1.12	5
35	66.88	0.88	-----	-
36	69.62	0.88	-1.12	5
37	72.38	0.88	-----	-
38	75.12	0.88	-1.12	5
39	80.62	0.88	-1.12	5
40	86.12	0.88	-1.12	5
41	91.62	0.88	-1.12	5
42	97.12	0.88	-1.12	5
43	102.62	0.88	-1.12	5
44	108.12	0.88	-1.12	5
45	113.62	0.88	-1.12	5
46	14.62	6.38	4.38	3
47	31.12	6.38	4.38	3
48	53.12	6.38	4.38	3
49	75.12	6.38	4.38	5
50	97.12	6.38	4.38	3
51	14.62	11.88	9.88	3

Table 1 Concluded.

<u>Designation</u>	<u>Coaxial thermocouple</u>		<u>Pressure tap.</u>	
	<u>x. inch</u>	<u>y. inch</u>	<u>y. inch</u>	<u>gage range. psia</u>
52	20.12	11.88	9.88	3
53	31.12	11.88	9.88	3
54	42.12	11.88	9.88	5
55	53.12	11.88	9.88	3
56	64.12	11.88	9.88	3
57	75.12	11.88	9.88	5
58	97.12	11.88	9.88	3
59	14.62	17.38	15.38	5
60	31.12	17.38	15.38	5
61	53.12	17.38	15.38	5
62	75.12	17.38	15.38	5
63	97.12	17.38	15.38	5

and their coordinates are tabulated in Table 2. The initial locations of the probes, in terms of distance, z , from the wall, and other details are given in Tables 3 through 5. All of the probe distances from the wall were measured after initial installation, and again after the rake assemblies were relocated on the test panel. As an additional check, the probe heights were measured after the first two runs of the test series and at the end of the test series. The only appreciable changes observed in the probe heights (i.e.: $> \pm 0.001$ inches) apparently occurred during relocation of the rake assemblies on the test panel. All probe distances from the wall are given with the tabulated boundary-layer data in Appendix H.

2.2.1 Surface Pressure Orifices and Coaxial Thermocouples

To measure spanwise and longitudinal pressure gradients on the plate, 52 surface pressure orifices were distributed over the plate as shown in Fig. 4. The orifices incorporated 0.062 inch I.D. tubes mounted into the plate which were attached to strain gage type pressure transducers located inside the panel holder. The tube lengths ranged from 1 to 3 feet. The response time for the instrumentation was no greater than 1.0 seconds.

To measure surface temperatures and infer heating rates, 63 chromel-constantan (Type E) coaxial surface thermocouples (Medtherm model number TCS-061-E-60-10670) were placed at strategic locations on the plate. The coaxial thermocouples consisted of a chromel outer tube with an axial, inner constantan wire. Prior to assembly, the constantan wire was flame sprayed with alumina insulation to a thickness of 0.0005 inches. The thermocouple junction was formed using a vacuum deposited chromium plating, 1 to 2 microns thick, over the sensing end of the thermocouple. Because this plating

Table 2 Boundary-Layer Rake Assembly Locations

Designation	x. inches*	y. inches**
1	49.00	-10.12
2	71.00	-10.12
3	32.50	0.00
4	49.00	0.00
5	60.00	0.00
6	71.00	0.00
7	86.12	0.00
8	49.00	10.88
9	71.00	10.88

* x location corresponds to measurement location

** y location corresponds to centerline of rake assembly

Table 3 Initial Pitot Pressure Probe Locations

Designation	z, inches (to probe centerline)			gage range, psia
	Rake #1	Rake #2	Rake #3	
1	0.023	0.020	0.020	
2	0.073	0.074	0.063	50
3	0.106	0.113	0.097	50
4	0.152	0.143	0.130	50
5	0.200	0.218	0.200	50
6	0.300	0.308	0.300	50
7	0.400	0.384	0.400	75
8	0.500	0.486	0.500	75
9	0.600	0.600	0.600	100
10	0.700	0.700	0.700	100
11	0.800	0.800	0.800	100
12	1.000	1.000	1.000	100
13	1.250	1.250	1.250	100
14	1.500	1.500	1.500	100
15	1.750	1.750	1.750	100
16	2.000	2.000	2.000	100
17	2.500	2.500	2.500	100

Table 4 Initial Static Pressure Probe Locations

z, inches (to probe centerline)				
Designation	Rake #1	Rake #2	Rake #3	gage range, psia
1	0.500	0.500	0.500	3
2	1.500	1.500	1.500	3
3	2.500	2.500	2.500	3

Table 5 Initial Total Temperature Probe Locations

z, inches			
Designation	Rake #1	Rake #2	Rake #3
1	0.060 (A) *	0.035 (B) *	0.060 (A)
2	0.180 (A)	0.100 (B)	0.180 (A)
3	0.300 (A)	0.165 (B)	0.300 (B)
4	0.420 (A)	0.230 (B)	0.420 (A)
5	0.540 (A)	0.295 (B)	0.540 (A)
6	0.660 (A)	0.360 (B)	0.660 (A)
7	0.800 (A)	0.425 (B)	0.800 (A)
8	1.000 (A)	0.540 (B)	1.000 (A)
9	1.400 (A)	0.600 (B)	1.400 (A)
10	1.900 (A)	0.800 (A)	1.900 (A)
11	2.500 (A)	1.000 (A)	2.500 (A)
12	-----	1.400 (A)	-----
13	-----	1.900 (A)	-----
14	-----	2.200 (B)	-----
15	-----	2.500 (A)	-----

* probe type (See Fig. 11.)

was very thin, the temperature at the junction was assumed to be uniform. Therefore any extraneous thermoelectric effects produced by dissimilar metal contact at the thermocouple junction should be negligible. The outside diameter of the thermocouples measured 0.061 inches. To eliminate extraneous thermoelectric effects from mounting the thermocouples in a dissimilar metal, the coaxial thermocouples were mounted in electrically insulated 0.311 inch diameter chromel plugs, as shown in Fig. 5. The electrical insulation consisted of a 0.001 inch thick polyester film with a 0.0015 inch thick silicon adhesive. The manufacturer claims the insulation is good up to 860 °R, which exceeds the maximum measured wall temperature of 790 °R. The electrical insulation also provided thermal insulation from the surrounding nickel. Because of the differences between the thermal properties of chromel and nickel, thermal distortion of the boundary layer due to wall temperature differences was a concern. This effect was evaluated by comparing estimated surface heating rates for a constant wall temperature and for a wall temperature discontinuity. (See Appendix C.) Thermal boundary-layer distortions were found to be minimal.

2.2.2 Boundary-Layer Rake Assemblies

The boundary-layer rake assemblies each consisted of individual fixed rakes for measuring pitot pressure, static pressure, and total temperature, as shown in Fig. 6. These three parameters were used to obtain Mach number, total temperature, and velocity distributions through the boundary layer. A top view showing the arrangement of the rakes in the rake assembly plug is given in Fig. 7. Flow calculations, assuming inviscid compressible flow, were used to establish the distance between rakes for maintaining supersonic flow and

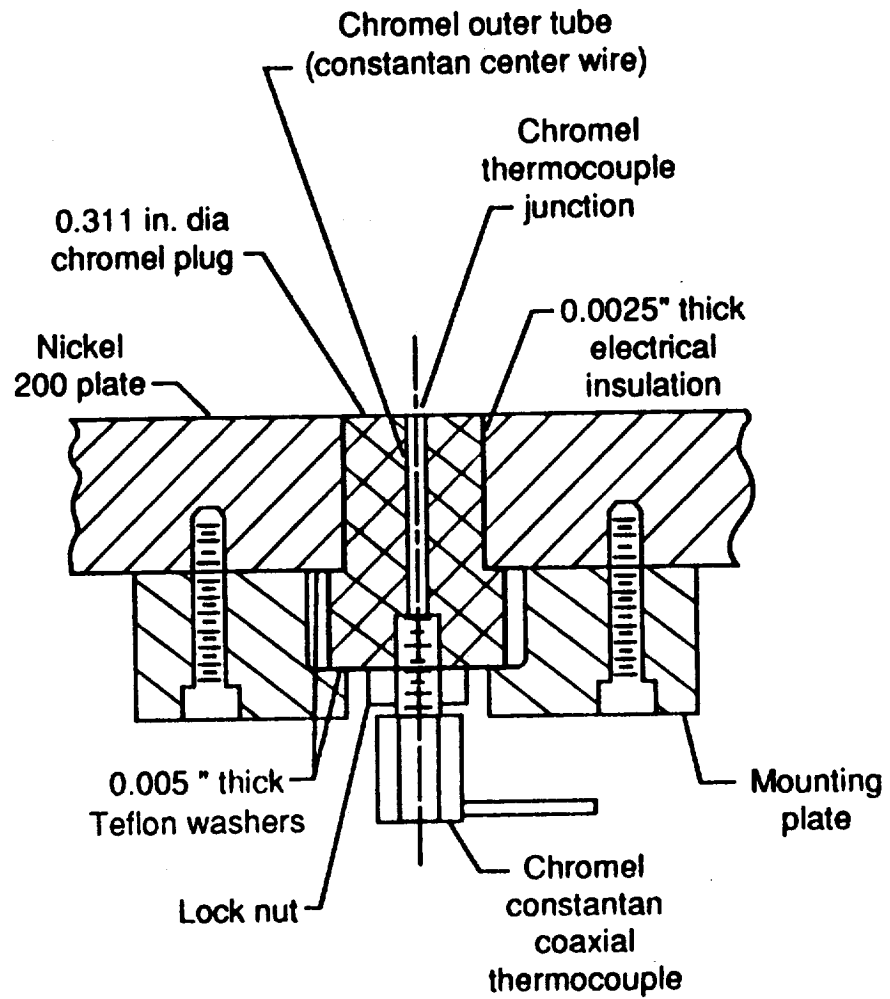


Fig. 5. Coaxial thermocouple mounting details.

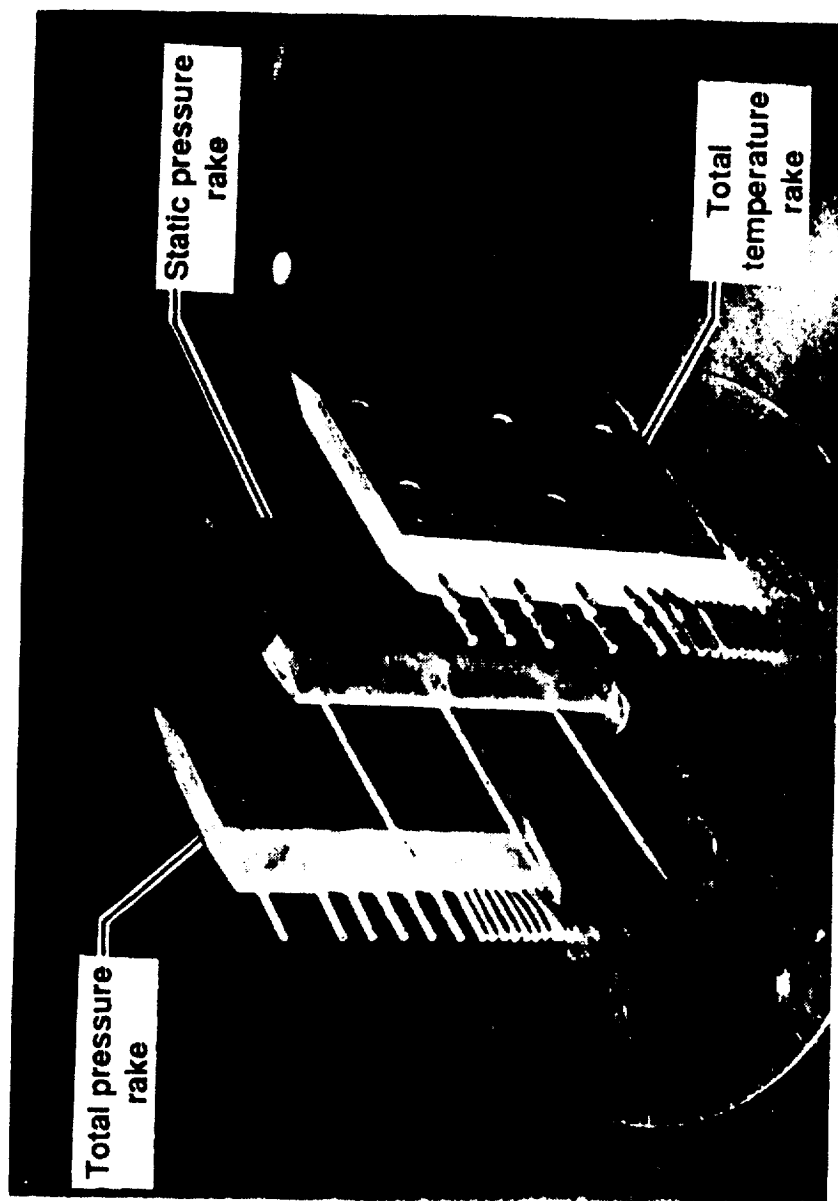


Fig. 6. Boundary-layer rake assembly.

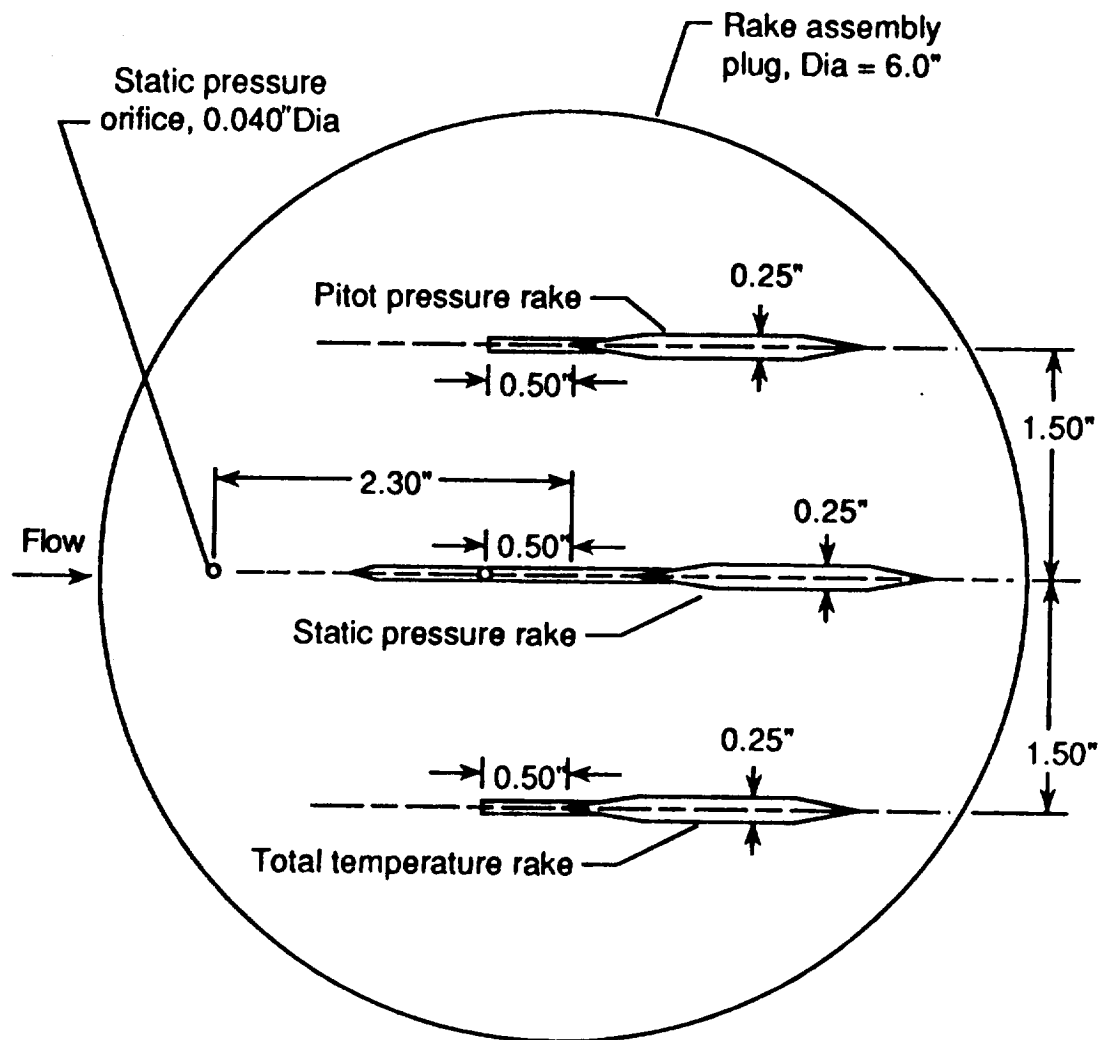


Fig. 7. Top view of boundary-layer rake assembly.

minimizing interference. Also the rakes for the static probes were located between the pitot and total temperature rakes to minimize losses from the pitot and total temperature probe bow shocks. The oil flow photograph in Fig. 8 indicates a discrete bow shock ahead of each rake, indicating supersonic flow between the rakes. In addition to the rakes, a static pressure port (See Fig. 7.) was located in the rake assembly plug to obtain static pressure at the wall and to serve as a backup measurement for the static pressure probes.

The pitot pressure rake, shown schematically in Fig. 9, consisted of a brass strut which was cast around 17 monel pitot probes. The rake was cast to provide good thermal contact between the probes and the rake body. Brass was chosen as the rake material because of its ease in casting and because of its high thermal diffusivity. Monel was used for the probes because it survived the casting process better than stainless steel. (Its survival was due in part to its higher thermal diffusivity.) The probes located within 0.5 inches of the wall were flattened horizontally to minimize vertical averaging effects, while maintaining an opening which was large enough to facilitate rapid sensor response times. Calculations of response time were made using the approach of Sinclair and Robins [27] to determine whether the tube openings were large enough. These calculations indicate that the measured pressure is 99 percent of the actual pressure within 0.25 seconds.

The minimum distance between probe centers specified in the design was 2.0 probe heights as recommended by Keener and Hopkins [28]. However, because of manufacturing difficulties and the tendency of the probe heights to vary from run to run, height measurements showed that the four probes nearest the wall were occasionally less than 1.5 probe heights of each

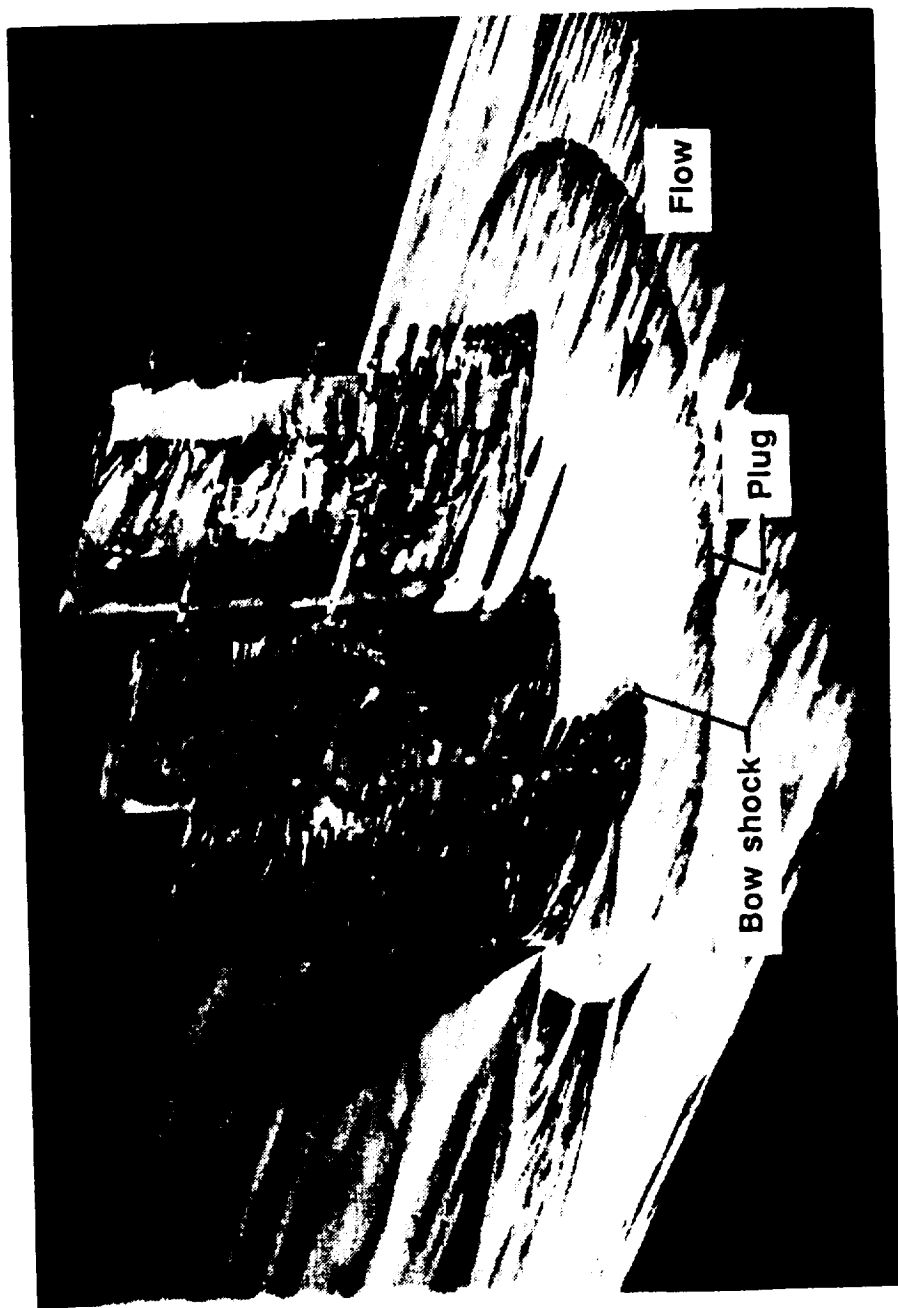


Fig. 8. Surface flow around a rake assembly.

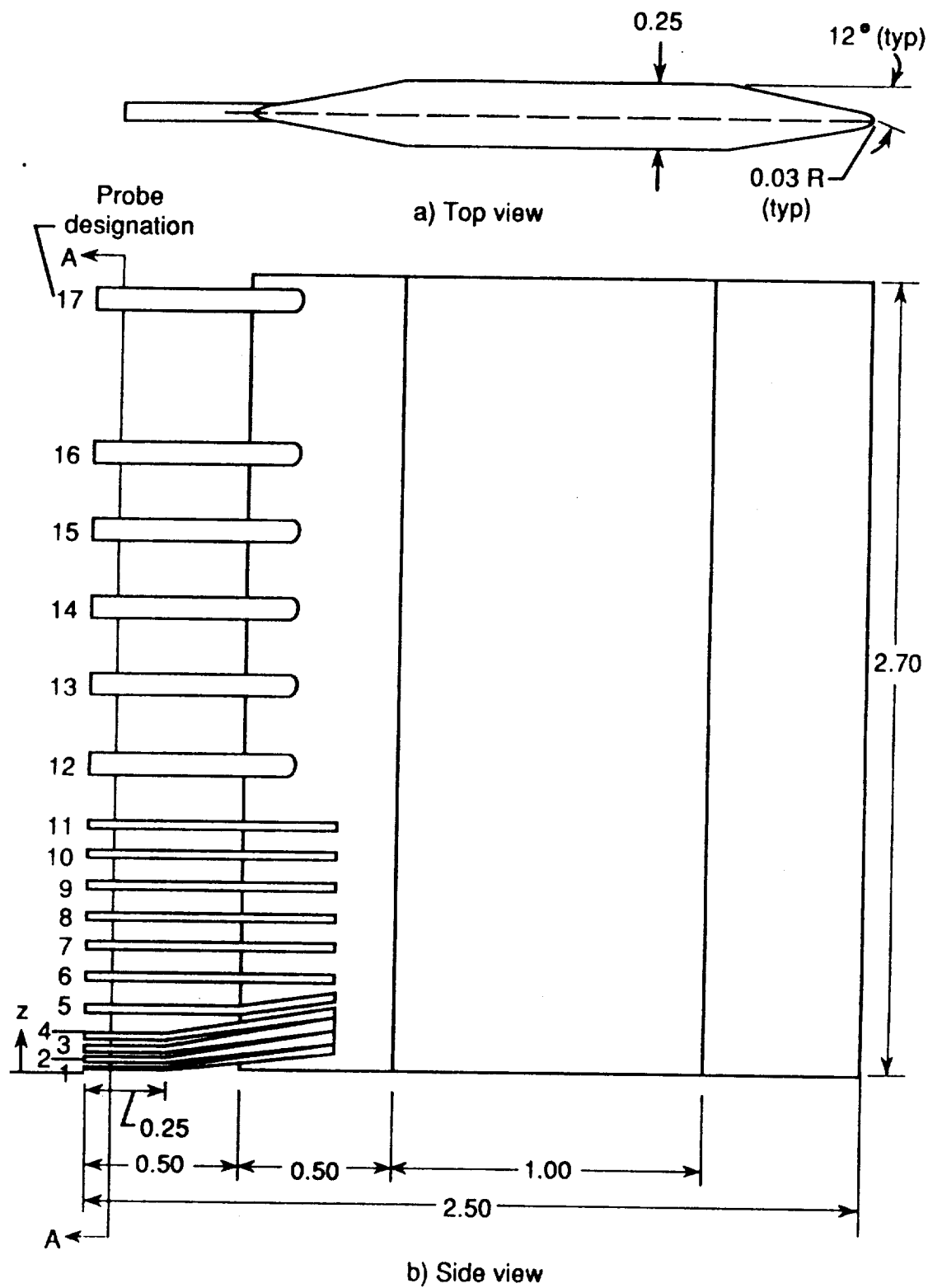
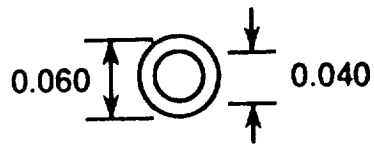
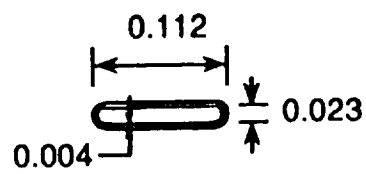


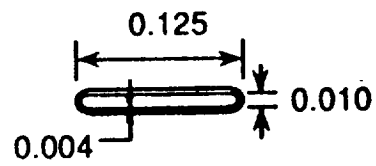
Fig. 9. Details of pitot pressure rake. (All dimensions are in inches.)



Probes 12-17



Probes 5-11



Probes 1-4

c) Section A-A

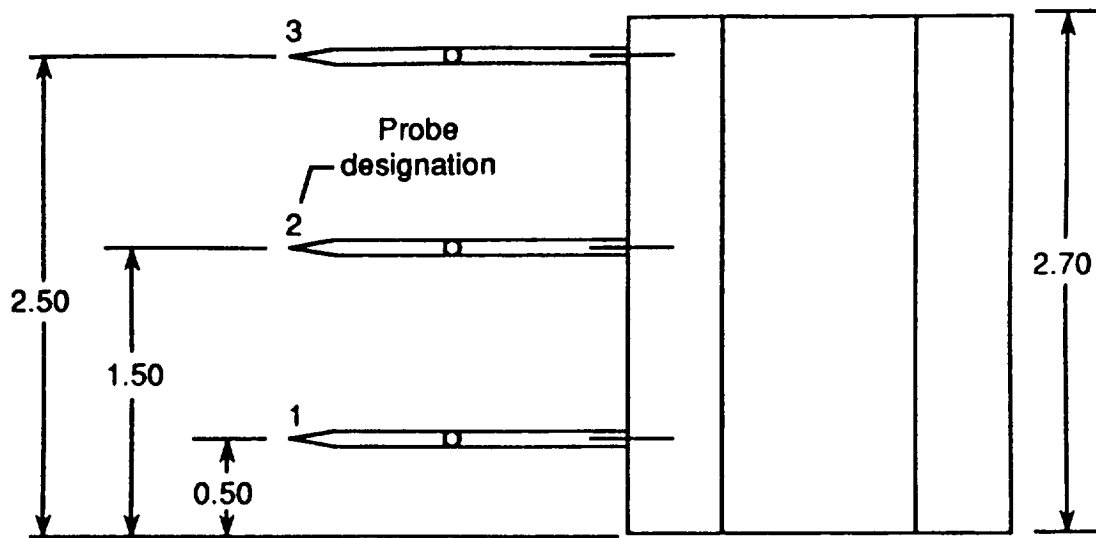
(Scale - 8:1)

Fig. 9. Concluded.

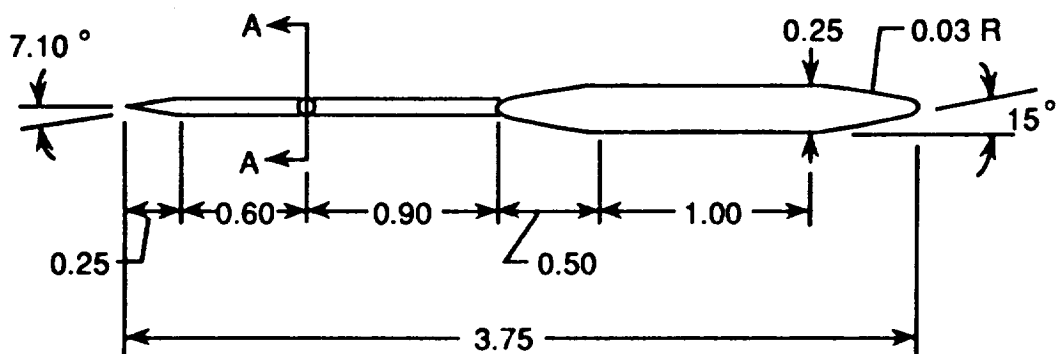
other. Probe interference problems were a definite possibility for these probes.

To determine if there were any static pressure variations through the boundary layer due to free-stream variations, the static pressure rake shown in Fig. 10 was used. This rake also consisted of a brass strut cast around monel probes. The static pressure probes were designed using the guidelines given by Behrens [29], who recommended spacing the static pressure holes 10 probe diameters from the cone shoulder and 14 diameters from the rake body. Response time estimates were used to determine appropriate hole diameters, again using the method of Sinclair and Robins [27]. These calculations indicate that the measured pressure is 99 percent of the actual pressure within 1.0 second. Probe spacing was determined using shock wave angle charts for a cone [30] to estimate shock locations and avoid interference effects between probes.

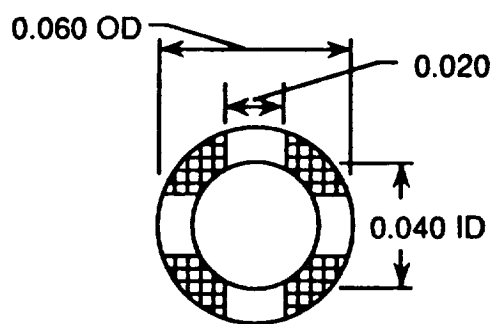
Total temperature distributions were measured through the boundary layer using two different types of probes. The initial total temperature probe design, referred to as probe A, is shown in Fig. 11a and consisted of a platinum-platinum, 13% rhodium thermocouple (Type R) mounted inside a 0.005 in. thick platinum-20% rhodium radiation shield. Two vent holes were drilled in the shield to allow the probe to aspirate. Type 308 stainless steel tubing was used to prevent the thin platinum shield from being crushed by the set screws used to hold the probes in the rake. To obtain measurements closer to the wall, a second probe (probe B) was used. This probe, shown in Fig. 11b, was very similar to probe A, except that it lacked a stainless steel set screw shield. These probes were mounted in two different rake strut designs, designated rake A and rake B, as shown in Figs 12a and 12b, respectively.



a) Side view



b) Top view



c) Section A-A

Fig. 10. Static pressure rake details. (All dimensions are in inches.)

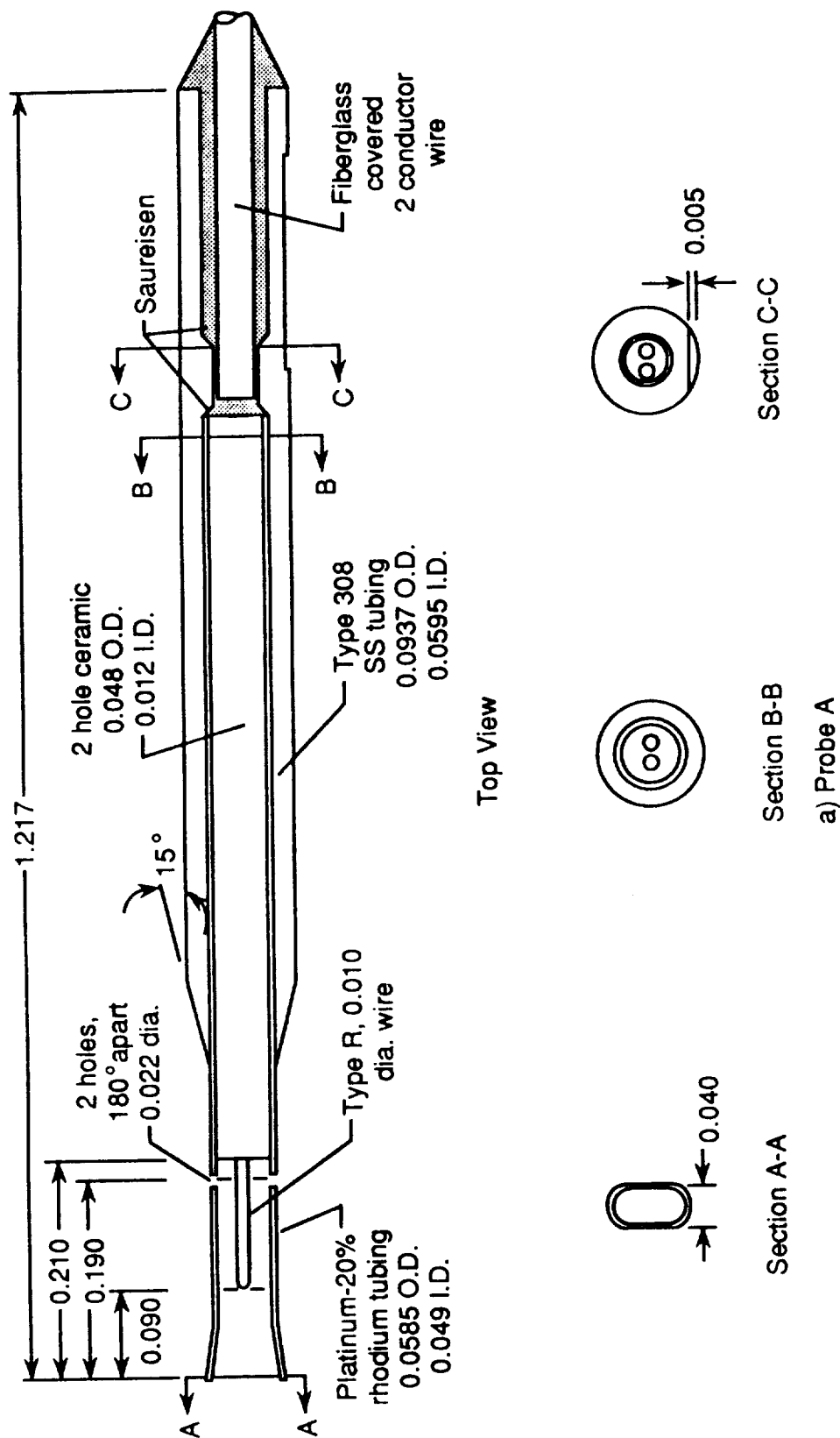


Fig. 11. Total temperature probes. (All dimensions are in inches.)

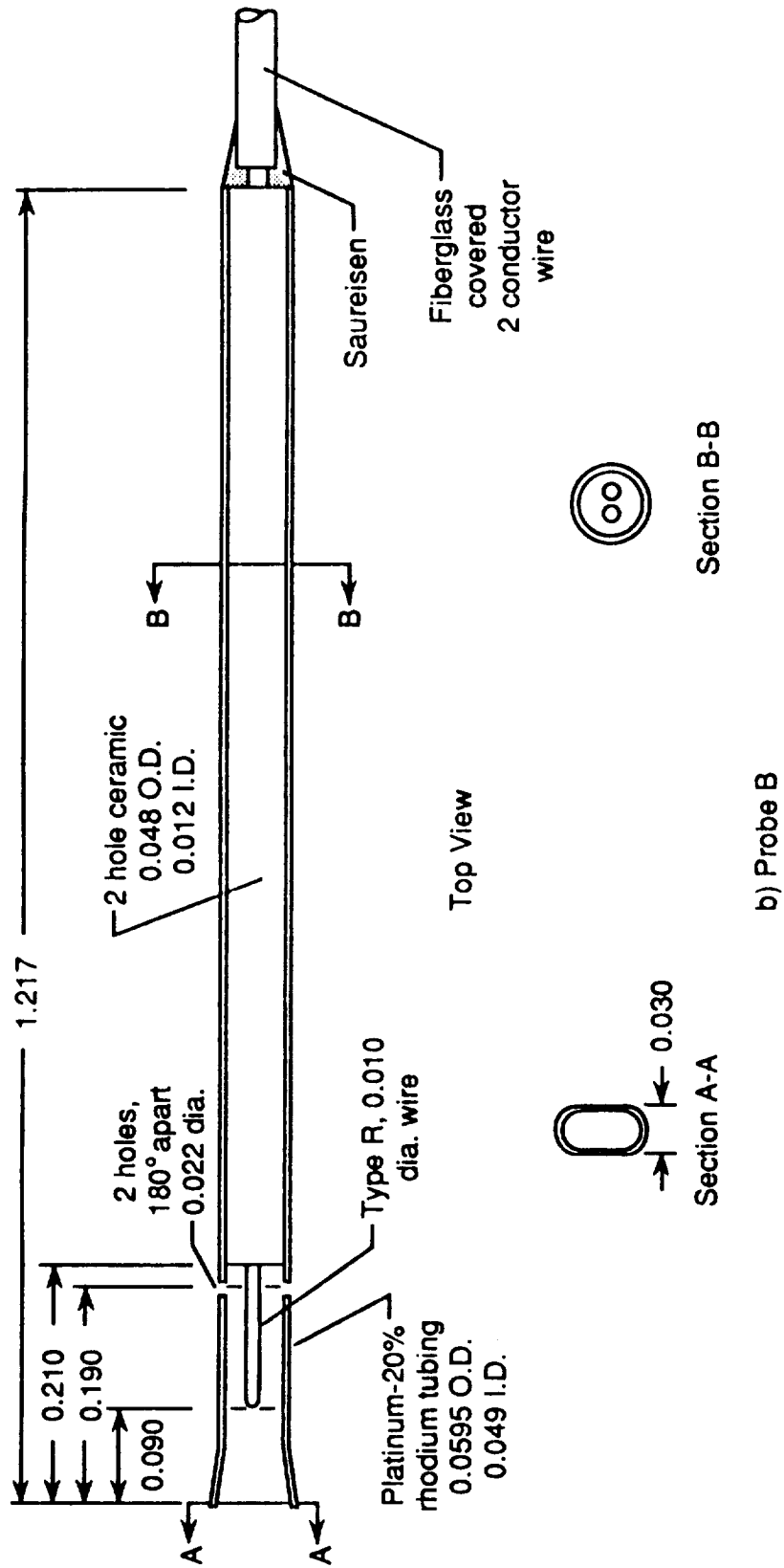
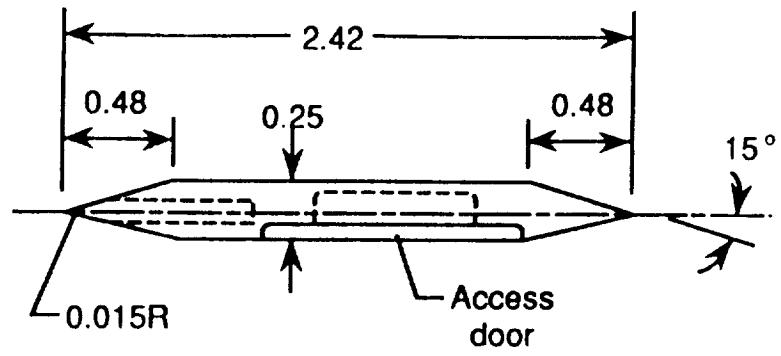
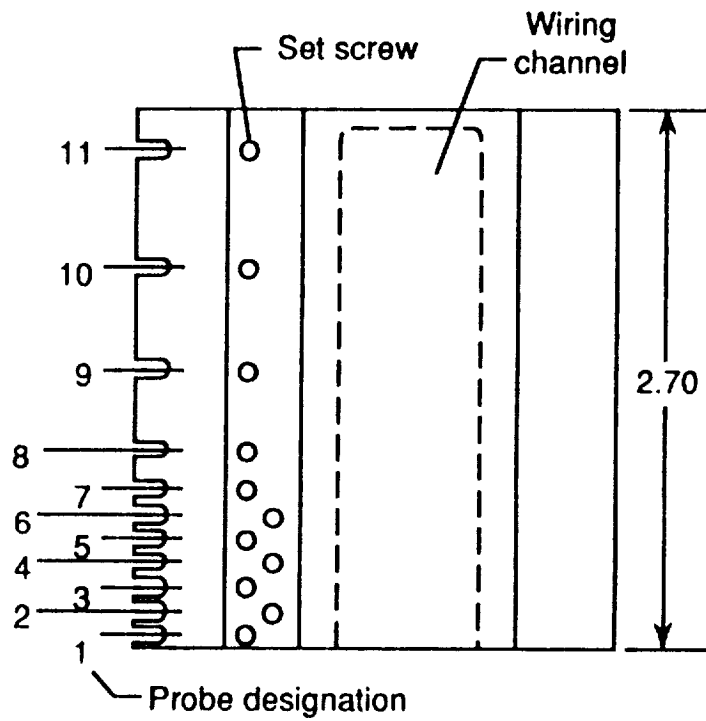


Fig. 11. Concluded.



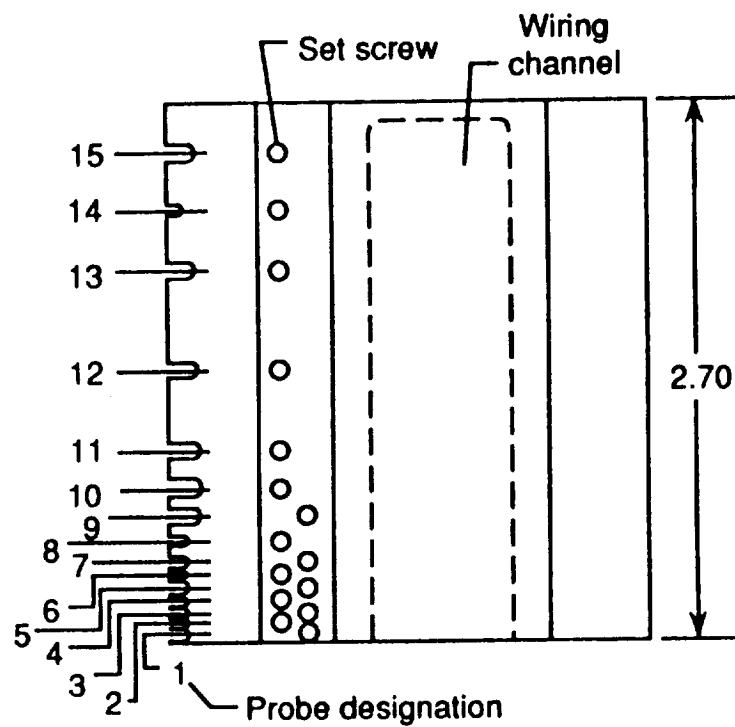
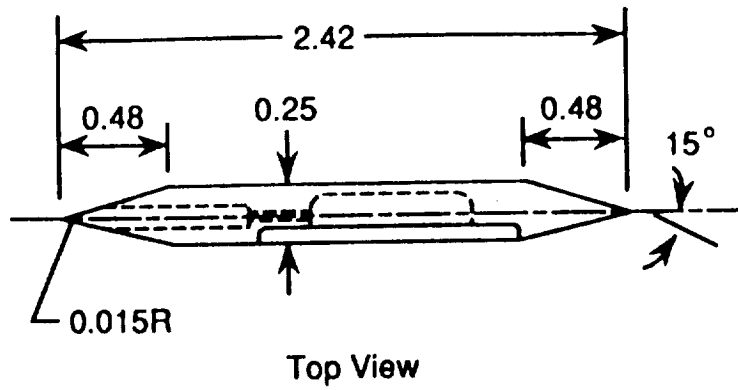
Top View



Side View

a) Rake A

Fig. 12. Total temperature rake (All dimensions are in inches.)



b) Rake B

Fig. 12. Concluded.

Rake A, the initial design, contained 11 type A probes. Rake B contained a total of 15 temperature probes with 8 type B probes located within 0.54 inches of the wall and the remainder being type A probes. Both rakes were machined rather than cast to facilitate replacement of damaged temperature probes and also to minimize conduction errors due to thermal contact. Brass was selected for the rake struts for its high thermal diffusivity, a characteristic necessary for survival during exposure to the high temperature free-stream.

2.3 Data Acquisition, Reduction, and Uncertainties

Pressure transducer and thermocouple outputs were recorded at a rate of 20 times per second using a digital data acquisition system. All signals were filtered with 10 Hz low pass filters and digitized prior to being recorded on magnetic tape. Additional details of the data acquisition equipment are given by Nowak et al. [31].

Pressure data were obtained with strain-gage transducers having nonlinearity errors of less than 0.25 percent of full scale. Gage ranges were selected to be compatible with anticipated measurements. The full scale values of the gages used were 3, 5, and 7.5 psia for surface pressure measurements, 3 psia for the static pressure measurements, and 50, 75, and 100 psia for the pitot pressure measurements, as indicated in Tables 1, 3, and 5. Hence for the gages employed, the nonlinearity errors ranged from 0.0075 to 0.25 psia. To correct for gage offset, (i.e.: slight voltage drifts in the data acquisition equipment) all surface and static pressure outputs were adjusted to correspond to the pressure measured by a precision low pressure gage mounted in the wind tunnel pod. This measurement was obtained prior to

model entry into the flow. Previous surveys of pod pressure have been made to show that there are no significant pressure variations in the pod prior to model insertion and a constant pressure assumption is justified. The gages used for pitot pressure measurements were corrected to barometric pressure prior to tunnel start-up. Overall, the uncertainty of the pressure measurements, including the data acquisition uncertainty, was estimated to be less than ± 1 percent [31].

The temperature histories obtained from the coaxial thermocouples were converted to heating rates using a numerical method which models the thermocouples as a one-dimensional, semi-infinite slab with temperature-dependent properties. The program solves the one-dimensional heat equation using the measured surface temperature as one of the boundary conditions. The other boundary condition is the assumption that the temperature gradient is zero at the opposite end of the thermocouple. The temperature at each node point through the thermocouple thickness was then calculated at each time step using the thermal properties of chromel. Heating rates were calculated at the surface using Fourier's law and a three point backward difference to approximate the temperature difference. The conduction errors in the heating rates resulting from these assumptions were estimated using a finite element thermal analysis program [32]. Because of difficulties in modeling the thin layer of insulation between the chromel plug and surrounding nickel, the conduction errors were bracketed by modeling an uninsulated and a perfectly insulated plug. The calculated errors were -6.5% and -0.3%, respectively at the peak heating condition. Because of the uncertainty in the actual conduction error and because the error is believed to be much less than the -6.5% calculated for the uninsulated case, the data

were not corrected for lateral conduction effects. Additional details regarding the conduction error estimates are presented in Appendix D. Radiation errors, determined to be negligible, are also discussed.

To assess the errors in the total temperature measurements, the total temperatures measured outside the boundary layer were correlated with those measured in the combustor. The probe total temperatures are within 6 percent of the average combustor total temperature and are not corrected. The error in total temperature is estimated to be no worse than -6.0%. Additional details of this correlation and the uncertainties are given in Appendix E.

Mach numbers in the boundary layer were calculated from the measured static and pitot pressures using thermodynamic and transport properties of methane-air combustion products, as given by Leyhe and Howell [33]. The pressures measured with the static pressure probes showed anomalous behavior, as will be discussed in section 3.3.1. Therefore, the pressure measured at the orifice ahead of the static pressure rake, which is shown in Fig. 7, was used to calculate the Mach number distributions. This pressure was assumed to be constant across the height of the rake, which is considered to be a reasonable assumption according to the correlation presented by Bushnell, et al. [34]. Bushnell's correlation estimates a static pressure variation through the boundary layer of only 2.5% at Mach 5. The overall error in the Mach numbers is estimated to be 2.5%

Velocity distributions were calculated from the inferred Mach numbers and static temperatures using the standard equation:

$$U = M (\gamma RT)^{0.5} \quad (1)$$

In Eq. (1), the static temperature, T , was calculated using the total temperature measured by the total temperature probes, the local Mach number, M , and the thermodynamic and transport properties of methane-air combustion products given by Leyhe and Howell [33]. The error in the velocities is estimated to be no greater than 5.5%.

2.4 Test Facility

The NASA Langley 8-foot High Temperature Tunnel (8' HTT), shown schematically in Fig. 13, is a large blowdown wind tunnel which operates at a nominal Mach number of 6.8 and simulates pressure altitudes between 80,000 and 120,000 feet. The high energy test medium is obtained by burning a mixture of methane and air under high pressure in the combustor. The combustion products are expanded to the test chamber Mach number by means of an axisymmetric conical contoured nozzle having an exit diameter of 8 feet. The stream in the test chamber is a free jet which enters a straight tube supersonic diffuser where it is pumped to the atmosphere by means of a single-stage annular air ejector. The tunnel operates at total temperatures from 2300 °R to 3600 °R, free-stream dynamic pressures from 1.7 to 12.5 psia, and free-stream unit Reynolds numbers between 0.3×10^6 and 3.0×10^6 per foot. The maximum run time is 120 seconds.

Models are kept in the pod below the test chamber (Fig. 14) during tunnel start-up and shutdown to minimize aerodynamic loads. Once flow conditions are established, the model is inserted into the flow using a hydraulically actuated elevator. The insertion time from the edge of the test

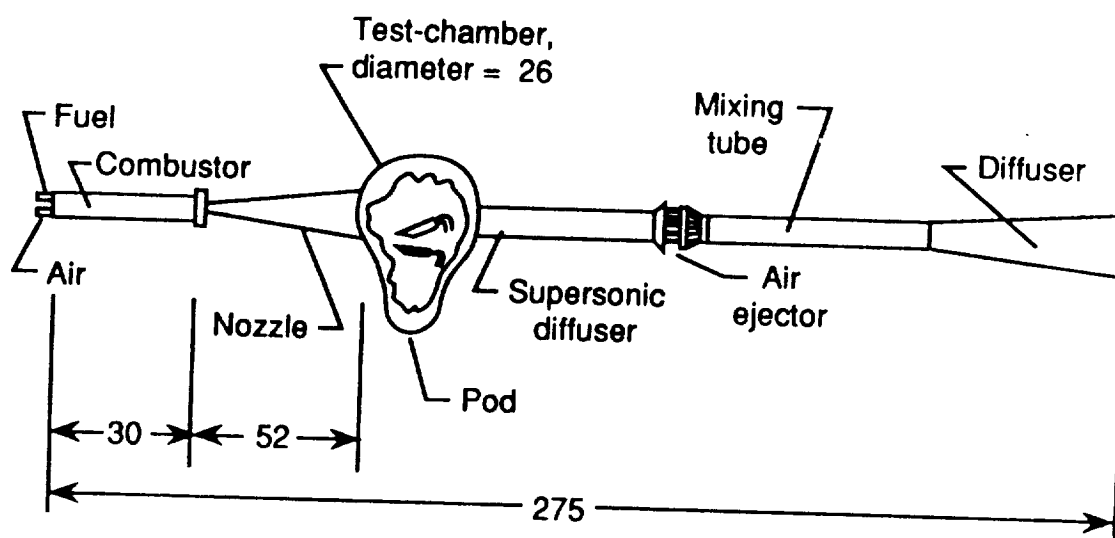


Fig. 13. The NASA Langley 8-foot high-temperature tunnel.
(All dimensions are in feet.)

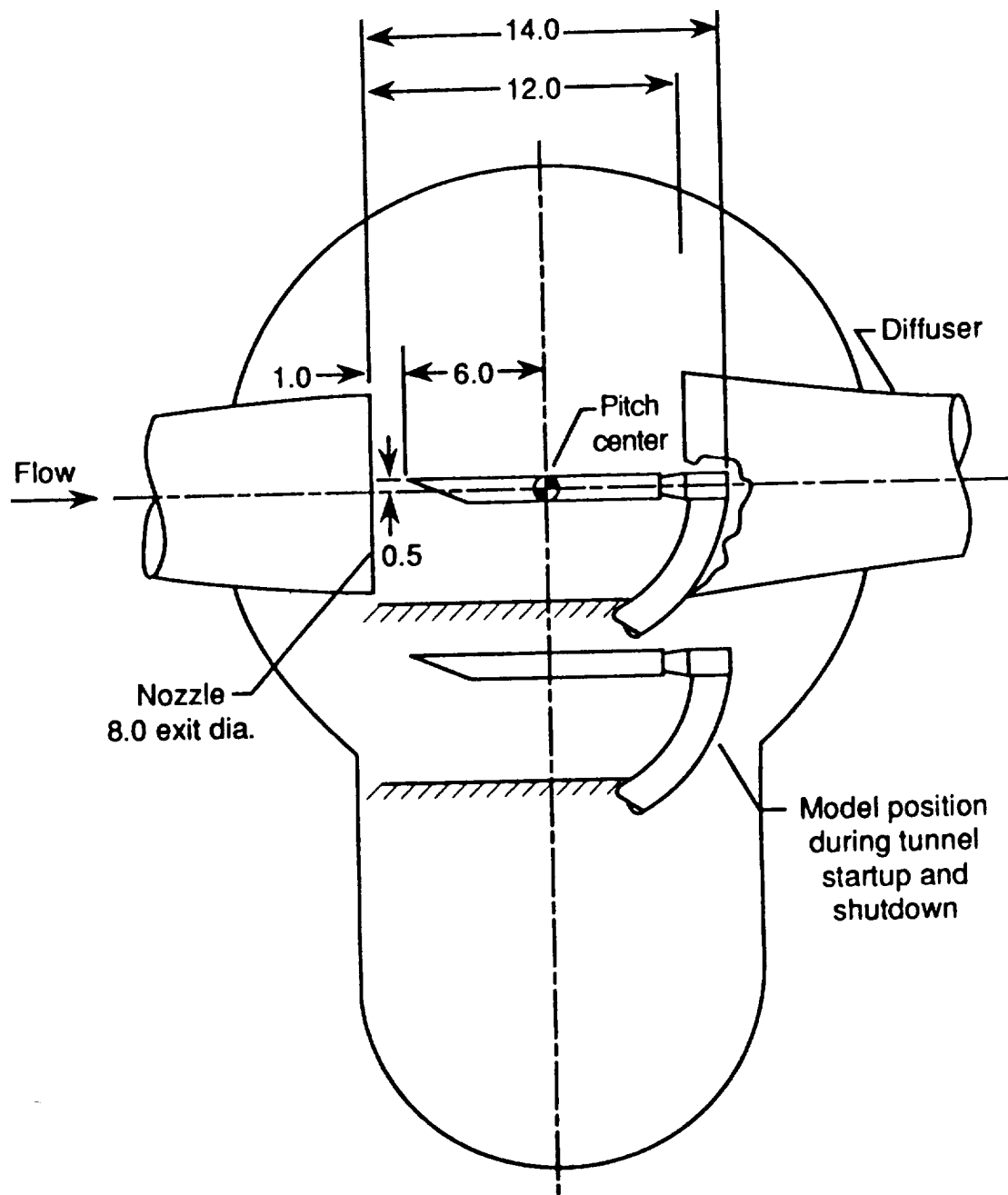


Fig. 14. Cross-sectional view of test chamber of the Langley 8-foot High Temperature Tunnel. (All dimensions are in feet.)

core to the tunnel centerline for the present model was 1.0 second. Prior to tunnel shutdown, the model is withdrawn from the flow.

2.5 Test Conditions

The model was tested at a total of 16 combinations of tunnel operating conditions to determine the boundary-layer characteristics. Most of the tests were conducted at a nominal combustor total temperature of 3300 °R, corresponding to a ratio of adiabatic wall temperature to wall temperature of 5.4. The nominal free-stream Mach number was 6.6 and the free-stream unit Reynolds number ranged from 5.5×10^5 /ft to 1.8×10^7 /ft. The model was tested at two nominal angles of attack of 5 and 13 degrees to produce boundary-layer edge Mach numbers of 6.2 and 5.0, respectively. (The model was pitched down for positive angles of attack.) The corresponding momentum thickness Reynolds number ranged from 400 to 7800. Two additional runs were conducted at a lower nominal combustor total temperature of 2700 °R, corresponding to a ratio of adiabatic wall temperature to wall temperature of 4.4. The model was tested at an angle of attack of 10.8 degrees to match the boundary-layer edge Mach number of 5.0 obtained at the higher combustor total temperature condition. Detailed free-stream flow conditions are given in Table 6. Local conditions corresponding to the rake assembly locations are given in Table 7. Boundary-layer quantities derived from the rake measurements are given in Table 8. The runs are grouped according to the local Mach and unit Reynolds number.

The first three runs (runs 6, 7, and 9) were used primarily to obtain detailed surface pressure and heating rate distributions. Three rake

Table 6 Nominal Free-Stream Flow Conditions

RUN	M _∞	T _{tc} °R	T _∞ °R	H _t btu/lbm	P _{tc} psia	P _{t∞} psia	P _∞ psia	ρ _∞ lbmft ³ x 10 ⁴	γ _∞	U _∞ ft/s	Re _∞ 1/ft x 10 ⁻⁶
9	6.254	3220.	407.	951.	1500.	744.	.180	0.360	1.38	6506.	0.841
10	6.64	3350.	417.	1007.	1500.	860.	.179	0.350	1.38	6706.	0.826
12	6.63	3330.	415.	998.	1500.	840.	.179	0.351	1.38	6675.	0.828
19	6.64	3350.	417.	1007.	1490.	854.	.178	0.348	1.38	6706.	0.821
30	6.56	3260.	410.	968.	1500.	777.	.180	0.357	1.38	6567.	0.836
32	6.63	3340.	416.	1002.	1500.	850.	.179	0.351	1.38	6690.	0.827
16	6.76	3470.	424.	1057.	1970.	1302.	.234	0.449	1.38	6883.	1.070
6	6.54	3240.	408.	960.	2500.	1267.	.300	0.597	1.38	6537.	1.400
18	6.58	3280.	411.	977.	2480.	1314.	.297	0.587	1.38	6598.	1.380
31	6.65	3360.	417.	1011.	2500.	1449.	.298	0.582	1.38	6721.	1.380
33	6.55	3250.	409.	964.	3280.	1681.	.393	0.782	1.38	6552.	1.830
24	6.03	2670.	365.	744.	1740.	485.	.210	0.467	1.38	5702.	1.040
22	6.04	2680.	366.	748.	2320.	654.	.279	0.621	1.38	5716.	1.380
25	6.63	3330.	415.	998.	1000.	560.	.119	0.234	1.38	6675.	0.552
11	6.65	3360.	417.	1011.	2000.	1159.	.239	0.465	1.38	6721.	1.100
7	6.57	3270.	411.	972.	2500.	1310.	.299	0.593	1.38	6583.	1.390

Table 7 Local Conditions Corresponding To Rake Locations

RUN	RAKE NO.	X (in)	Y (in)	α (deg)	M_a	P.W. (psia)	T_{aw} (°F)	β_a (°)	Re _h Ref	$\rho_a \times 10^{-3}$	P.W. (psia)	U_a (ft/sec)	T_{aw} (°F)
10	1	49.00	10.88	13.05	4.98	1.30	5.00	3.90	2.56	4.93	3.74	27.0	3130
	2	49.00	0.00	13.05	4.99	0.32	5.54	3.90	2.56	4.93	3.74	27.0	3130
	3	49.00	-10.12	13.05	4.93	1.90	5.46	3.32	2.57	4.07	3.08	27.3	3170
12	1	49.00	10.88	12.98	5.11	0.325	5.56	2.65	2.89	4.60	3.27	29.2	3230
	2	49.00	0.00	12.98	4.93	0.97	5.42	3.73	2.78	3.81	2.40	24.4	3150
	3	49.00	-10.12	12.98	4.98	0.97	5.26	3.90	2.85	3.34	2.07	23.0	3110
30	1	86.12	0.00	12.38	4.95	0.933	5.15	4.33	2.65	3.53	2.07	22.9	3050
	2	86.12	0.00	12.72	4.96	0.336	5.33	4.63	2.32	3.72	2.26	23.4	3100
	3	86.12	-10.12	12.35	4.94	1.35	5.70	3.77	2.50	3.64	3.03	23.9	3160
18	1	49.00	10.88	12.32	4.96	1.73	5.25	4.39	2.94	3.68	3.71	22.6	3060
	2	49.00	0.00	12.32	4.95	1.36	5.22	5.31	2.99	3.16	3.15	21.6	3030
	3	49.00	-10.12	12.32	4.99	1.71	5.24	7.20	3.03	3.64	3.51	22.3	3040
31	1	36.12	0.00	13.03	4.88	1.56	5.54	8.31	2.40	3.03	3.49	22.5	3210
	2	36.12	0.00	12.70	4.92	2.12	5.41	11.07	2.58	2.82	4.00	21.3	3140
	3	36.12	-10.12	10.85	5.14	0.84	4.51	3.38	3.48	4.03	2.23	24.9	2630
22	1	49.00	10.88	10.82	5.10	1.11	4.48	4.09	3.39	4.11	2.23	25.0	2480
	2	49.00	0.00	10.82	5.05	1.04	4.05	3.87	3.19	3.95	2.92	24.7	2610
	3	49.00	-10.12	10.82	4.97	1.10	4.20	4.12	3.68	3.71	2.70	23.7	2440
25	1	49.00	10.88	4.97	6.27	0.222	5.31	0.71	4.00	6.00	1.20	34.6	3100
	2	49.00	0.00	4.97	6.33	0.122	5.30	0.84	5.32	5.75	1.11	33.9	3090
	3	49.00	-10.12	4.97	6.19	0.122	5.31	0.96	4.91	5.37	1.07	32.3	2860
11*	1	49.00	10.88	4.93	6.37	0.450	5.50	1.46	5.97	5.02	2.05	32.3	3270

*Signal conditioner for rakes 2 and 3 failed

Table 8 Boundary Layer Quantities Derived From Rake Measurements

RUN	RAKE NO.	x (in)	y (in)	δ (in)	δ^+ (in)	$\theta \times 10^{-2}$ (in)	$\frac{\delta^+}{\theta}$	Δ (in)	G	$\delta_H \times 10^{-2}$ (in)	$\frac{\delta_H}{\delta^+}$	$\frac{\delta_H}{\theta}$	N	$Re_{\delta^+} \times 10^{-4}$	$Re_{\theta} \times 10^3$
10	1	49.00	10.88	0.54	0.186	3.88	4.79	1.39	6.08	6.64	0.249	1.20	5.41	1.06	2.22
	2	49.00	0.00	0.47	0.169	2.82	5.99	1.40	5.66	3.09	0.183	1.10	6.80	0.97	1.61
	3	49.00	-10.12	0.66	0.221	4.01	5.51	1.64	5.22	4.72	0.214	1.18	6.77	1.26	2.29
12	1	49.00	10.88	0.58	0.219	3.77	5.81	1.24	4.91	4.66	0.213	1.24	5.81	1.18	2.04
	1	49.00	10.88	0.59	0.209	4.11	5.08	1.80	5.94	4.97	0.238	1.21	5.74	1.16	2.29
	2	60.00	0.00	0.66	0.259	4.18	6.20	2.43	6.83	3.99	0.154	0.95	5.81	1.39	2.24
19	3	71.00	-10.12	0.85	0.314	5.42	5.79	2.37	6.82	5.15	0.164	0.95	5.94	1.72	2.98
30	2	86.12	0.00	0.92	0.355	5.61	6.32	3.68	6.47	6.44	0.181	1.15	6.30	1.99	3.15
	2	86.12	0.00	0.97	0.361	6.31	5.72	3.78	6.51	6.02	0.166	0.95	5.90	2.03	3.53
16	1	49.00	10.88	0.59	0.199	4.15	4.80	1.92	6.20	4.89	0.246	1.04	5.63	1.53	3.19
	2	60.00	0.00	0.68	0.244	4.54	5.37	2.54	6.42	4.71	0.193	1.09	5.80	1.72	3.21
	3	71.00	-10.12	0.86	0.303	5.26	5.76	2.67	6.69	5.39	0.178	1.02	6.68	2.21	3.84
18	1	49.00	10.88	0.06	0.206	3.94	5.23	1.75	6.28	4.59	0.223	1.16	6.12	2.06	4.91
	2	49.00	0.00	0.72	0.256	4.70	5.45	2.59	6.72	4.82	0.188	1.03	6.36	2.39	4.39
	3	49.00	-10.12	0.84	0.285	5.14	5.55	2.64	6.68	5.61	0.197	1.09	6.86	2.96	5.56
31	2	86.12	0.00	1.03	0.373	6.53	5.71	3.99	6.59	7.02	0.188	1.08	6.40	3.60	6.30
	2	86.12	0.00	1.00	0.370	6.10	6.06	4.05	6.86	6.91	0.187	1.43	6.79	4.75	7.84
24	1	49.00	10.88	0.52	0.194	3.30	5.88	1.45	5.62	4.65	0.243	1.45	6.01	1.16	1.97
	2	61.00	0.00	0.52	0.222	3.12	7.12	1.77	6.41	3.80	0.168	1.22	5.82	1.21	1.71
	3	71.00	-10.12	0.61	0.273	3.74	7.28	2.14	6.17	4.87	0.178	1.30	5.80	1.57	2.15
22	1	49.00	10.88	0.48	0.191	3.20	5.97	1.64	5.98	4.78	0.250	1.49	5.90	1.50	2.52
	2	60.00	0.00	0.55	0.226	3.29	6.87	1.84	6.36	4.61	0.204	1.40	6.05	1.65	2.40
	3	71.00	-10.12	0.61	0.259	3.75	6.91	2.12	6.15	5.10	0.197	1.36	6.00	1.98	2.86
25	1	49.00	10.88	0.52	0.154	3.50	4.40	1.04	4.25	5.27	0.342	1.50	6.56	0.226	0.514
	2	60.00	0.00	0.49	0.208	2.74	7.59	1.16	5.00	2.14	0.103	0.78	6.16	0.297	0.391
	3	71.00	-10.12	0.70	0.302	3.66	8.25	1.82	4.49	3.28	0.108	0.90	6.81	0.447	0.541
11	1	49.00	10.88	0.54	0.176	3.56	4.94	1.31	5.65	5.24	0.298	1.47	6.02	0.524	1.06

assemblies were then installed to assess spanwise variations in the boundary layer (run 10). The rake assemblies were then installed along a diagonal to assess streamwise variations. The diagonal arrangement was necessary to avoid interference between rake assemblies and minimize the number of runs. The final four runs (runs 30 through 33) were conducted with a single rake assembly installed at the aft most location from the leading edge. Note that the majority of the runs were made at an angle of attack of 13 degrees. This angle of attack was found to be necessary to produce Reynolds numbers which were high enough to produce large zones of equilibrium turbulent boundary layers, as discussed further in Chapter 4.

Chapter 3

RESULTS AND DISCUSSION OF SURFACE AND BOUNDARY LAYER MEASUREMENTS

The surface pressure and heating rate data presented in this chapter have been selected to show repeatability and flow uniformity as a function of angle of attack and Reynolds number. Boundary-layer distributions, consisting primarily of Mach number, total temperature, and velocity measurements, are then examined for uniformity as a function of spanwise and longitudinal position, Reynolds number, and ratio of adiabatic wall temperature to wall temperature. A limited number of static pressure distributions are also presented to assess static pressure variations in the boundary layer. The velocity distributions are correlated in terms of a power law exponent as a function of momentum thickness Reynolds number. Also total temperature variations with velocity in the boundary layer are shown and compared with the linear Crocco-Busemann relationship [22 and 23] and the quadratic relationship given by Bushnell et. al. [35].

The data are not shown for every run; however all the data are tabulated in Appendices G and H. Surface pressures, wall temperatures, heating rates, and Stanton numbers are tabulated for each run in Appendix G. Boundary-layer distributions, consisting of total temperature, static pressure, pitot pressure, Mach number, and velocity are tabulated in Appendix H.

3.1 Surface Pressure Distributions

3.1.1 Data Repeatability

Longitudinal surface pressure distributions for two runs are presented in Fig. 15 to demonstrate typical repeatability of the test conditions and model data. The data were obtained at a nominal angle of attack of 12.8° , free-stream Mach number of 6.6, and free-stream unit Reynolds number of 0.83×10^6 per foot. The ratio of adiabatic wall temperature to wall temperature, T_{aw}/T_w , was 5.6. The magnitudes of the surface pressures and their sensing locations were normalized by the free-stream static pressure and the length of the plate, respectively. The measurements show excellent repeatability and indicate that any differences between sets of measurements can be attributed to variations in flow conditions rather than anomalous instrumentation or facility behavior. The longitudinal gradients evident in the distributions along with spanwise gradients are discussed in detail in section 3.1.3.

3.1.2 Effect of Boundary-Layer Rake Assemblies

Longitudinal surface pressure distributions are shown in Fig. 16 for runs without (Run 6) and with (Run 18) the rake assemblies installed on the plate. The data were obtained at a nominal angle of attack of 12.9° , free-stream Mach number of 6.5, and free-stream unit Reynolds number of 1.4×10^6 per foot. The temperature ratio, T_{aw}/T_w , was 5.6. As anticipated, the surface pressures are in good agreement, except downstream of the rakes. Therefore,

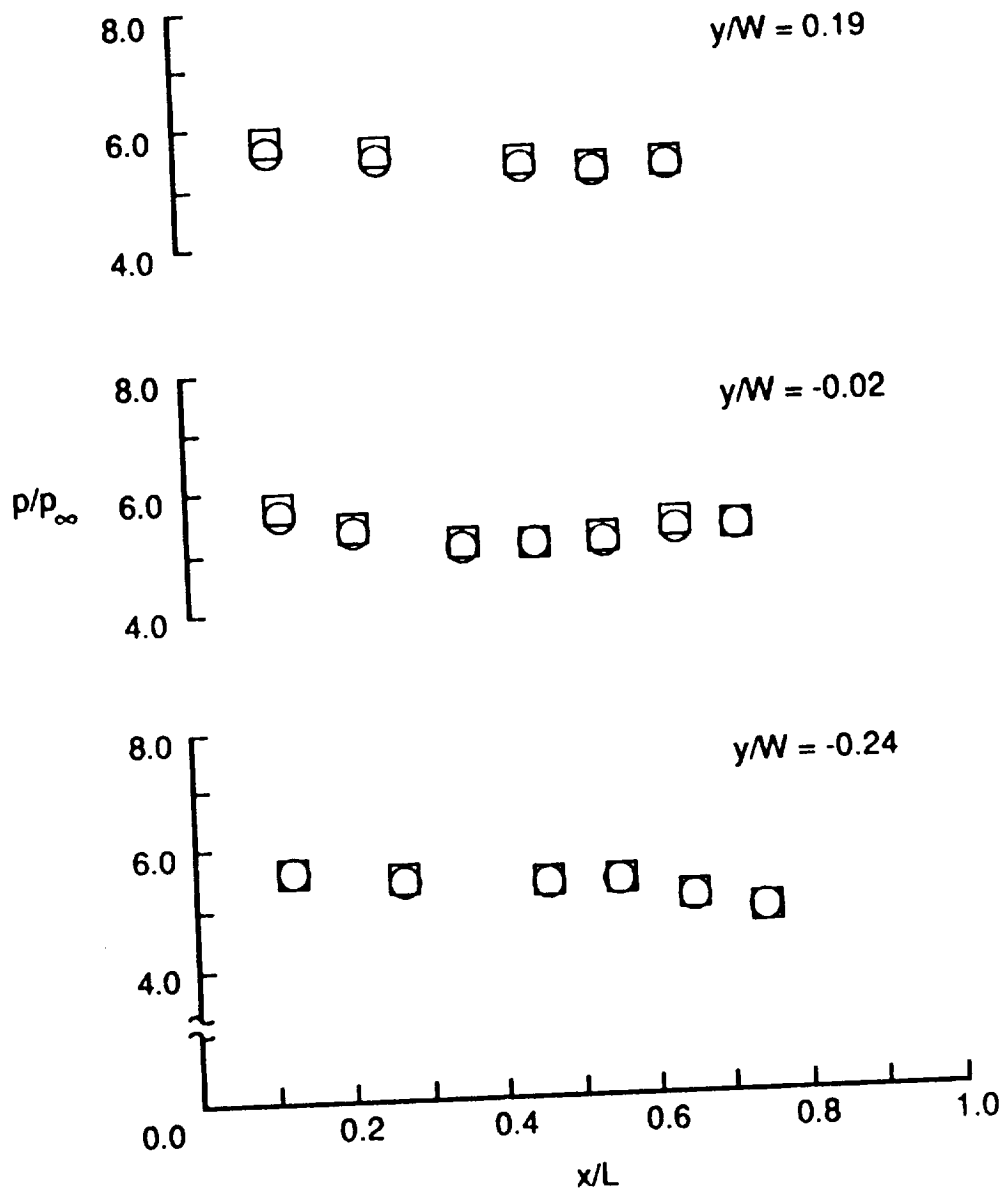
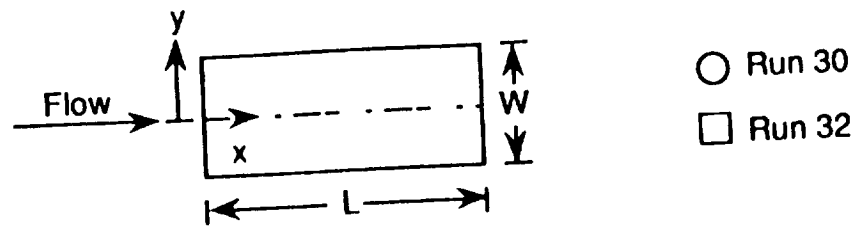


Fig. 15. Surface pressure repeatability.
 $(M_\infty = 6.6, \alpha = 12.8^\circ, Re_\infty = 0.83 \times 10^6 / \text{ft.}, T_{aw} / T_w = 5.6)$

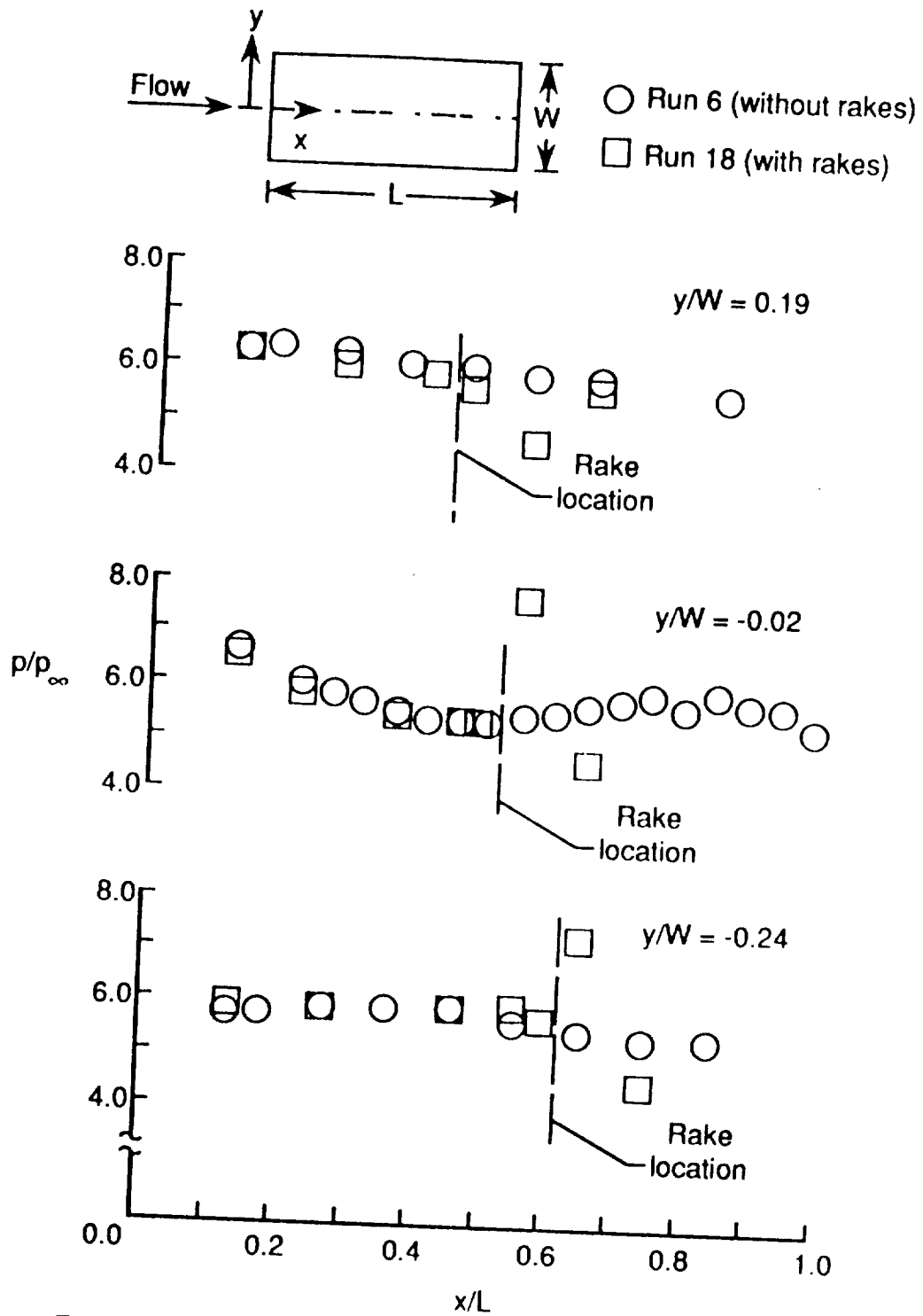


Fig. 16. Effect of boundary-layer rake assemblies on surface pressure distributions.
 $(M_\infty = 6.5, \alpha = 12.9^\circ, Re_\infty = 1.4 \times 10^6 / \text{ft.}, T_{aw} / T_w = 5.6)$

the measurements obtained ahead of the rakes can be assumed to be in undisturbed flow and not affected by the presence of the rakes.

3.1.3 Effect of Angle of Attack

Detailed longitudinal and spanwise surface pressure distributions are shown in Figs. 17 and 18, respectively, for angles of attack of 5.6° and 13.0° . The data were obtained at a nominal free-stream Mach number of 6.5, a free-stream unit Reynolds number of 1.4×10^6 per foot, and a temperature ratio, T_{aw}/T_w , of 5.6. Predicted pressures, indicated by the solid and dashed lines, (See Fig. 17.) were obtained using oblique shock theory [30] and boundary-layer induced pressure theory [36]. These two types of predictions are shown for comparison purposes. In the spanwise distributions (Fig. 18), the expected uniform pressure regions are indicated. These regions result from the finite width of the plate and were determined by calculating the angle of characteristic lines using the local Mach number. The characteristic lines, indicated by the dashed lines in Fig. 18, were calculated for both $\alpha = 5.6^\circ$ and 13.0° using the corresponding local Mach numbers.

For the lower angle of attack, $\alpha = 5.6^\circ$, both the longitudinal and spanwise pressure distributions shown in Figs. 17 and 18a are uniform, indicating that the boundary layer can be classified essentially as a zero pressure gradient boundary layer. However, at $\alpha = 13.0^\circ$, pressure gradients are evident in certain areas of the plate. Longitudinal pressure gradients are present at $\alpha = 13.0^\circ$ (Fig. 17) in the leading edge region near the centerline of the plate ($y/W = 0.19, 0.08, -0.02$, and -0.13). These gradients are larger than predicted by boundary-layer induced pressure theory, and are hence due in part to some other phenomena. In the spanwise distributions for $\alpha = 13.0^\circ$,

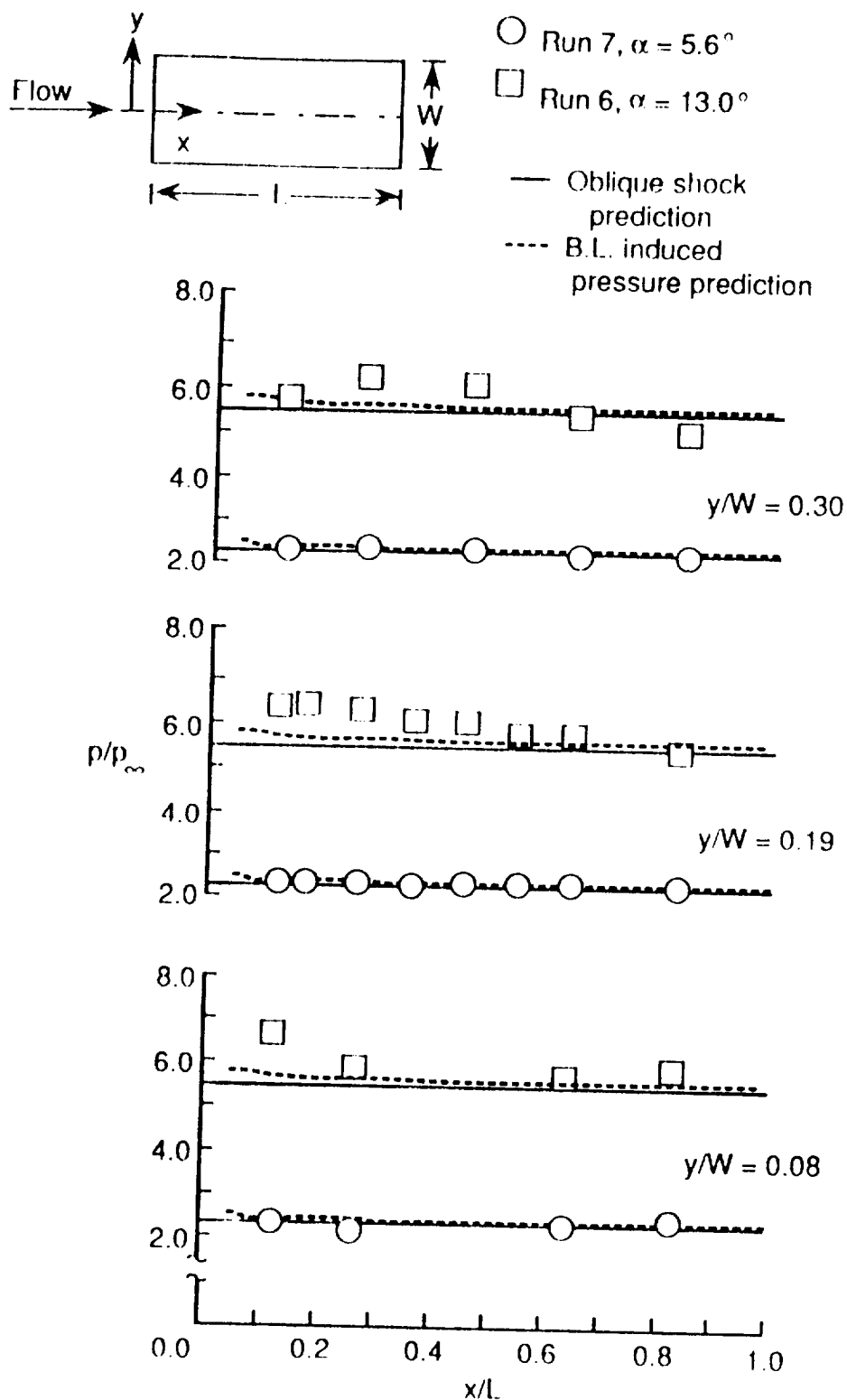


Fig. 17. Effect of angle of attack on longitudinal surface pressure distributions.
 ($M_\infty = 6.5$, $Re_\infty = 1.4 \times 10^6$ /ft., $T_{aw}/T_w = 5.6$)

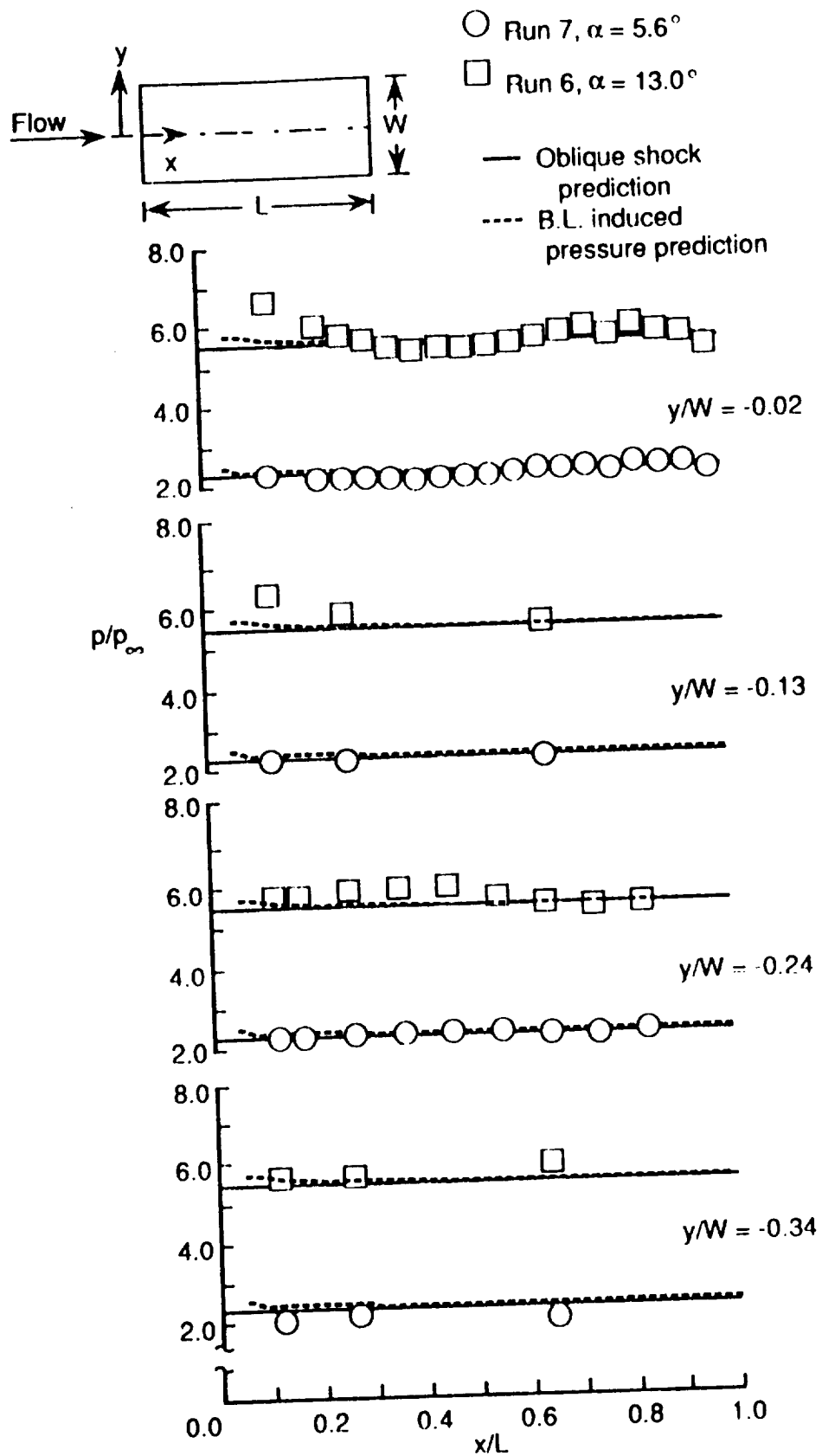
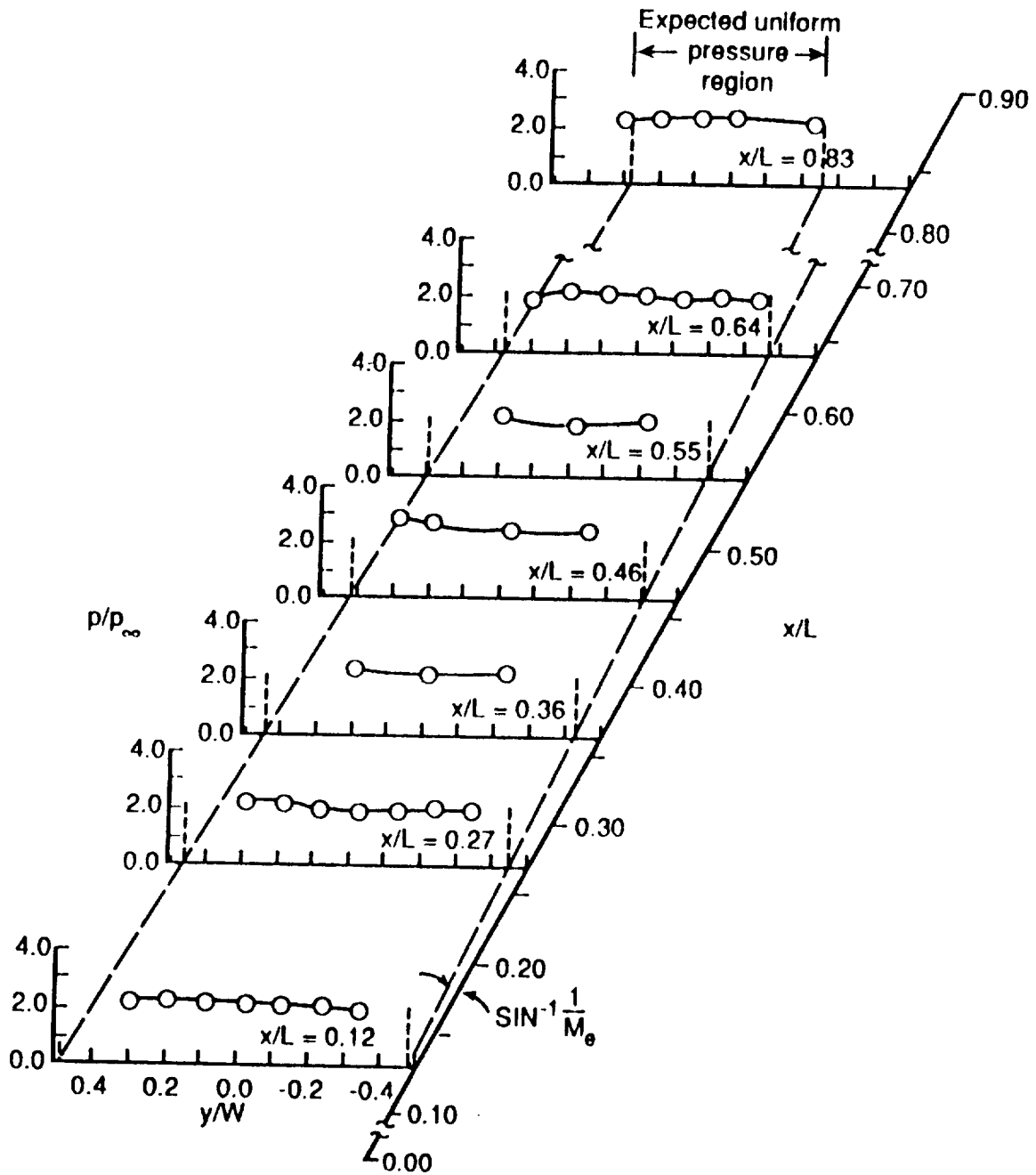


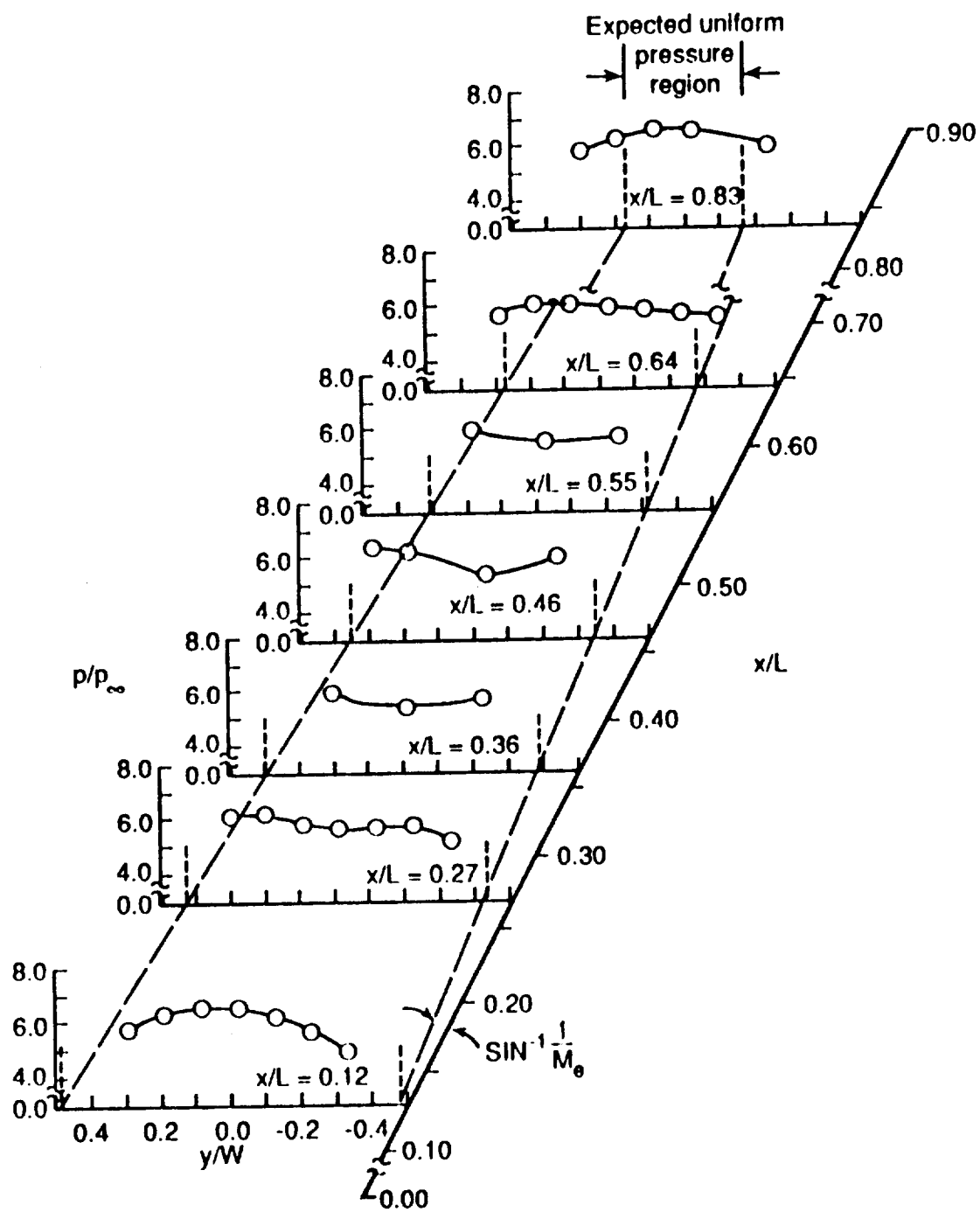
Fig. 17. Concluded.



a) $\alpha = 5.6^\circ$ (Run 7)

Fig. 18. Spanwise surface pressure distributions.

($M_\infty = 6.5$, $Re_\infty = 1.4 \times 10^6$ /ft., $T_{aw}/T_w = 5.6$)



b) $\alpha = 13.0^\circ$ (Run 6)

Fig. 18. Concluded.

(Fig. 18b) pressure gradients are evident near the leading edge at $x/L = 0.12$. These gradients diminish gradually with distance from the leading edge and are nearly zero at $x/L = 0.55$. The spanwise pressure gradients near the trailing edge at $x/L = 0.83$ can be explained by disturbances resulting from the finite width of the plate. As illustrated by the characteristic lines in Fig. 18, these disturbances gradually propagate towards the centerline of the plate, varying linearly with distance from the leading edge. The longitudinal and spanwise gradients near the leading edge are most likely the result of pressure variations in the test section core, as discussed in Appendix F. The pitot and static pressures measured in the test section core show gradients across the height of the core which diminish with distance from the nozzle exit. Similar gradients across the span of the test core would explain why the spanwise pressure gradients on the plate surface diminish with distance from the leading edge. It is noted that the model is exposed to a smaller portion of the test core at small angles of attack. The model should experience smaller spanwise free-stream pressure gradients near the leading edge of the plate at $\alpha = 5.6^\circ$, because it is nominally in the center of the core flow, producing more uniform pressure distributions in this region. Also, the angle of the characteristic lines is smaller at smaller angles of attack, resulting in more gradual deterioration of the spanwise pressure field due to finite width.

3.1.4 Effect of Free-Stream Unit Reynolds Number

The effect of free-stream unit Reynolds number on the longitudinal surface pressure distributions is shown in Fig. 19 for a nominal angle of attack of 13° and a nominal free-stream Mach number of 6.6. The slight differences in the overall pressure levels is probably due to small differences in angle of

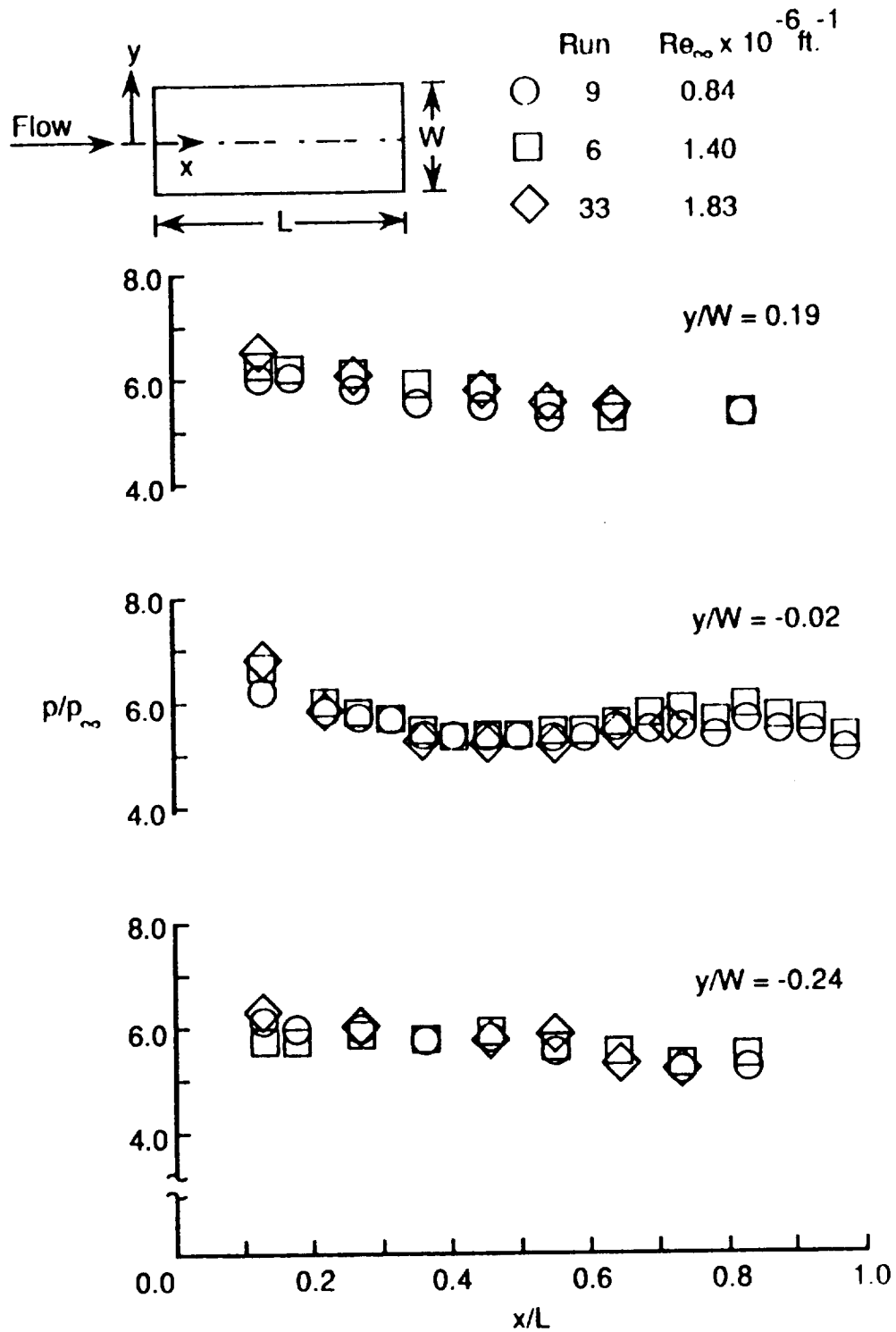


Fig. 19. Effect of free-stream unit Reynolds number on longitudinal surface pressure distributions. ($M_\infty = 6.6$, $\alpha = 13.0^\circ$, $T_{aw}/T_w = 5.6$)

attack and free-stream Mach number between the three runs. The trends in the data, however, are independent of the free-stream unit Reynolds number.

3.2 Surface Heating Rate Distributions

Longitudinal and spanwise surface heating rates are presented in this section to assess conditions in which transition from laminar to turbulent flow is complete and also to identify conditions in which the boundary layer may be affected by spanwise variations in transition location. The longitudinal heating rate distributions are nondimensionalized in terms of Stanton and Reynolds number distributions calculated at a reference temperature. The reference temperature is defined in terms of enthalpy using a correlation given by Eckert [37]:

$$H^* = H_e + 0.50 (H_w - H_e) + 0.22 (H_{aw} - H_e) \quad (2)$$

The temperature corresponding to the reference enthalpy was then obtained from temperature-enthalpy charts for methane-air combustion products given by Leyhe and Howell [33].

Laminar and turbulent Stanton number predictions are presented with the longitudinal distributions to assist in defining conditions in which the boundary layer is turbulent. These predictions were obtained using the equations given by Kays and Crawford [38], which are:

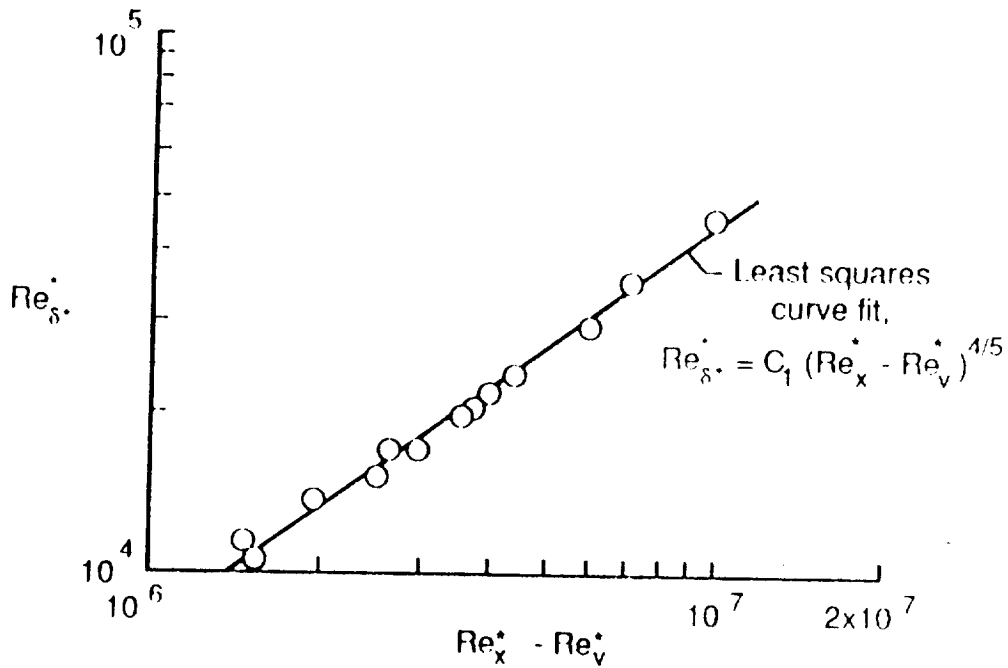
$$St^* = 0.332 Pr^{*-2/3} Re_x^{*-1/2} \quad (\text{laminar}) \quad (3)$$

$$St^* = 0.0287 Pr^{*-0.40} (Re_x^* - Re_v^*)^{-1/5} \quad (\text{turbulent}) \quad (4)$$

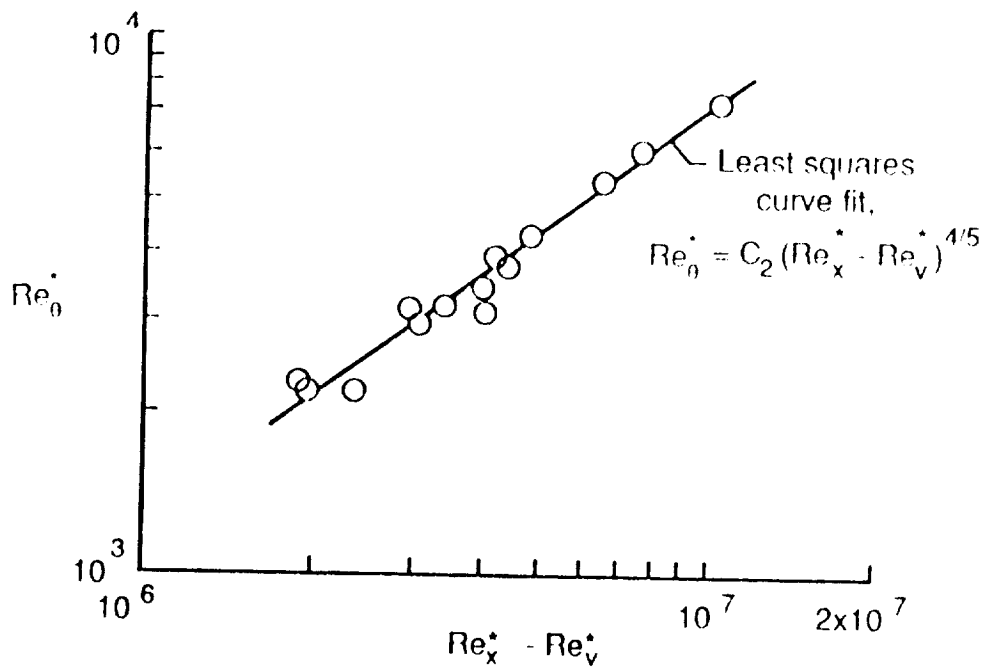
In Eq. (4), Re_v^* is the Reynolds number corresponding to the virtual origin of the turbulent boundary layer. For the turbulent predictions presented with the heating rate data, Re_v^* was determined by first calculating the local Reynolds number, Re_x^* , corresponding to a displacement thickness Reynolds number, $Re_{\delta^*}^*$, of zero using a least squares curve fit. This resulted in a local Reynolds number, Re_x^* , of 0.85×10^6 . This exercise was repeated using the momentum thickness Reynolds number and yielded a Re_x^* of 1.27×10^6 . An average value of 1.06×10^6 was then used for Re_v^* in Eq. (4). The variations of displacement thickness Reynolds number and momentum thickness Reynolds number with local Reynolds number are presented in Fig. 20. Both quantities vary by an approximate 4/5 power with local Reynolds number, as one would expect for a turbulent boundary layer. The constants C_1 and C_2 shown in the least squares curve fit equations (See Fig. 20.) are 0.0195 and 0.119, respectively. The displacement and momentum thicknesses were determined from measurements obtained from the boundary-layer rakes, as will be discussed in Chapter 4.

3.2.1 Effect of Angle of Attack

The effect of angle of attack on longitudinal and spanwise heating rate distributions is shown in Figs. 21 and 22, respectively. The longitudinal heating rates are presented in terms of a Stanton number variation with local Reynolds number. The spanwise heating rates are scaled by the heating rates measured along the centerline of the plate. The data were obtained at a nominal free-stream Mach number of 6.5 and a free-stream unit Reynolds number of $1.4 \times 10^6 \text{ ft}^{-1}$. The temperature ratio, T_{aw}/T_w , was 5.6.



a) Displacement thickness Reynolds number variation with local Reynolds number



b) Momentum thickness Reynolds number variation with local Reynolds number

Fig. 20. Correlation of displacement and momentum thickness Reynolds number with local Reynolds number.

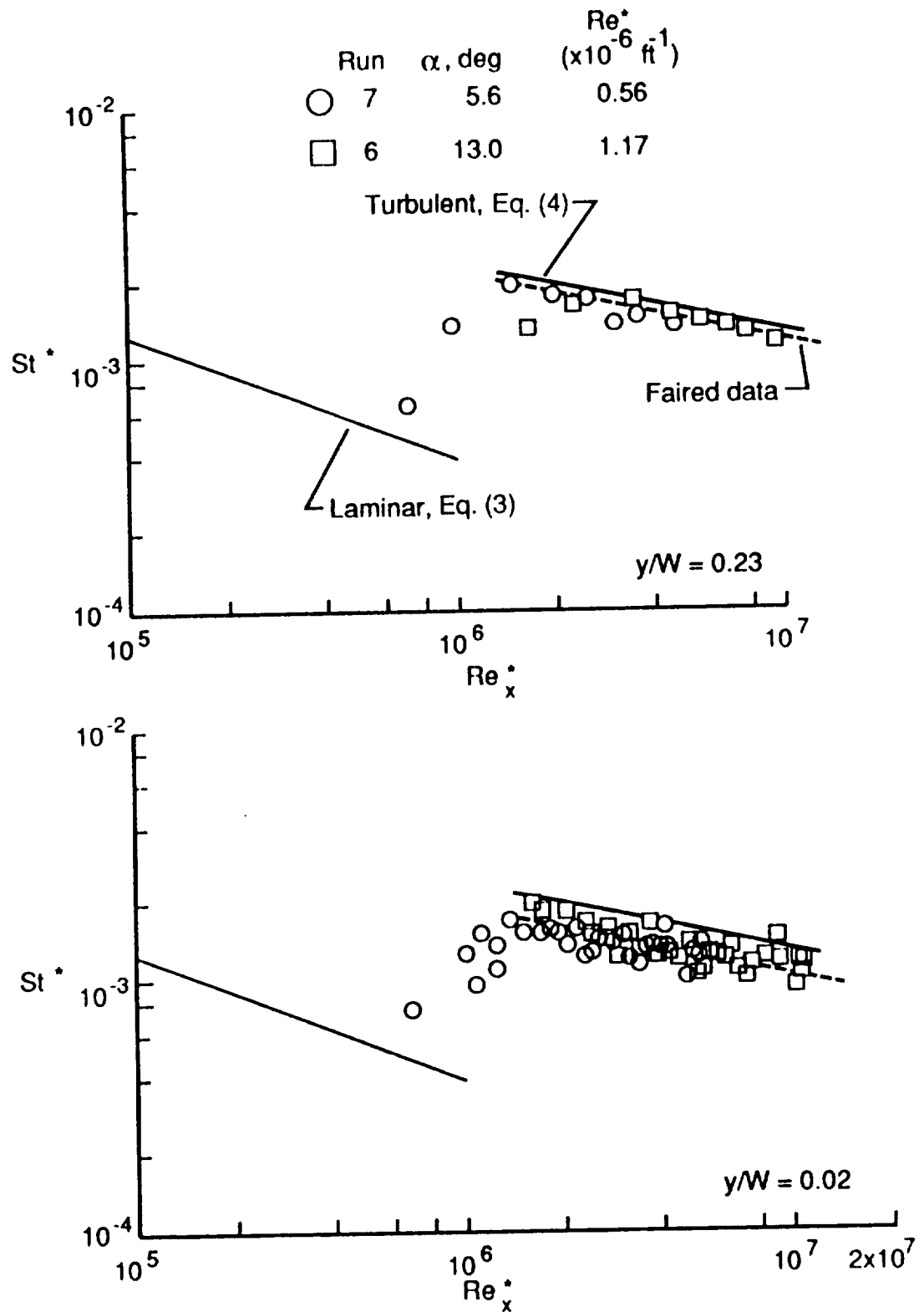


Fig. 21. Longitudinal surface Stanton number distributions for various angles of attack.

($M_\infty = 6.5$, $Re_\infty = 1.4 \times 10^6 / \text{ft.}$, $T_{aw} / T_w = 5.6$)

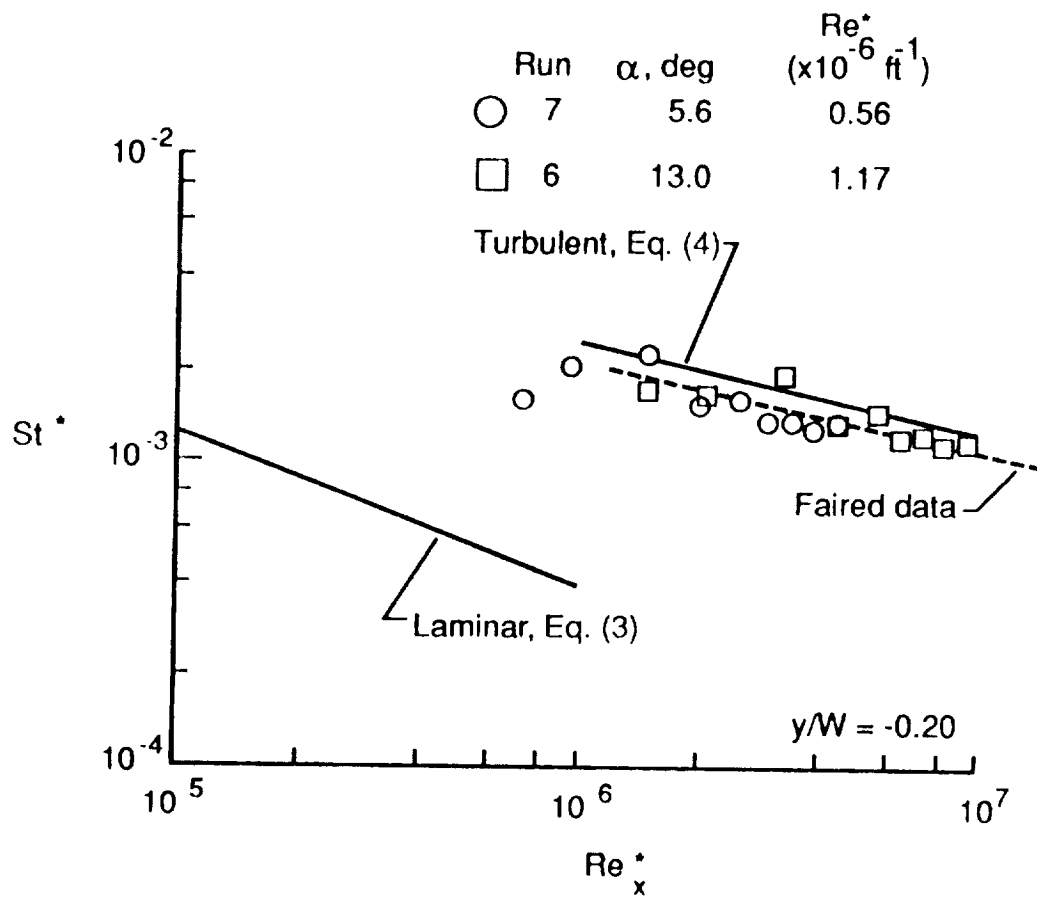
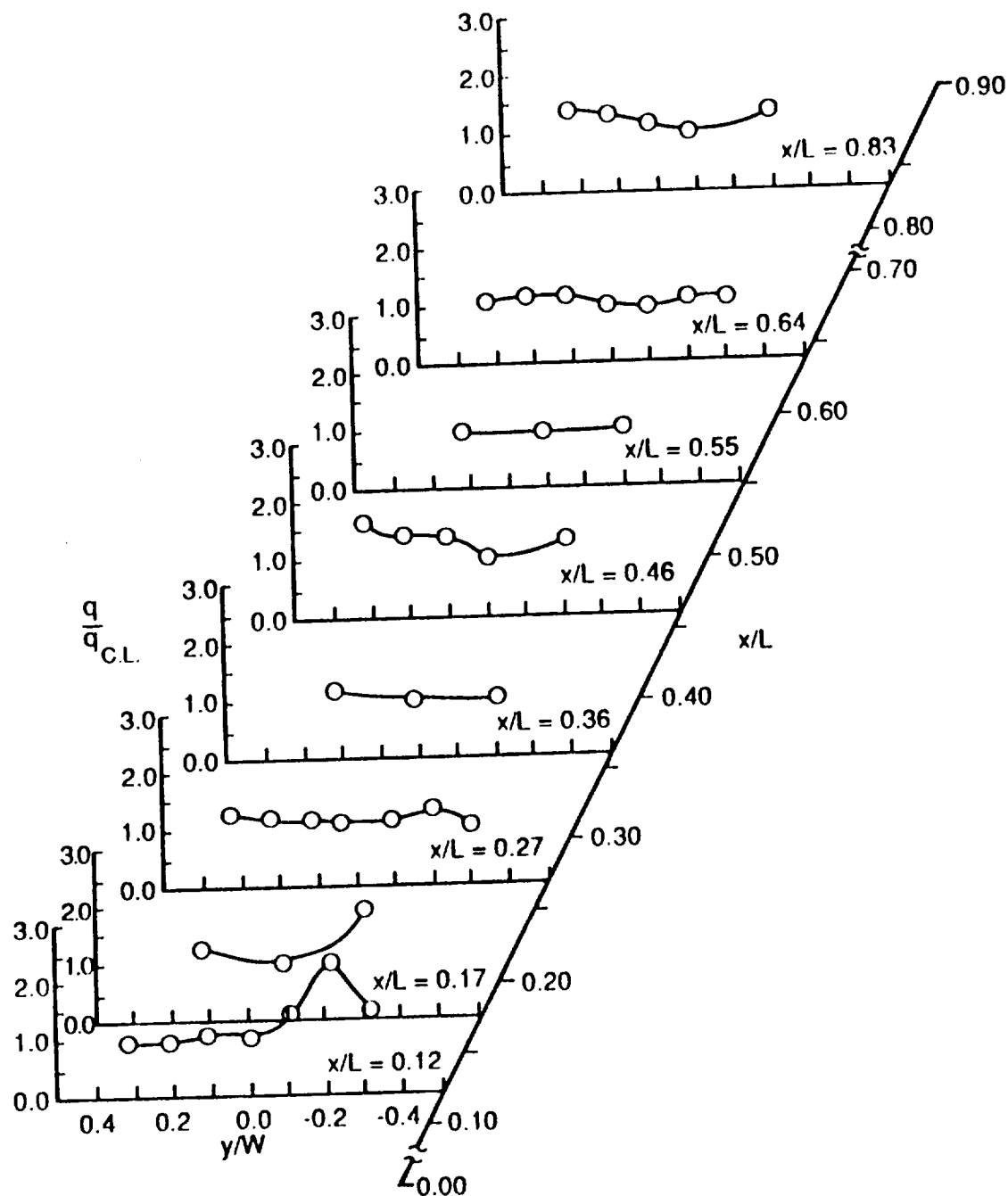
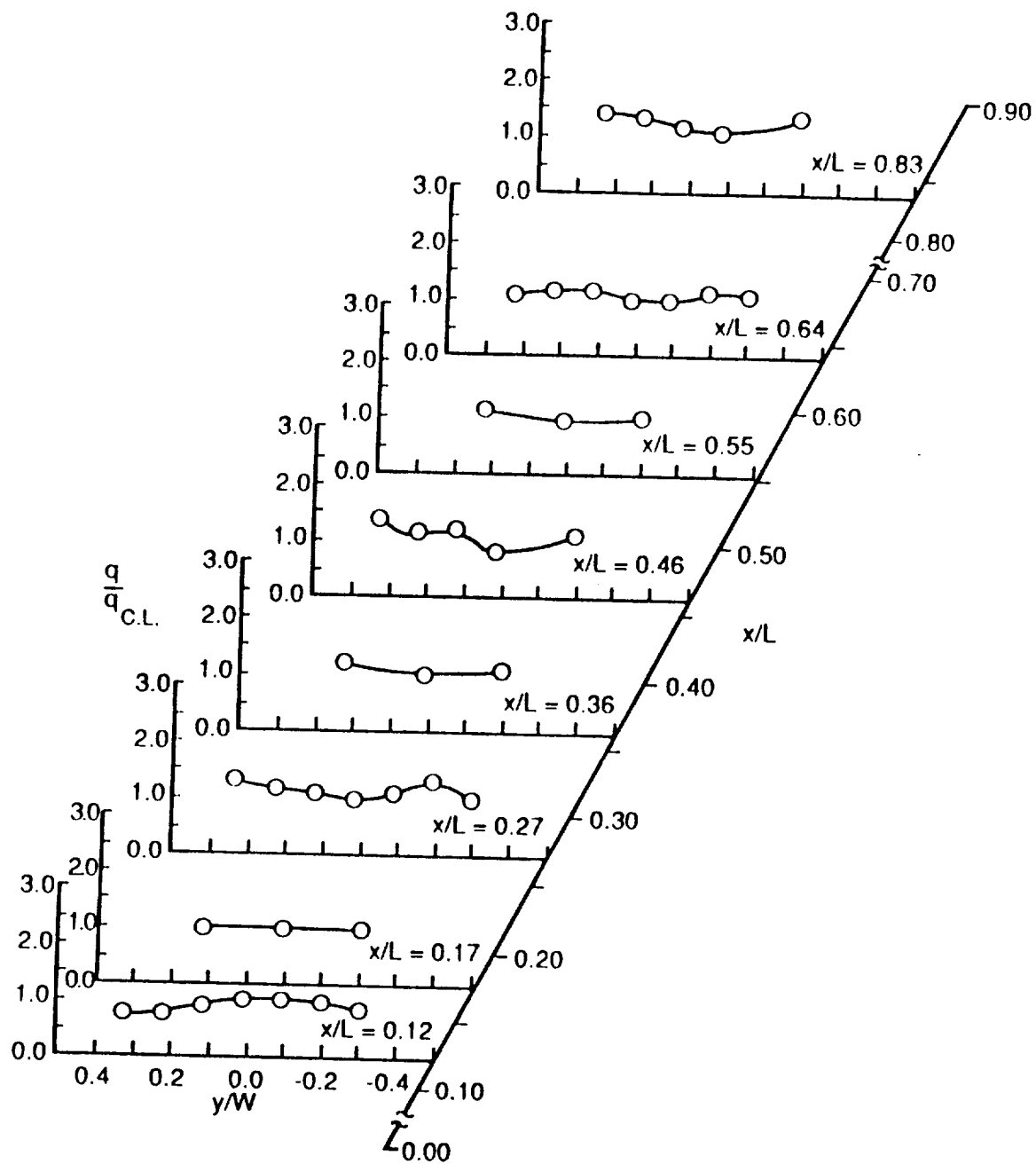


Fig. 21. Concluded.



a) $\alpha = 5.6^\circ$ (Run 7)

Fig. 22. Spanwise surface heating rate distributions.
 $(M_\infty = 6.5, Re_\infty = 1.4 \times 10^6 / ft., T_{aw}/T_w = 5.6)$



b) $\alpha = 13.0^\circ$ (Run 6)

Fig. 22. Concluded.

In Fig. 21, three longitudinal Stanton number distributions are shown for both $\alpha = 5.6^\circ$, and 13.0° . Also shown with the data are the laminar and turbulent heating predictions given by Eqs. (3) and (4), respectively. The data indicate that transition begins near $Re_x^* = 6 \times 10^5$ and is complete by $Re_x^* = 2 \times 10^6$. For the higher angle of attack of 13.0° , the data indicate that the flow is turbulent over a larger portion of the plate due to the higher local unit Reynolds number. For $Re_x^* > 2 \times 10^6$, all three distributions for both angles of attack show the same trend as the turbulent prediction, which is essentially a correlation of incompressible heating rate data. However, the data are generally below the predicted levels by approximately 13, 20, and 16 percent at $y/W=0.23$, 0.02 , and -0.20 , respectively. These discrepancies may result from errors in determining Re_v^* for Eq. (4). However, because of the $1/5$ th power variation of Stanton number with Reynolds number, large changes in Re_v^* are required to fit Eq. (4) to the heating rate data at each longitudinal station. The resulting values for Re_v^* required to fit Eq. (4) to the data are 5.6×10^5 , -8.4×10^5 , and 2.2×10^5 for $y/W=0.23$, 0.02 , and -0.20 , respectively. Therefore, the discrepancies most likely result from other causes.

The spanwise distributions for $\alpha = 5.6^\circ$ (Fig. 22a) show uneven heating close to the leading edge ($x/L = 0.12$ and 0.17). Because the spanwise pressure distributions are relatively uniform in this region for $\alpha = 5.6^\circ$, (See Fig. 18a.) this uneven heating is indicative of spanwise variations in transition location. The spanwise distributions for $\alpha = 13.0^\circ$ (Fig. 22b) show more uniform heating in this region. This is because transition occurs closer to the leading edge, as indicated by the longitudinal Stanton number distributions in Fig. 21. From $x/L = 0.27$ to $x/L = 0.83$, the trends in the spanwise heating rate

distributions for both angles of attack agree well with each other and with the trends in the pressure distributions shown in Fig. 18.

3.2.2 Effect of Free-Stream Unit Reynolds Number

The effect of free-stream unit Reynolds number on longitudinal Stanton number distributions is shown in Fig. 23. The data were obtained at a nominal angle of attack of 13 degrees, a free-stream Mach number of 6.5, and a temperature ratio, T_{aw}/T_w , of 5.6. As with the longitudinal distributions, discussed in section 3.2.1, the distributions indicate that transition is complete for all three unit Reynolds numbers by $Re^*_x = 2 \times 10^6$. Also, the data are below the predicted turbulent levels by as much as 20 percent. As anticipated, the longitudinal distributions show that transition is completed closer to the leading edge as unit Reynolds number is increased.

3.2.3 Correlation of Heating Rates

The longitudinal surface heating rates for a variety of test conditions are presented in terms of Stanton and Reynolds number in Fig. 24. The data are shown for nominal angles of attack of 5.6° and 13° and local unit Reynolds numbers ranging from 0.21×10^6 to 1.51×10^6 per foot. Laminar and turbulent predictions, given by Eqs. (3) and (4) respectively, are also presented with the data. The data from the lowest Reynolds number condition indicate that transition begins at Re^*_x between 3×10^5 and 4×10^5 , which is slightly lower than indicated by the run 7 data shown in Fig. 21. The heating rate data also show that transition is completed by $Re^*_x = 2 \times 10^6$. The momentum thickness and displacement thickness Reynolds numbers corresponding to the local unit Reynolds number for the end of transition are 1200 and 7100, respectively, as

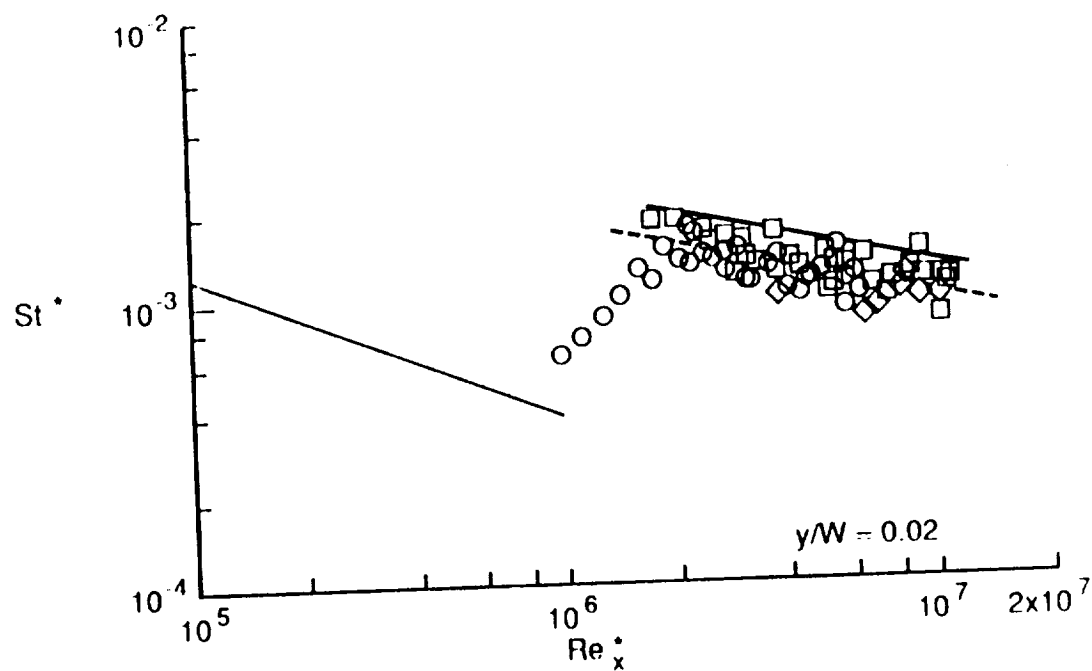
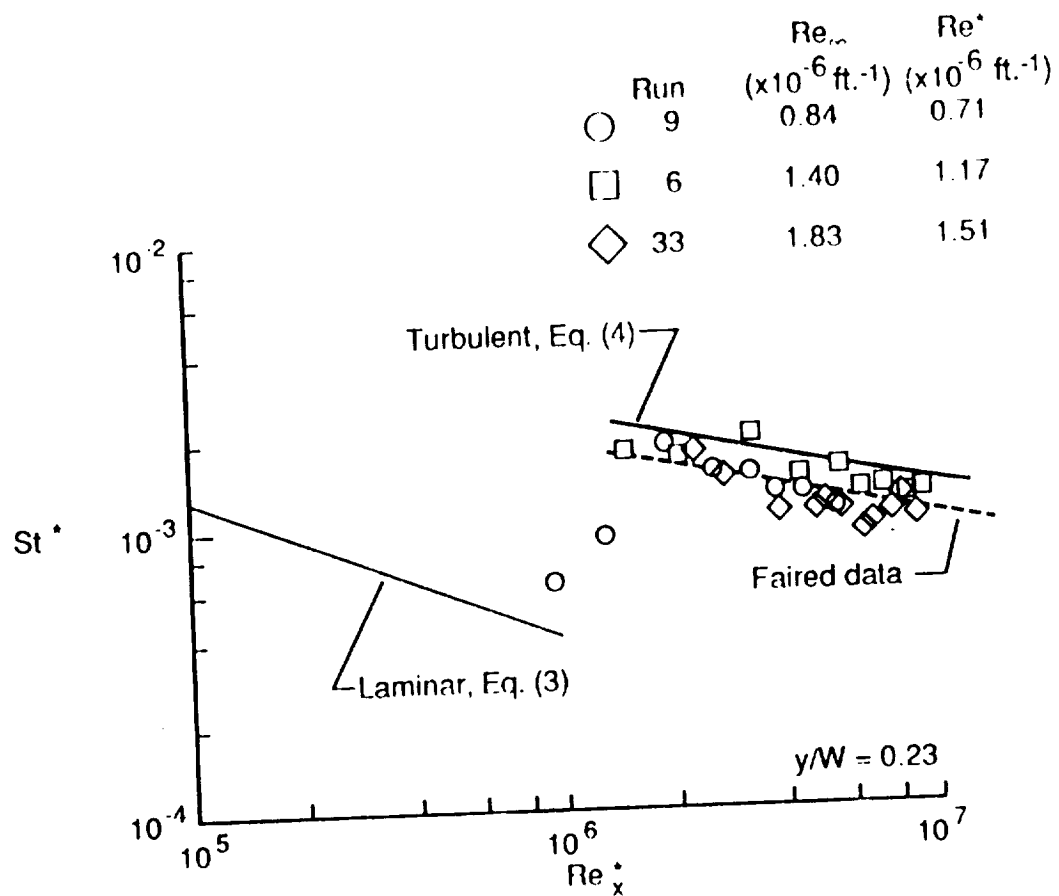


Fig. 23. Longitudinal surface Stanton number distributions for various unit Reynolds numbers.
($M_\infty = 6.5$, $\alpha = 13.0^\circ$, $T_{aw}/T_w = 5.6$)

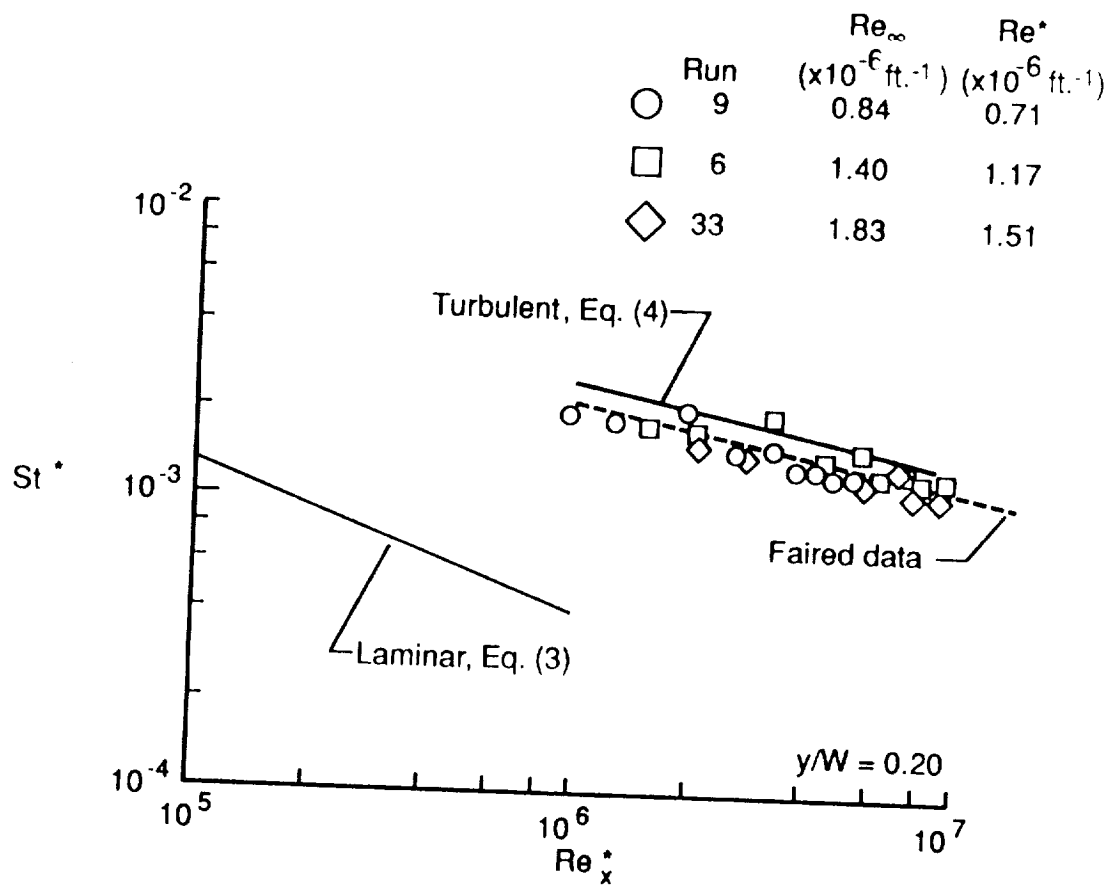


Fig. 23. Concluded.

Run	Re_∞ ($\times 10^{-6} \text{ ft.}^{-1}$)	Re^* ($\times 10^6 \text{ ft.}^{-1}$)	α (deg.)
○ 25	0.55	0.21	5.7
□ 7	1.39	0.56	5.6
◇ 9	0.84	0.71	13.0
△ 6	1.40	1.17	13.0
▽ 33	1.83	1.51	12.7

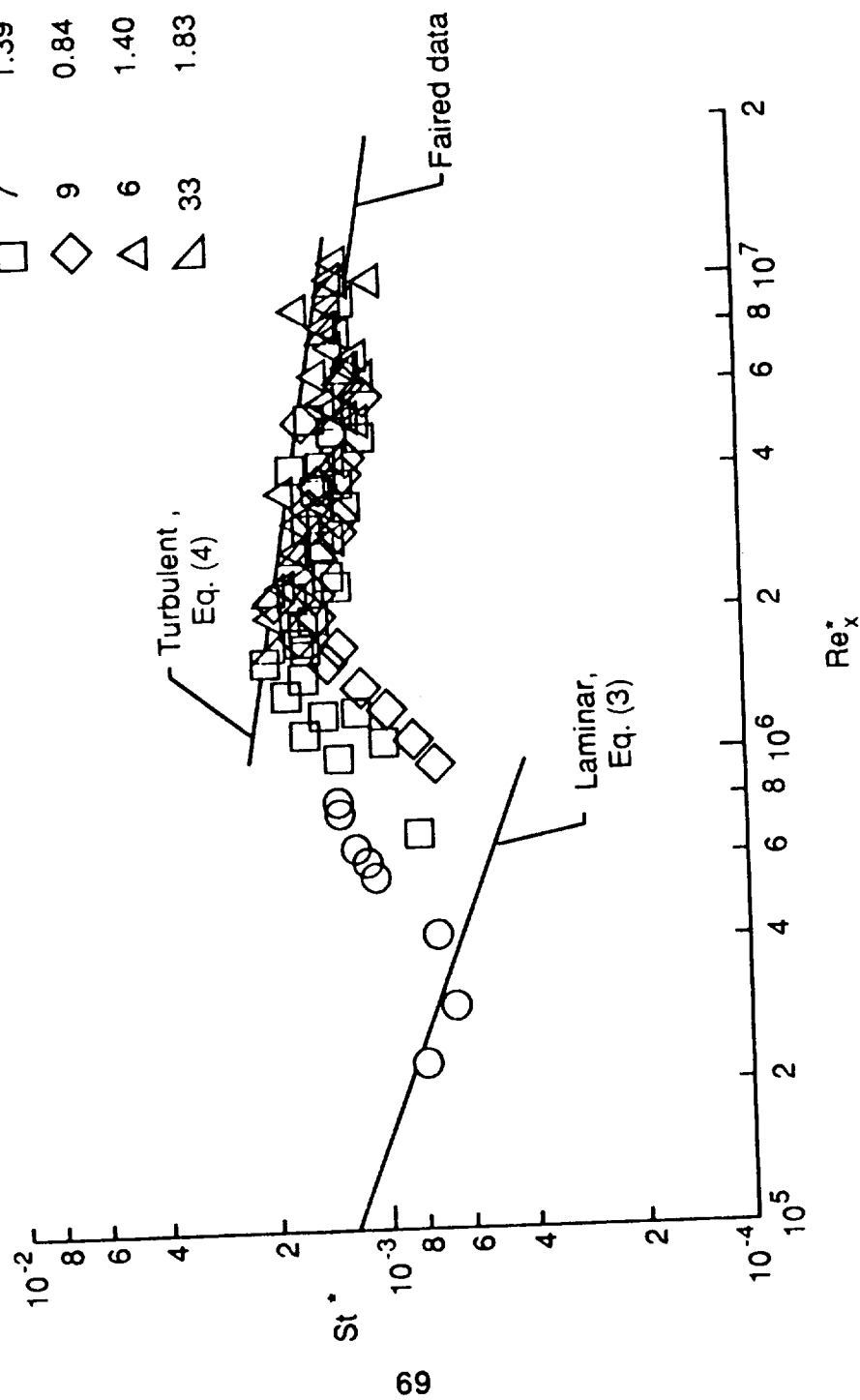


Fig. 24. Correlation of heating rates for various test conditions. ($y/W = 0.02$, $T_{aw} = 5.6$).

determined from the least squares curve fit equations given in Fig. 20. The faired line for the turbulent data has the same slope as the turbulent prediction given by Eq. (4), but is approximately 20% below the prediction.

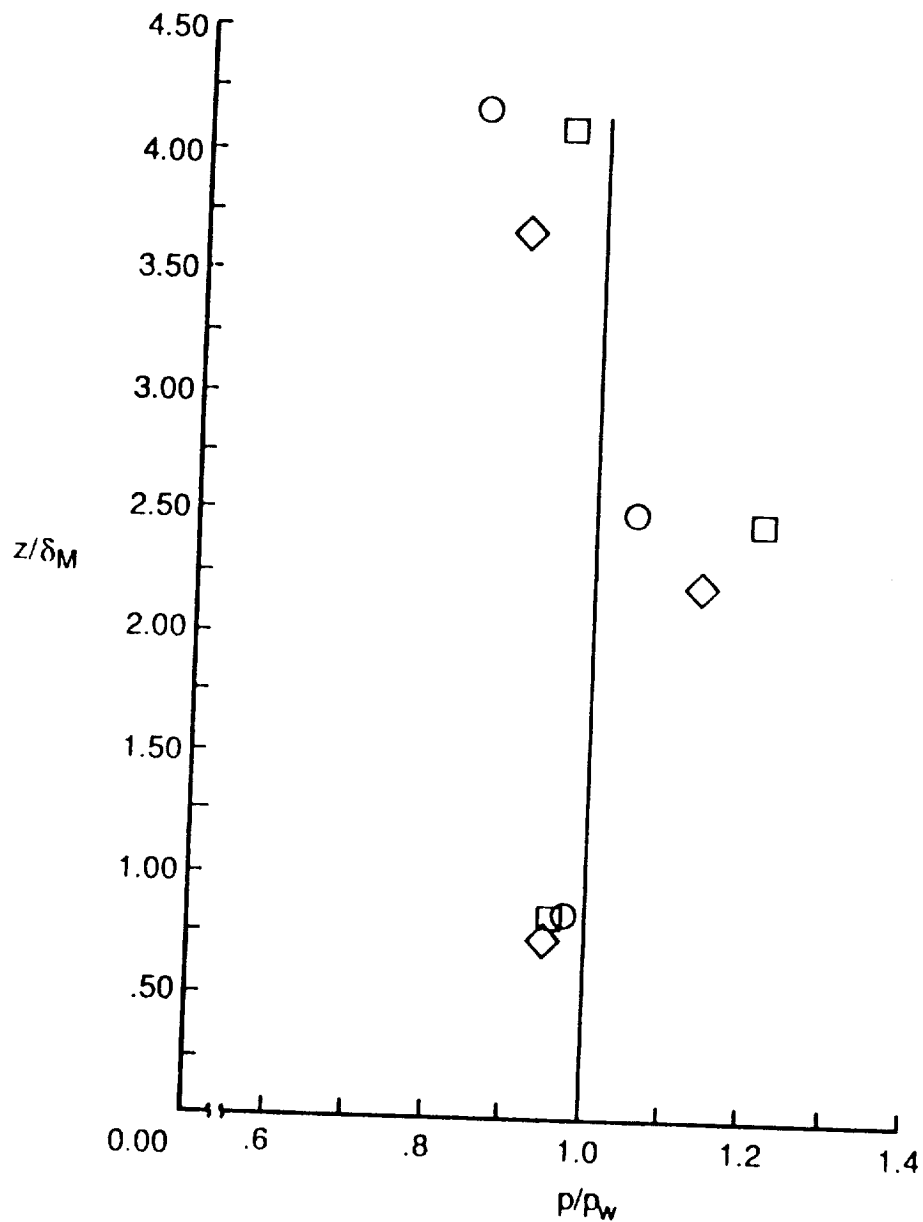
3.3 Boundary-Layer Distributions

3.3.1 Static Pressure Distributions

Static pressure distributions are presented in this section to assess static pressure variations in the boundary layer. The distributions are shown for various free-stream unit Reynolds numbers and at four locations on the plate in Fig. 25. The data were obtained at a nominal angle of attack of 12.9° , a free-stream Mach number of 6.6, and a temperature ratio, T_{aw}/T_w , of 5.4. The boundary-layer edge Mach number was typically 5.0. The static pressures are scaled with respect to the surface pressure measured at the orifice ahead of the static pressure rake (Fig. 7). The vertical locations of the static pressures are normalized with respect to the boundary-layer thickness, δ_M , which was determined from the corresponding Mach number distribution.

For a Mach 5, turbulent boundary layer, the static pressure at the wall should be 2.5 percent greater than the static pressure measured at the edge of the boundary layer, according to the correlation presented by Bushnell, et. al. [34]. Bushnell speculated that this variation is due, in part, to velocity fluctuations in the boundary layer. For the present study, all of the static pressure distributions show larger variations; however, only the first probe is within the boundary layer. The measurements from this probe are typically 5.0 percent less than the wall measurements (Figs. 25a, 25b, and 25d), except for the measurements shown in Fig. 25c, which are approximately 15 percent below the wall measurement. For the present study, free-stream surveys (Appendix F) suggest slight static pressure variations; however, the probe spacing for these surveys was 6.0 inches, compared to 1.0 inches for the boundary-layer probes. The reason why the static pressure probe

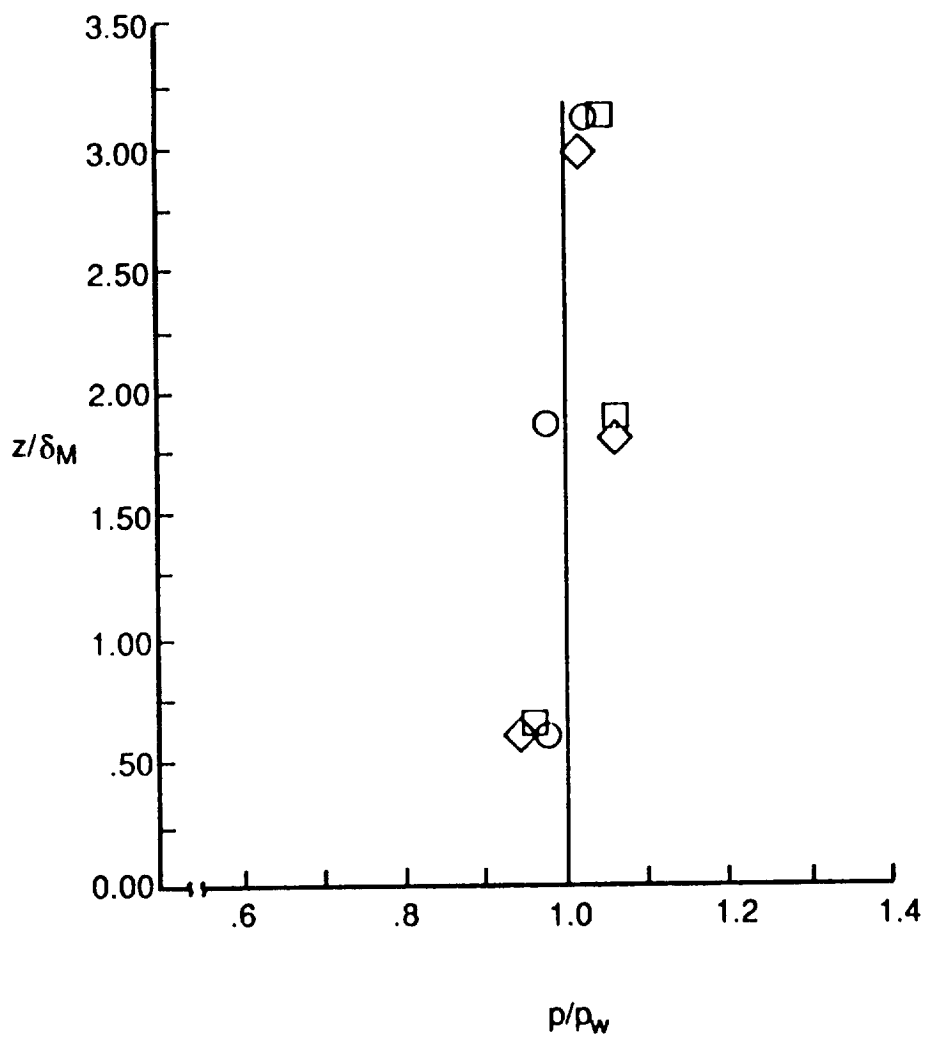
	Run	$Re_{\infty} \times 10^{-6}, ft^{-1}$	$\delta_M, in.$	$p_w, psia$
○	19	0.82	0.58	0.98
□	16	1.07	0.55	1.35
◇	18	1.38	0.59	1.71



a) $x/L = 0.42, y/W = 0.21$

Fig. 25. Static pressure distributions for various free-stream unit Reynolds numbers.
 $(\alpha = 12.9^\circ, T_{aw}/T_w = 5.4)$

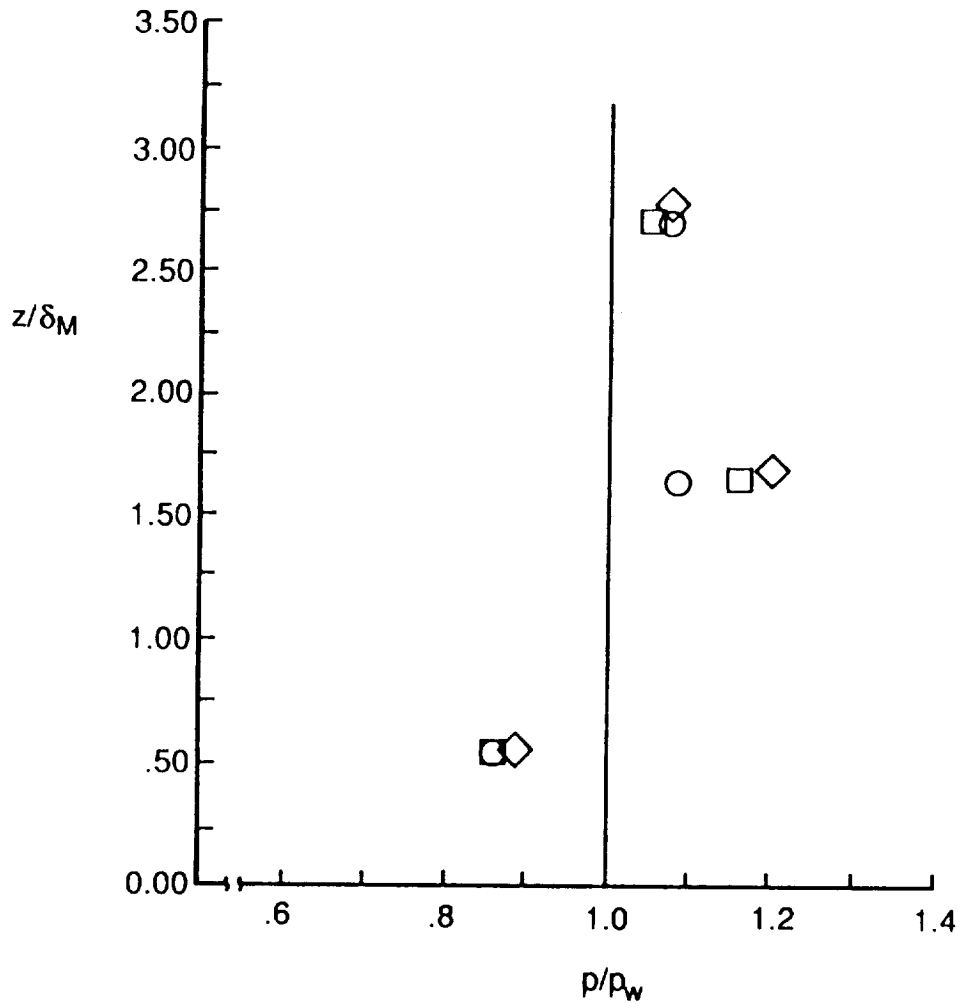
	Run	$Re_{\infty} \times 10^{-6}, ft^{-1}$	$\delta_M, in.$	$p_w, psia$
○	19	0.82	0.72	0.90
□	16	1.07	0.68	1.21
◇	18	1.38	0.74	1.56



b) $x/L = 0.51, y/W = 0.00$

Fig. 25. Continued.

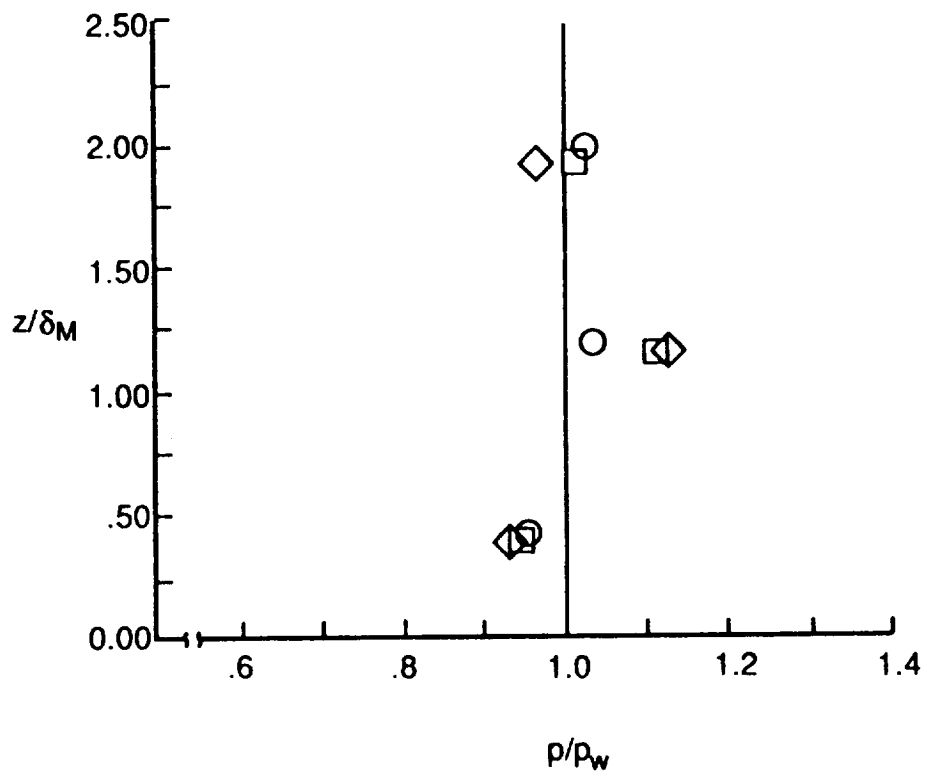
Run	$Re_{\infty} \times 10^{-6}, ft^{-1}$	$\delta_M, in.$	$p_w, psia$
○ 19	0.82	0.91	0.88
□ 16	1.07	0.91	1.28
◇ 18	1.38	0.88	1.66



c) $x/L = 0.61, y/W = -0.20$

Fig. 25. Continued.

Run	$Re_{\infty} \times 10^{-6}, ft^{-1}$	$\delta_M, in.$	$p_w, psia$
○ 32	0.83	1.01	0.94
□ 31	1.38	1.16	1.66
◇ 33	1.83	1.14	2.12



d) $x/L = 0.74, y/W = 0.00$

Fig. 25. Concluded.

measurements show larger variations than indicated by Bushnell's correlation and by the test core measurements, is not known at this time. Because the wall static pressure measurement gives a reasonable average and is typically within 5 percent of the static pressure probe measurements within the boundary layer, the static pressure measured at the wall was used to calculate the Mach numbers assuming a constant pressure across the height of the rake.

3.3.2 Spanwise and Longitudinal Variations

To assess spanwise variations, Mach number, total temperature, and velocity distributions from run 10 are shown in Figs. 26, 27, and 28, respectively. The distributions were obtained at three locations across the span of the plate and at a normalized distance from the leading edge, x/L , of 0.42. The free-stream unit Reynolds number was 0.83×10^6 per foot, the angle of attack was 13.0° , and the temperature ratio was 5.5.

The Mach numbers and their locations (Fig. 26) were scaled by the boundary-layer edge Mach number, M_e , and the boundary-layer thickness, δ_M , corresponding to the location of the edge Mach number. The edge Mach number was obtained by averaging the Mach numbers measured outside the boundary layer. The boundary-layer thickness, δ_M , was obtained using a least squares curve fit of the Mach number data known to be within the boundary layer and extrapolating the curve to the edge Mach number. The normalized Mach number distributions and the boundary-layer edge Mach numbers show very little spanwise variation. However, the boundary-layer thickness, δ_M , varies approximately 20 percent from $y/W = 0.00$ to -0.20 . This variation may be attributed, at least in part, to uneven transition. Also, the surface pressure

	y/W	δ_M (in.)	M_e	Re_0
○	0.21	0.51	4.98	2220
□	0.00	0.51	4.99	1610
◇	-0.20	0.64	4.93	2290

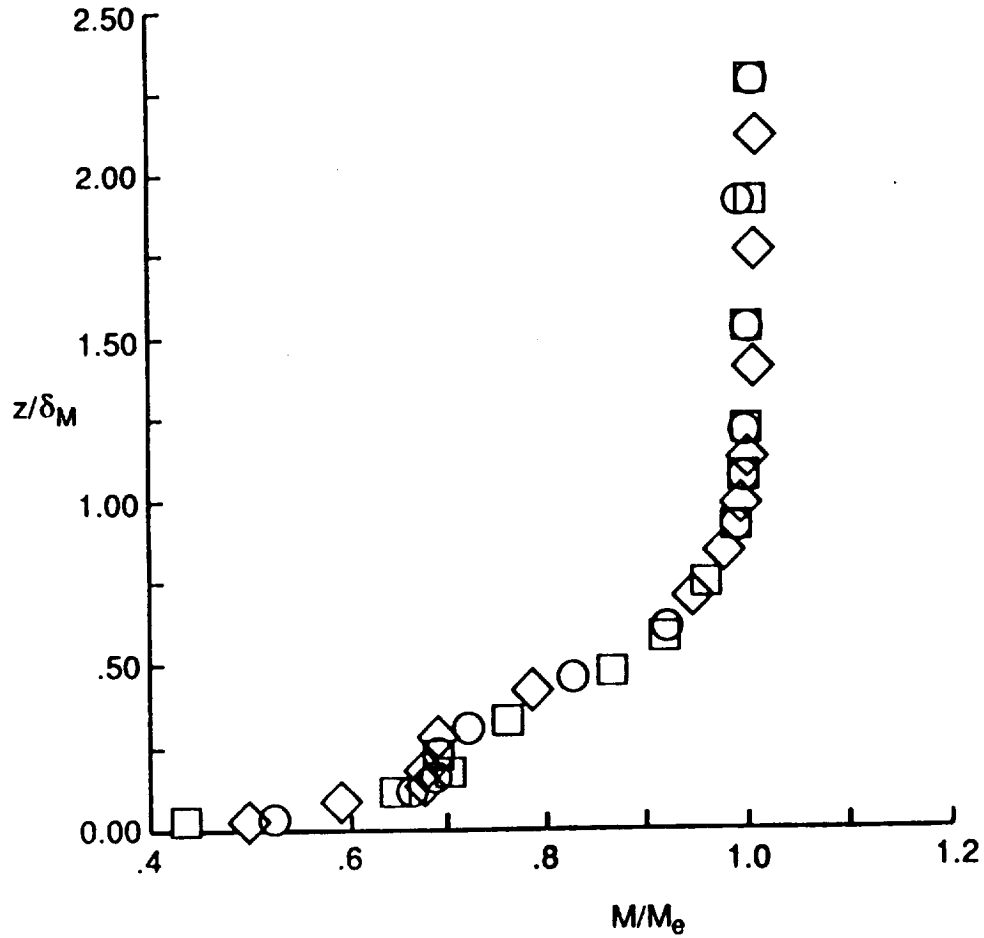


Fig. 26. Mach number distributions for various locations across the span of the plate.
(run 10, $x/L = 0.42$, $Re_\infty = 0.83 \times 10^6 \text{ ft}^{-1}$, $\alpha = 13.0^\circ$, $T_{aw}/T_w = 5.5$)

	y/W	δ_T , in.	T_{le} , °R	Re_0
○	0.21	0.58	3190	2220
□	0.00	0.48	3210	1610
◇	-0.20	0.73	3170	2290

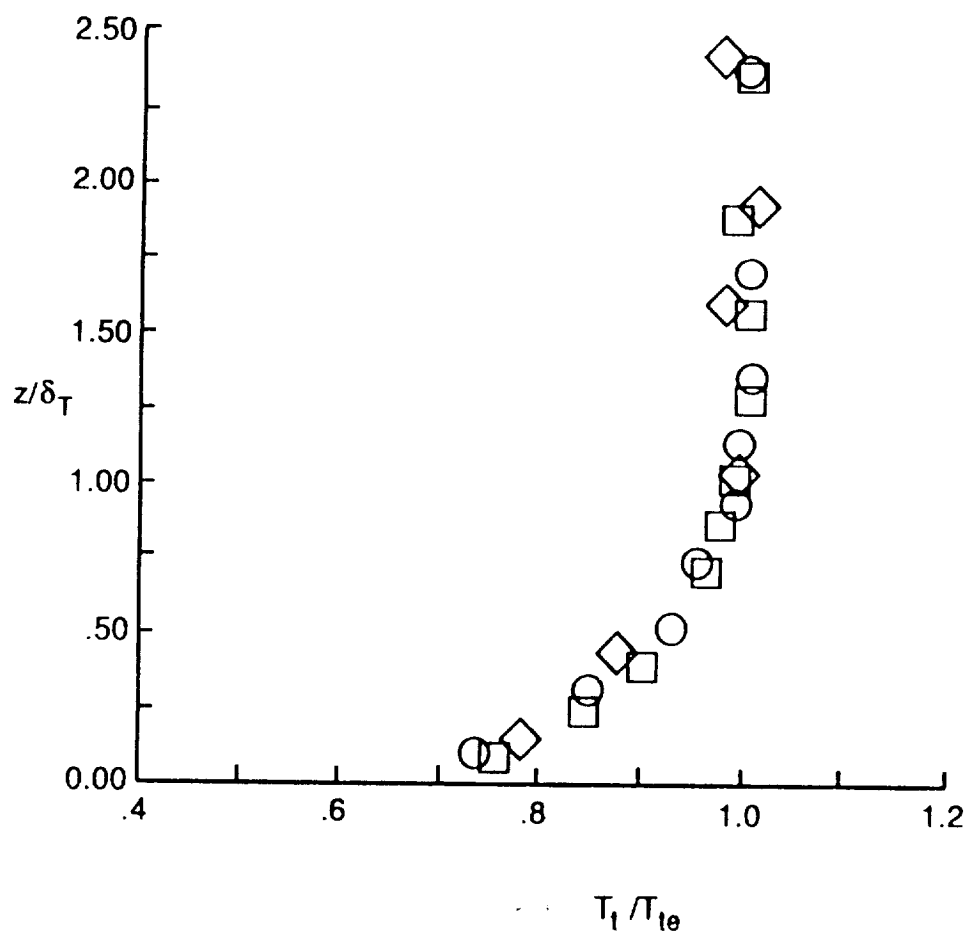


Fig. 27. Total temperature distributions for various locations across the span of the plate.
(run 10, $x/L = 0.42$, $Re_\infty = 0.83 \times 10^6$ ft.⁻¹, $\alpha = 13.0$, ° $T_{aw}/T_w = 5.5$)

	y/W	$\delta_T, \text{in.}$	$U_\theta, \text{ft/s}$	Re_θ
○	0.21	0.54	6200	2220
□	0.00	0.47	6210	1610
◇	-0.20	0.66	6100	2290

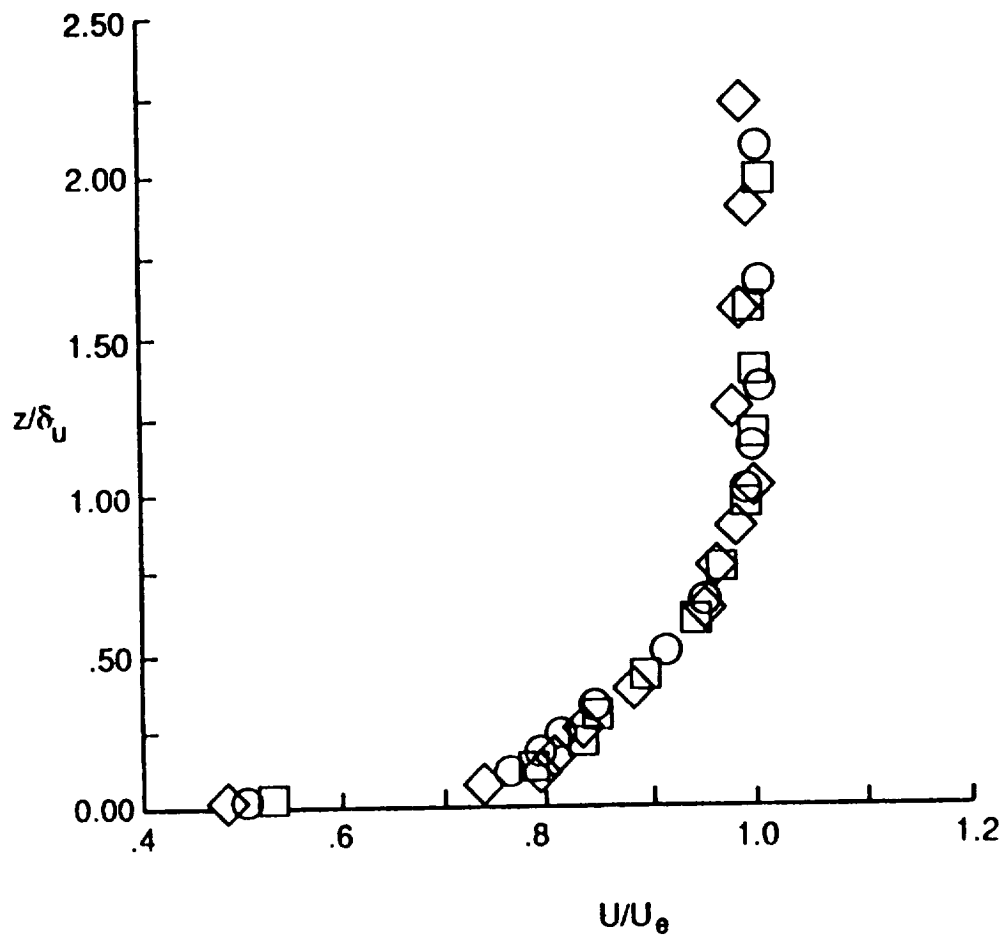


Fig. 28. Velocity distributions at various locations across the span of the plate.
(run 10, $x/L = 0.42$, $Re_\infty = 0.83 \times 10^6 \text{ ft}^{-1}$,
 $\alpha = 13.0^\circ$, $T_{aw}/T_w = 5.5$)

distributions at a nearby location ($x/L = 0.46$) indicate spanwise pressure gradients are present. (See Fig. 18b.) All the distributions show an inflection near $z/\delta_M = 0.25$, which may be a result of interference between the four pitot probes located closest to the wall. As mentioned in section 2.2.2, these probes were closer than the guidelines given by Keener and Hopkins [28] due to manufacturing difficulties and the tendency of the probe heights to permanently deflect during the runs. Because these four measurements appear to be in error, they were not used in the least squares curve fits to determine δ_M .

The total temperatures and their locations (Fig. 27) were scaled by the boundary-layer edge temperature, T_{te} , and the thermal boundary-layer thickness, δ_T , corresponding to the location of the edge total temperature. These quantities, T_{te} and δ_T , were obtained using the same procedure described for obtaining the edge Mach number, M_e , and boundary-layer thickness, δ_M . As with the Mach number distributions, the normalized total temperature distributions and the boundary-layer edge total temperatures show little spanwise variation. However, the thermal boundary-layer thickness, δ_T , varies approximately 34 percent from $y/W=0.00$ to -0.20 . Note that none of the total temperature distributions (Fig. 27) show the inflection near $z/\delta_T = 0.25$, evident in the Mach number distributions.

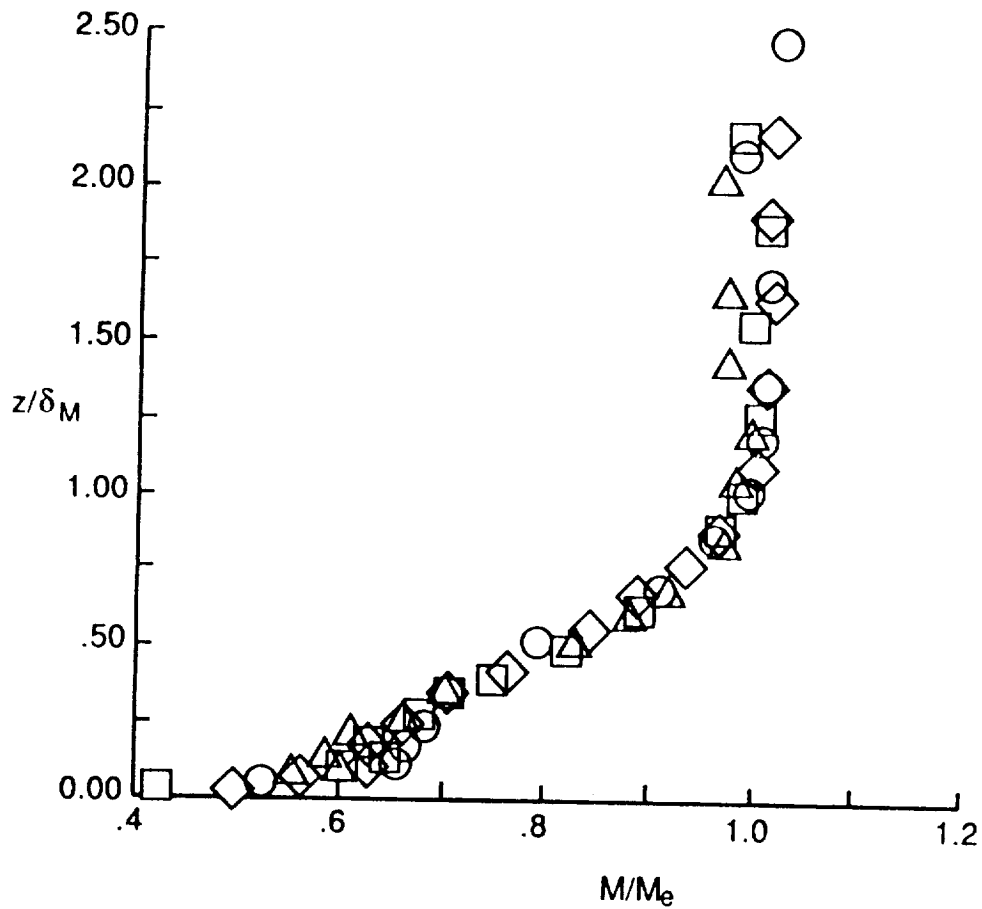
The velocity distributions, scaled by the boundary-layer edge velocity, U_e , and the velocity boundary-layer thickness, δ_U , (Fig. 28) also show only slight spanwise variations. However, the boundary-layer thickness, δ_U , varies approximately 29 percent from $y/W=0.00$ to -0.20 . Note that the velocity boundary-layer thickness, δ_U , is consistently smaller than the thermal boundary-layer thickness, δ_T . Because the Prandtl number for the flow is 0.76

(implying that the thermal boundary layer should be thicker), this is an expected result. As with the Mach number distributions, the velocity distributions also show an inflection near $z/\delta_U = 0.25$. Because the velocities were calculated from the Mach numbers, this inflection may also result from interference between the four pitot probes closest to the wall.

To assess longitudinal variations, Mach number, total temperature, and velocity distributions are shown in Figs. 29, 30, and 31, respectively. The data shown in Figs. 29a, 30a, and 31a were obtained at an angle of attack of 12.8° , a free-stream unit Reynolds number of 0.82×10^6 /ft, and a temperature ratio of 5.3. These are nominally the same conditions as the data shown for the spanwise assessment. Longitudinal variations are also shown for a higher Reynolds number of 1.38×10^6 /ft (Figs. 29b, 30b, and 31b) and a lower angle of attack of 5° (Figs. 29c, 30c, and 31c).

The Mach number distributions (Fig. 29a) show longitudinal variations for both $z/\delta_M < 0.25$ and for $z/\delta_M > 1.25$. Also, the boundary-layer edge Mach number varies slightly between locations. The variations for $z/\delta_M > 1.25$ as well as the edge Mach number variations are probably caused by slight Mach number variations in the free-stream. (See Appendix F.) The variations noted in the inflection for $z/\delta_M < 0.25$, may result from a combined effect of pitot probe interference and boundary-layer growth. The Mach number distributions obtained at the higher unit Reynolds number of 1.38×10^6 /ft (Fig. 29b) show similar trends. However, the distributions obtained at the lower angle of attack of 5° (Fig. 29c) show less variation with location for $z/\delta_M > 1.25$. This probably results from a decreasing influence of test core variations in Mach number with decreasing angle of attack, as noted with the surface pressure distributions discussed in section 3.1.3. As anticipated, the boundary-layer thicknesses,

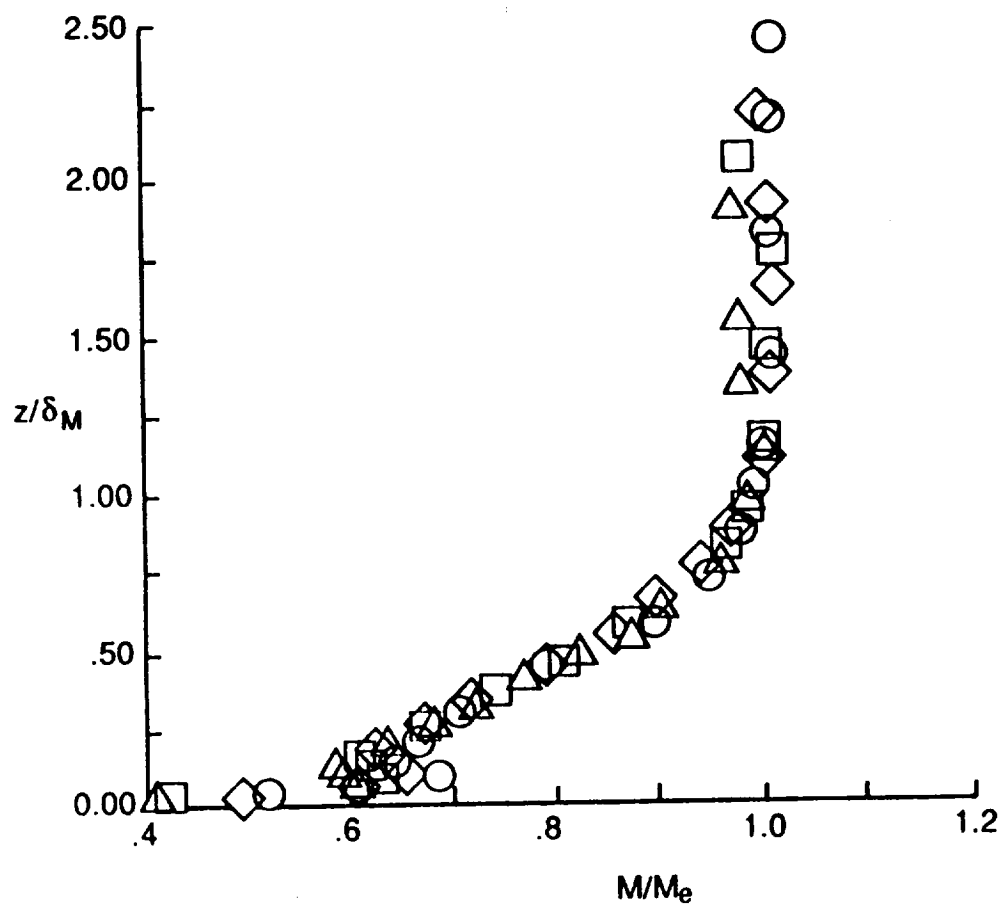
	Run	x/L	y/W	δ_M , in.	M_e	Re_0
○	19	0.42	0.21	0.58	4.93	2290
□	19	0.51	0.00	0.72	4.98	2240
◇	19	0.61	-0.20	0.91	4.86	2980
△	32	0.74	0.00	1.01	4.96	3530



a) $\alpha = 12.8^\circ$, $Re_\infty = 0.82 \times 10^6 \text{ ft.}^{-1}$

Fig. 29. Mach number distributions for various locations on the plate.
($T_{aw}/T_w = 5.3$)

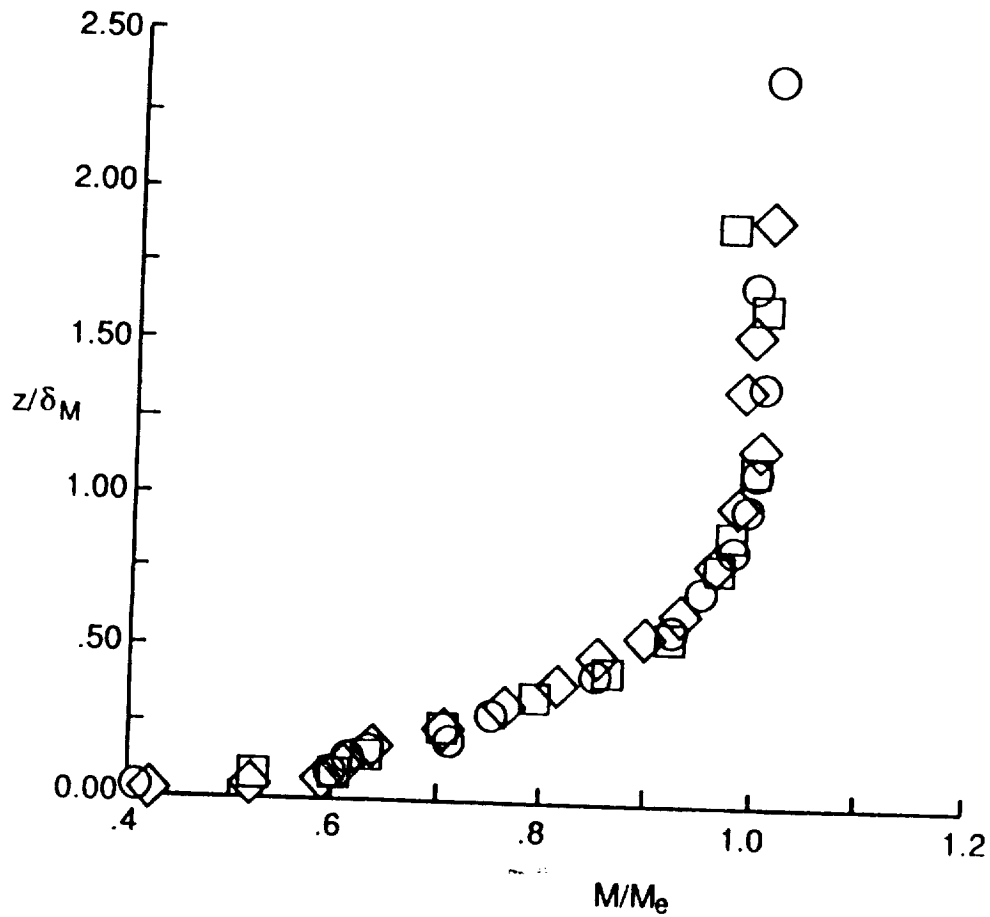
	Run	x/L	y/W	δ_M , in.	M_e	Re_0
○	18	0.42	0.21	0.59	4.96	4010
□	18	0.51	0.00	0.74	4.96	4390
◇	18	0.61	-0.20	0.88	4.89	5560
△	31	0.74	0.00	1.16	4.88	6300



b) $\alpha = 12.9^\circ$, $Re_\infty = 1.38 \times 10^6 \text{ ft.}^{-1}$

Fig. 29. Continued.

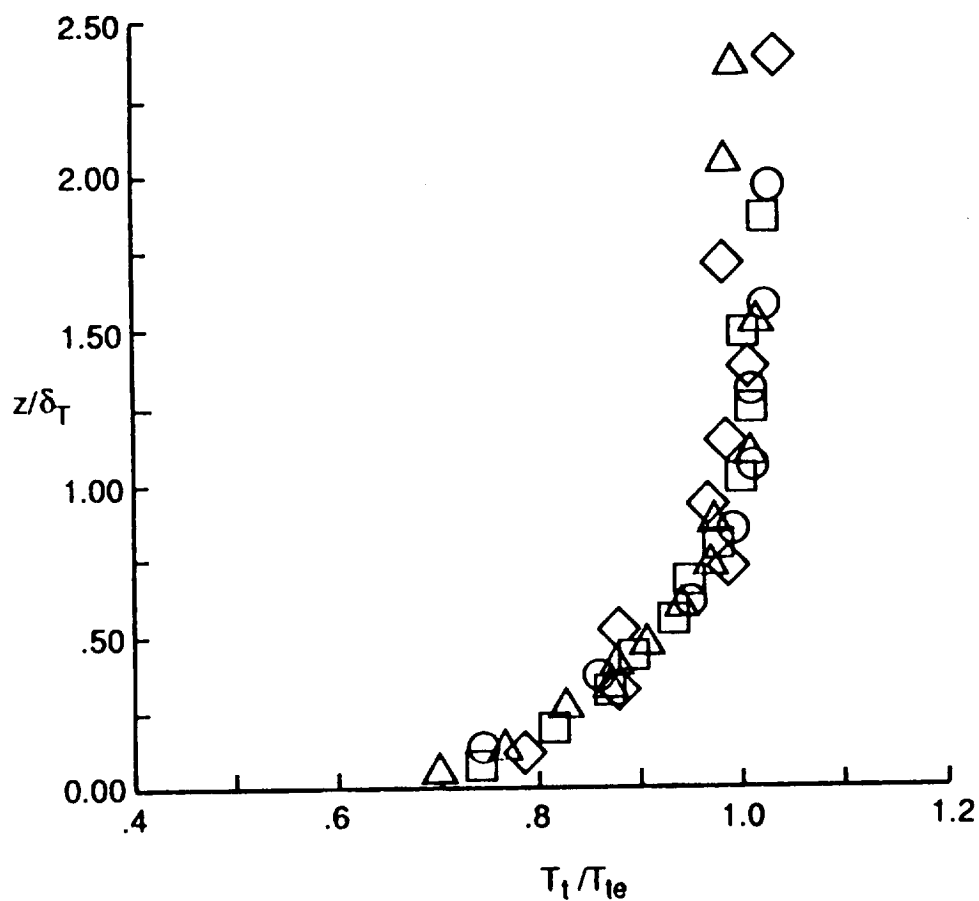
	Run	x/L	y/W	δ_M , in.	M_e	Re_θ
○	25	0.42	0.21	0.52	6.27	514
□	25	0.51	0.00	0.61	6.33	391
◇	25	0.61	-0.20	0.97	6.19	541



c) $\alpha = 5.0^\circ$, $Re_\infty = 0.55 \times 10^6 \text{ ft.}^{-1}$

Fig. 29. Concluded.

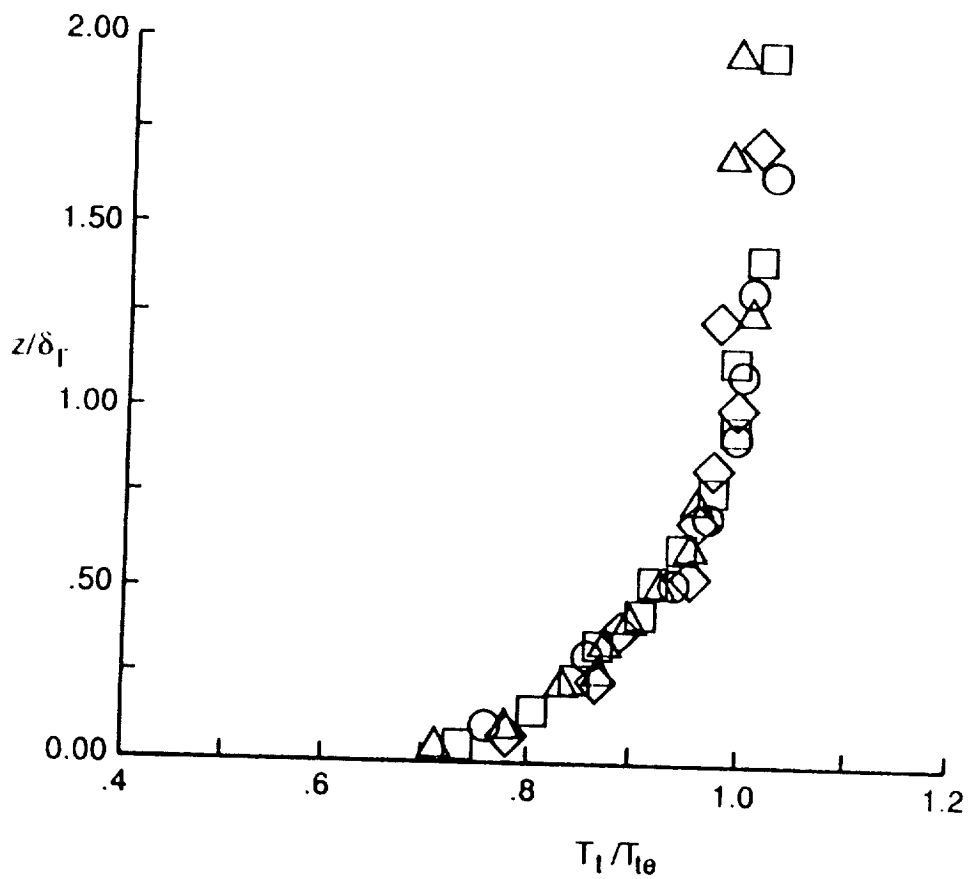
	Run	x/L	y/W	δ_T , in.	T_{te} , °R	Re_0
○	19	0.42	0.21	0.64	3150	2290
□	19	0.51	0.00	0.69	3110	2240
◇	19	0.61	-0.20	0.91	3050	2980
△	32	0.74	0.00	1.00	3100	3530



a) $\alpha = 12.9^\circ$, $Re_\infty = 0.82 \times 10^6 \text{ ft.}^{-1}$

Fig. 30. Total temperature distributions for various locations on the plate.
($T_{aw}/T_w = 5.3$)

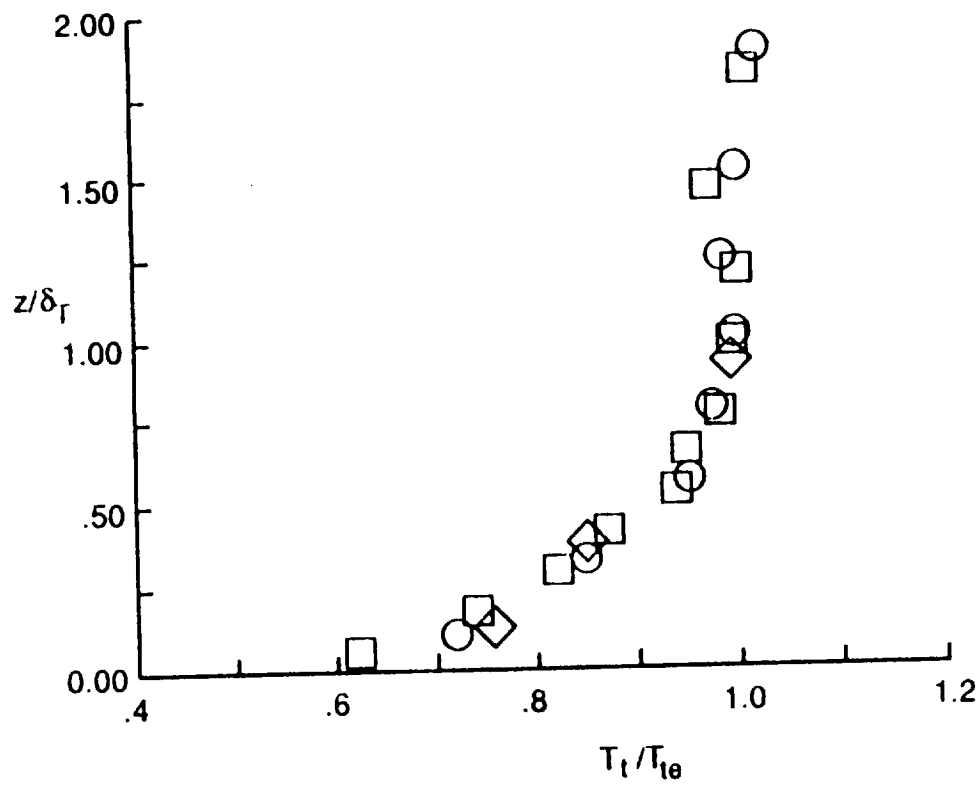
	Run	x/L	y/W	δ_T , in.	T_{te} , °R	Re_0
○	18	0.42	0.21	0.63	3060	4010
□	18	0.51	0.00	0.76	3030	4390
◇	18	0.61	-0.20	0.91	3040	5560
△	31	0.74	0.00	1.13	3210	6300



b) $\alpha = 12.9^\circ$, $Re_\infty = 1.38 \times 10^6 \text{ ft.}^{-1}$

Fig. 30. Continued.

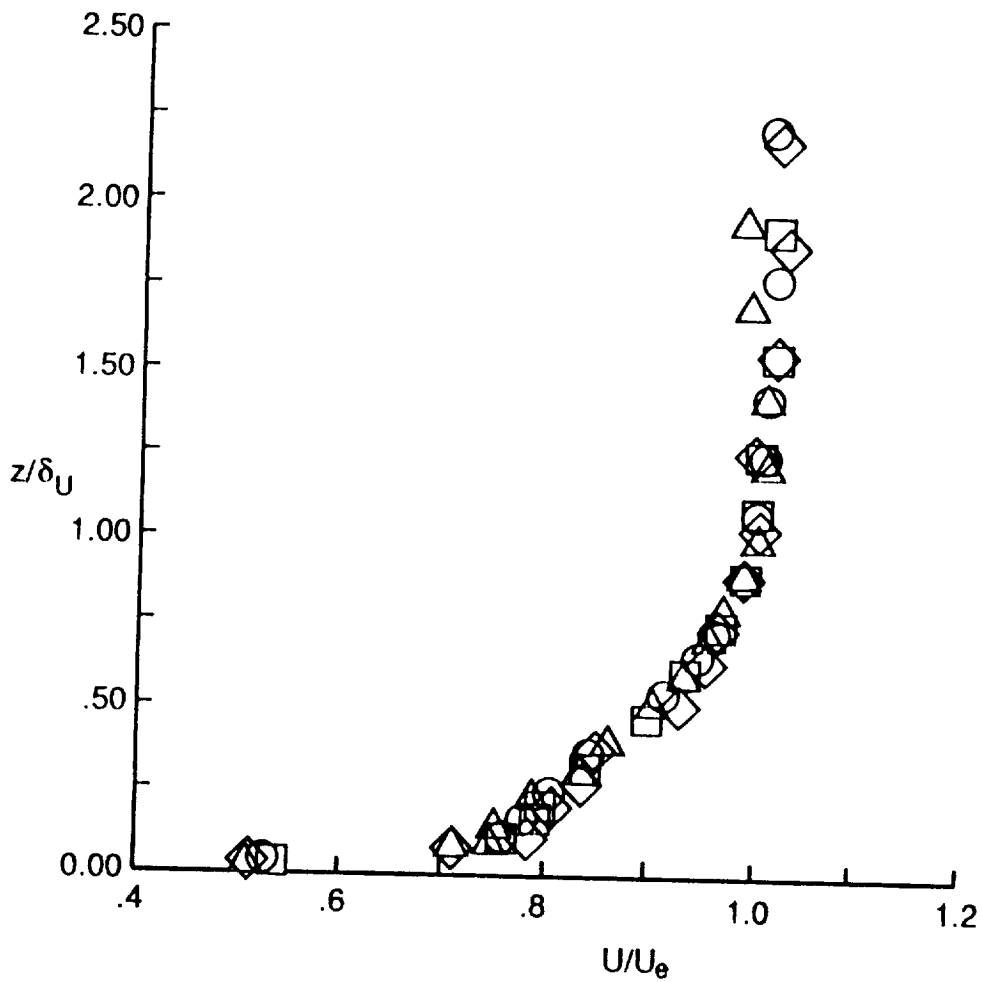
	Run	x/L	y/W	δ_1 , in.	T_{te} , °R	Re_0
○	25	0.42	0.21	0.54	3100	514
□	25	0.51	0.00	0.42	3090	391
◇	25	0.61	-0.20	0.53	2860	541



c) $\alpha = 5.0^\circ$, $Re_\infty = 0.55 \times 10^6 \text{ ft.}^{-1}$

Fig. 30. Concluded.

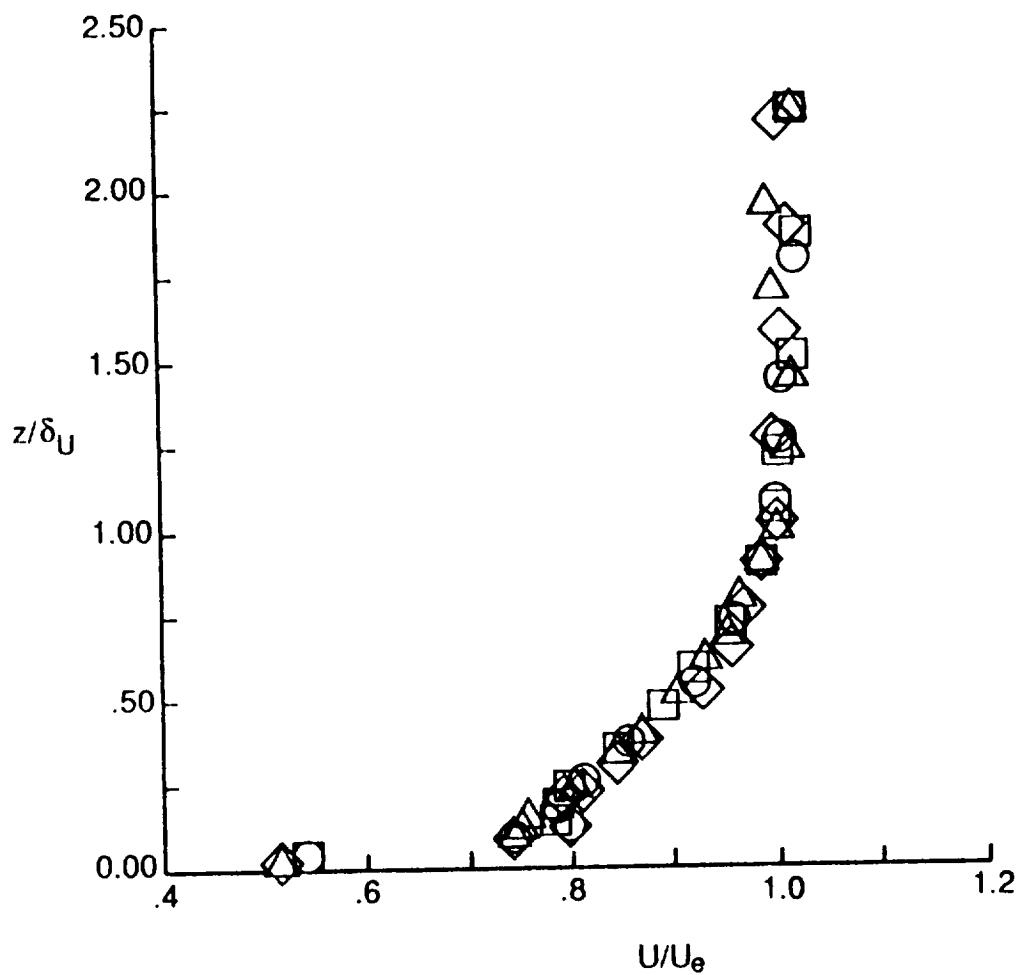
Run	x/L	y/W	δ_U , in.	U_e , ft/s	Re_θ
○ 19	0.42	0.21	0.59	6160	2290
□ 19	0.51	0.00	0.66	6080	2240
◇ 19	0.61	-0.20	0.86	5970	2980
△ 32	0.74	0.00	0.97	6080	3530



a) $\alpha = 12.9^\circ$, $Re_\infty = 0.82 \times 10^6 \text{ ft.}^{-1}$

Fig. 31. Velocity distributions for various locations on the plate.
($T_{aw}/T_w = 5.3$)

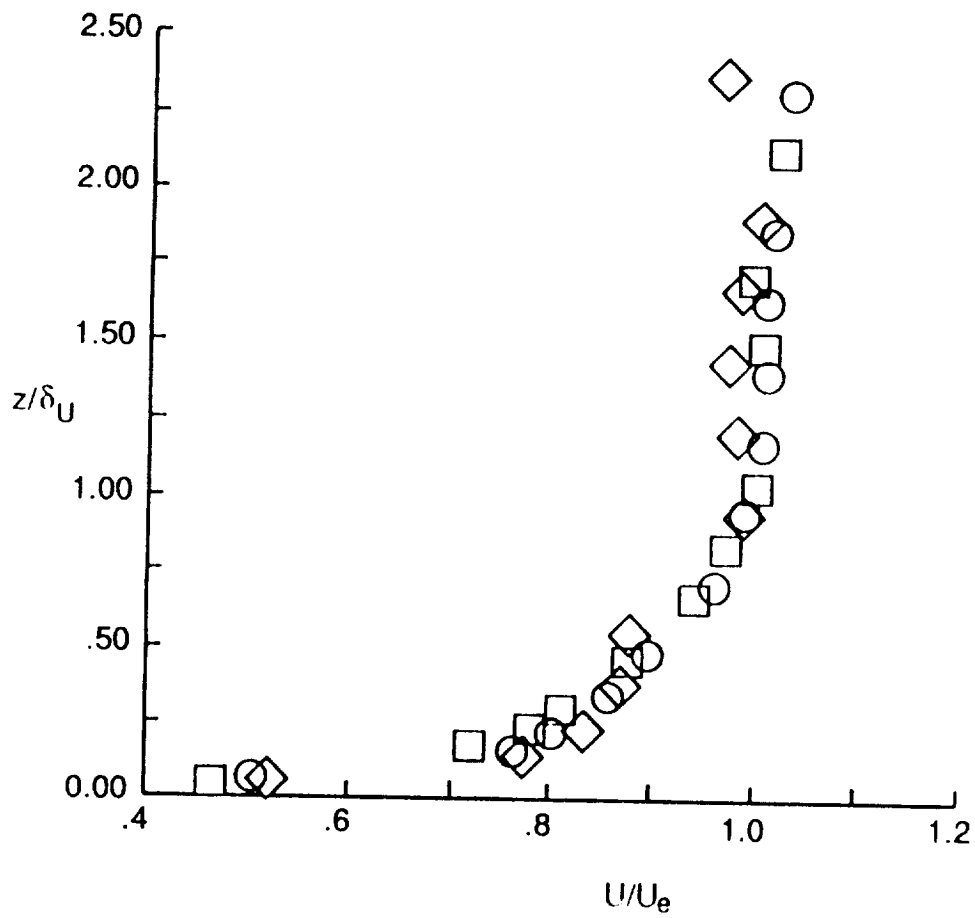
Run	x/L	y/W	δ_U , in.	U_e , ft/s	Re_0
○ 18	0.42	0.21	0.60	6020	4010
□ 18	0.51	0.00	0.72	6040	4390
◇ 18	0.61	-0.20	0.84	5920	5560
△ 31	0.74	0.00	1.03	6200	6300



b) $\alpha = 12.9^\circ$, $Re_\infty = 1.38 \times 10^6 \text{ ft.}^{-1}$

Fig. 31. Continued.

Run	x/L	y/W	δ_U , in.	U_e , ft/s	Re_θ
○ 25	0.42	0.21	0.52	6330	514
□ 25	0.51	0.00	0.49	6300	391
◇ 25	0.61	-0.20	0.70	5760	541



c) $\alpha = 5.0^\circ$, $Re_\infty = 0.55 \times 10^6 \text{ ft.}^{-1}$

Fig. 31. Concluded.

δ_M , show a general increase with distance for all three conditions. (Figs. 29a, 29b, and 29c) Also, for the two highest free-stream unit Reynolds number test conditions (Figs. 29a and 29b), the momentum thickness Reynolds number, Re^*_θ , generally increases with distance from the leading edge and is above the level of 1200 indicated in section 3.2.3 for the end of transition. However, for the lower angle of attack, lower free-stream unit Reynolds number condition (Fig. 29c), Re^*_θ , is well below 1200 at all three locations, indicating that the boundary layer is transitional.

The total temperature distributions (Fig. 30a) show longitudinal variations for $z/\delta_T > 1.25$, similar to the variations noted in the Mach number distributions. Also the boundary-layer edge total temperature varies between locations. As with the Mach number distributions, these variations are probably caused by test core variations. The total temperature distributions at the higher Reynolds number condition (Fig. 30b) show similar variations with location as those obtained at the lower Reynolds number condition (Fig. 30a). The total temperature distributions obtained at $\alpha = 5^\circ$ (Fig. 30c) also show less of a variation with location. Overall, the trends are similar to those noted with the Mach number distributions, except that the total temperatures do not show the inflection near $z/\delta_T = 0.25$. The thickness of the thermal layer, δ_T , shows a general increase with distance from the leading edge for the total temperature distributions obtained at the higher Reynolds numbers (Figs. 30a and 30b). However, the thermal boundary layer thicknesses obtained at the lower Reynolds number and angle of attack condition (Fig. 30c) do not show a general increase with distance from the leading edge. This may be caused by a combination of spanwise variations in transition location and errors in interpreting the boundary-layer edge thicknesses. Visual observations of the

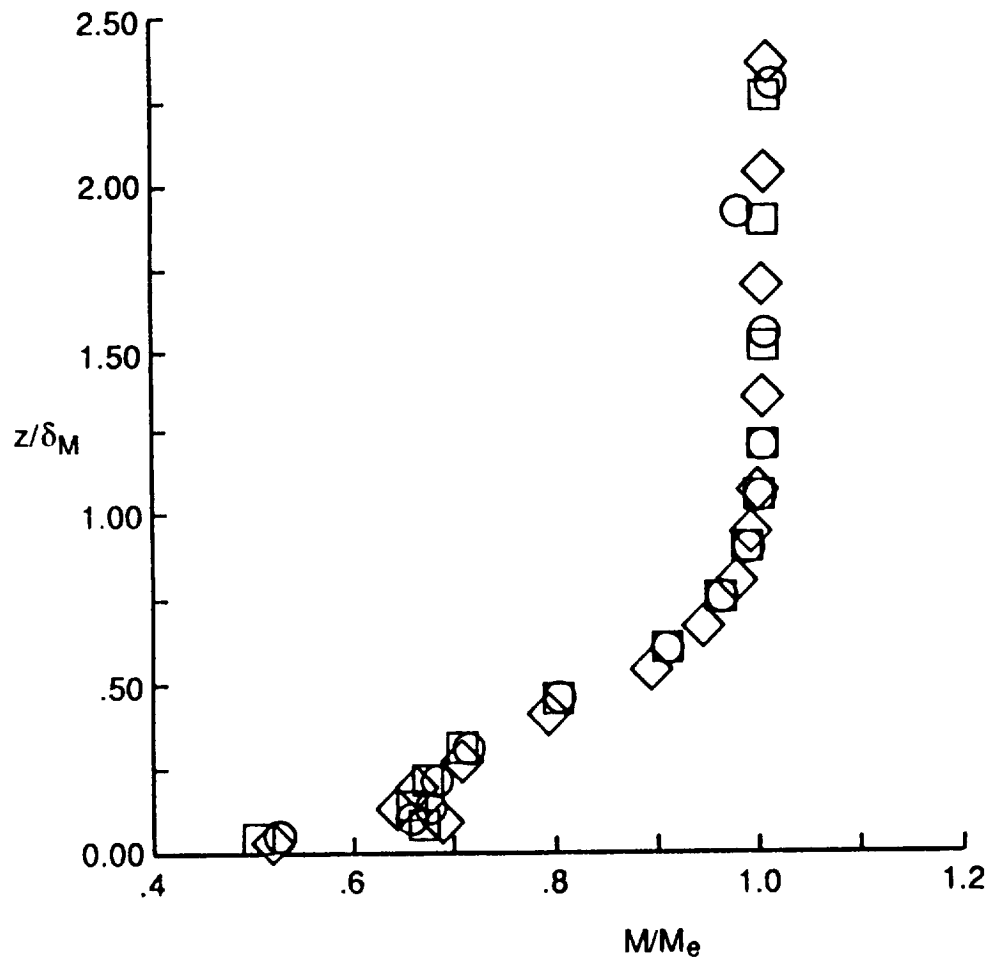
total temperature probes used in the total temperature rake at $x/L=0.61$ indicate that some of the thermocouple beads were in contact with the radiation shield. This could result in errors in interpreting the edge of the thermal layer.

The velocity distributions (Figs. 31a, 31b, and 31c) show similar trends to the Mach number and total temperature distributions. This is an expected result because the velocities were calculated from both the Mach numbers and the total temperatures, as discussed in section 2.3. As noted with the thermal boundary-layer thicknesses, the velocity boundary-layer thicknesses, δ_U , increase with distance from the leading edge for the velocity distributions obtained at the higher Reynolds numbers (Figs. 31a and 31b). However, the boundary-layer thicknesses obtained at the lowest Reynolds number condition (Fig. 31c) show a decrease at $x/L=0.51$. Again this may be caused by a combination of spanwise variations in transition location and errors in interpreting the boundary-layer thickness. The velocity boundary-layer thicknesses, δ_U , are smaller than the thermal boundary-layer thicknesses, δ_T , as was noted in the spanwise distributions. Again this is an expected result because the Prandtl number is greater than one.

3.3.3 Effect of Free-Stream Unit Reynolds Number

Mach number, total temperature, and velocity distributions are shown in Figs. 32, 33, and 34, respectively, to assess any anomalous effect of free-stream unit Reynolds number. The data were obtained for free-stream unit Reynolds numbers ranging from 0.82×10^6 to 1.83×10^6 per foot and are shown for four locations on the plate. The nominal angle of attack and temperature ratio were 12.9° , and 5.4, respectively. The momentum thickness

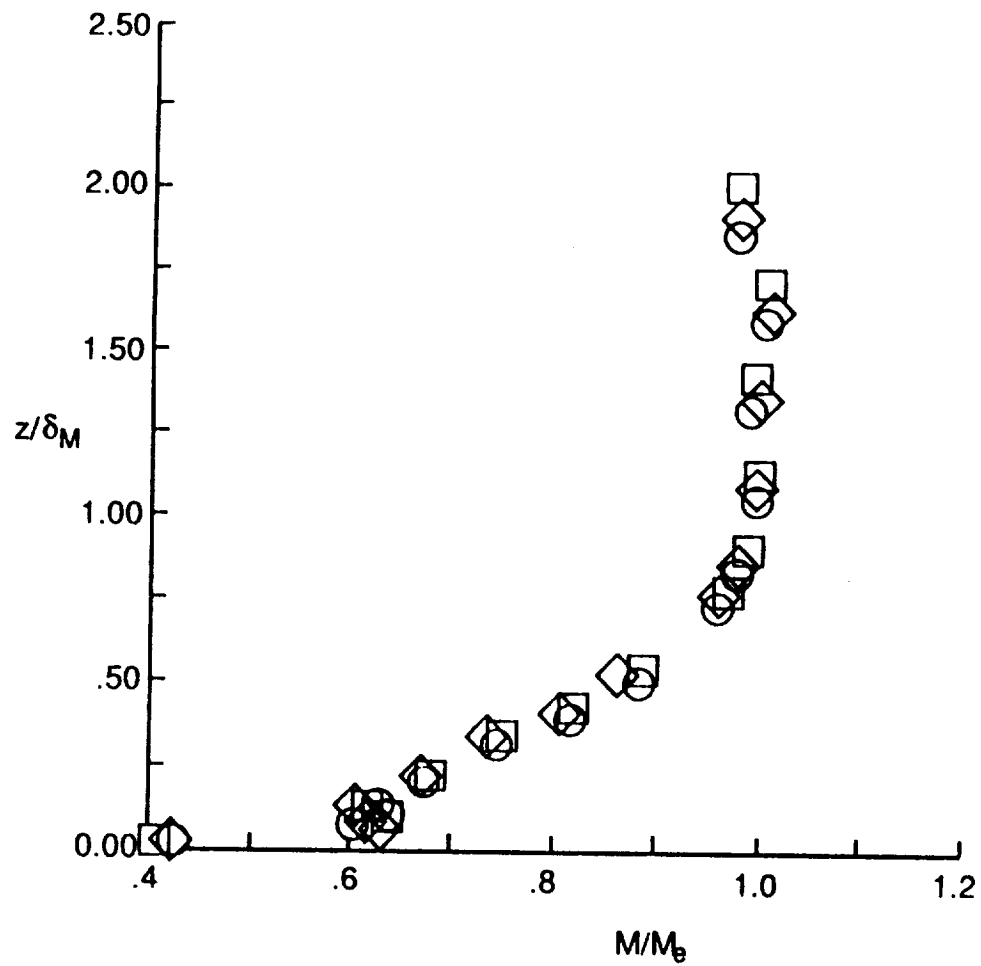
	Run	$Re_{\infty} \times 10^{-6}, ft^{-1}$	$\delta_M, in.$	M_e	Re_0
○	19	0.82	0.58	4.93	2290
□	16	1.07	0.55	4.94	3190
◇	18	1.38	0.59	4.96	4010



a) $x/L = 0.42, y/W = 0.21$

Fig. 32. Mach number distributions for various free-stream unit Reynolds numbers.
 $(\alpha = 12.9^\circ, T_{aw}/T_w = 5.4)$

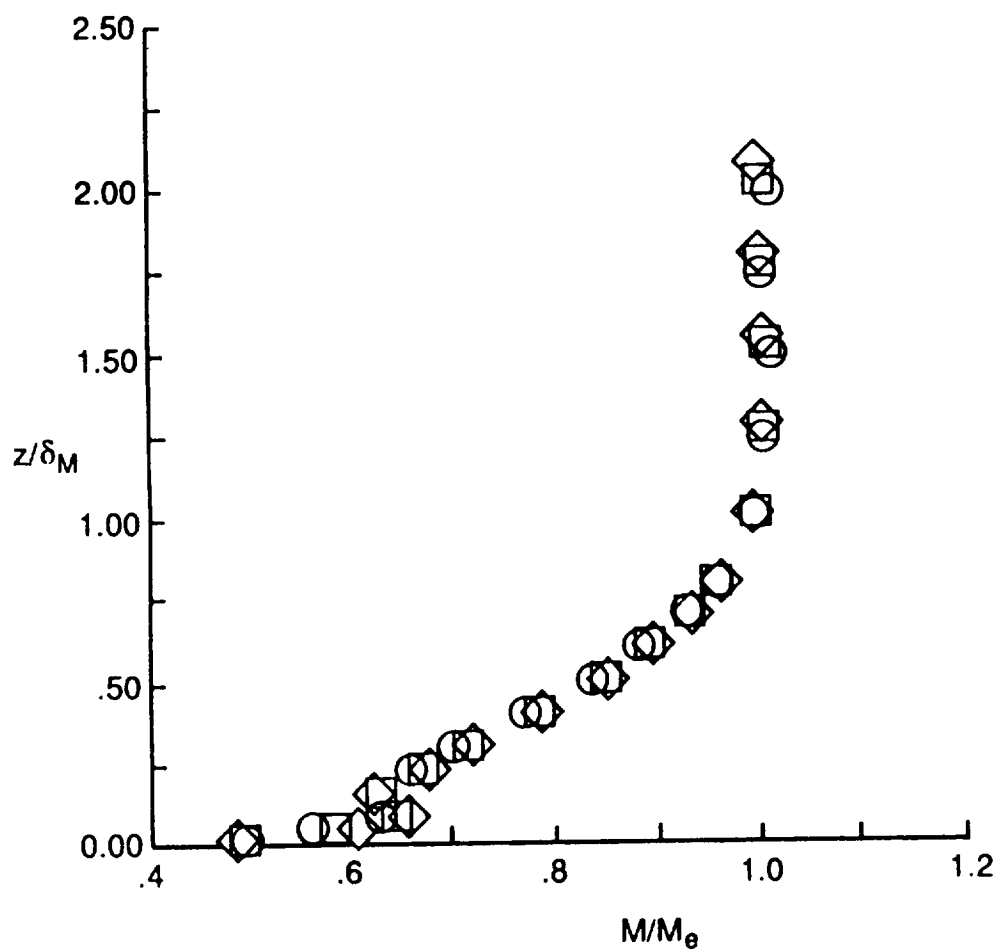
	Run	$Re_{\infty} \times 10^{-6}, ft^{-1}$	$\delta_M, in.$	M_e	Re_0^*
○	19	0.82	0.72	4.98	2240
□	16	1.07	0.68	4.94	3210
◇	18	1.38	0.74	4.96	4390



b) $x/L = 0.51, y/W = 0.00$

Fig. 32. Continued.

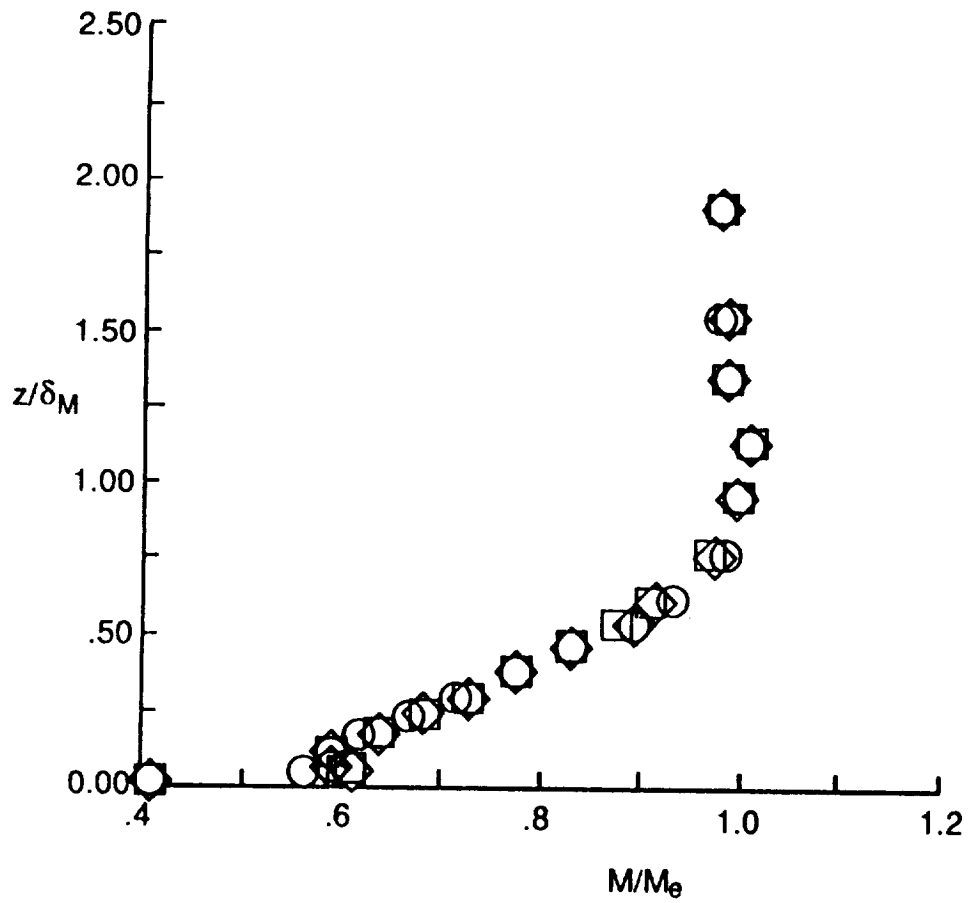
	Run	$Re_{\infty} \times 10^{-6}, ft^{-1}$	$\delta_M, in.$	M_e	Re_{θ}^*
○	19	0.82	0.91	4.86	2980
□	16	1.07	0.91	4.95	3840
◇	18	1.38	0.88	4.89	5560



c) $x/L = 0.61, y/W = -0.20$

Fig. 32. Continued.

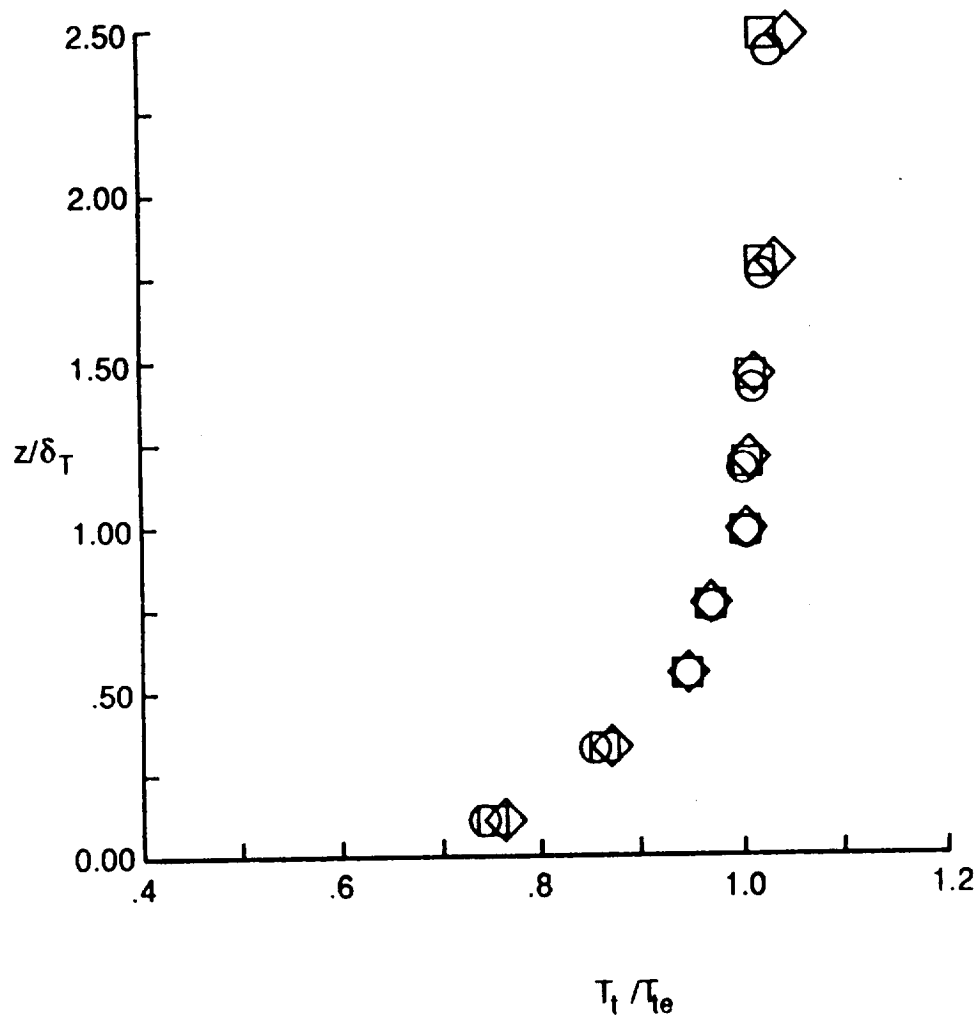
	Run	$Re_{\infty} \times 10^{-6}, ft^{-1}$	$\delta_M, in.$	M_e	Re_{θ}
○	32	0.83	1.01	4.96	3530
□	31	1.38	1.16	4.88	6300
◇	33	1.83	1.14	4.92	7840



d) $x/L = 0.74, y/W = 0.00$

Fig. 32. Concluded.

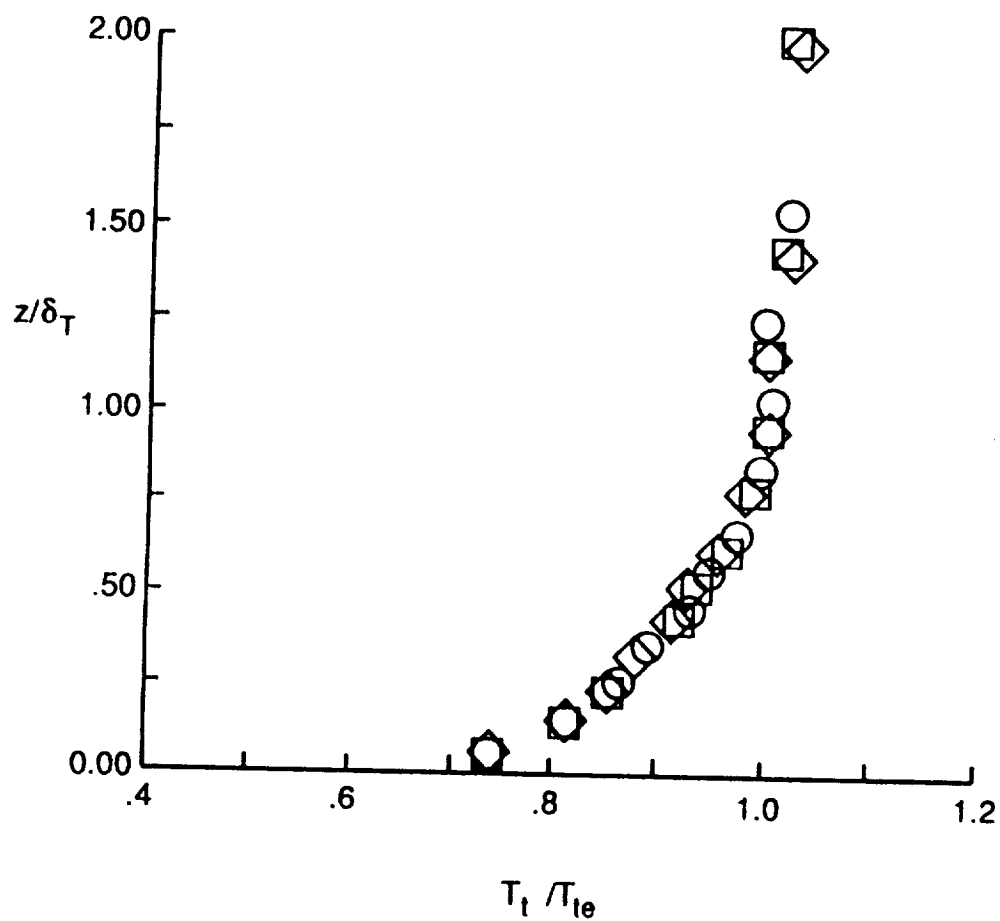
	Run	$Re_\infty \times 10^{-6}, ft^{-1}$	$\delta_T, in.$	$T_{te}, ^\circ R$	Re_0
○	19	0.82	0.64	3130	2290
□	16	1.07	0.62	3310	3190
◇	18	1.38	0.63	3060	4010



a) $x/L = 0.42, y/W = 0.21$

Fig. 33. Total temperature distributions for various free-stream unit Reynolds numbers. ($\alpha = 12.9^\circ, T_{aw}/T_w = 5.4$)

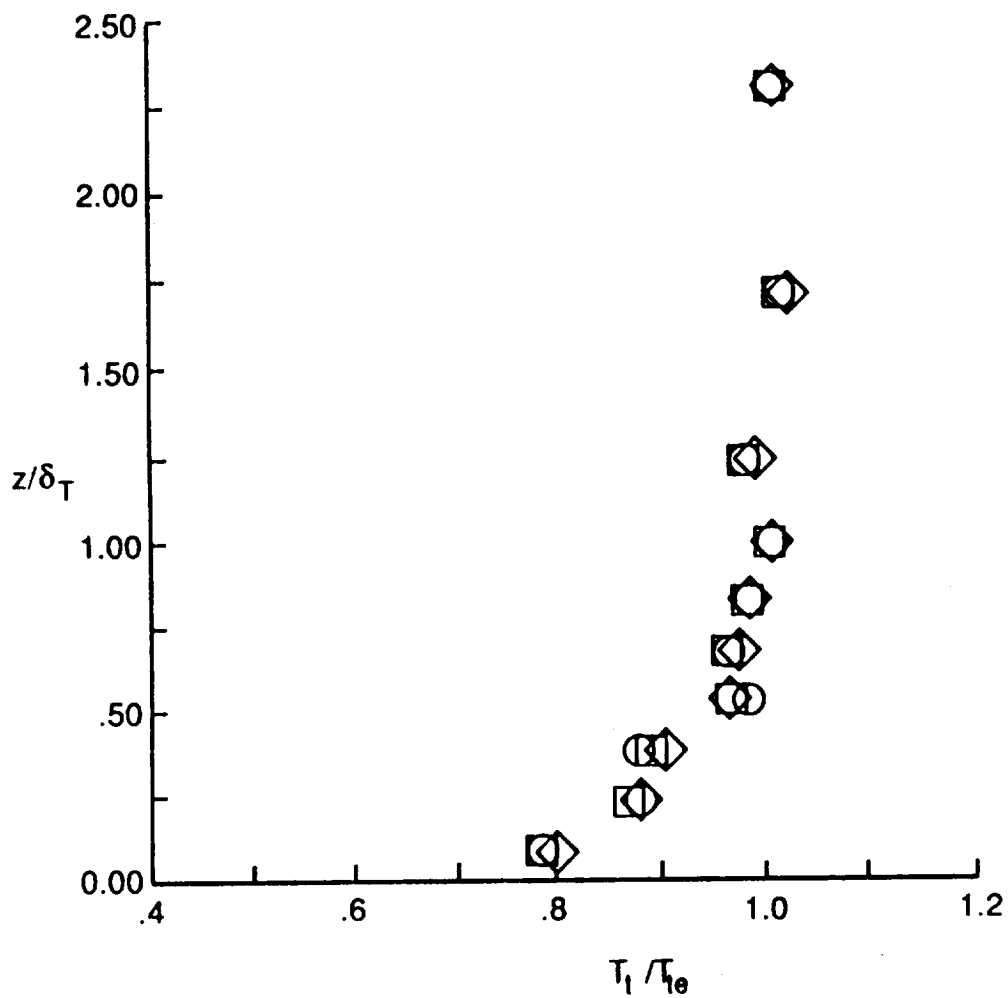
	Run	$Re_{\infty} \times 10^{-6}, ft^{-1}$	$\delta_T, in.$	$T_{te}, ^\circ R$	Re_{θ}^*
○	19	0.82	0.69	3110	2240
□	16	1.07	0.72	3270	3210
◇	18	1.38	0.76	3030	4390



b) $x/L = 0.51, y/W = 0.00$

Fig. 33. Continued.

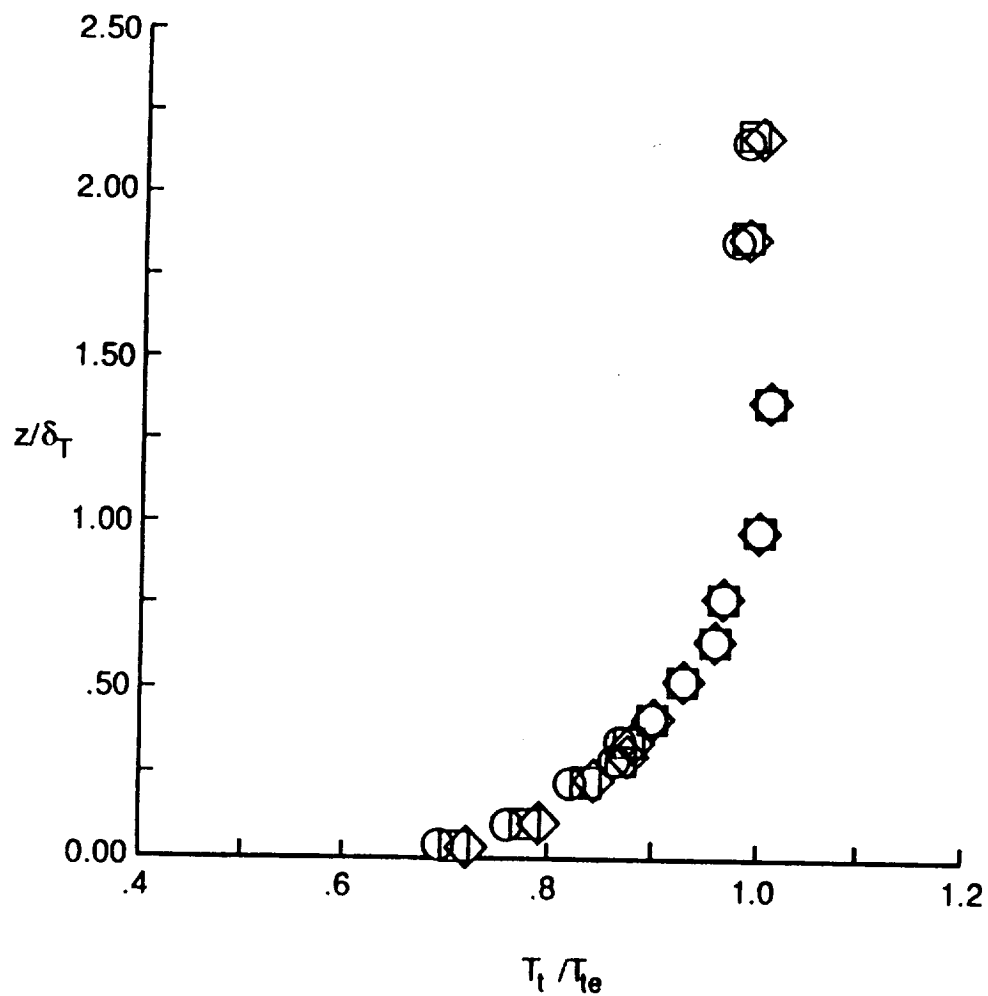
	Run	$Re_{\infty} \times 10^{-6}, ft^{-1}$	$\delta_T, in.$	$T_{te}, ^\circ R$	Re_0
○	19	0.82	0.91	3050	2980
□	16	1.07	0.89	3160	3840
◇	18	1.38	0.91	3040	5560



c) $x/L = 0.61, y/W = -0.20$

Fig. 33. Continued.

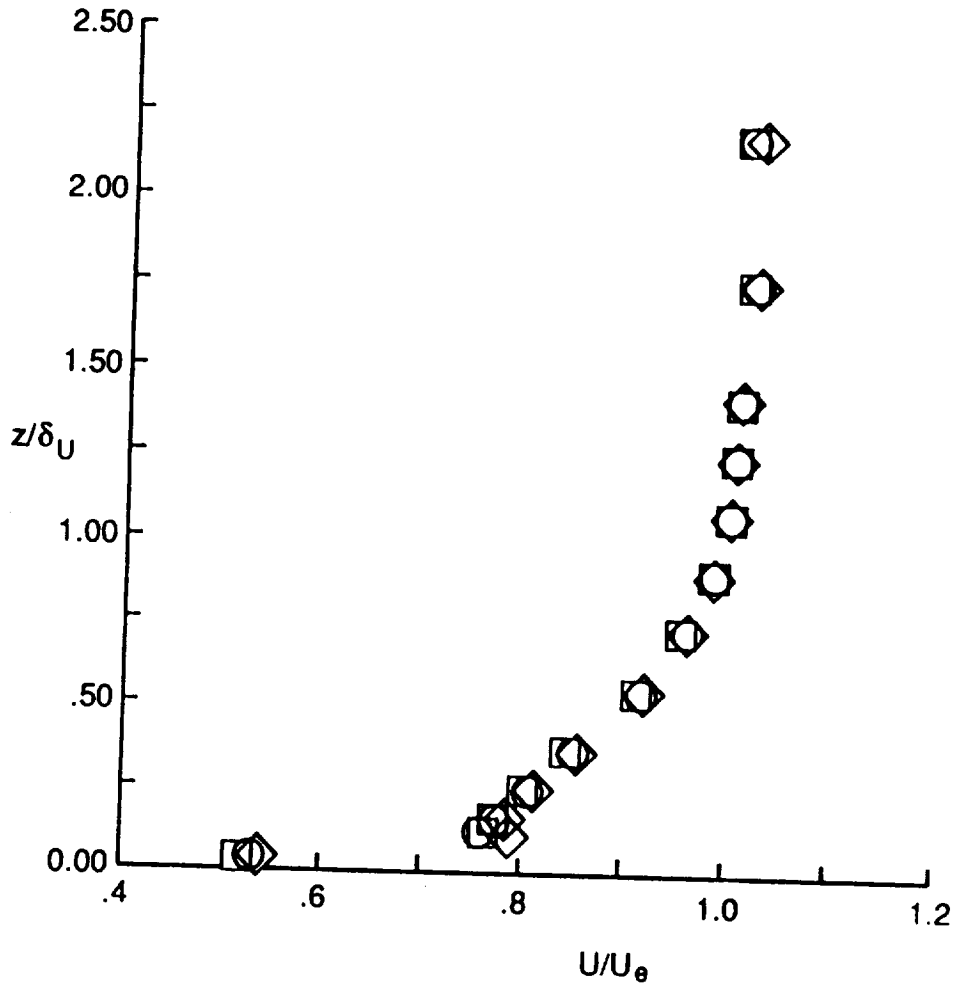
	Run	$Re_{\infty} \times 10^{-6}, ft^{-1}$	$\delta_T, in.$	$T_{te}, ^\circ R$	Re_{θ}'
○	32	0.83	1.00	3100	3530
□	31	1.38	1.13	3210	6300
◇	33	1.83	1.15	3140	7840



d) $x/L = 0.74, y/W = 0.00$

Fig. 33. Concluded.

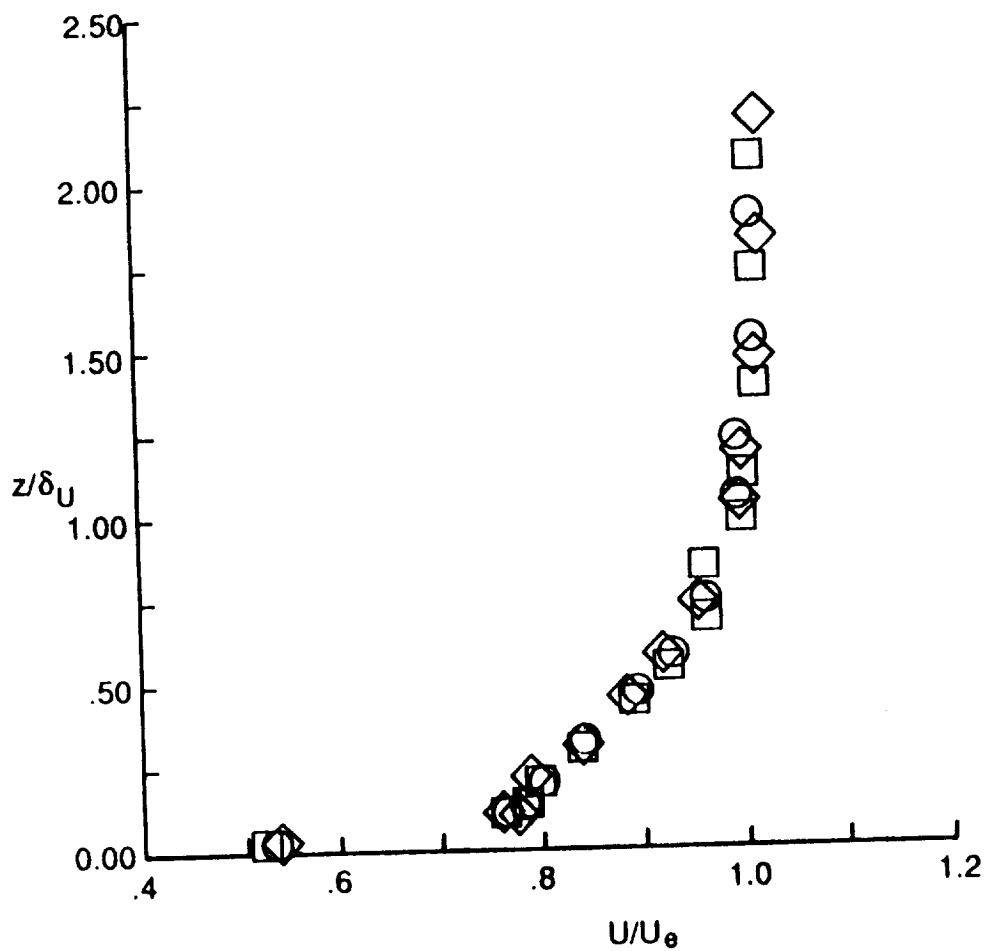
	Run	$Re_\infty \times 10^6, \text{ft}^{-1}$	$\delta_U, \text{in.}$	$U_\theta, \text{ft/s}$	Re_θ^*
○	19	0.82	0.59	6160	2290
□	16	1.07	0.59	6340	3190
◇	18	1.38	0.60	6020	4010



a) $x/L = 0.42, y/W = 0.21$

Fig. 34. Velocity distributions for various free-stream unit Reynolds numbers. ($\alpha = 12.9^\circ, T_{aw}/T_w = 5.4$)

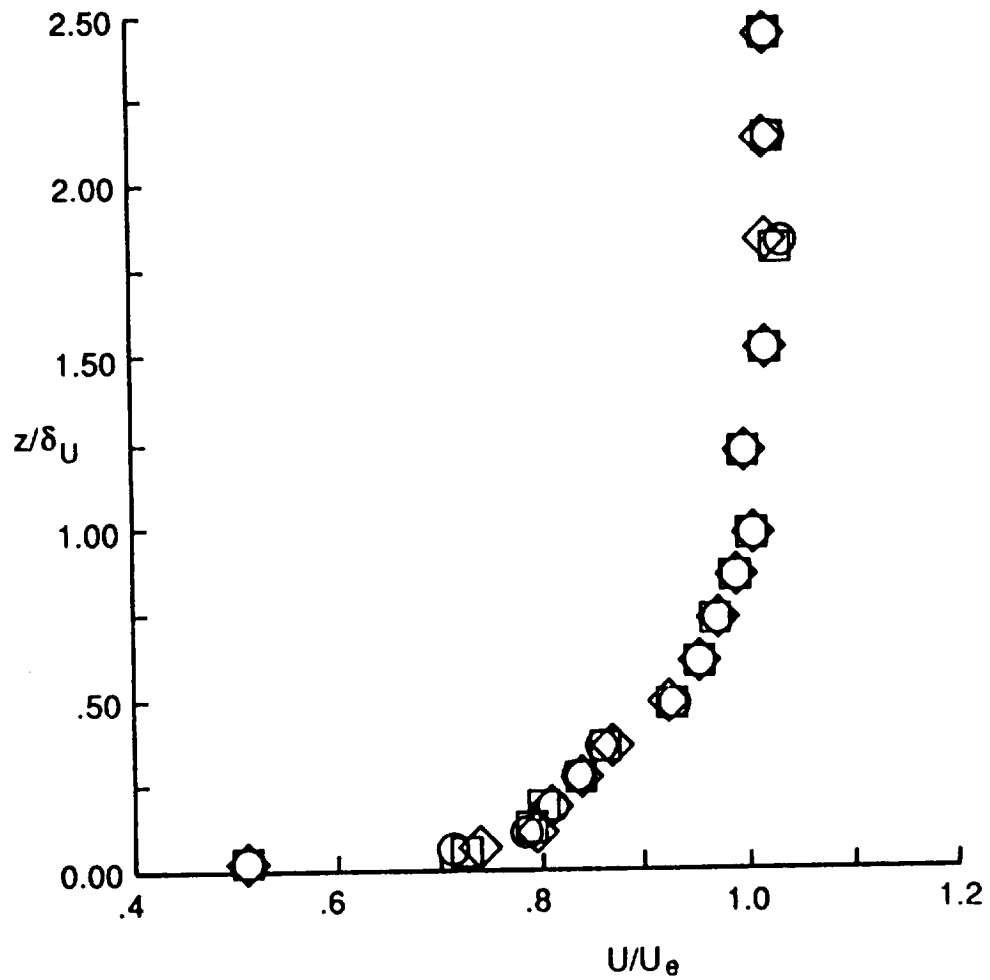
	Run	$Re_{\infty} \times 10^6, \text{ft.}^{-1}$	$\delta_U, \text{in.}$	$U_{\theta}, \text{ft/s}$	Re_{θ}^*
○	19	0.82	0.66	6080	2240
□	16	1.07	0.68	6300	3210
◇	18	1.38	0.72	6040	4390



b) $x/L = 0.51, y/W = 0.00$

Fig. 34. Continued.

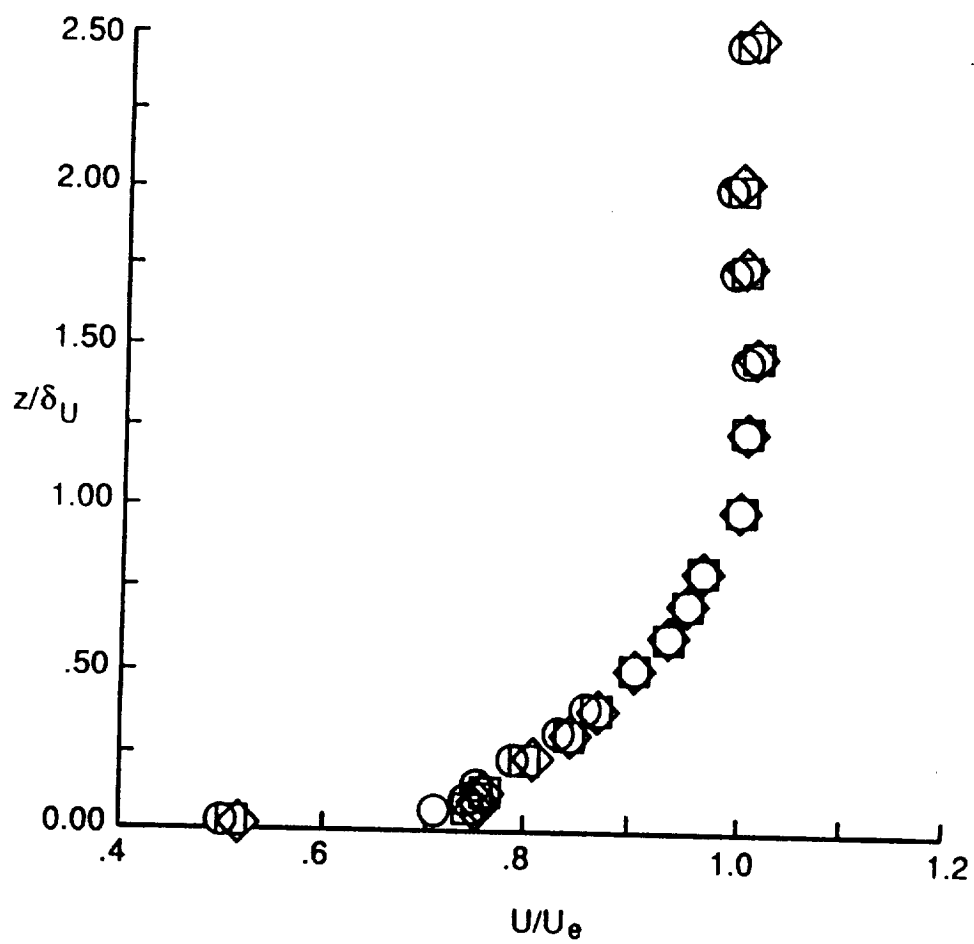
	Run	$Re_\infty \times 10^6, \text{ft.}^{-1}$	$\delta_U, \text{in.}$	$U_\theta, \text{ft/s}$	Re_θ^*
○	19	0.82	0.86	5970	2980
□	16	1.07	0.86	6140	3840
◇	18	1.38	0.84	5920	5560



c) $x/L = 0.61, y/W = -0.20$

Fig. 34. Continued.

	Run	$Re_{\infty} \times 10^6, ft^{-1}$	$\delta_U, in.$	$U_e, ft/s$	Re_{θ}^*
○	32	0.83	0.97	6080	3530
□	31	1.38	1.03	6200	6300
◇	33	1.83	1.00	6080	7840



d) $x/L = 0.74, y/W = 0.00$

Fig. 34. Concluded.

Reynolds number, Re_θ^* , ranges from 2240 to 7840, and is therefore well above the nominal value of 1200 which is assumed to correspond to the end of transition.

The normalized Mach number distributions (Figs. 32a through 32d) show little variation with free-stream unit Reynolds number. Note that as the boundary-layer thickness increases with distance downstream from the leading edge (Figs. 32a through 32d), the inflection in the Mach number profiles mentioned in section 3.3.2 moves closer to the wall. This result, along with the observation that the four probes closest to the wall were too close, based on the guidelines discussed in section 2.2.2, indicates that the inflection most likely results from pitot probe interference. Therefore, the accuracy of the four Mach number data points closest to the wall is questionable.

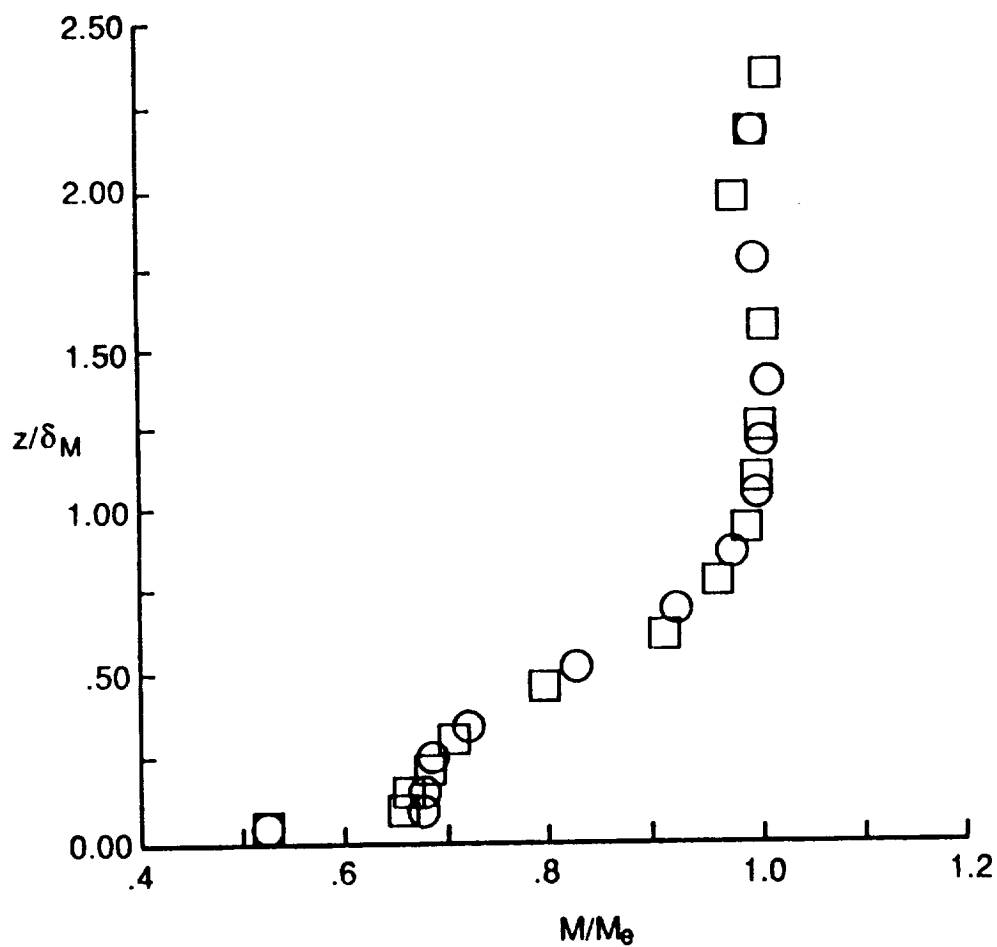
As with the normalized Mach number distributions, the normalized total temperature distributions (Figs. 33a through 33d) show no effect of free-stream Reynolds number variations. The irregularities shown in the total temperature distributions obtained at $x/L = 0.61$ are caused by contact between the thermocouple bead and the radiation shield, as mentioned previously.

The normalized velocity distributions (Figs. 34a through 34d) also show no effect of free-stream unit Reynolds number. Because the velocity distributions were calculated from the Mach number distributions, the four data points closest to the wall are in error because of probe interference.

3.3.4 Effect of Temperature Ratio

Normalized distributions of Mach number, total temperature, and velocity are shown in Figs. 35 through 37 to assess any effects of temperature ratio. The data are shown for temperature ratios of 4.4 and 5.4, a nominal

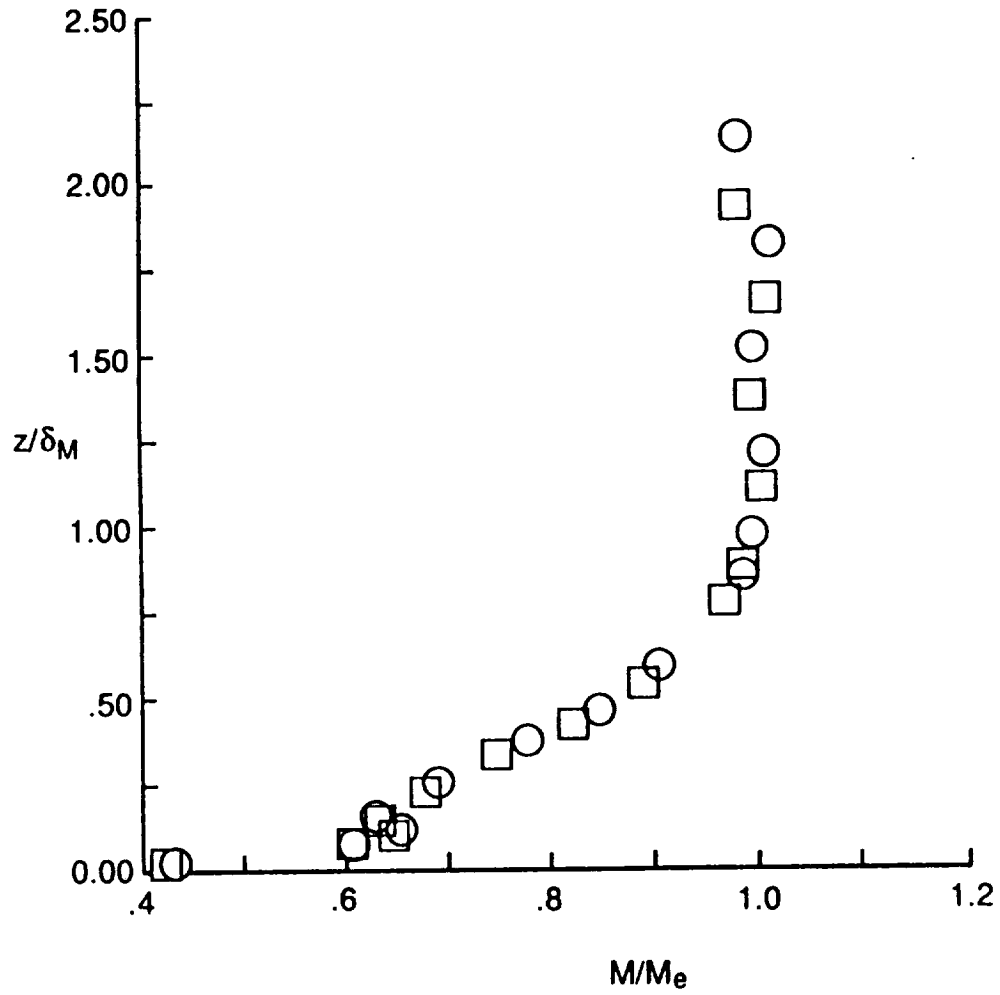
	Run	T_{aw}/T_w	δ_M , in.	M_θ	α , deg.	Re_θ^*
○	24	4.4	0.55	5.14	10.8	1970
□	19	5.4	0.58	4.93	12.8	2290



a) $x/L = 0.42$, $y/W = 0.21$

Fig. 35. Mach number distributions for various temperature ratios.
($Re^* = 0.69 \times 10^6 ft^{-1}$.)

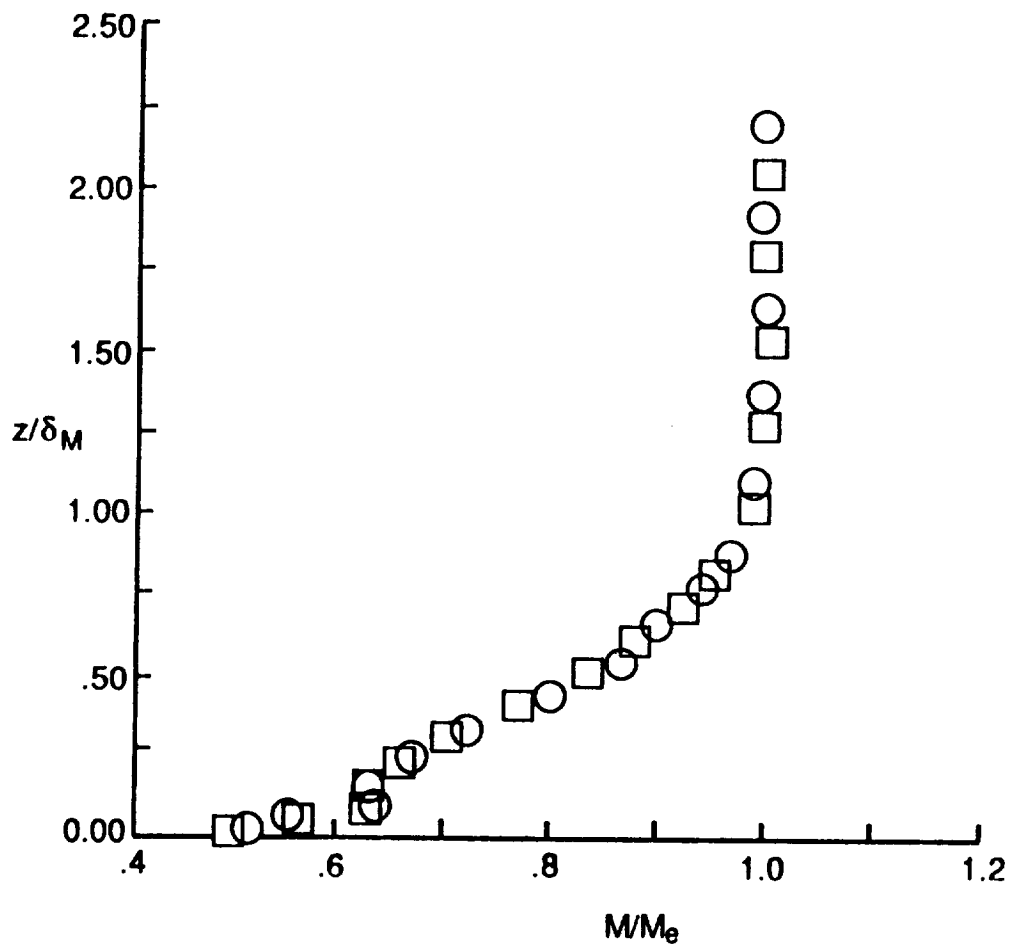
	Run	T_{aw}/T_w	δ_M , in.	M_θ	α , deg.	Re_θ
○	24	4.4	0.65	5.16	10.8	1710
□	19	5.4	0.72	4.98	12.8	2240



b) $x/L = 0.51$, $y/W = 0.00$

Fig. 35. Continued.

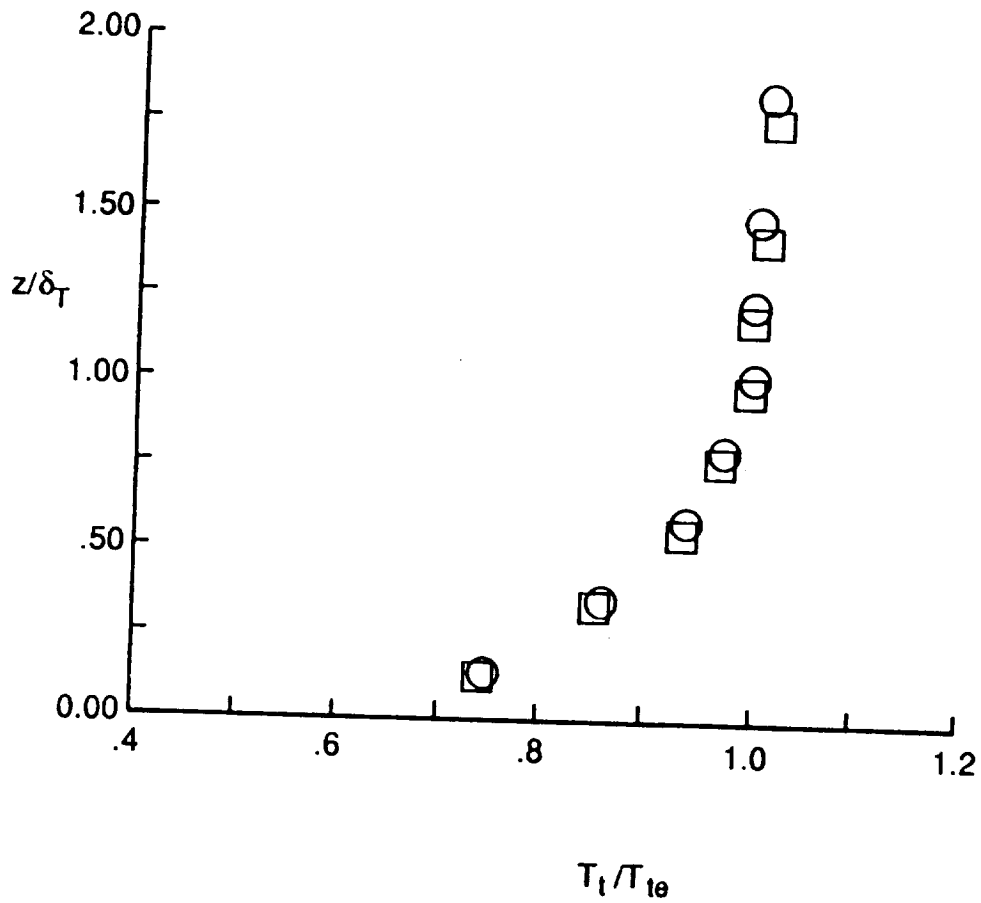
	Run	T_{aw}/T_w	δ_M , in.	M_θ	α , deg.	Re_θ
○	24	4.4	0.81	4.97	10.8	2150
□	19	5.4	0.91	4.86	12.8	2980



c) $x/L = 0.61$, $y/W = -0.20$

Fig. 35. Concluded.

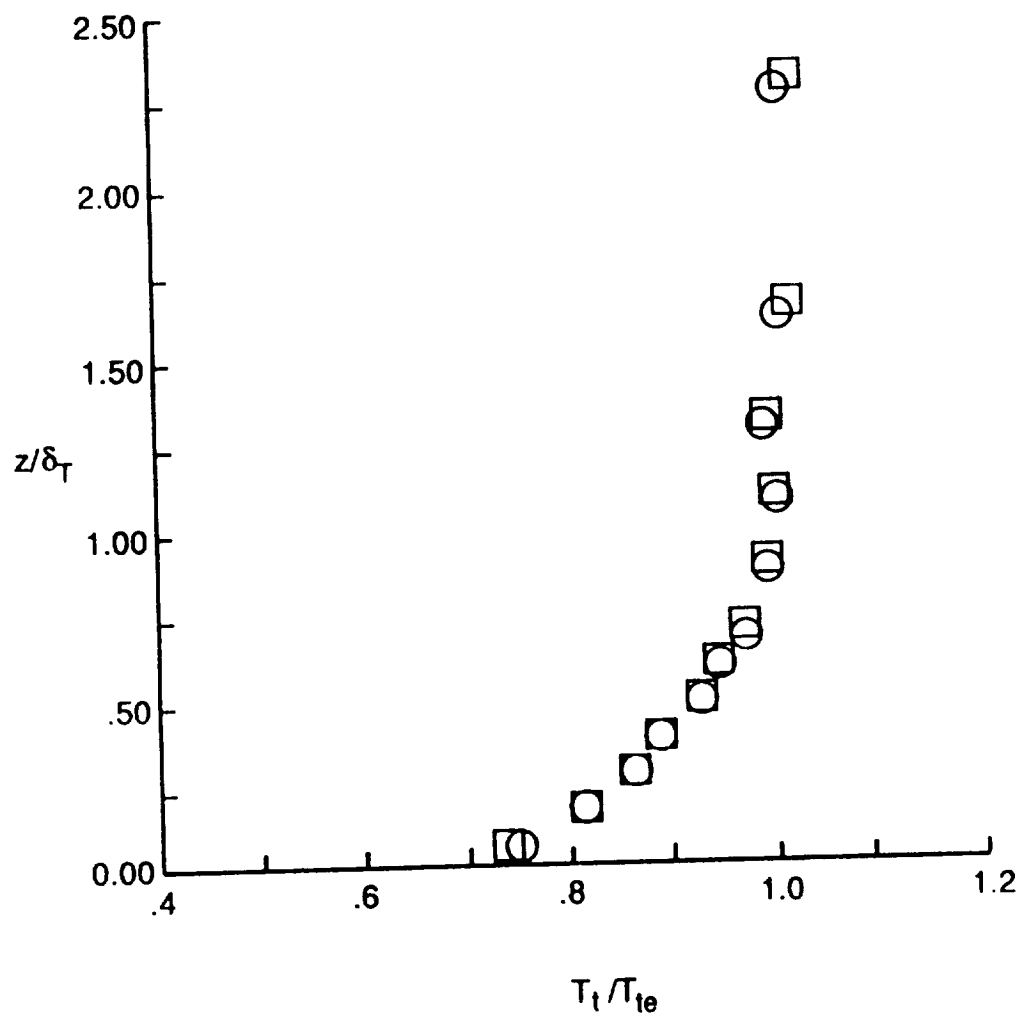
	Run	T_{aw}/T_w	δ_T , in.	T_{te} , °R	Re_θ^*
○	24	4.4	0.57	2630	1970
□	19	5.4	0.64	3150	2290



a) $x/L = 0.42$, $y/W = 0.21$

Fig. 36. Total temperature distributions
for various temperature ratios.
($Re^* = 0.69 \times 10^6 \text{ ft}^{-1}$, $M_\theta = 5.0$)

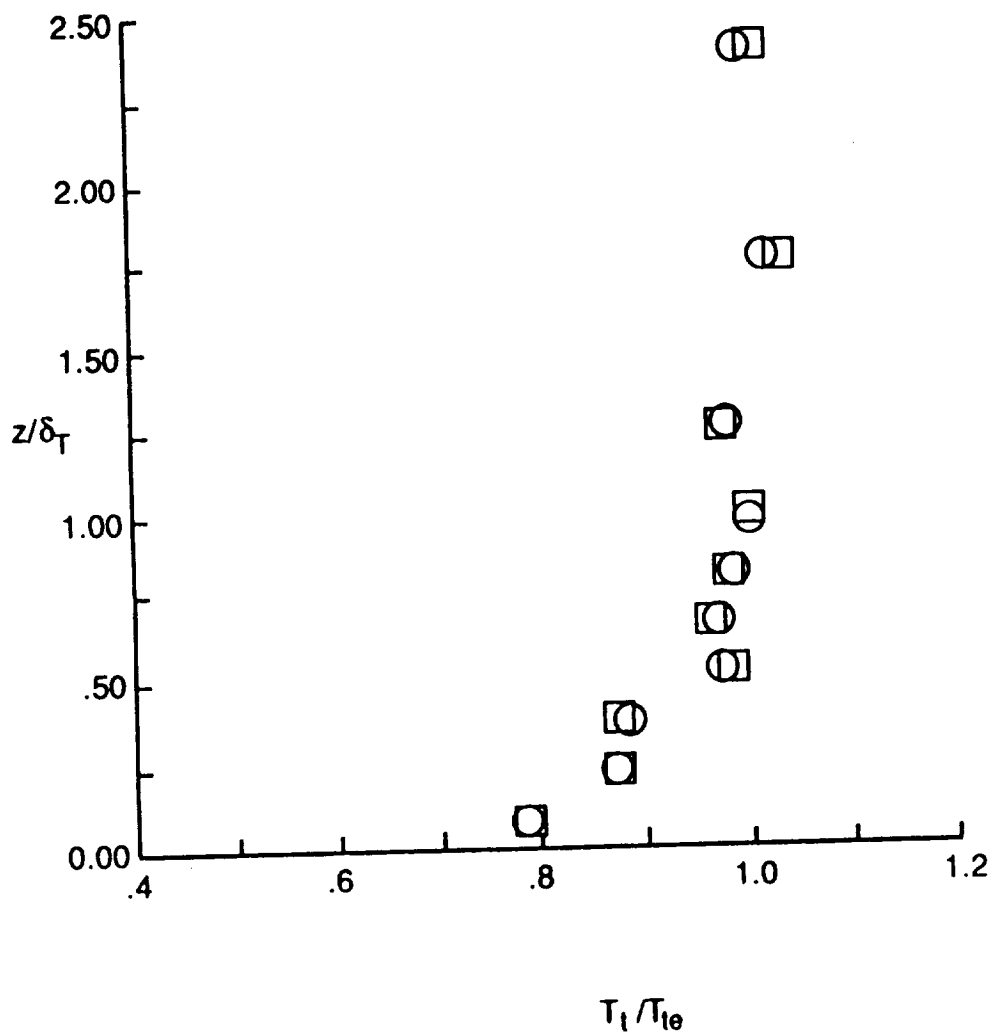
	Run	T_{aw}/T_w	δ_T , in.	T_{te} , °R	Re_θ^*
○	24	4.4	0.61	2600	1710
□	19	5.4	0.69	3110	2240



b) $x/L = 0.51$, $y/W = 0.00$

Fig. 36. Continued.

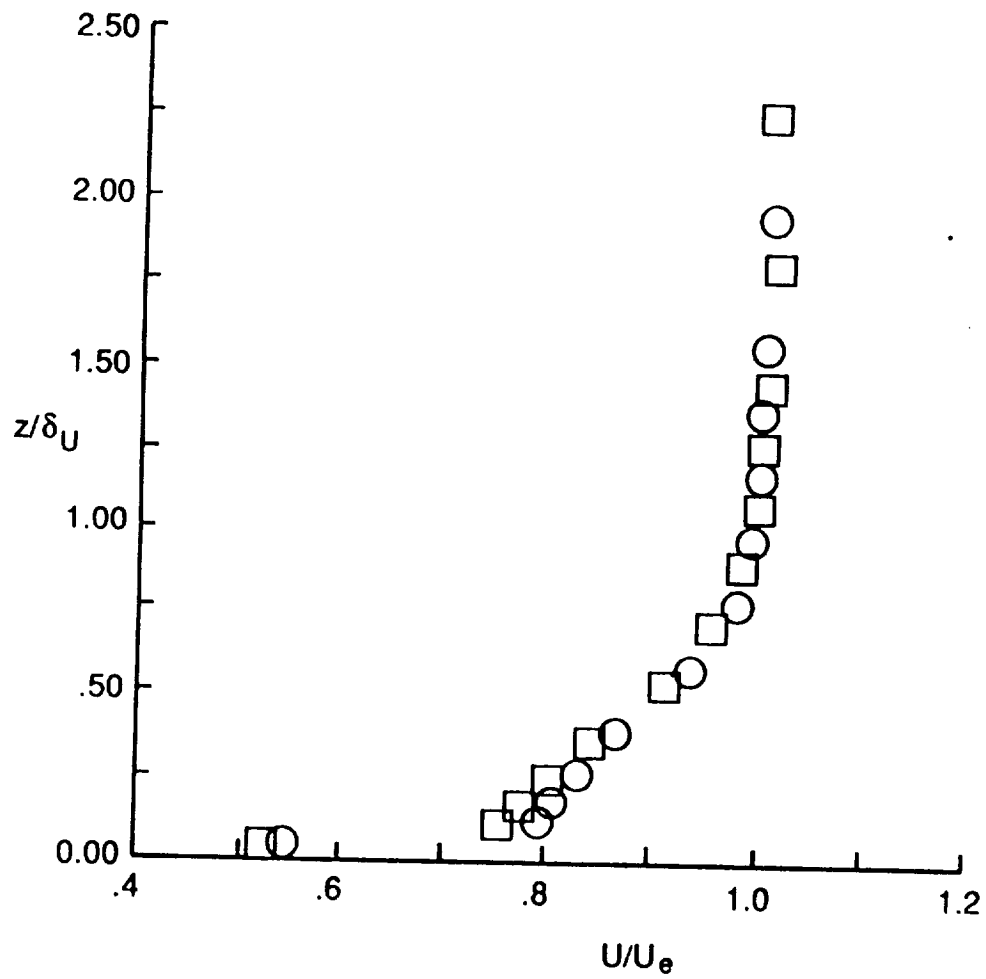
	Run	T_{aw}/T_w	δ_T , in.	T_{le} , °R	Re_0
○	24	4.4	0.82	2480	2150
□	19	5.4	0.91	3050	2980



c) $x/L = 0.61$, $y/W = -0.20$

Fig. 36. Concluded.

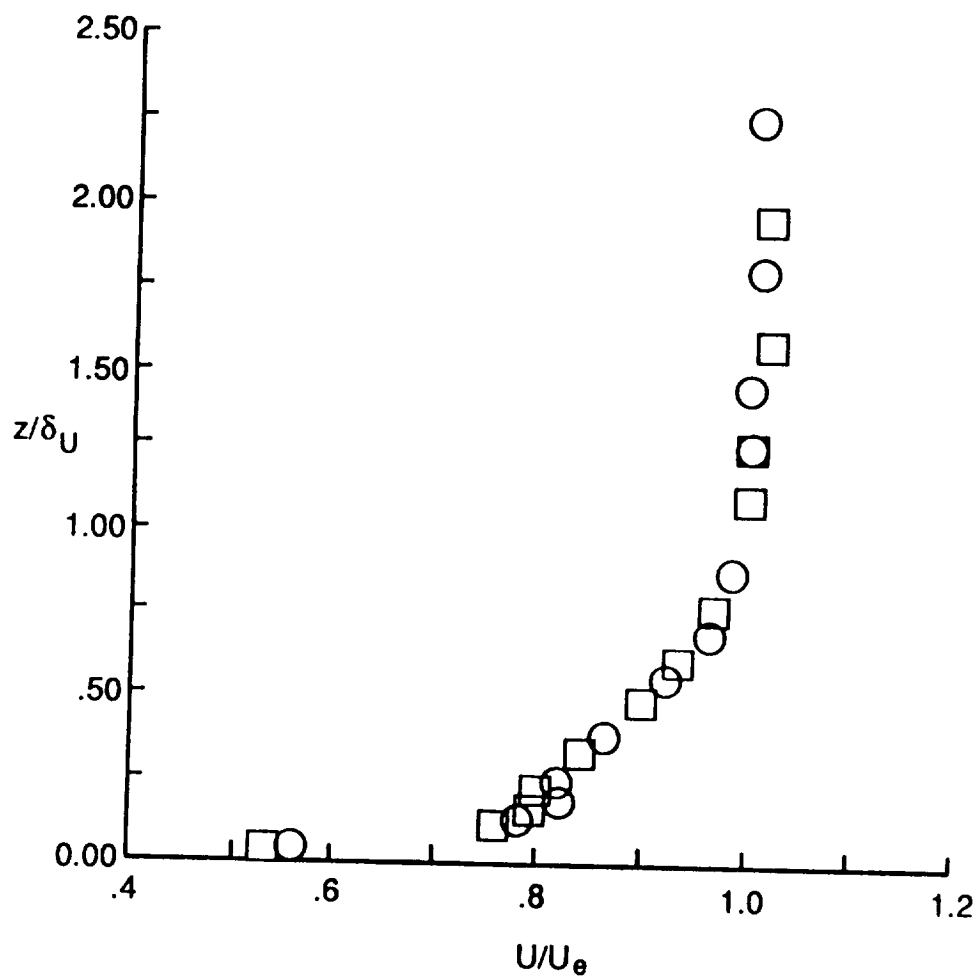
	Run	T_{aw}/T_w	δ_U , in.	U_θ , ft/s	Re_θ^*
○	24	4.4	0.52	5540	1970
□	19	5.4	0.59	6160	2290



a) $x/L = 0.42$, $y/W = 0.21$

Fig. 37. Velocity distributions for various temperature ratios.
 $(Re^* = 0.69 \times 10^6 \text{ ft}^{-1}, M_e = 5.0)$

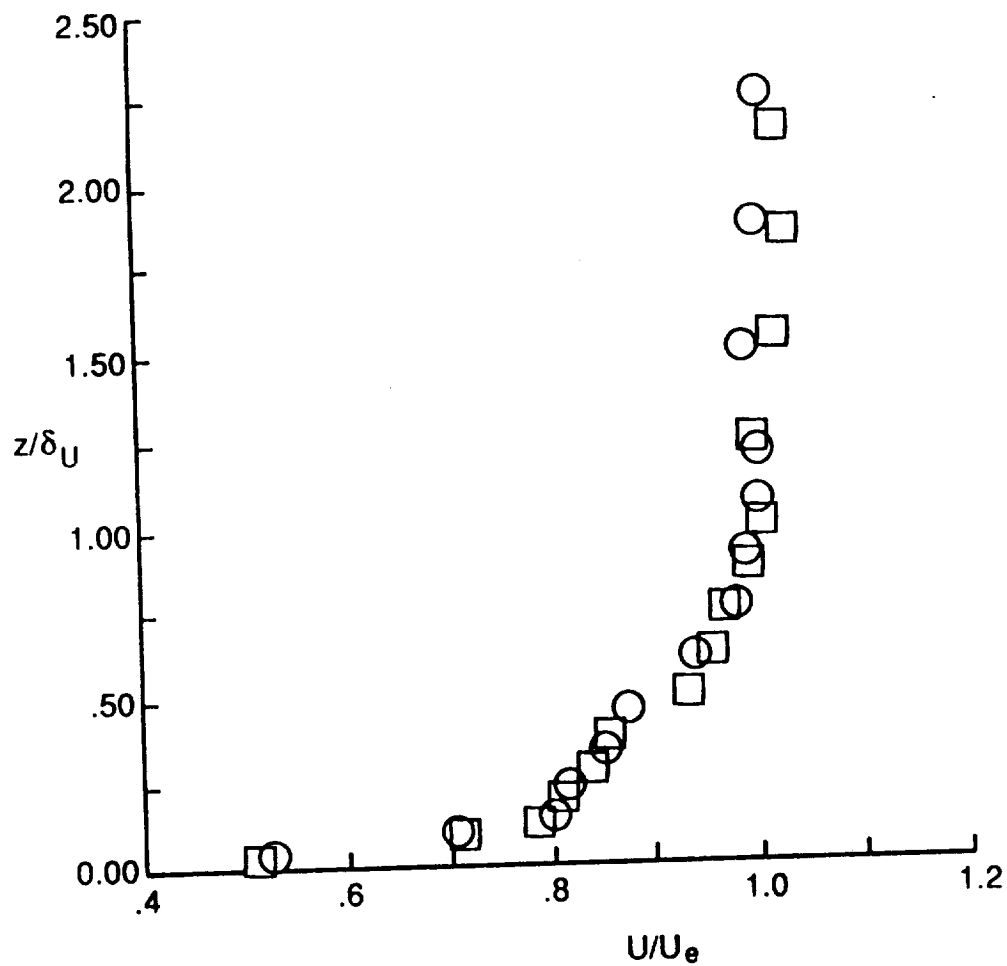
	Run	T_{aw}/T_w	δ_U , in.	U_e , ft/s	Re_θ
○	24	4.4	0.52	5480	1710
□	19	5.4	0.66	6080	2240



b) $x/L = 0.51$, $y/W = 0.00$

Fig. 37. Continued.

	Run	T_{aw}/T_w	δ_U , in.	U_e , ft/s	Re_θ
○	24	4.4	0.61	5330	2150
□	19	5.4	0.86	5920	2980



c) $x/L = 0.61$, $y/W = -0.20$

Fig. 37. Concluded.

Mach number of 5.0, and a local unit Reynolds number of $0.69 \times 10^6/\text{ft}$. The momentum thickness Reynolds number, Re_θ^* , ranges from 1710 to 2980 and is therefore above the level of 1200 corresponding to the end of transition. The distributions are shown for three locations on the plate surface.

The Mach number distributions (Figs. 35a through 35c) show no significant variation with temperature ratio. This can also be said of the total temperature distributions (Figs. 36a through 36c) and of the velocity distributions (Figs. 37a through 37c). Overall, these results indicate that there are no anomalous effects due to temperature ratio variation, at least for the present range of test conditions. Note however, that for a given location and local unit Reynolds number, the momentum thickness Reynolds number, Re_θ^* , tends to be smaller at the lower temperature ratio of 4.4. This is because the momentum thicknesses are smaller as a result of the difference in density variation in the boundary layer.

3.3.5 Correlation of Velocity Power Law Exponent

The velocity distributions are correlated in terms of the power law exponent as a function of momentum thickness Reynolds number, Re_θ , (Fig. 38). Note that for the present correlation, Re_θ is based on boundary-layer edge conditions to be consistent with previous investigations. The power law exponent, N , was calculated using the following relationship:

$$\frac{U}{U_e} = \left(\frac{z}{\delta_U} \right)^{1/N} \quad (5)$$

The exponent, N , and velocity boundary-layer thickness, δ_U , were obtained by first calculating an average edge velocity, U_e , using the data known to be outside the boundary layer and then applying a least squares curve fit, as

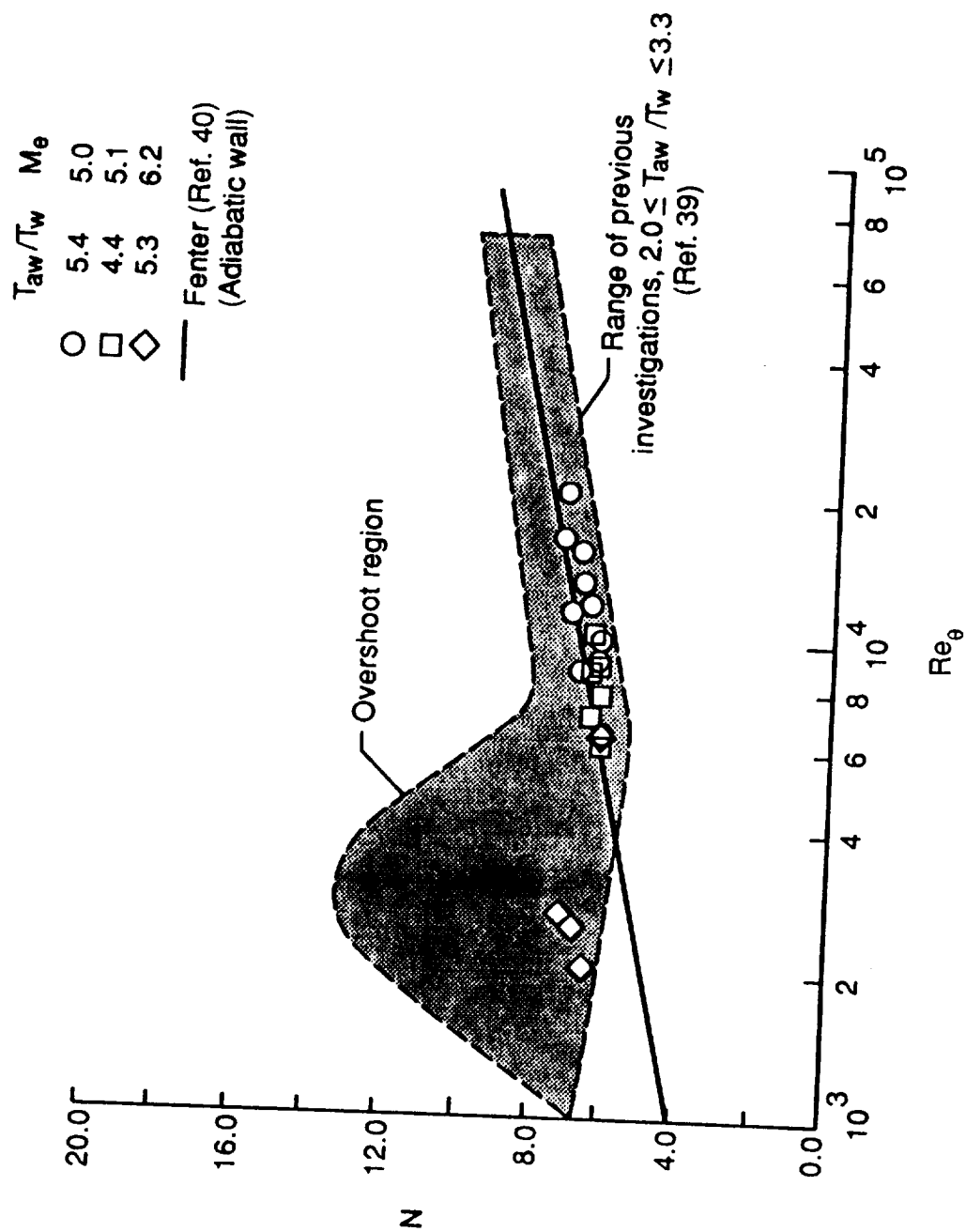


Fig. 38. Power law exponent variation with Re_θ .

discussed in section 3.3.2. The four velocity measurements closest to the wall were neglected because of the pitot probe interference problem previously mentioned.

The power law exponents for the present investigation are shown in Fig. 38 with the results from a previous investigation by Hopkins et. al. [39] at nonadiabatic wall conditions ($2.0 \leq T_{aw}/T_w \leq 3.3$). Note that the temperature ratio, T_{aw}/T_w , for the present investigation ranges from 4.4 to 5.6. Fenter's empirical curve for adiabatic wall data [40] is also shown for comparison purposes. Hopkins et. al. noted an "overshoot" region in their data for Re_θ below 6×10^3 , which was absent from their finite-difference calculations for equilibrium flow conditions. They attributed this overshoot to nonequilibrium flow. Overall, the exponents from the present investigation show trends similar to the Hopkins' data and the three data points near $Re_\theta = 2 \times 10^3$ are contained within Hopkins' overshoot region. These three data points correspond to an Re_θ^* ranging from 390 to 540, which was shown previously to indicate a transitional boundary layer. For Re_θ above 6×10^3 , the exponents show a slight increase with Re_θ as shown by Hopkins' data and Fenter's adiabatic wall data. Overall, the velocity distributions for the present test conditions can be represented by a nominal power law exponent of 6.3 for Re_θ above 6×10^3 . There appears to be no effect of temperature ratio on the trends or overall levels of the the power law exponents.

3.3.6 Total Temperature Variation with Velocity

Total temperature variations with velocity in the boundary layer are presented in this section at various locations on the plate and at various test conditions. The velocities affected by the probe interference problem cited in

section 3.3.2 have been corrected using the power law exponent calculated for the corresponding velocity profile. For comparison purposes, the linear Crocco-Busemann temperature-velocity relationship [22 and 23] and the quadratic relationship given by Bushnell et al. [35] are also presented. The linear relationship can be derived from the energy equation for a two-dimensional boundary layer assuming $T = T(U)$. This relationship is given as:

$$\frac{T_T - T_w}{T_{Te} - T_w} = \frac{U}{U_e} \quad (6)$$

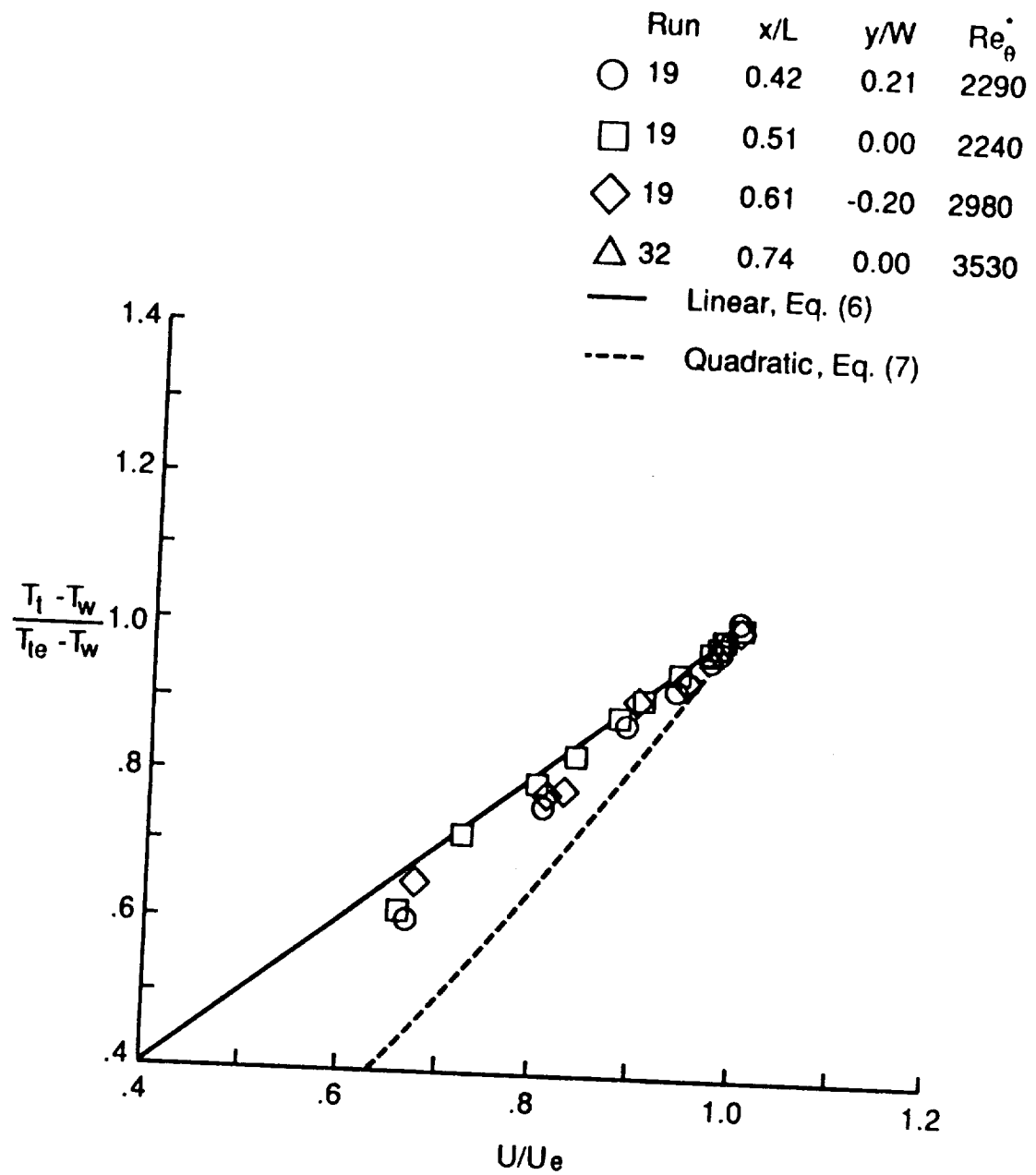
The linear relationship is valid for zero pressure gradient, constant wall temperature, calorically perfect boundary layers with a Prandtl number of unity. This relationship is also valid for constant-radius nozzle flows, as discussed by Bushnell [35], provided that the effects upstream pressure and temperature gradients have dissipated.

The quadratic relationship given by Bushnell et al. [35] is a curve fit of all the nozzle wall data available at the time. This relationship is given as:

$$\frac{T_T - T_w}{T_{Te} - T_w} = \left(\frac{U}{U_e} \right)^2 \quad (7)$$

Using finite-difference calculations, Bushnell showed that the difference between the two relationships is primarily due to the upstream favorable pressure gradient history of nozzle wall boundary layers. Bushnell's results indicate that the temperature-velocity distributions approach the linear Crocco-Busemann relation at large distances downstream from where the nozzle radius is constant.

Total temperature variations with velocity are shown in Fig. 39a for a local unit Reynolds number of 0.69×10^6 /ft, a boundary-layer edge Mach



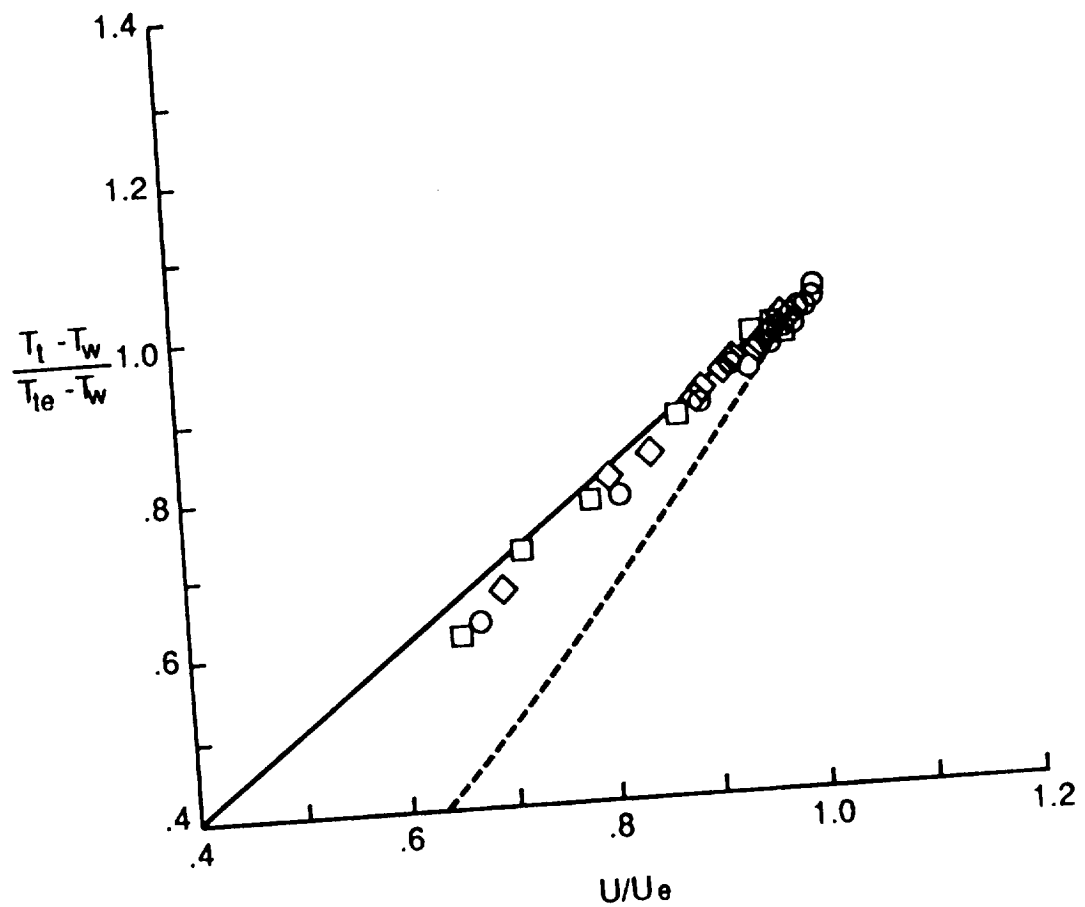
a) $Re^* = 0.69 \times 10^6 \text{ ft.}^{-1}$, $Me = 5.0$, $T_{aw}/T_w = 5.3$

Fig. 39. Total temperature variations with velocity in the boundary layer for various locations on the plate.

number of 5.0, and a temperature ratio, T_{aw}/T_w , of 5.4. The momentum thickness Reynolds number, Re^*_θ , ranges from 2240 to 3530. Overall, the data agree reasonably well with the linear Crocco-Busemann relationship. The data obtained at the higher unit Reynolds numbers of 0.92×10^6 , 1.17×10^6 , and 1.51×10^6 /ft, (Figs. 39b, 39c, and 39d), for which Re^*_θ ranges from 3190 to 7840 also agree well with the linear relationship. However, the data obtained at the lower temperature ratio of 4.4 (Figs. 39e and 39f) are between the linear and quadratic relationships. Note that Re^*_θ is lower for the low temperature data, ranging from 1710 to 2860. At the lowest unit Reynolds number condition of 0.21×10^6 /ft (Fig. 39g) for which Re^*_θ ranges from 391 to 541, the data agree best with the quadratic relationship. As previously mentioned, these values of Re^*_θ are considered to be transitional.

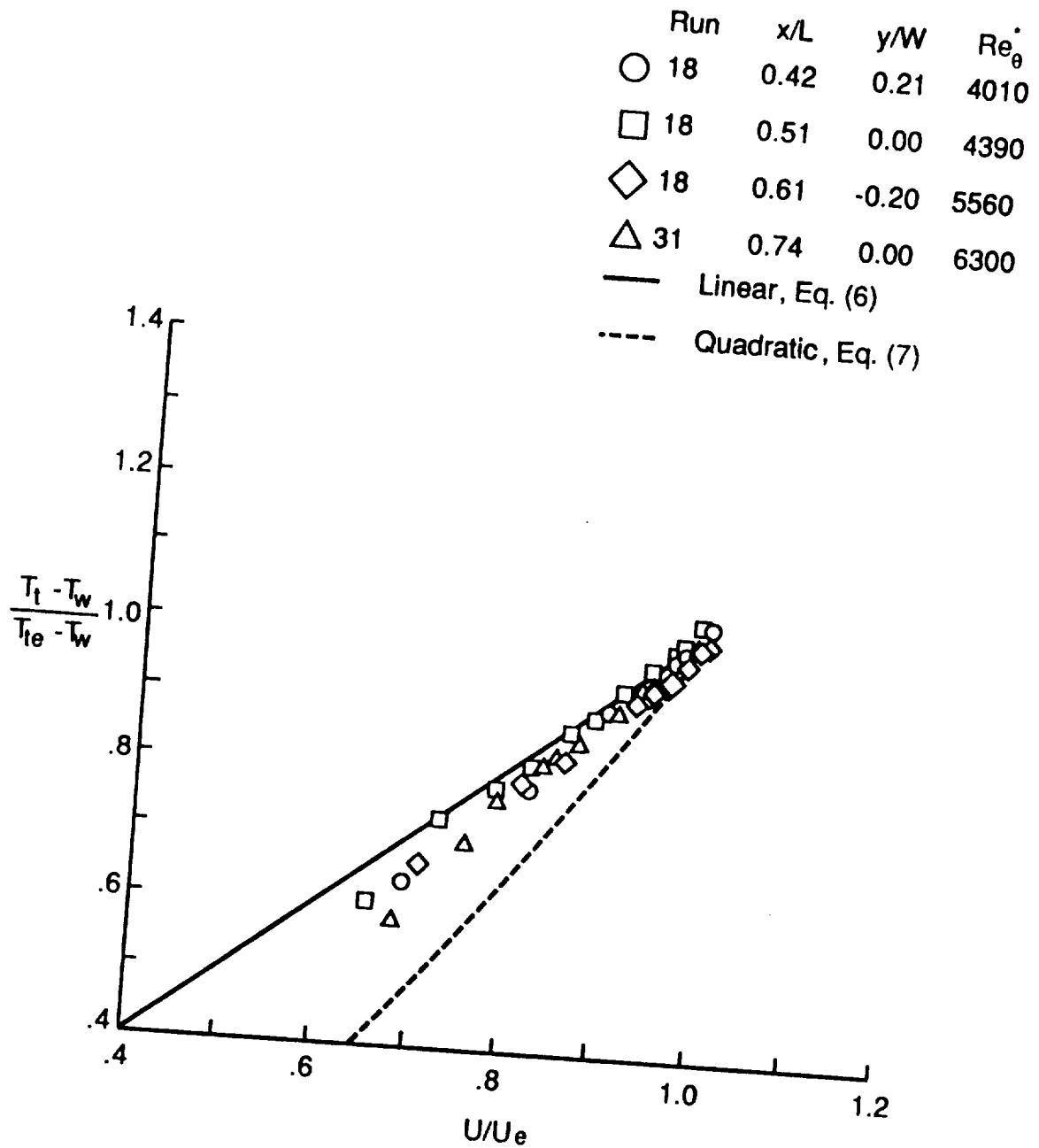
According to Fernholz and Finley [11], however, the tendency of the temperature-velocity profiles to approach a quadratic relationship is evident in other flat plate data and does not necessarily indicate that the boundary layer is in turbulent nonequilibrium. They cite inaccuracies in wall and total temperature measurements as a possible reason for the data to approach a quadratic relation. Therefore, other methods of evaluating turbulent equilibrium are necessary before any conclusions can be made. These evaluations are discussed in detail in Chapter 4.

Run	x/L	y/W	Re_θ
○ 16	0.42	0.21	3190
□ 16	0.51	0.00	3210
◇ 16	0.61	-0.20	3840
—	Linear, Eq. (6)		
- - -	Quadratic, Eq. (7)		



b) $Re^* = 0.92 \times 10^6 \text{ ft.}^{-1}$, $M_e = 4.9$, $T_{aw}/T_w = 5.6$

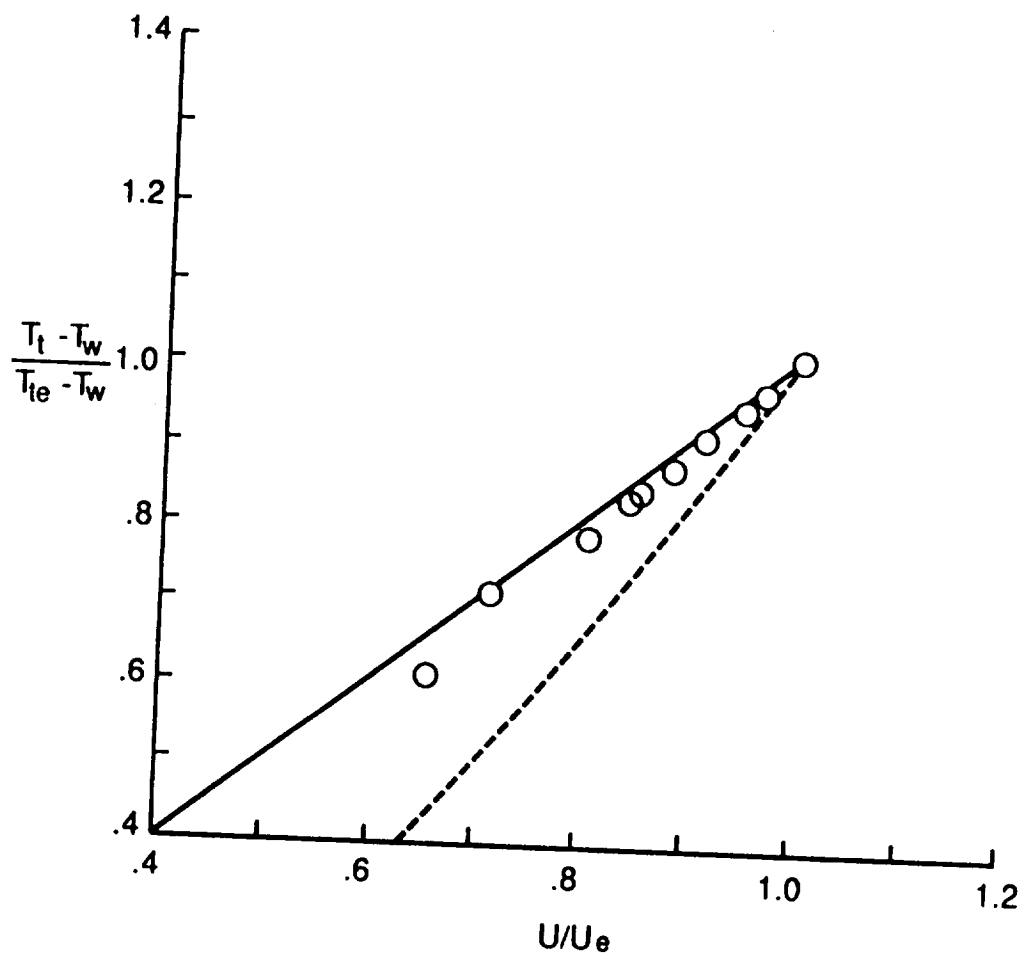
Fig. 39. Continued.



c) $Re^* = 1.17 \times 10^6 \text{ ft.}^{-1}$, $Me = 4.9$, $T_{aw}/T_w = 5.3$

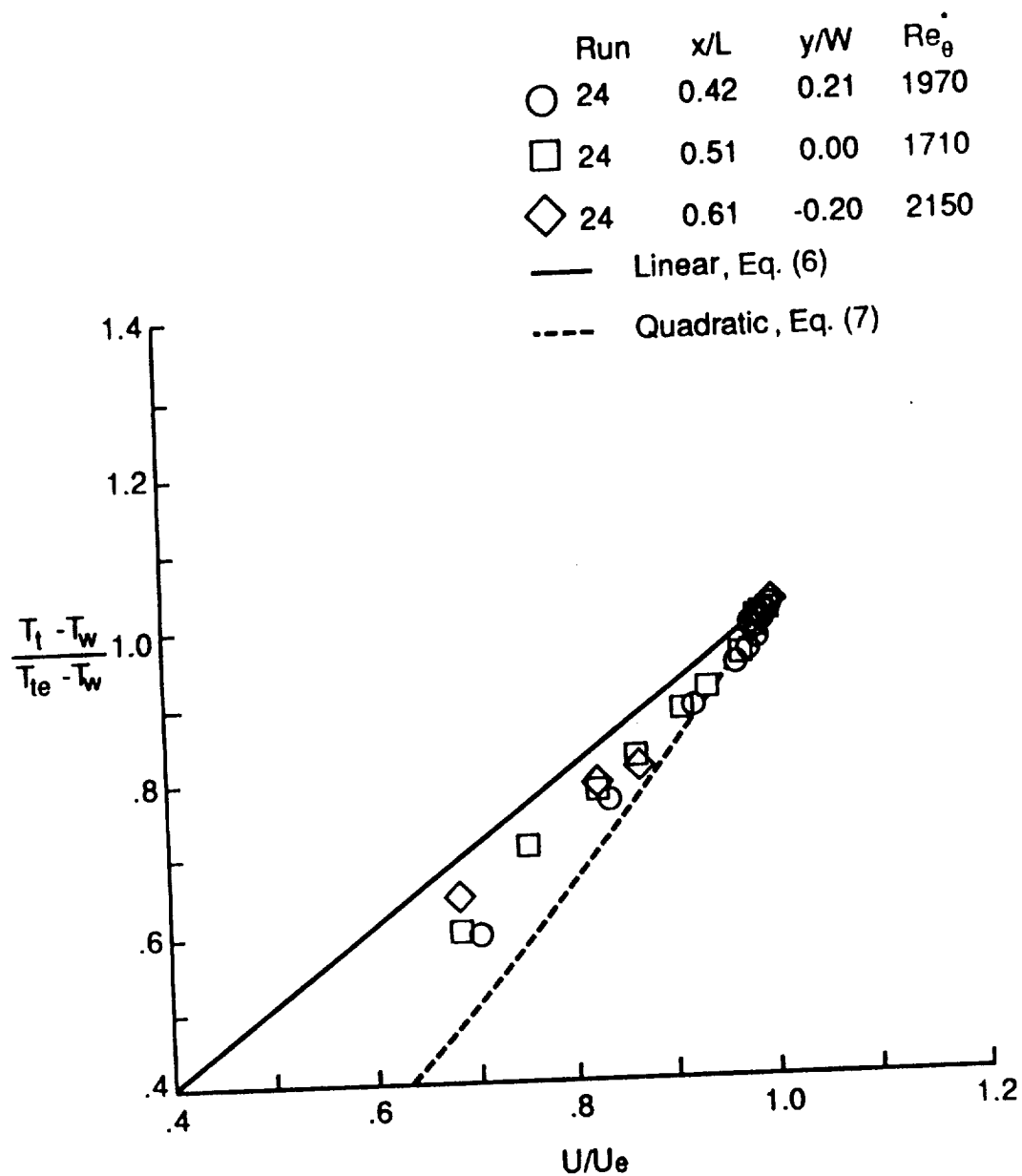
Fig. 39. Continued.

Run	x/L	y/W	Re_θ^*
○ 33	0.74	0.00	7840
— Linear, Eq. (6)			
- - - Quadratic, Eq. (7)			



d) $Re^* = 1.51 \times 10^6 \text{ ft.}^{-1}$, $M_e = 4.9$, $T_{aw}/T_w = 5.4$

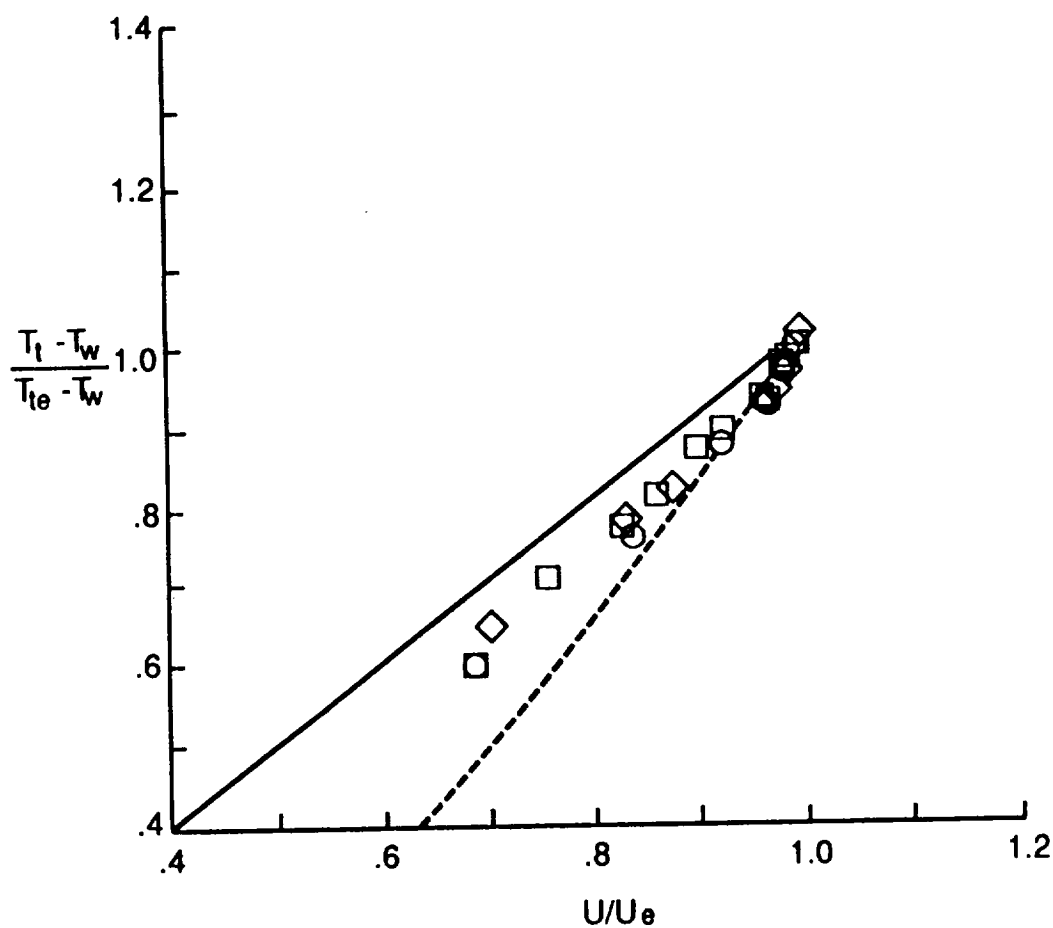
Fig. 39. Continued.



e) $Re^* = 0.69 \times 10^6 \text{ ft.}^{-1}$, $Me = 5.1$, $T_{aw}/T_w = 4.4$

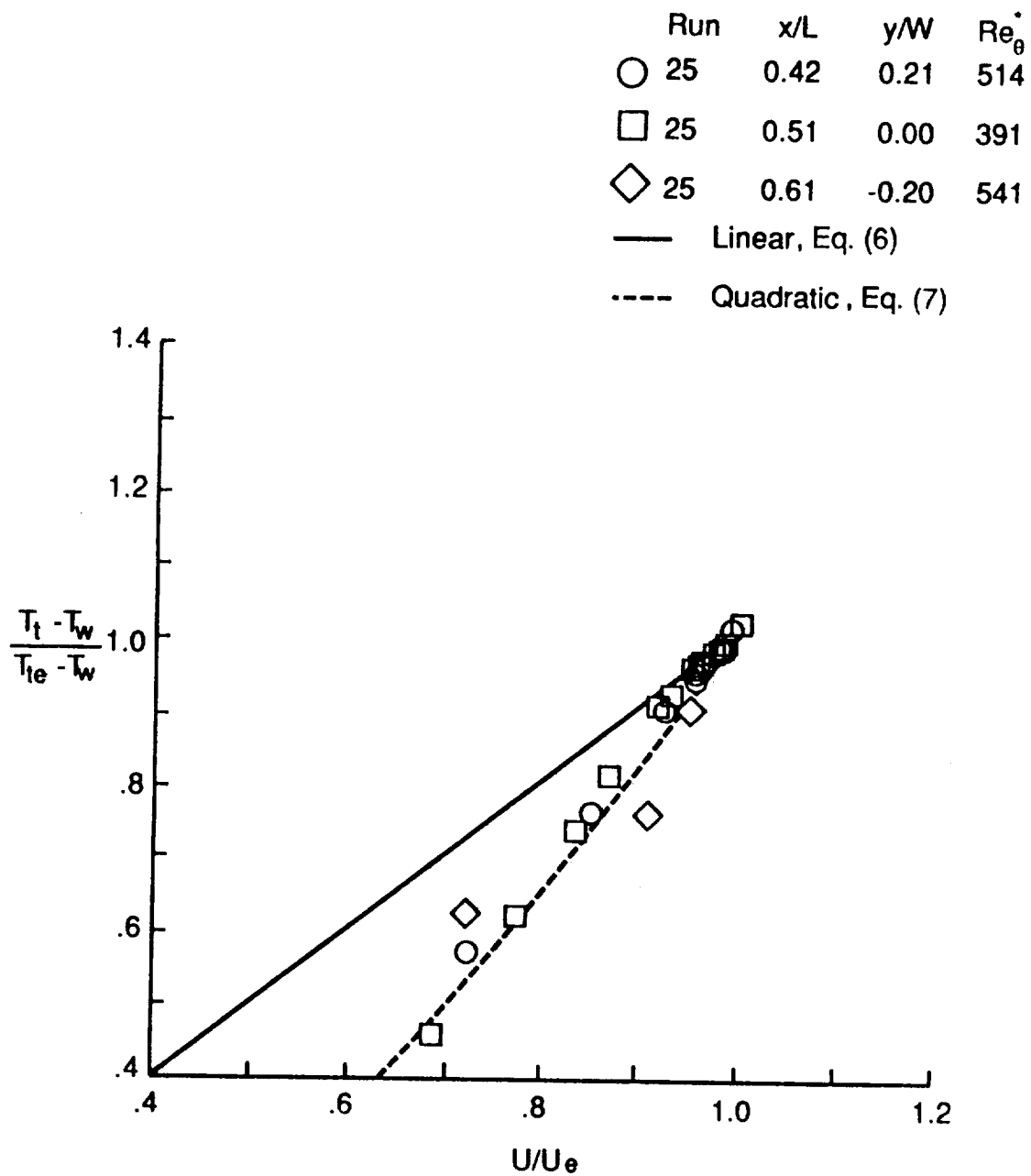
Fig. 39. Continued.

	Run	x/L	y/W	Re_0^*
○	22	0.42	0.21	2520
□	22	0.51	0.00	2400
◇	22	0.61	-0.20	2860
—	Linear, Eq. (6)			
- - -	Quadratic, Eq. (7)			



f) $Re^* = 0.92 \times 10^6 \text{ ft.}^{-1}$, $Me = 5.0$, $T_{aw}/T_w = 4.4$

Fig. 39. Continued.



g) $Re^* = 0.21 \times 10^6 \text{ ft.}^{-1}$, $M_e = 6.2$, $T_{aw}/T_w = 5.3$

Fig. 39. Concluded.

Chapter 4

ASSESSMENT OF EQUILIBRIUM TURBULENCE

To determine the test conditions necessary to achieve equilibrium turbulence, the velocity distributions from the present study are first compared with the classical profiles given by Coles [6]. The results of this comparison are presented in section 4.1. To aid in the assessment of equilibrium turbulence, shape factors were calculated from the velocity and total temperature profiles and are presented in section 4.2. The test conditions necessary for equilibrium turbulence are then summarized in section 4.3.

4.1 Comparison with Coles' Incompressible Profile

The measured velocity distributions presented in this section are compared with the classical profile given for a turbulent boundary layer by Coles [6]. Coles' equation is expressed in wall coordinates as:

$$\frac{U}{U_\tau} = \frac{1}{K} \ln \left(\frac{z U_\tau}{\nu} \right) + C + \frac{2\Pi}{K} \sin^2 \left(\frac{\pi}{2} \frac{z}{\delta_U} \right) \quad (8)$$

where $\Pi = 0.8 (\beta + 0.5)^{0.75}$ and $\beta = (\delta^*/\tau_w)(dp/dx)$. Also, the constants K and C have been determined from pipe flow experiments as 0.41 and 5.0, respectively [9].

This equation is often expressed in defect form, which is given as:

$$\frac{U_e - U}{U_\tau} = \frac{-1}{K} \ln \frac{z}{\delta_U} + \frac{\Pi}{K} \left[2 - \sin^2 \left(\frac{\pi}{2} \frac{z}{\delta_U} \right) \right] \quad (9)$$

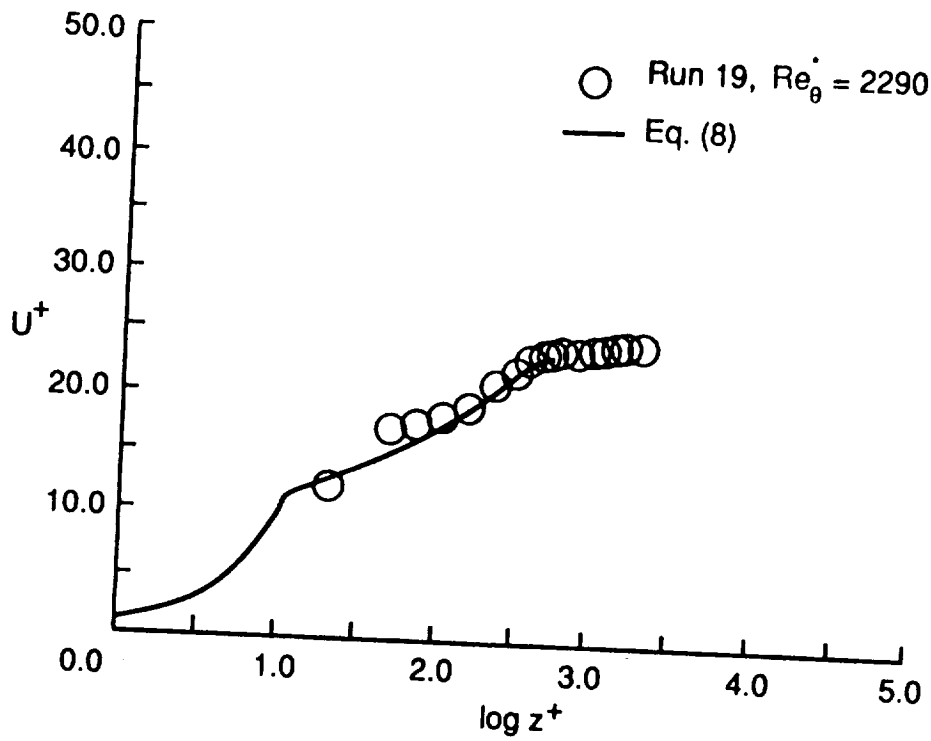
To account for density variations through the boundary layer, the present profiles have been transformed using the compressible transformation developed by van Driest [17]. Van Driest's transformation is given as:

$$\bar{U} = \frac{U_e}{a} \left\{ \sin^{-1} \left[\frac{(2a^2 U/U_e) - b}{Q} \right] + \sin^{-1} \frac{b}{Q} \right\} \quad (10)$$

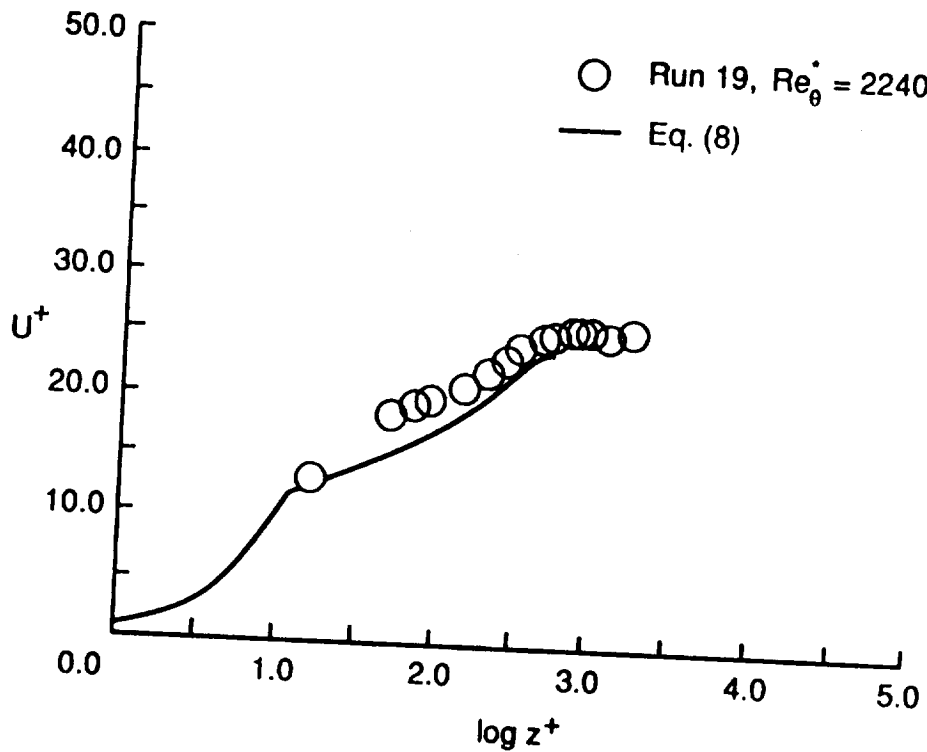
where:

$$a = \left(\frac{\gamma-1}{2} M_e^2 \frac{T_e}{T_{aw}} \right)^{1/2}, \quad b = \left(\frac{T_{aw}}{T_w} - 1 \right), \quad \text{and } Q = (b^2 + 4a^2)^{1/2}$$

The transformed velocity distributions in wall coordinates are shown in Figs. 40 through 46 at various locations on the plate and for various test conditions. The transformed velocities and their locations are expressed in terms of wall coordinates, which are given as $U^+ = U/U_\tau$ and $z^+ = zU_\tau/\nu$, respectively. The Reynolds number based on momentum thickness is also indicated for each profile. Because the local skin friction needed to calculate U_τ is not known and because the trends in the data are of primary interest, the local skin friction was adjusted to fit the transformed velocity data to Coles' incompressible curve.

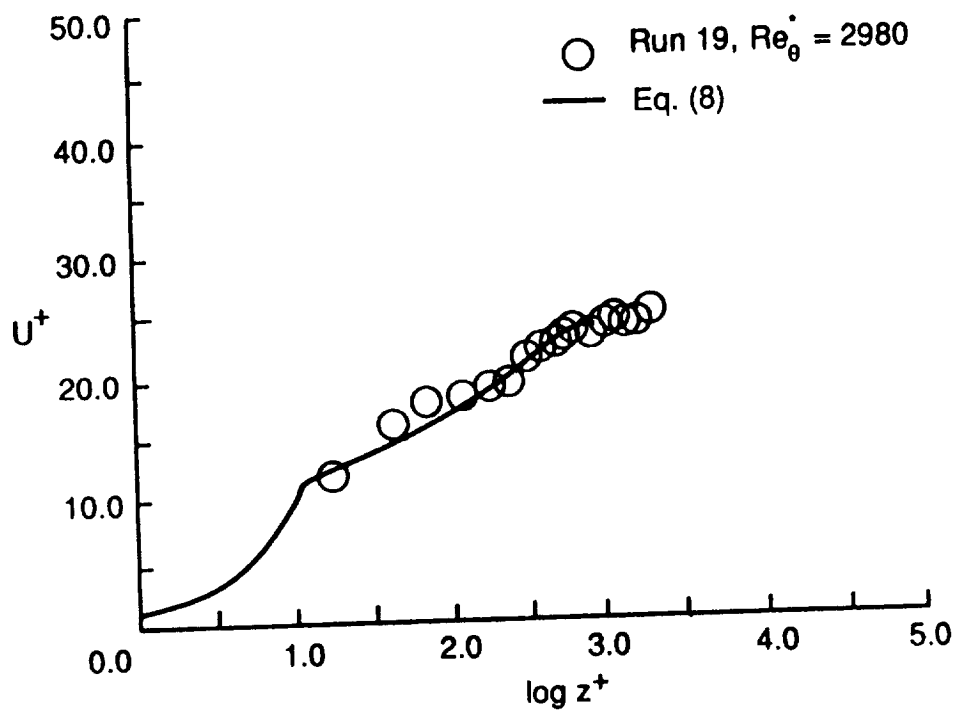


a) $x/L = 0.42, y/W = 0.21$

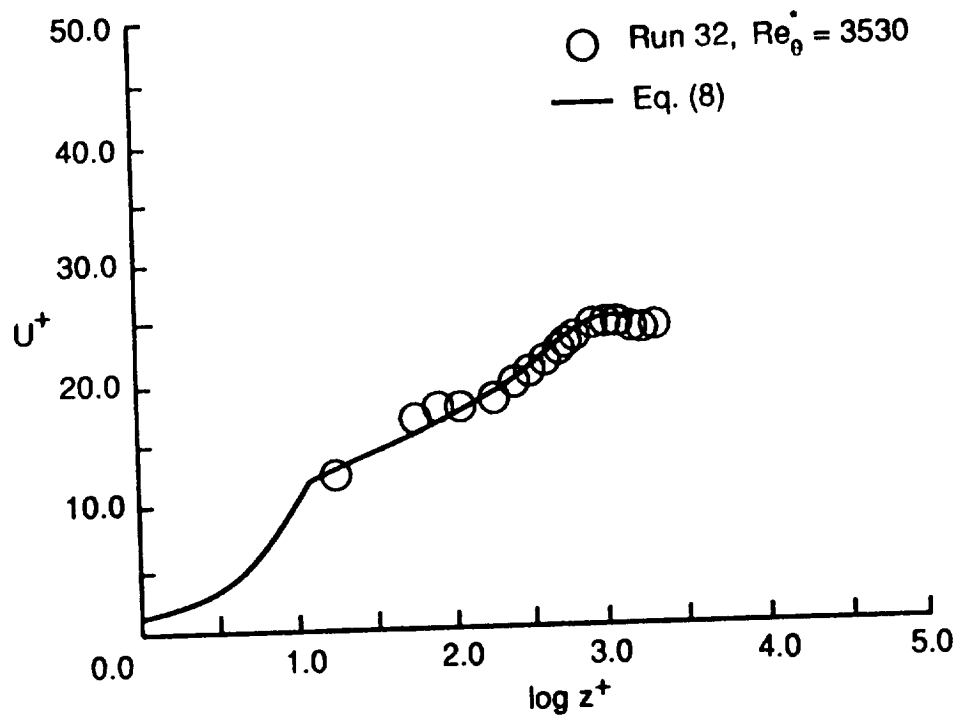


b) $x/L = 0.51, y/W = 0.00$

Fig. 40. Transformed velocity distributions in wall coordinates.
 $(Re^* = 0.69 \times 10^6 \text{ ft}^{-1}, M_\theta = 5.0, T_{aw}/T_w = 5.3)$



c) $x/L = 0.61, y/W = -0.20$



d) $x/L = 0.74, y/W = 0.00$

Fig. 40. Concluded.

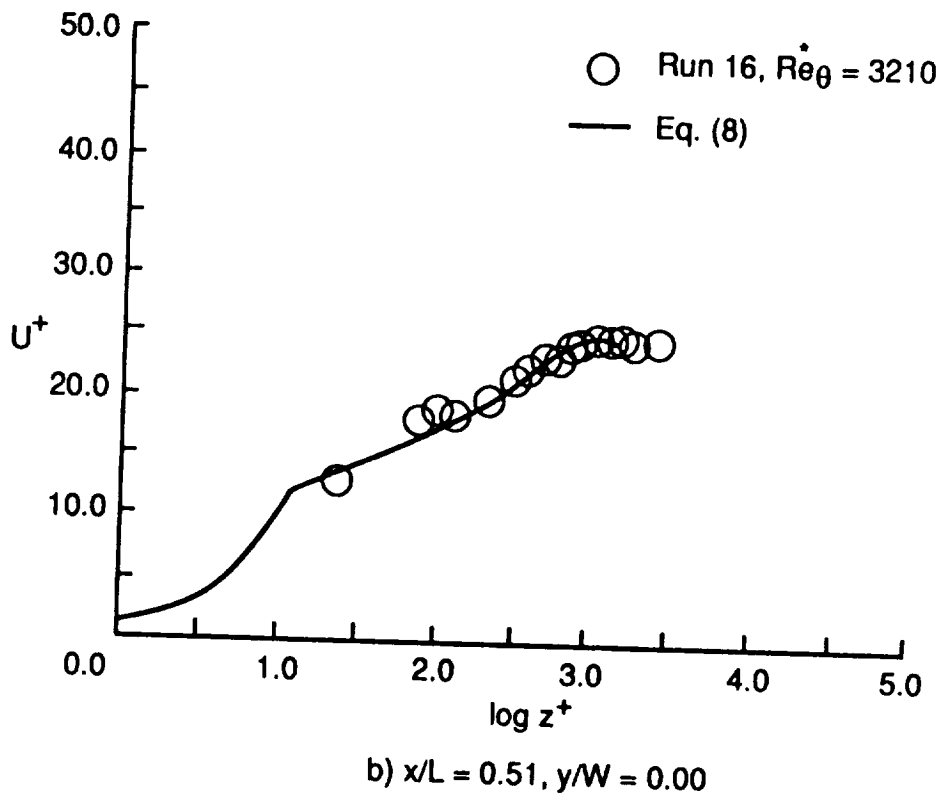
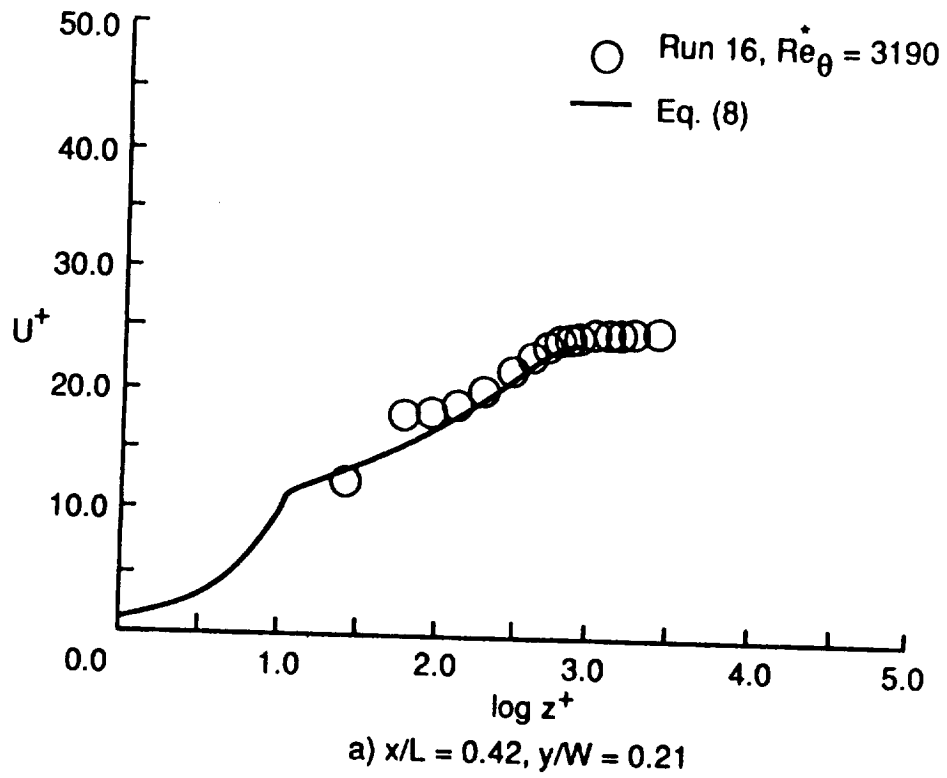


Fig. 41. Transformed velocity distributions in wall coordinates.
 $(Re^* = 0.92 \times 10^6 ft^{-1}, M_\theta = 4.9, T_{aw}/T_w = 5.6)$

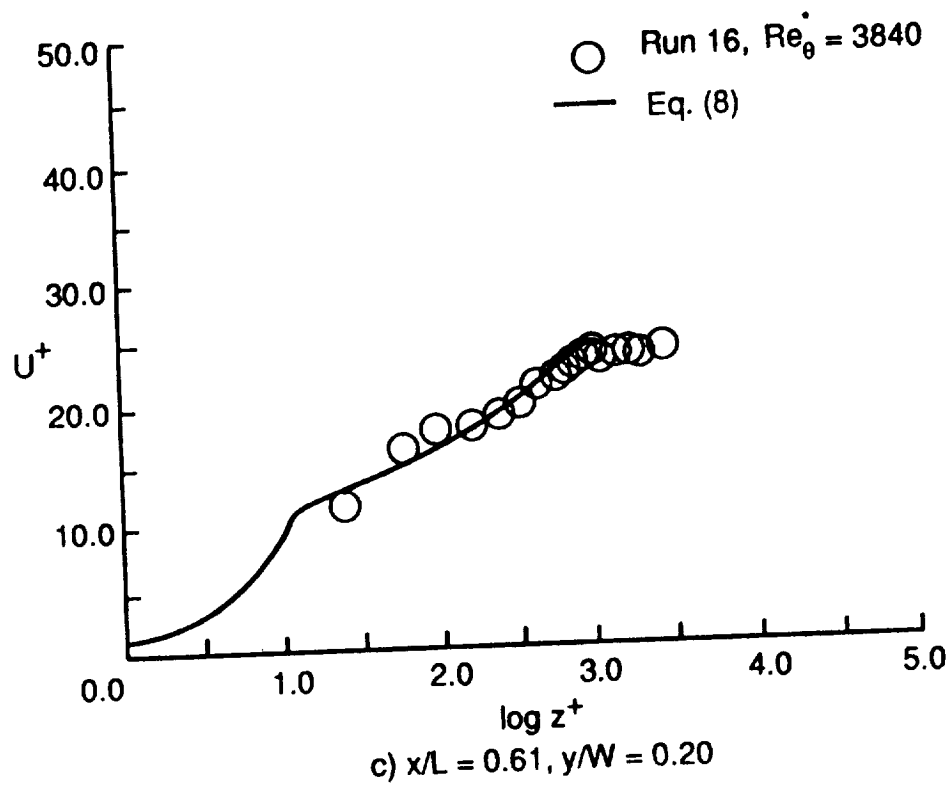


Fig. 41. Concluded.

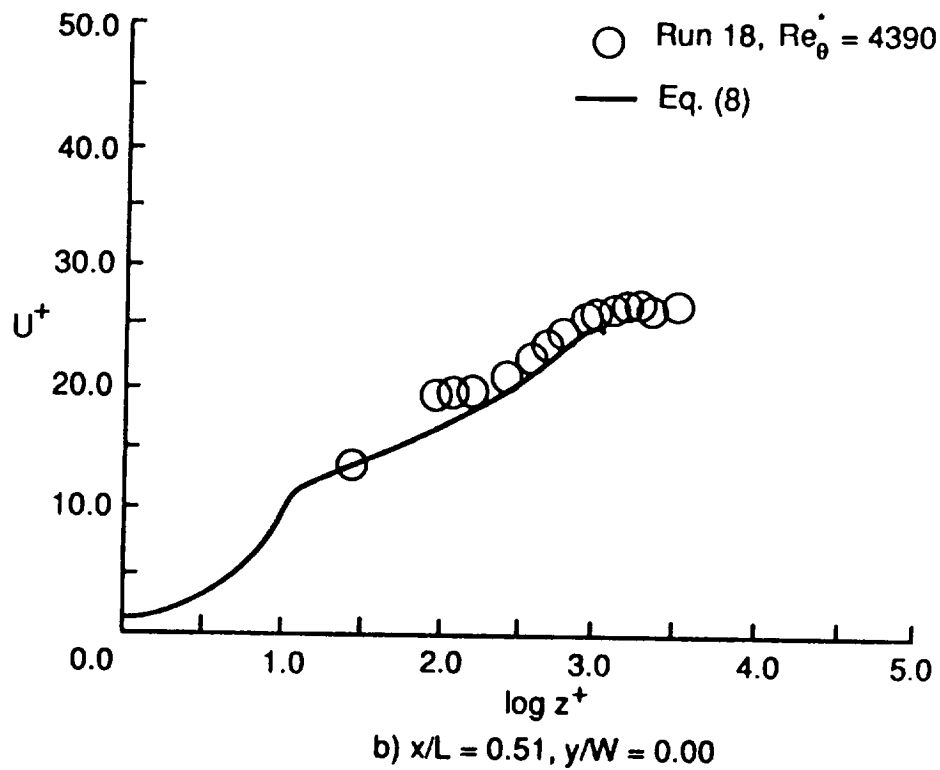
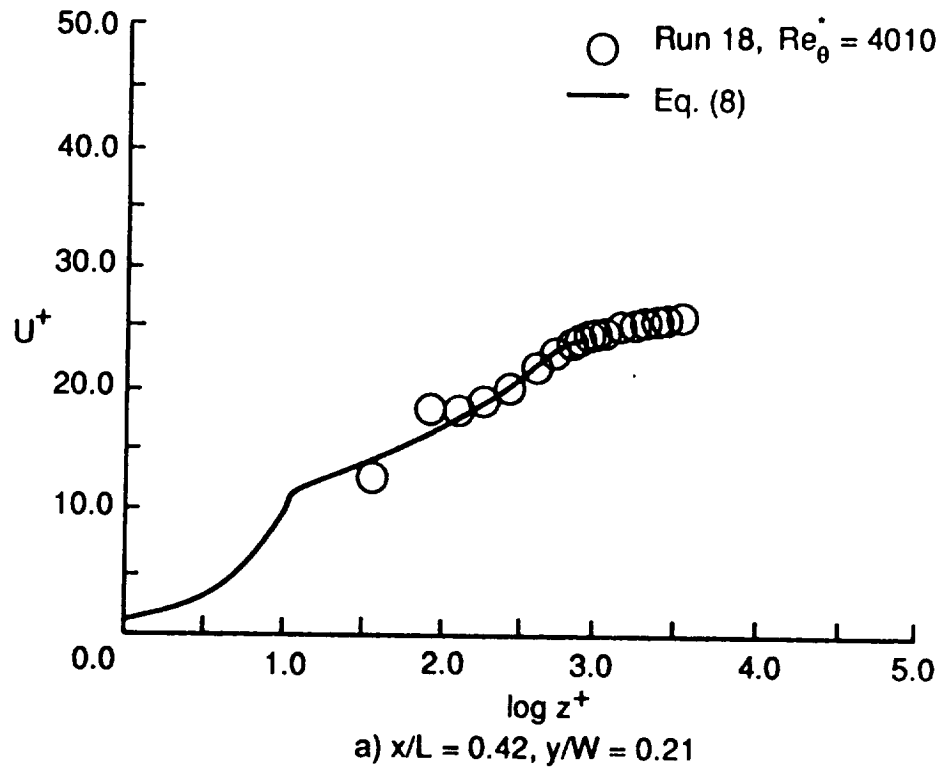


Fig. 42. Transformed velocity distributions in wall coordinates.
 $(Re^* = 1.17 \times 10^6 ft^{-1}, M_\theta = 4.9, T_{aw}/T_w = 5.3)$

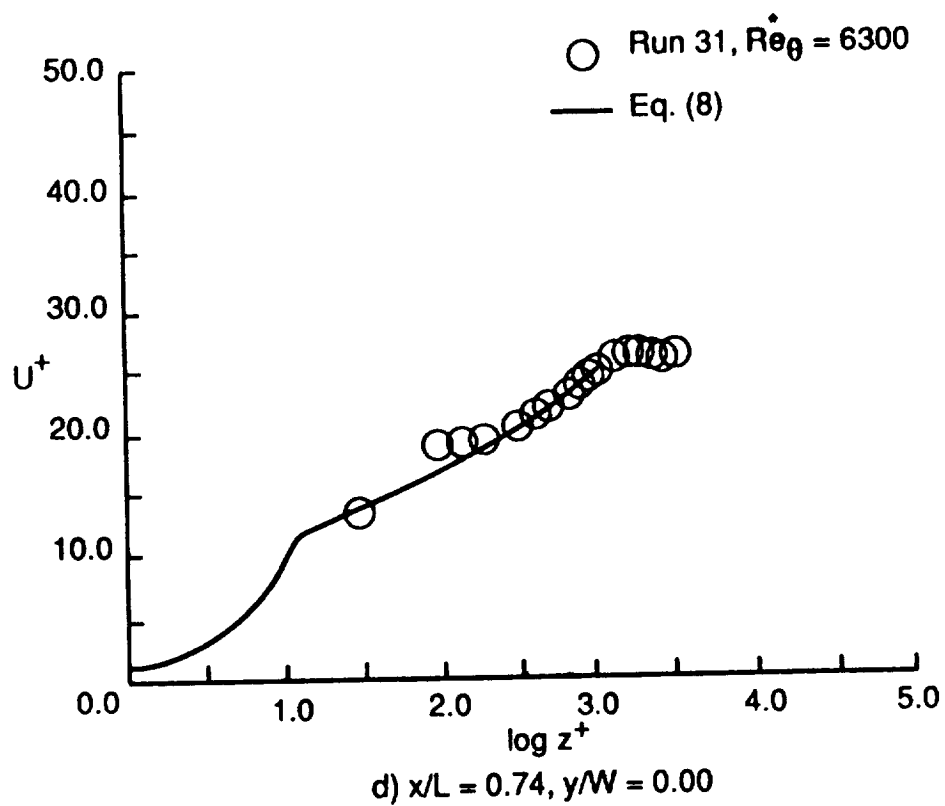
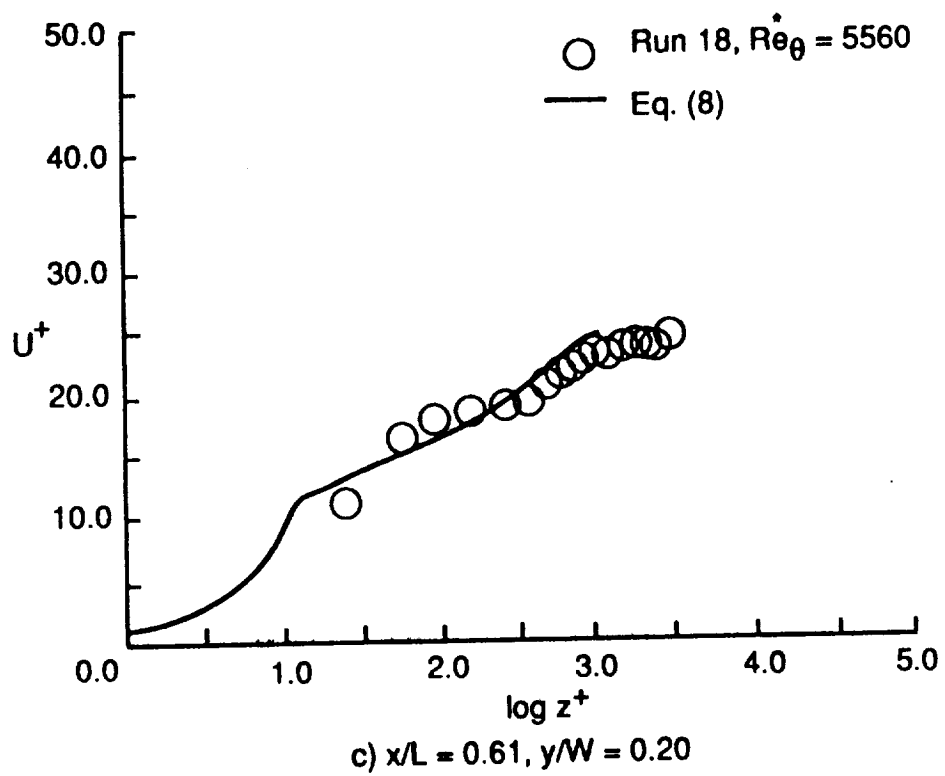


Fig. 42. Concluded.

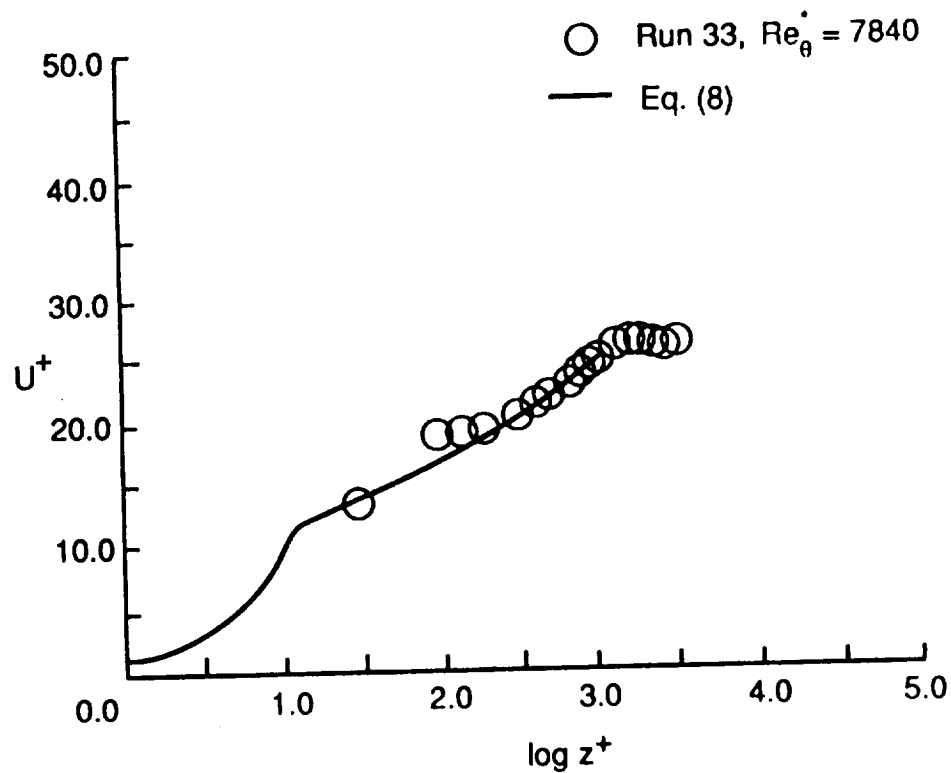


Fig. 43. Transformed velocity distributions in wall coordinates.
 ($Re^* = 1.51 \times 10^6 \text{ ft}^{-1}$, $M_{\theta} = 4.9$, $T_{aw}/T_w = 5.4$,
 $x/L = 0.74$, $y/W = 0.00$)

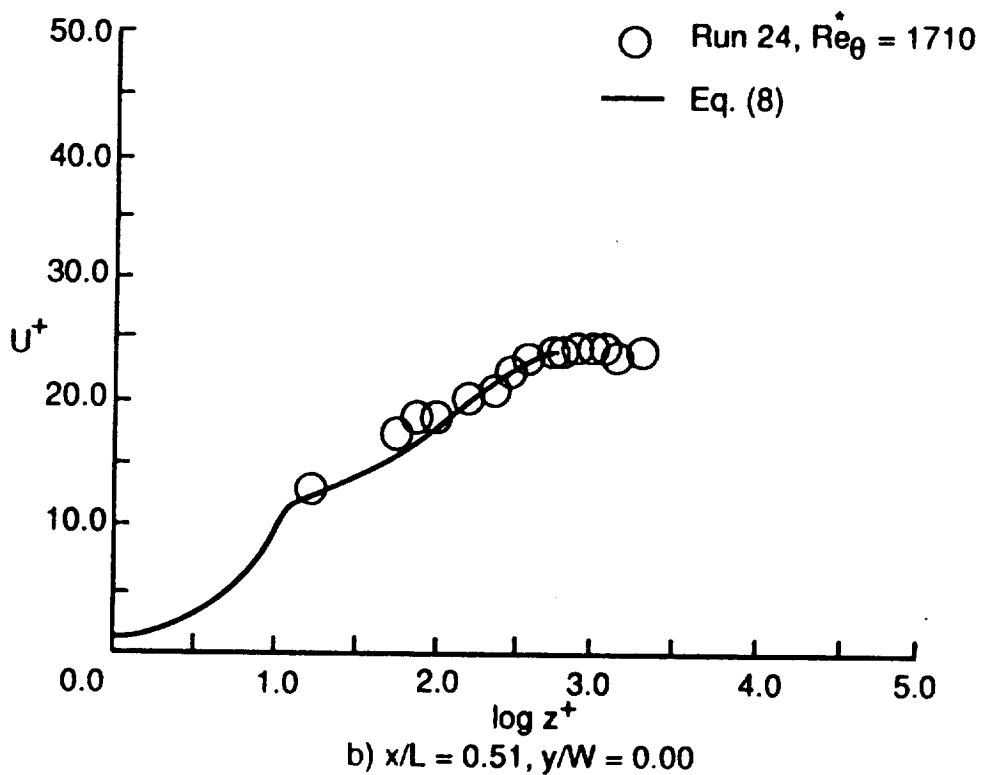
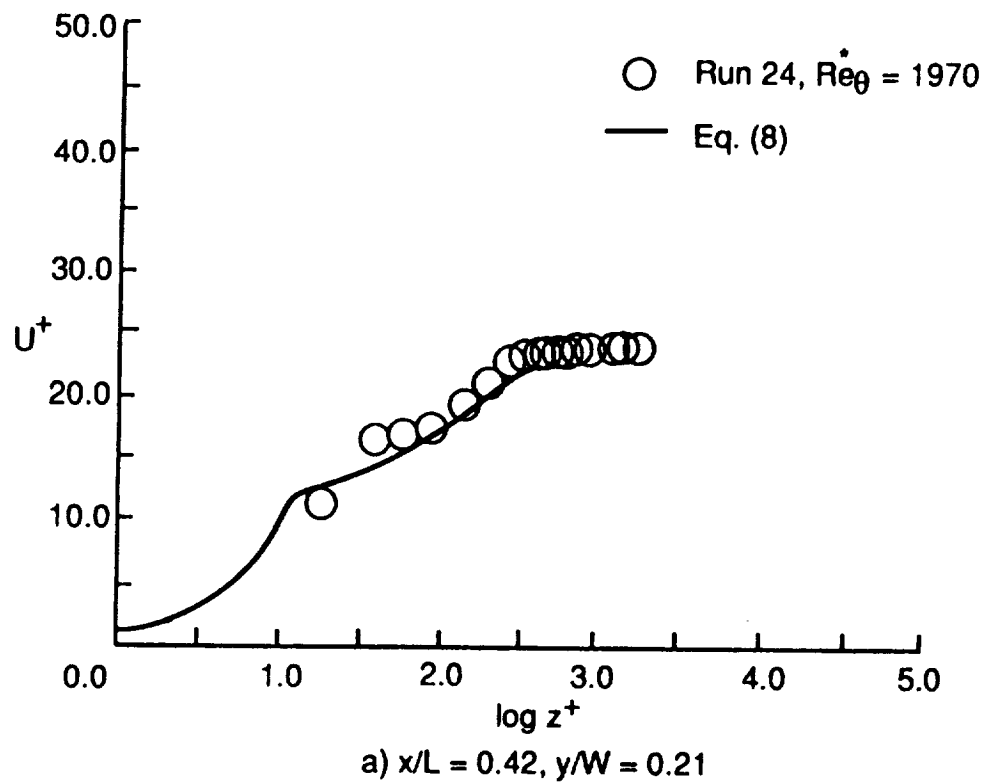
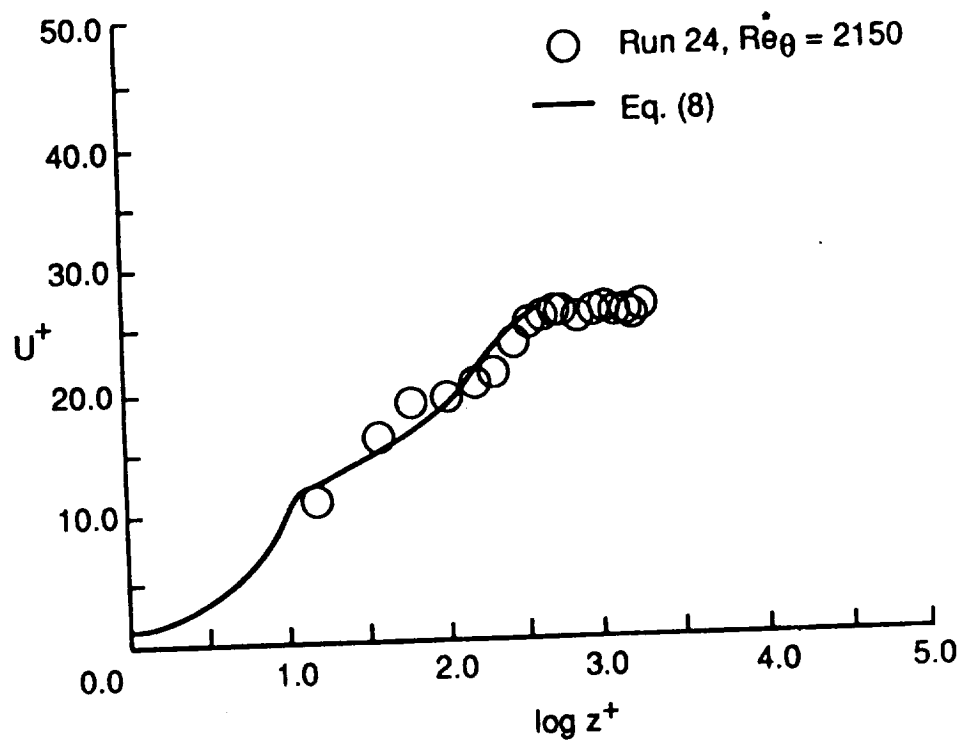
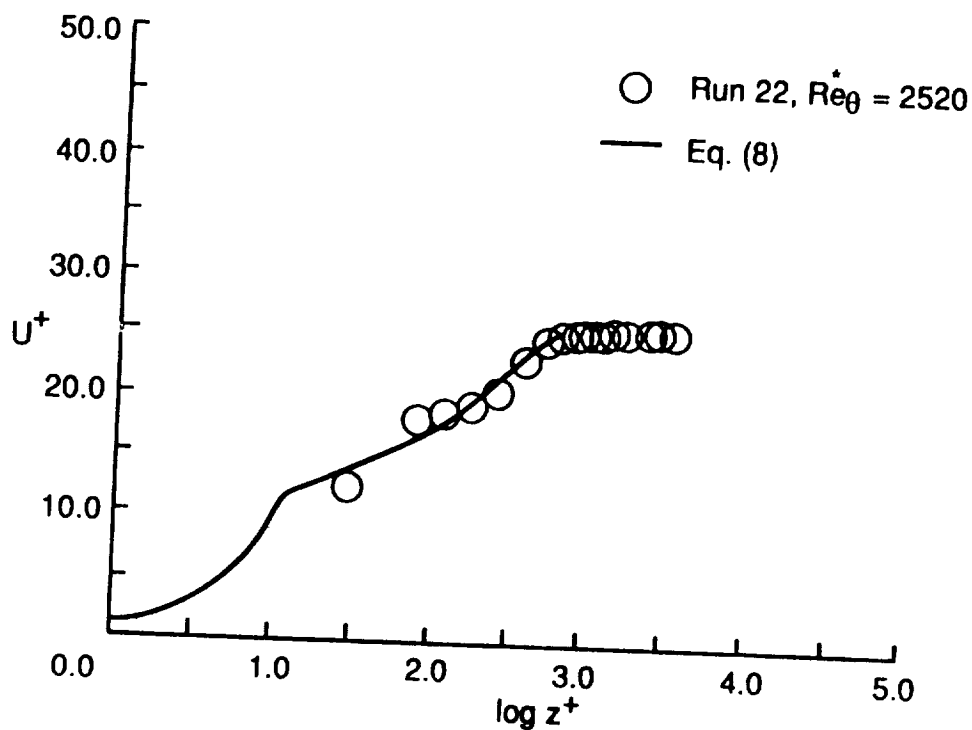


Fig. 44. Transformed velocity distributions in wall coordinates.
 $(Re^* = 0.69 \times 10^6 \text{ ft}^{-1}, M_e = 5.1, T_{aw}/T_w = 4.4)$

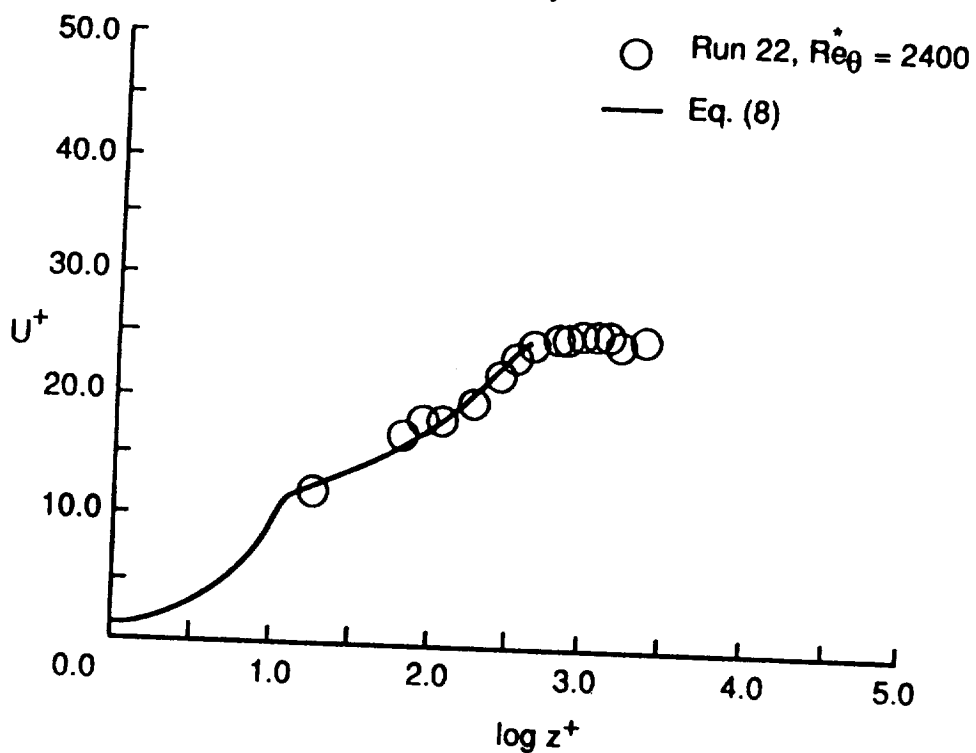


c) $x/L = 0.61, y/W = -0.20$

Fig. 44. Concluded.



a) $x/L = 0.42, y/W = 0.21$



b) $x/L = 0.51, y/W = 0.00$

Fig. 45. Transformed velocity distributions in wall coordinates.
 $(Re^* = 0.92 \times 10^6 ft^{-1}, M_e = 5.1, T_{aw}/T_w = 4.4)$

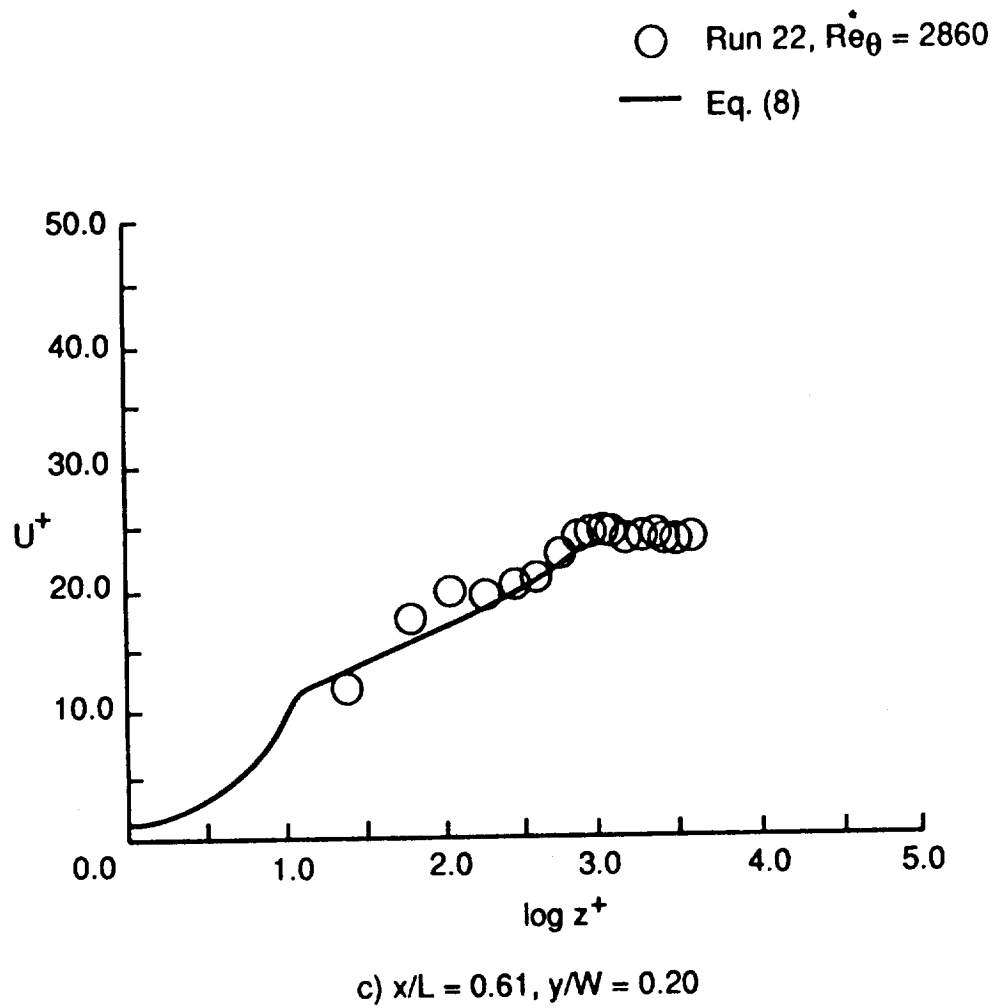
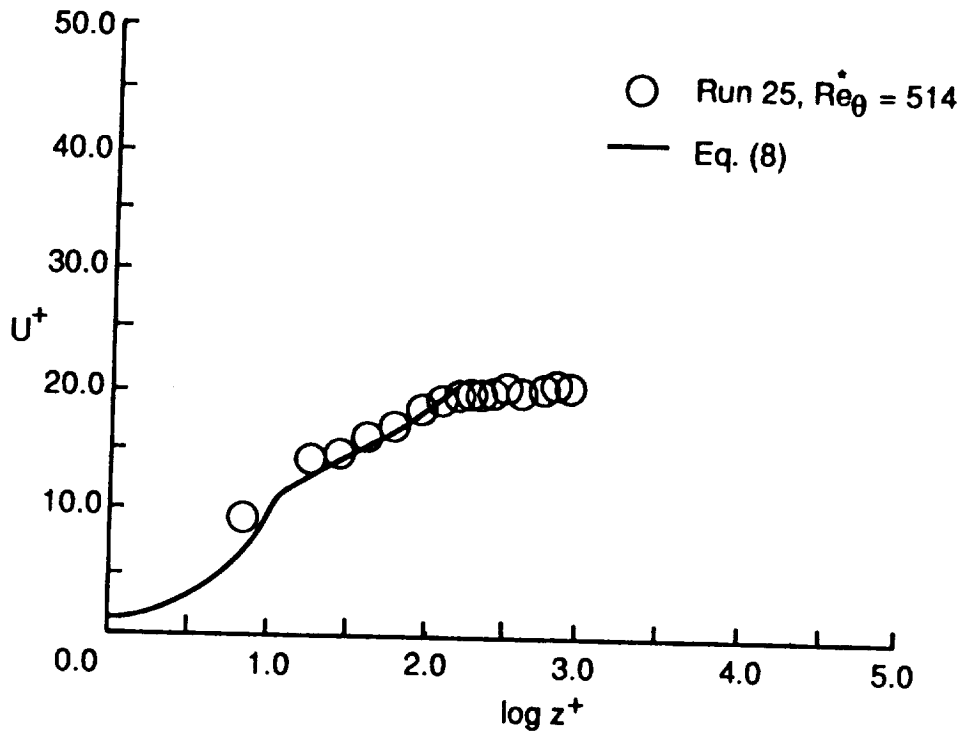
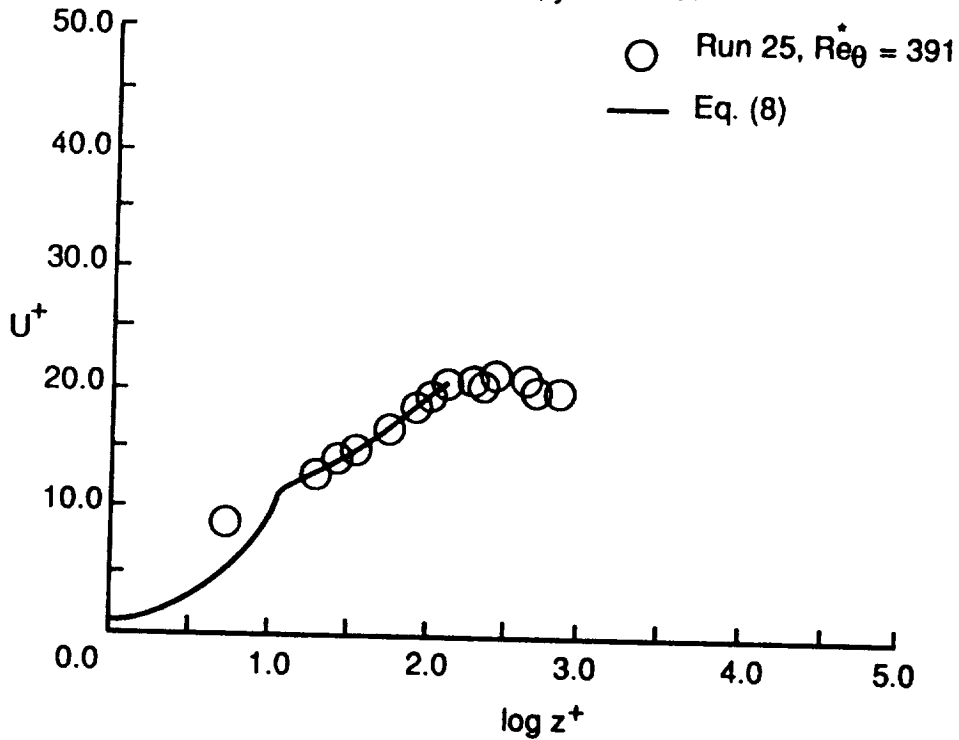


Fig. 45. Concluded.

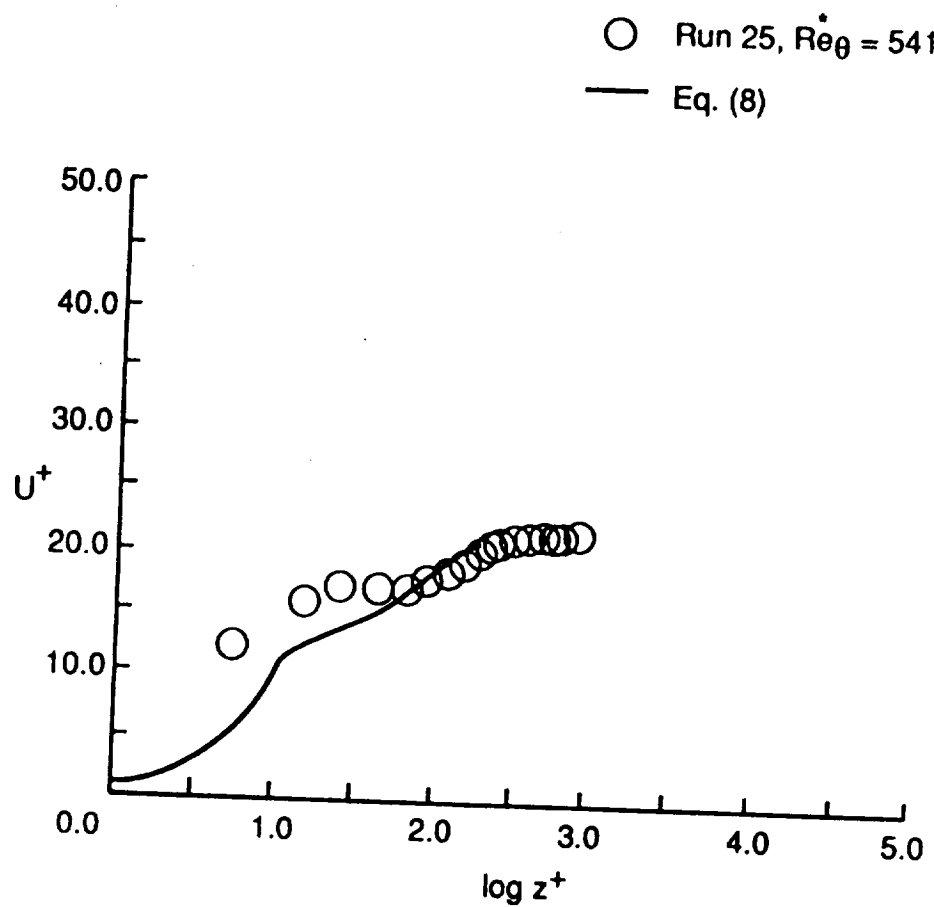


a) $x/L = 0.42, y/W = 0.21$



b) $x/L = 0.51, y/W = 0.00$

Fig. 46. Transformed velocity distributions in wall coordinates.
 $(Re^* = 0.21 \times 10^6 ft^{-1}, M_{\theta} = 6.2, T_{aw}/T_w = 5.3)$

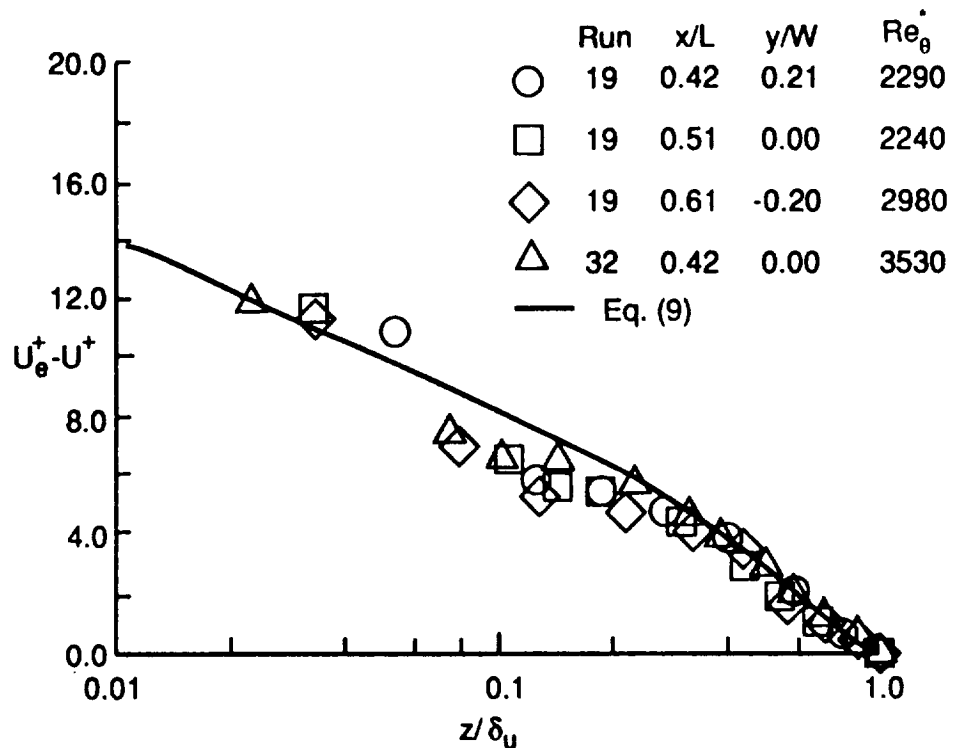


c) $x/L = 0.61$, $y/W = 0.20$

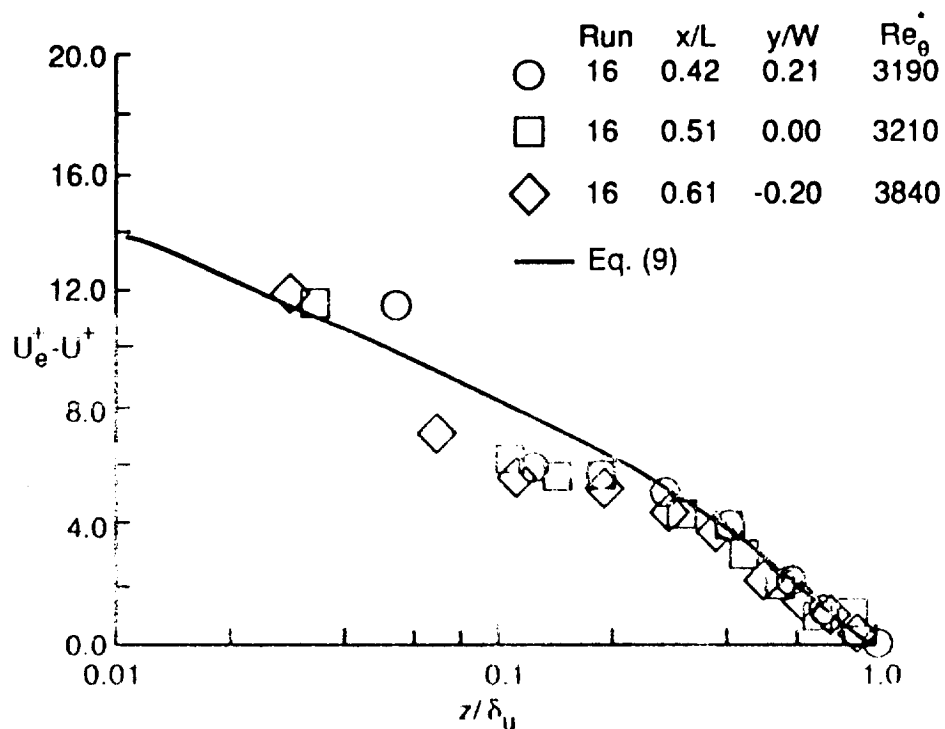
Fig. 46. Concluded.

The transformed velocities shown in Fig. 40 were obtained at a local unit Reynolds number of 0.69×10^6 /ft, a boundary-layer edge Mach number of 5.0, and a temperature ratio, T_{aw}/T_w , of 5.3. The momentum thickness Reynolds number, based on reference temperature conditions, Re^*_θ , ranges from 2240 to 3530. The trends in the data generally agree with the incompressible correlation of Coles [6], except for the data points closest to the wall, which were shown in section 3.3.2 to be adversely affected by probe interference. The trends in the data indicate equilibrium turbulence at this condition. The data obtained at the higher unit Reynolds numbers of 0.92×10^6 , 1.17×10^6 , and 1.51×10^6 /ft (Figs. 41, 42, and 43) also agree well with the incompressible correlation and indicates equilibrium turbulence. The momentum thickness Reynolds number for the data presented in Figs. 41 through 43 ranges from 2400 to 7840. The transformed data obtained at $T_{aw}/T_w = 4.4$ (Figs. 44 and 45) also agree with the trends of the incompressible correlation. The data obtained at the lowest unit Reynolds number condition (Fig. 46) also have trends similar to the incompressible correlation. However, the momentum thickness Reynolds numbers for the data were shown previously to be in the transitional range.

The transformed velocity profiles are plotted in defect coordinates for various locations on the plate and at various test conditions in Figs. 47 through 49. Also shown with the profiles is the velocity defect equation given by Eq. (9). The velocity distributions shown in Fig. 47 correspond to the velocity distributions plotted in wall coordinates in Figs. 40 through 43. The data were obtained at a nominal boundary-layer edge Mach number of 5.0 and a temperature ratio, T_{aw}/T_w , of 5.4. The local unit Reynolds number ranges from 0.69×10^6 to 1.51×10^6 /ft. The corresponding momentum thickness Reynolds



a) $Re^* = 0.69 \times 10^6 \text{ ft}^{-1}$



b) $Re^* = 0.92 \times 10^6 \text{ ft}^{-1}$

Fig. 47. Velocity distributions in defect coordinates.
($M_e = 5.0$, $T_{aw}/T_w = 5.4$)

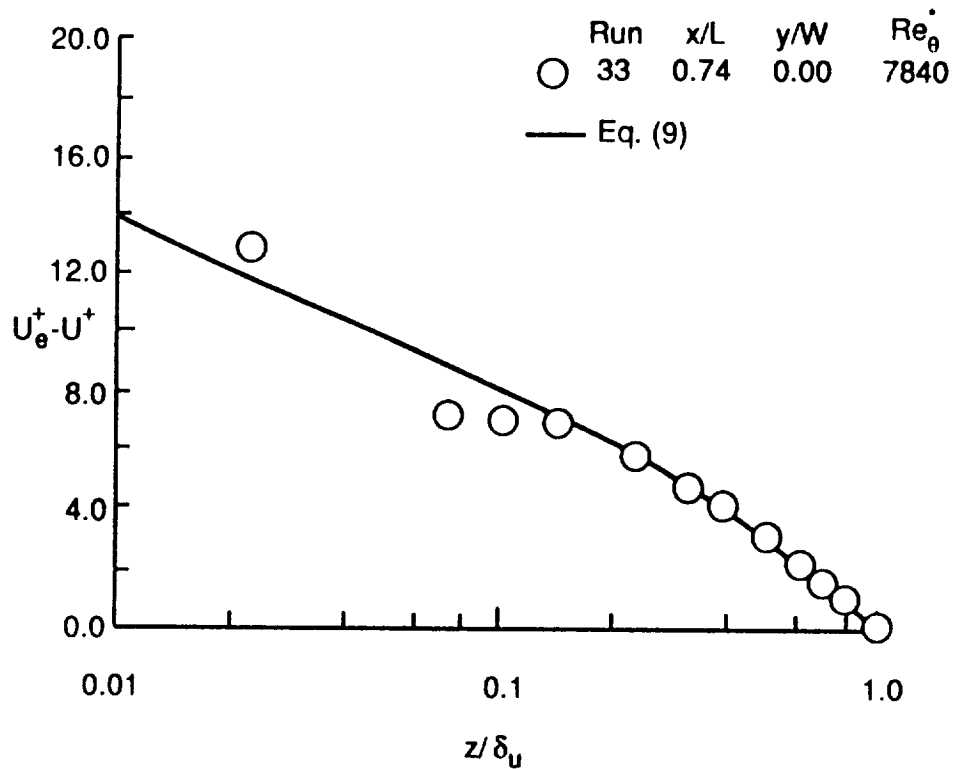
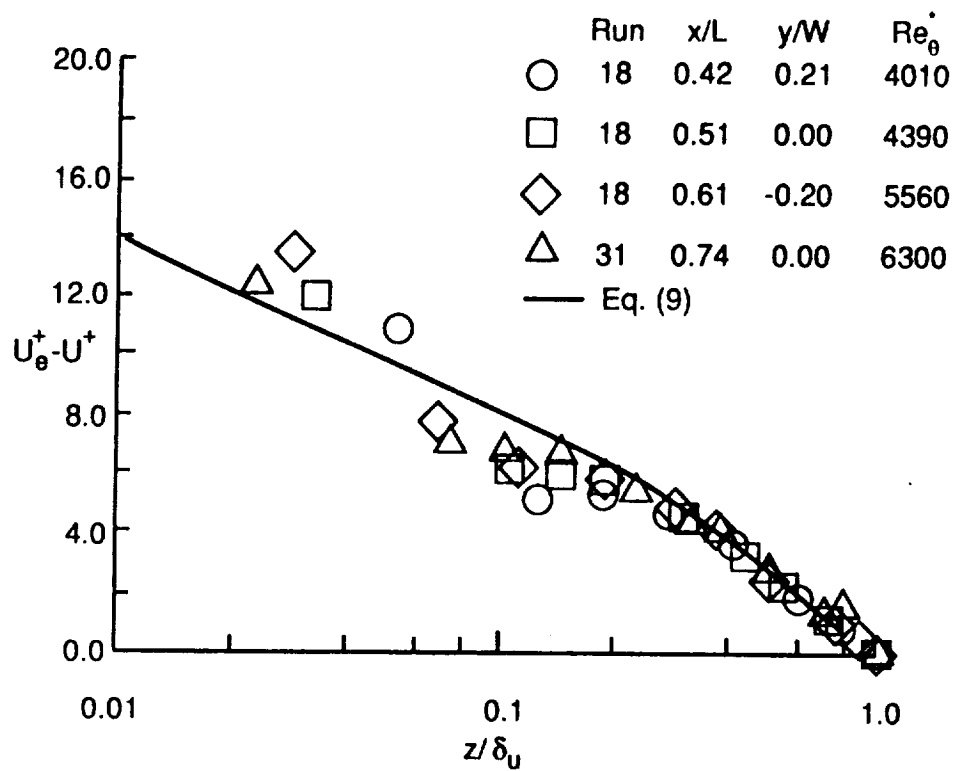


Fig. 47. Concluded.

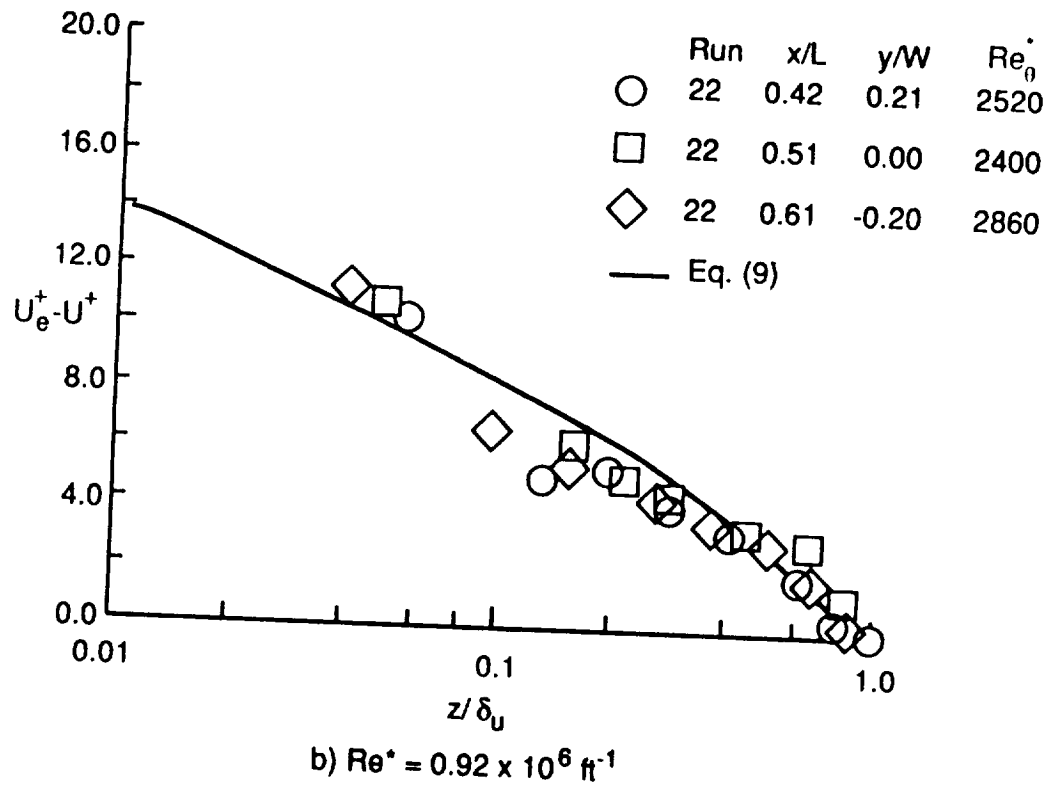
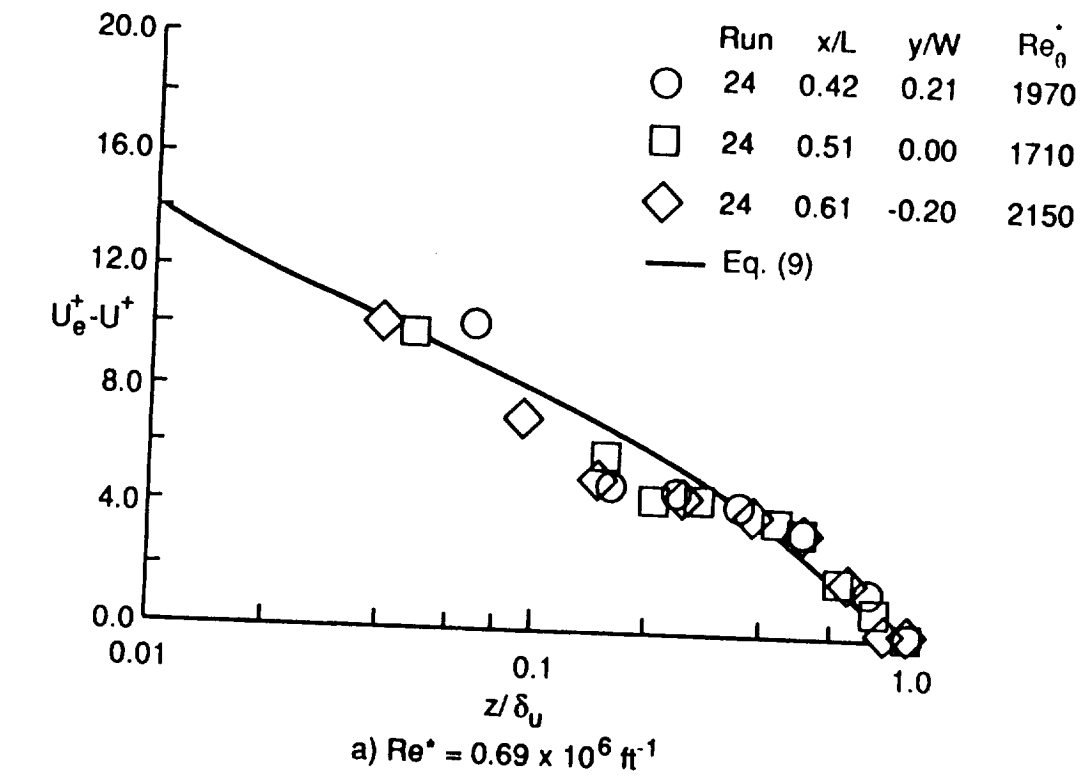


Fig. 48. Velocity distributions in defect coordinates.
($Me = 5.1, T_{aw}/T_w = 4.4$)

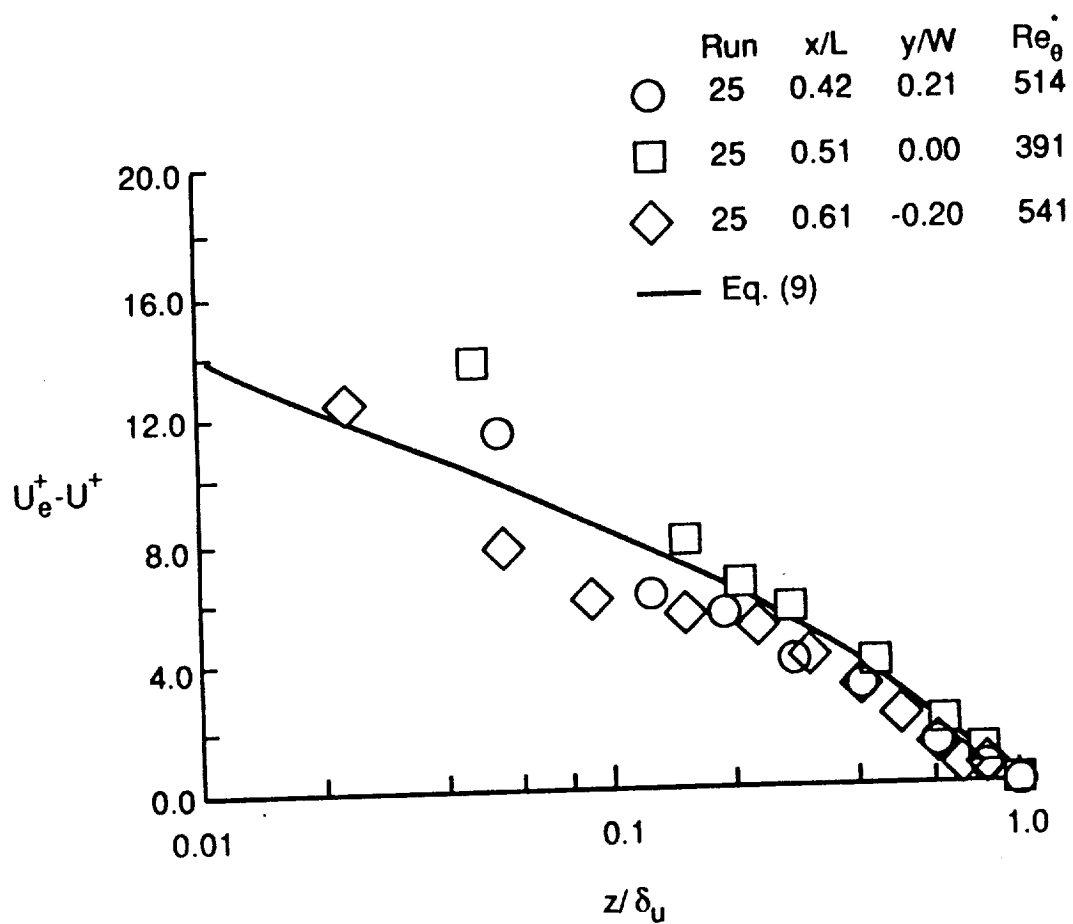


Fig. 49. Velocity distributions in defect coordinates.
 ($Me = 6.2$, $T_{aw}/T_w = 5.3$, $Re^* = 0.21 \times 10^6 \text{ ft}^{-1}$)

number, Re^*_θ , ranges from 2240 to 7840. The data appear to agree reasonably well with the defect equation, at least for $z/\delta_U > 0.25$. The discrepancy between the data and the defect equation for $z/\delta_U \leq 0.25$ results from probe interference, as discussed in section 3.3.2. At the lower temperature ratio of 4.4 (Fig. 48), the data do not agree as well with the trend or level of the defect equation for the range of momentum thickness Reynolds numbers considered ($1710 \leq Re^*_\theta \leq 2860$). This possibly indicates nonequilibrium flow, although the velocities plotted in wall coordinates agreed well with the trends of Coles' incompressible correlation, Eq. (8), and the heating rate data indicated transition is completed at an Re^*_θ of 1200. At the lowest Reynolds number condition (Fig. 49), the distributions show larger variations with location on the plate than at the higher Reynolds number conditions. As mentioned previously, the boundary layer is transitional at this condition.

The local skin friction coefficients derived from adjusting the transformed velocities to fit the incompressible equation of Coles, Eq. (8), are shown as a function of local Reynolds number, Re^*_x , in Fig. 50. Also shown with the data are laminar and turbulent predictions obtained by applying a Reynolds analogy relating heat transfer and skin friction to the laminar and turbulent heating rate equations (Eqs. (3) and (4), respectively) presented in section 3.2. The Reynolds analogy is given by White [9] as:

$$C_f^* = 2 St^* Pr^{*(2/3)} \quad (\text{laminar}) \quad (11)$$

$$C_f^* = 2 St^* Pr^{*(0.40)} \quad (\text{turbulent}) \quad (12)$$

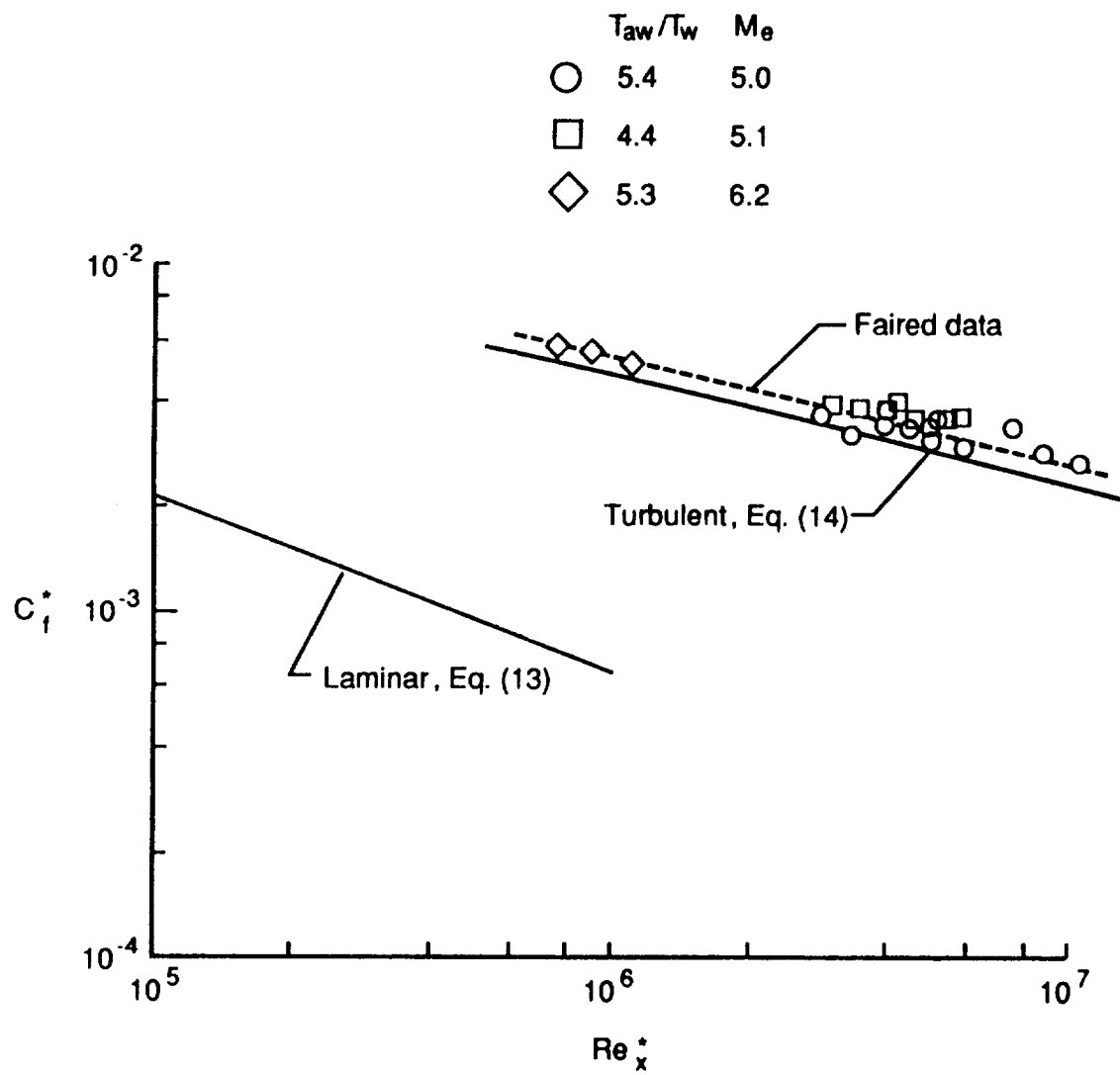


Fig. 50. Skin friction coefficients derived from transformed velocity distributions.

The resulting laminar and turbulent equations for skin friction coefficient are given, respectively, as:

$$C_f^* = 0.664 \text{Re}_x^*{}^{-1/2} \quad (\text{laminar}) \quad (13)$$

$$C_f^* = 0.0574 (\text{Re}_x^* - \text{Re}_v^*)^{-1/5} \quad (\text{turbulent}) \quad (14)$$

Note that all the data appear to be fully turbulent, although the momentum thickness Reynolds numbers for the lowest unit Reynolds number data (represented by the diamonds) were shown by the heating rate data to be in the transitional range. This may indicate that the momentum boundary layer approaches equilibrium turbulence at a lower Reynolds number than the thermal boundary layer. The data are approximately 18 percent above the turbulent prediction given by Eq. (14) and using the same Re_v^* of 1.06×10^6 used in the heating predictions discussed in section 3.2. The Re_v^* required to fit Eq. (14) to the data is approximately 1.6×10^6 .

4.2 Shape Factors

Shape factors are presented in this section to aid in the assessment of equilibrium turbulence. First, the standard hydraulic shape factor, δ^*/θ , is examined for uniformity, where:

$$\delta^* = \int_0^{\infty} \left(1 - \frac{\rho U}{\rho_e U_e} \right) dz \quad (15)$$

and:

$$\theta = \int_0^{\infty} \frac{\rho U}{\rho_e U_e} \left(1 - \frac{U}{U_e} \right) dz \quad (16)$$

In addition, Clauser's shape factor, G , was examined for uniformity. The equation for G is given as:

$$G = \frac{1}{\Delta} \int_0^{\infty} \left(\frac{U - U_e}{U_{\tau}} \right)^2 dz \quad (17)$$

where:

$$\Delta = \int_0^{\infty} \left(\frac{U_e - U}{U_{\tau}} \right) dz \quad (18)$$

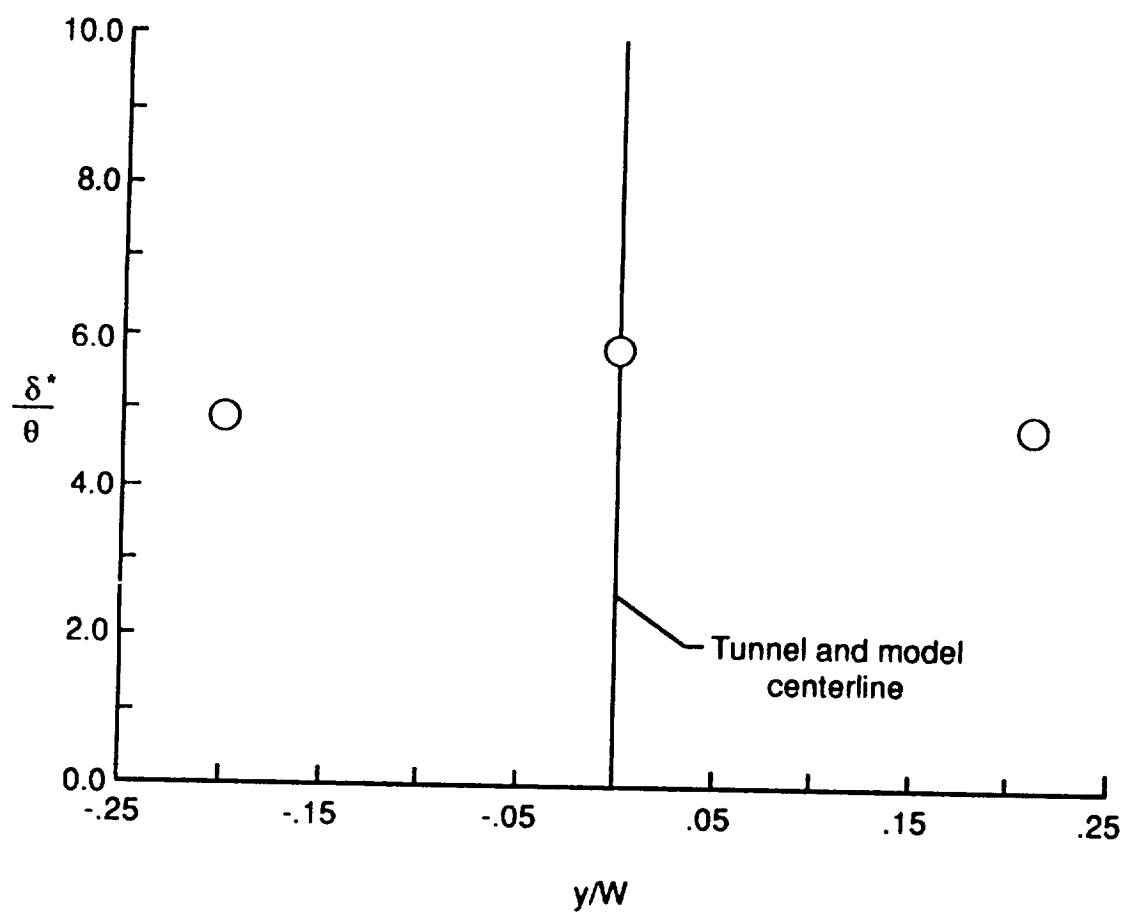
According to Clauser [5], $G = 6.1$ for a zero pressure gradient, equilibrium turbulent boundary layer.

Because a thermal boundary layer also exists for the present study, the thermal shape factors, δ_H/δ^* and δ_H/θ , were also examined for uniformity. For convenience, these shape factors are designated as thermal shape factors 1 and 2, respectively. The quantity δ_H represents the total enthalpy thickness which is given by Schlichting [4] as:

$$\delta_H = \int_0^{\infty} \frac{\rho U}{\rho_e U_e} \left(\frac{H_{te} - H_t}{H_{te} - H_w} \right) dz \quad (19)$$

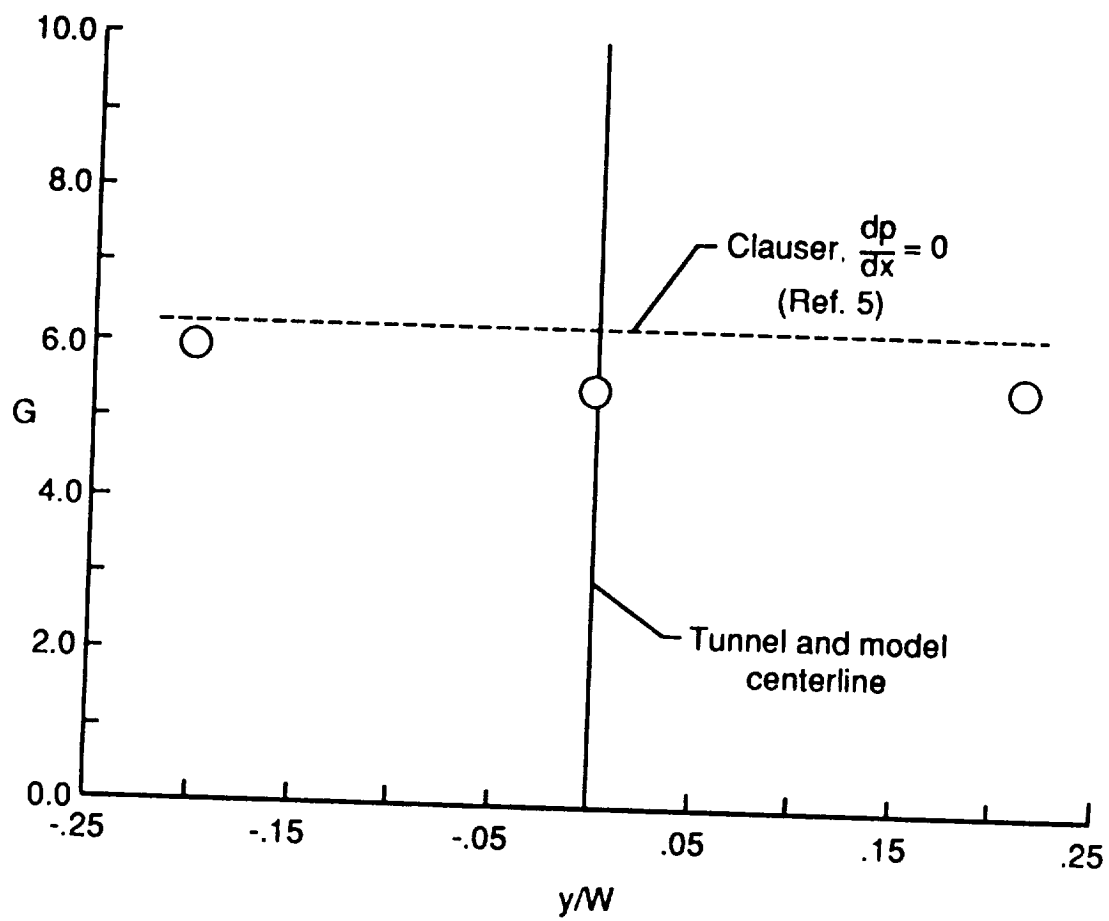
To obtain these shape factors, the velocity and density distributions inferred from the measurements were integrated over the thickness of the boundary layer. The velocities affected by probe interference were corrected using the appropriate power law variation prior to integrating the distributions.

In Fig. 51, the spanwise variation of the various shape factors are shown for run 10. The data were obtained at $x/L = 0.42$, a local unit Reynolds number of 0.69×10^6 /ft, a boundary-layer edge Mach number of 5.0, and a temperature ratio of 5.5. The corresponding momentum thickness Reynolds number, Re^*_θ , ranges from 1610 to 2290. The hydraulic shape factor, δ^*/θ , and thermal shape factor 1, δ_H/δ^* , show variations of approximately 20 and 26 percent, respectively. (See Figs. 51a and 51c.) In Figs. 51b and 51d, Clauser's shape factor, G , and thermal shape factor 2, δ_H/θ , are more nearly constant, varying approximately 14 and 8 percent, respectively, from $y/W=0.21$ to -0.20 . These shape factors are apparently less sensitive to flow variations and experimental errors. The spanwise variations in all of the shape factors may be caused by a spanwise variation in transition location at the run 10 test condition, as discussed in section 3.3.2. Also the surface pressure distribution at a nearby location ($x/L= 0.46$) indicates spanwise pressure gradients are present. (See Fig. 18b.) Because of the time constraints imposed by a major facility shutdown for modifications, data were not obtained at higher unit Reynolds numbers; therefore, the effect of higher Reynolds numbers on spanwise variations cannot be shown for the present experiment. However, because transition moves closer to the leading edge at higher unit Reynolds numbers, the effect of spanwise variation on transition location and on the spanwise shape factor distributions should diminish. It is therefore recommended that future experiments in the 8-foot High Temperature Tunnel



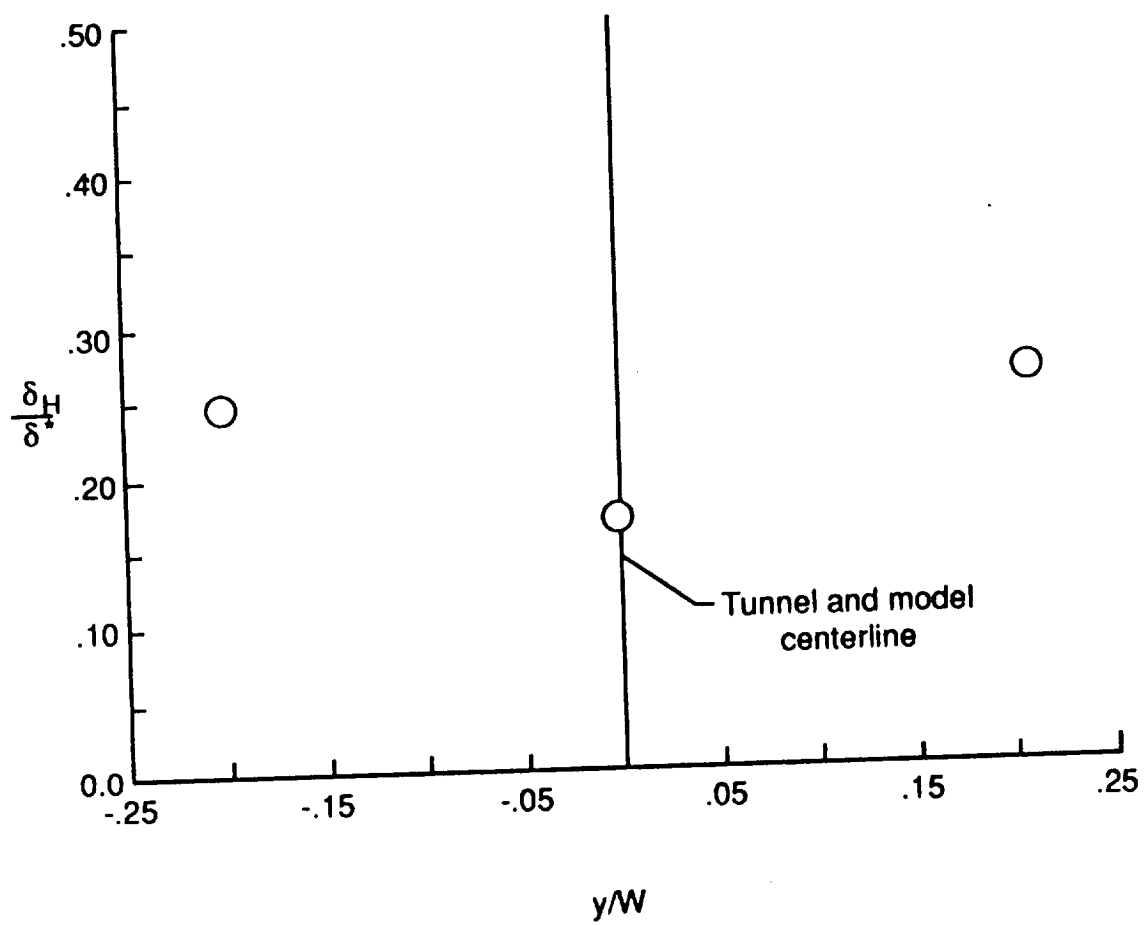
a) δ^*/θ

Fig. 51. Spanwise variation in shape factors.
 (Run 10, $x/L = 0.42$, $Re^* = 0.69 \times 10^6 \text{ ft}^{-1}$,
 $T_{aw}/T_w = 5.5$, $M_\theta = 5.0$)



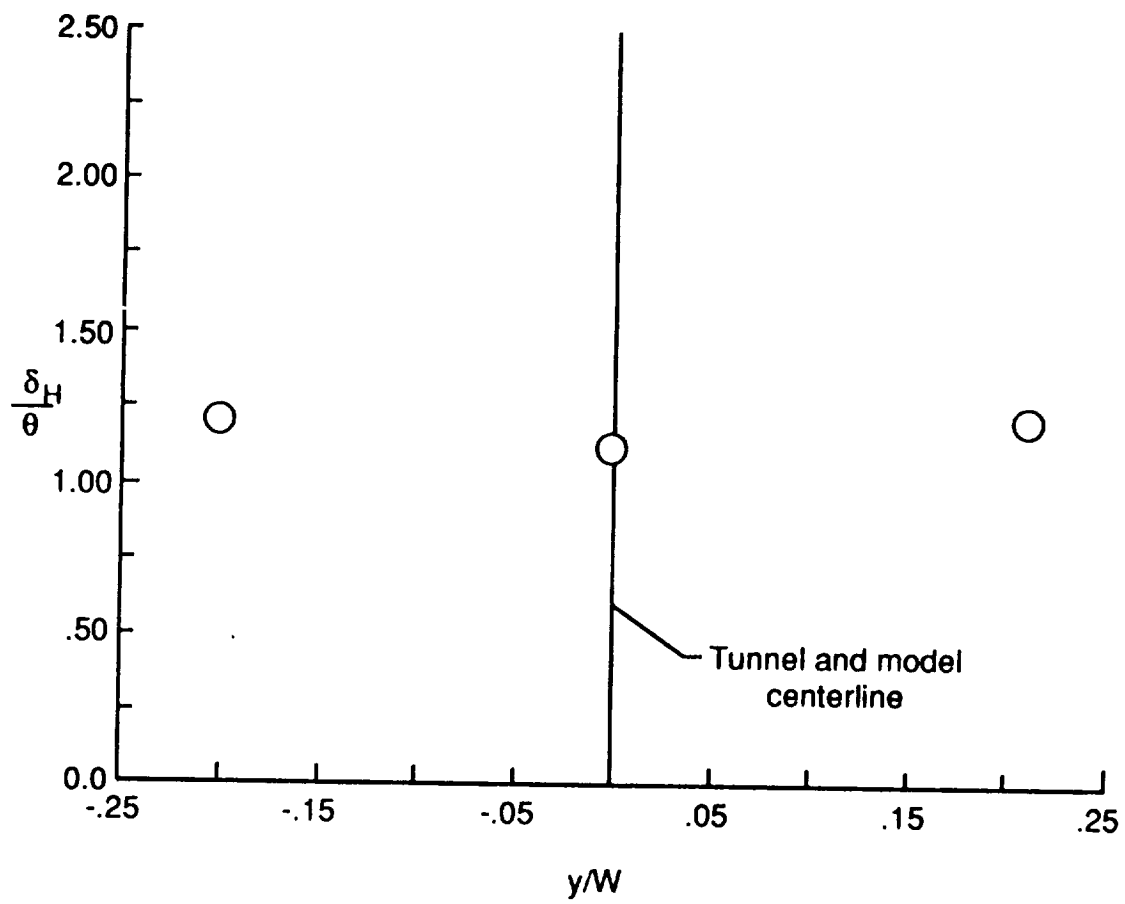
b) Clauser's shape factor, G

Fig. 51. Continued.



c) Thermal shape factor, δ_H/δ^*

Fig. 51. Continued.



d) Thermal shape factor, δ_H/θ

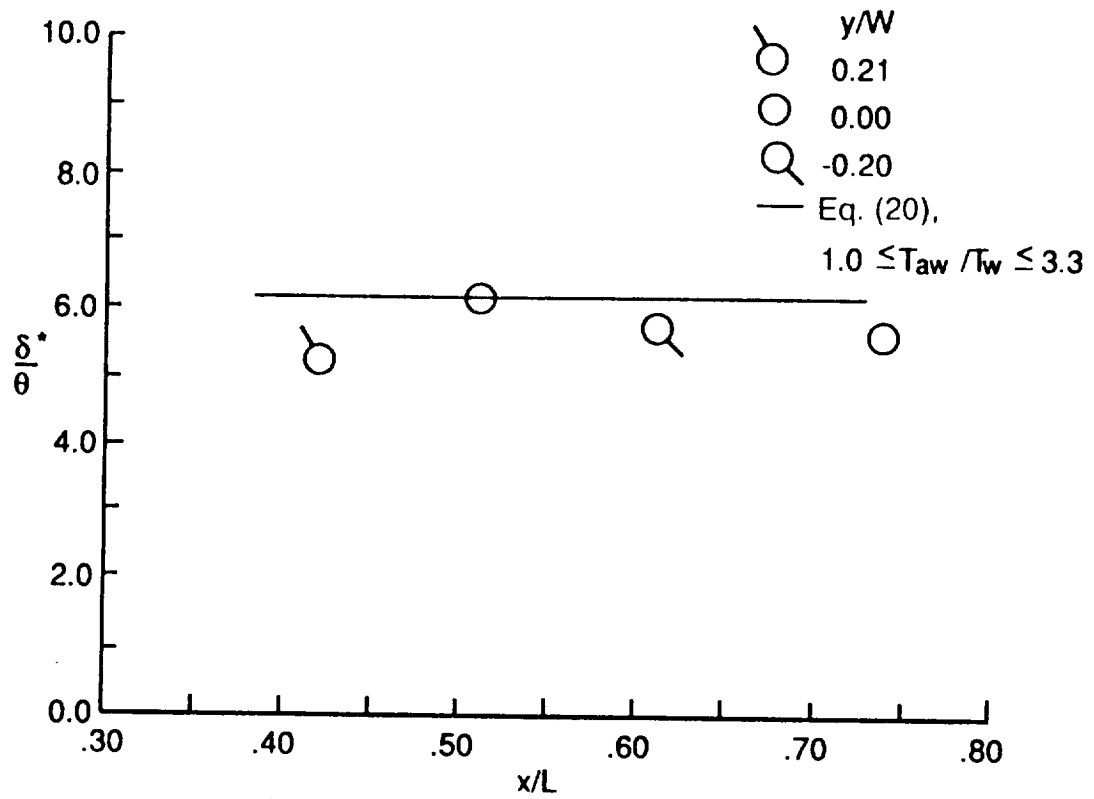
Fig. 51. Concluded.

involving equilibrium turbulent boundary layers be conducted at local unit Reynolds numbers higher than 0.69×10^6 /ft, at least for test articles located within 49 inches from the leading edge (i.e.: $x/L < 0.42$). The combustor total pressure corresponding to this Reynolds number should therefore be greater than 1500 psia for an angle of attack of 13° .

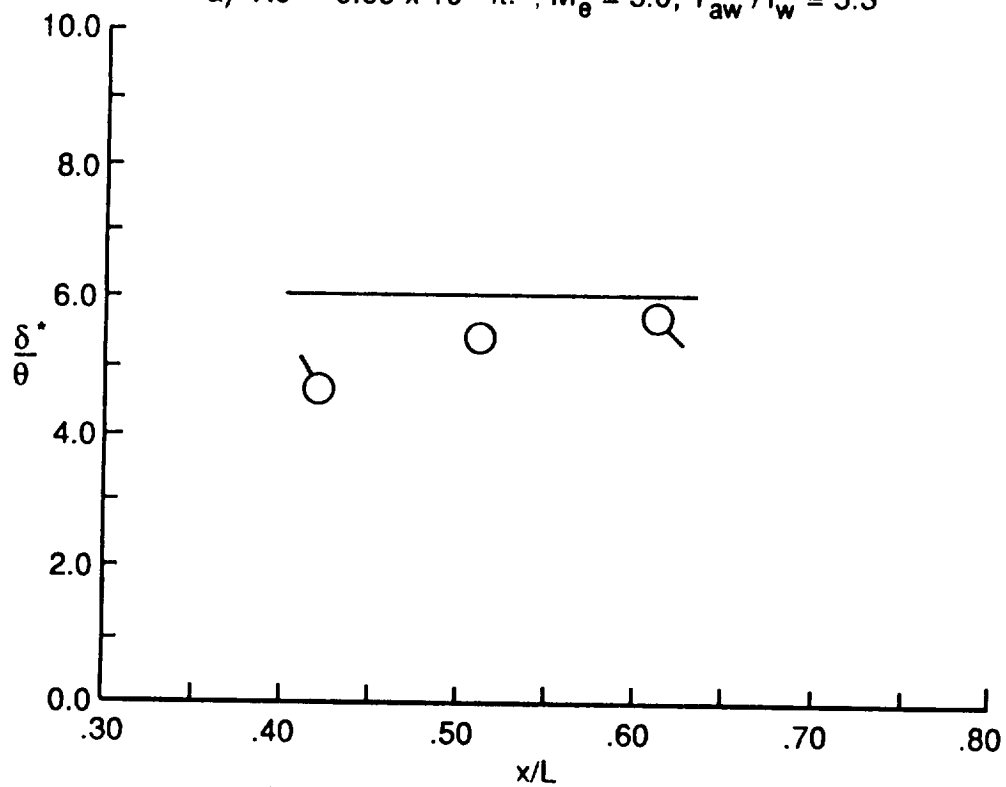
The effect of location on the hydraulic shape factor δ^*/θ is shown in Fig. 52. The data are shown for the plate centerline ($y/W = 0.00$) and off the plate centerline ($y/W = 0.21$ and -0.20) as indicated by the tick marks on the symbols. Also shown with the data is the empirical correlation of δ^*/θ with Mach number, power law exponent, and temperature ratio given by Hopkins et. al. [39]. Hopkins et. al. determined that for temperature ratios ranging from 1 (adiabatic) to 3.3, the ratio of displacement thickness to momentum thickness is approximated by:

$$\frac{\delta^*}{\theta} = \frac{(N + 2) (1 + 0.344 M_\theta^2)}{N [2 - (T_w/T_{aw})]^{1.17}} \quad (20)$$

The shape factors shown in Fig. 52a were obtained at a local unit Reynolds number of $Re^* = 0.69 \times 10^6$ /ft, a boundary-layer edge Mach number of 5.0, and a temperature ratio of 5.3. Between x/L of 0.51 and 0.74, the shape factors are uniform (Fig. 52a). However, at $x/L = 0.42$, the shape factor decreases. The data obtained at $Re^* = 0.92 \times 10^6$ (Fig. 52b) show a similar trend. The shape factors appear to be most uniform at the highest unit Reynolds number of 1.17×10^6 /ft (Fig. 52c). The nonuniformity in the shape factor distribution at $x/L = 0.42$ may result from nonuniform surface pressures, as indicated in the spanwise distribution for a nearby location ($x/L = 0.46$).

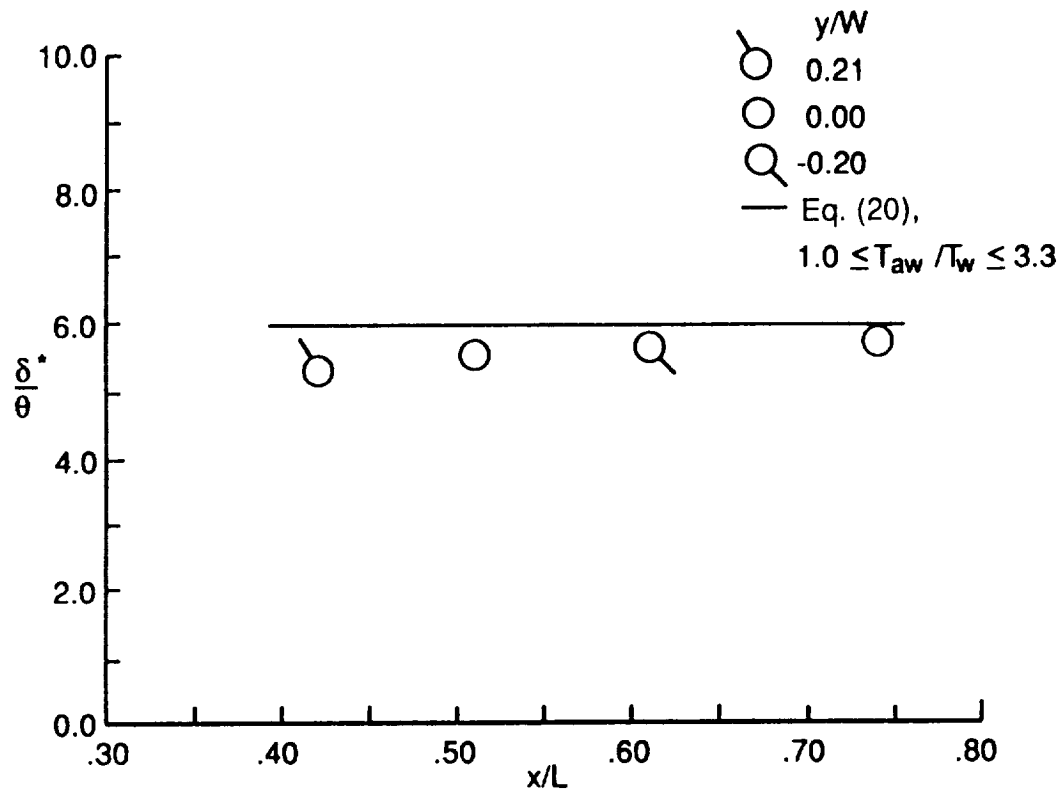


a) $Re^* = 0.69 \times 10^6 \text{ ft.}^{-1}$, $M_e = 5.0$, $T_{aw}/T_w = 5.3$

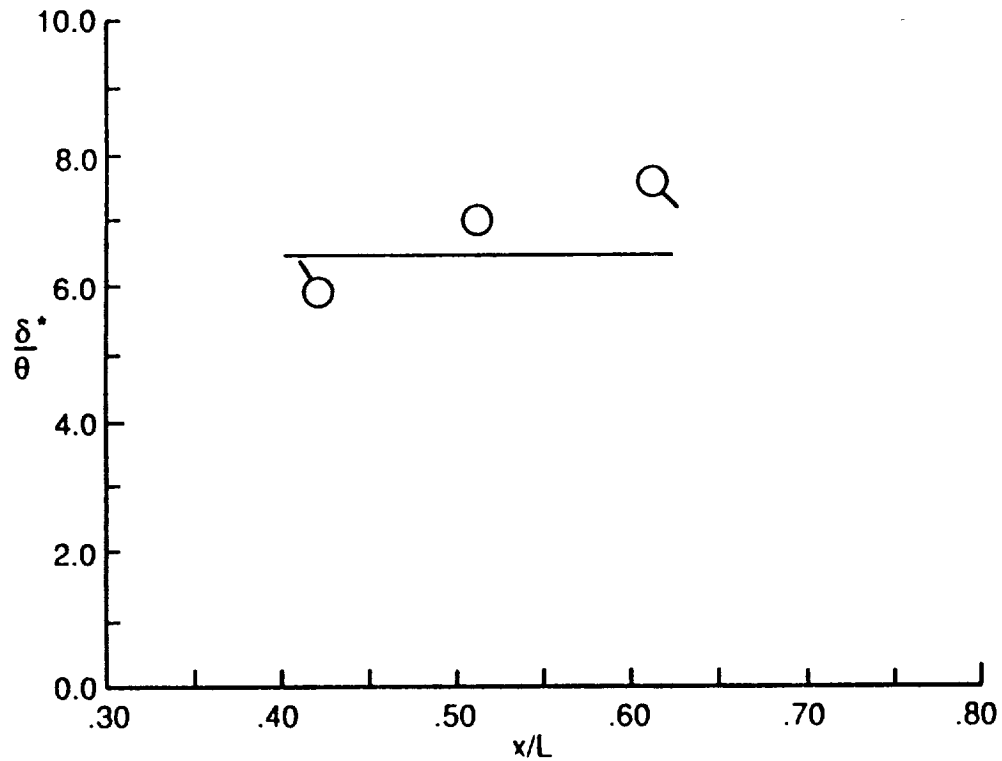


b) $Re^* = 0.92 \times 10^6 \text{ ft.}^{-1}$, $M_e = 4.9$, $T_{aw}/T_w = 5.6$

Fig. 52. Effect of location on shape factor, δ^*/θ .

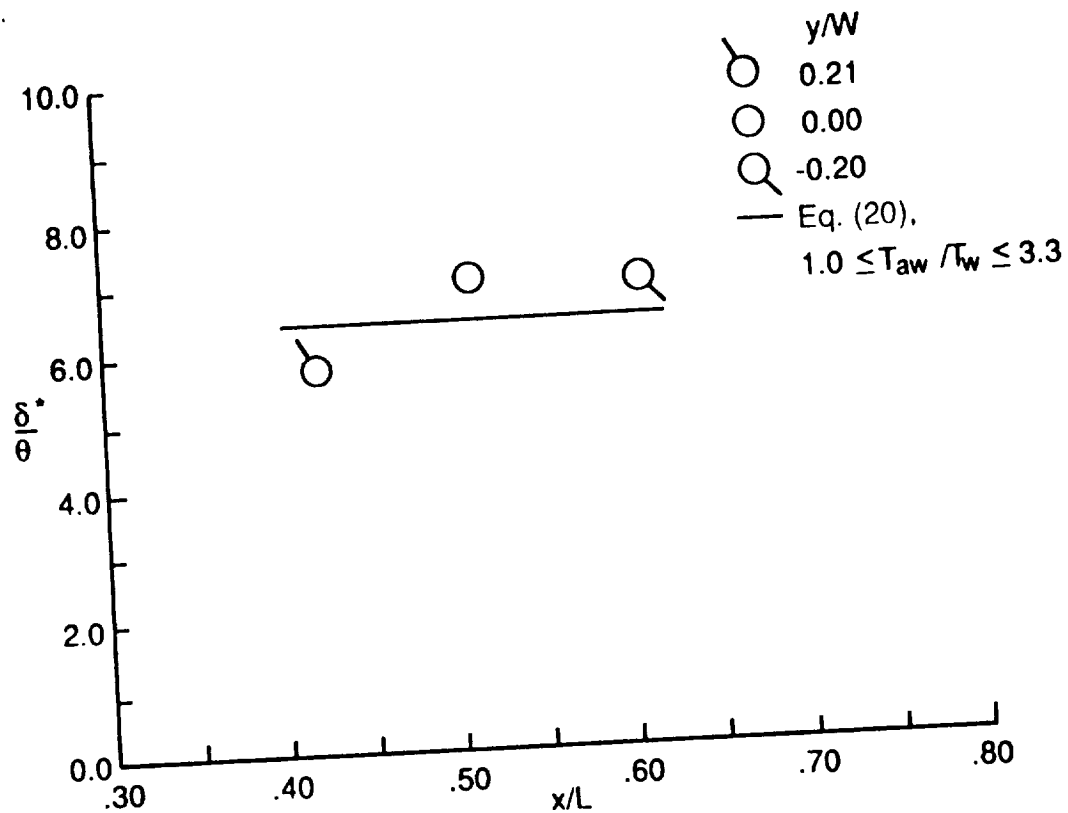


c) $Re^* = 1.17 \times 10^6 \text{ ft.}^{-1}$, $M_\theta = 4.9$, $T_{aw}/T_w = 5.3$

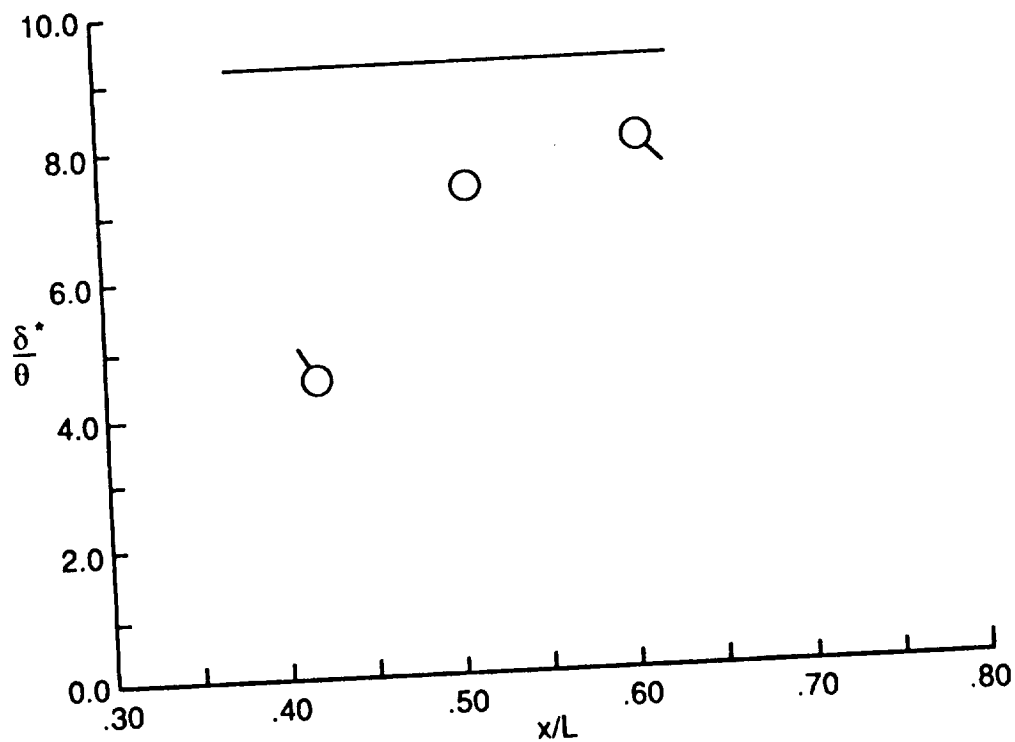


d) $Re^* = 0.69 \times 10^6 \text{ ft.}^{-1}$, $M_\theta = 5.1$, $T_{aw}/T_w = 4.4$

Fig. 52. Continued.



e) $Re^* = 0.92 \times 10^6 \text{ ft}^{-1}$, $M_e = 5.1$, $T_{aw}/T_w = 4.4$

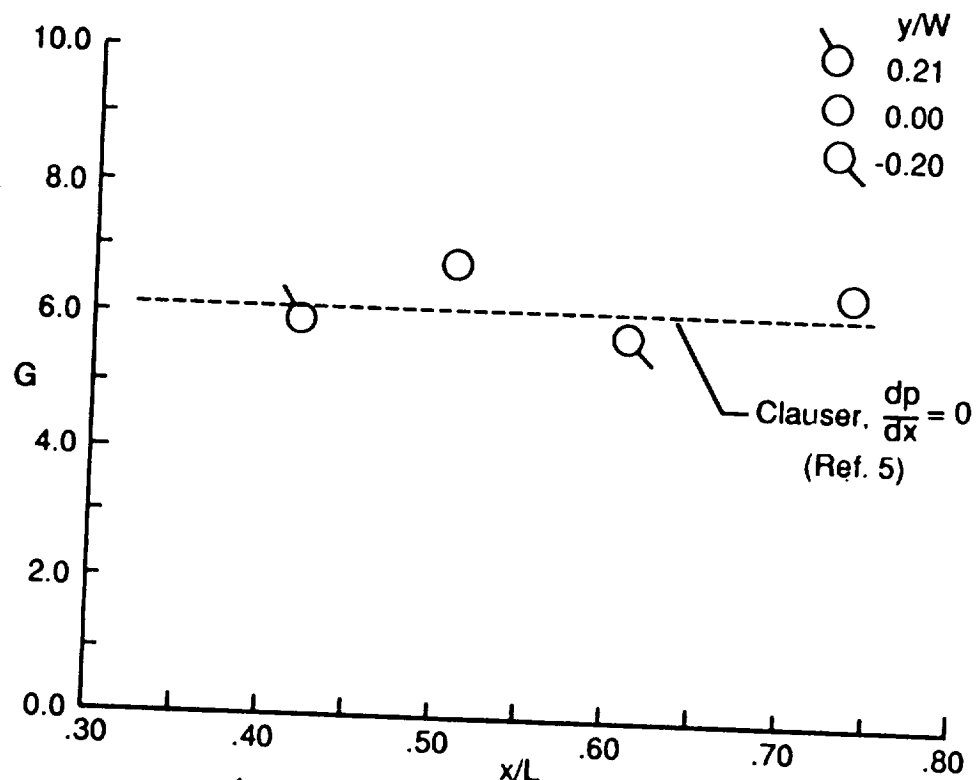


f) $Re^* = 0.21 \times 10^6 \text{ ft}^{-1}$, $M_e = 6.2$, $T_{aw}/T_w = 5.3$

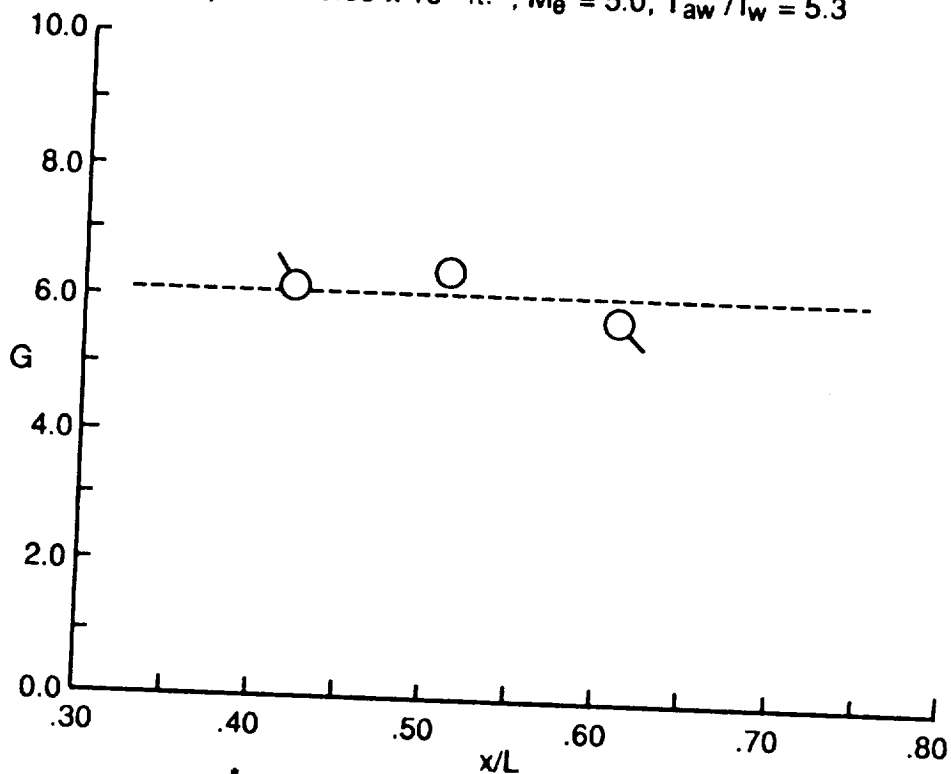
Fig. 52. Concluded.

(See Fig. 18b.) These gradients may be attributed to pressure gradients in the test section core, as discussed in section 3.1.3. Overall, the data obtained at a nominal temperature ratio of 5.4 are below the correlation given by Hopkins et. al. by an average of approximately 10%. This may indicate that the correlation requires a slight modification to extend its temperature ratio range to 5.4. The data obtained at the lower temperature ratio of 4.4 (Figs. 52d and 52e) tend to agree better with the Hopkins correlation in terms of overall level. However, the data are less uniform than the higher temperature ratio data for the same unit Reynolds number. Although these data were obtained at nearly the same edge Mach number and the same local unit Reynolds numbers as the higher temperature ratio data shown in Figs. 52a and 52b, the momentum thickness Reynolds numbers are consistently lower, ranging from 1710 to 2860. As noted in section 3.3.4, this is because the momentum thicknesses are lower, as a result of the difference in density variation in the boundary layer. This nonuniformity, along with the discrepancies between the velocity data and the velocity defect equation noted in section 4.1, may indicate nonequilibrium turbulence at the low temperature condition. The shape factors, δ^*/θ , obtained at the lowest Reynolds number condition (Fig. 52f) show even larger nonuniformities, also possibly indicating nonequilibrium turbulence. The boundary layer at this condition was shown to be transitional in section 3.3.2.

In Fig. 53, the effect of location on Clauser's shape factor, G , is shown for various test conditions. Also shown with the data is the level of 6.1 obtained by Clauser [5] for a zero pressure gradient, equilibrium turbulent boundary layer. As with the hydraulic shape factor, δ^*/θ , Clauser's shape factor is more uniform at higher unit Reynolds numbers. Overall, the shape

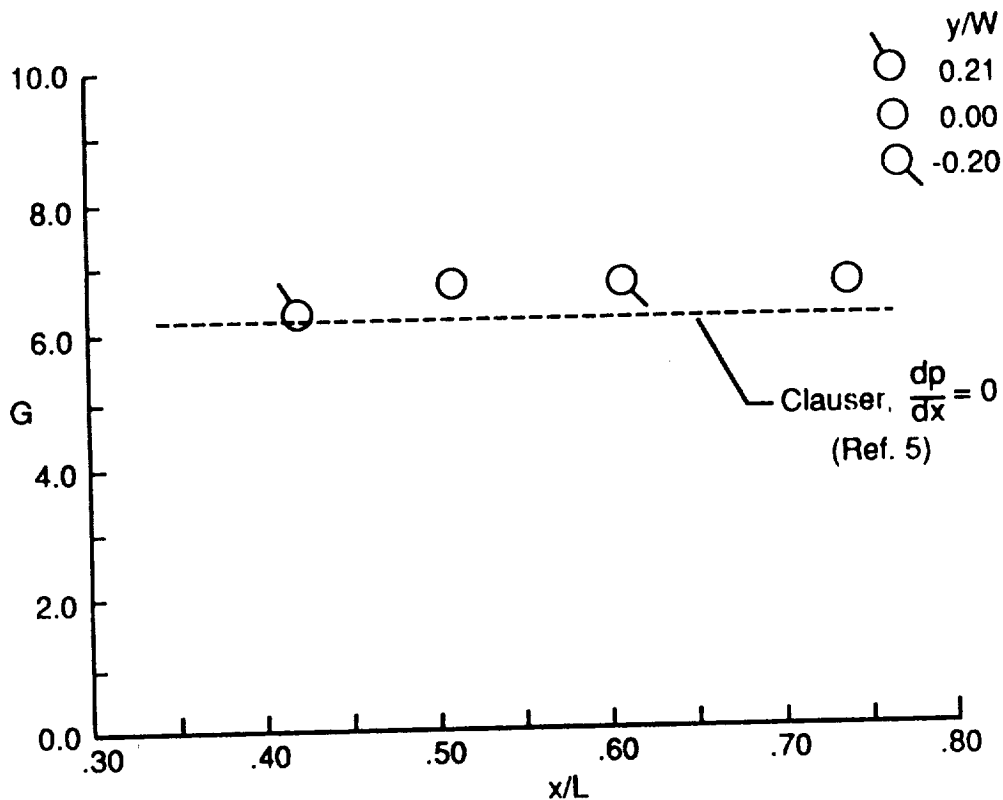


a) $Re^* = 0.69 \times 10^6 \text{ ft.}^{-1}$, $Me = 5.0$, $T_{aw}/T_w = 5.3$

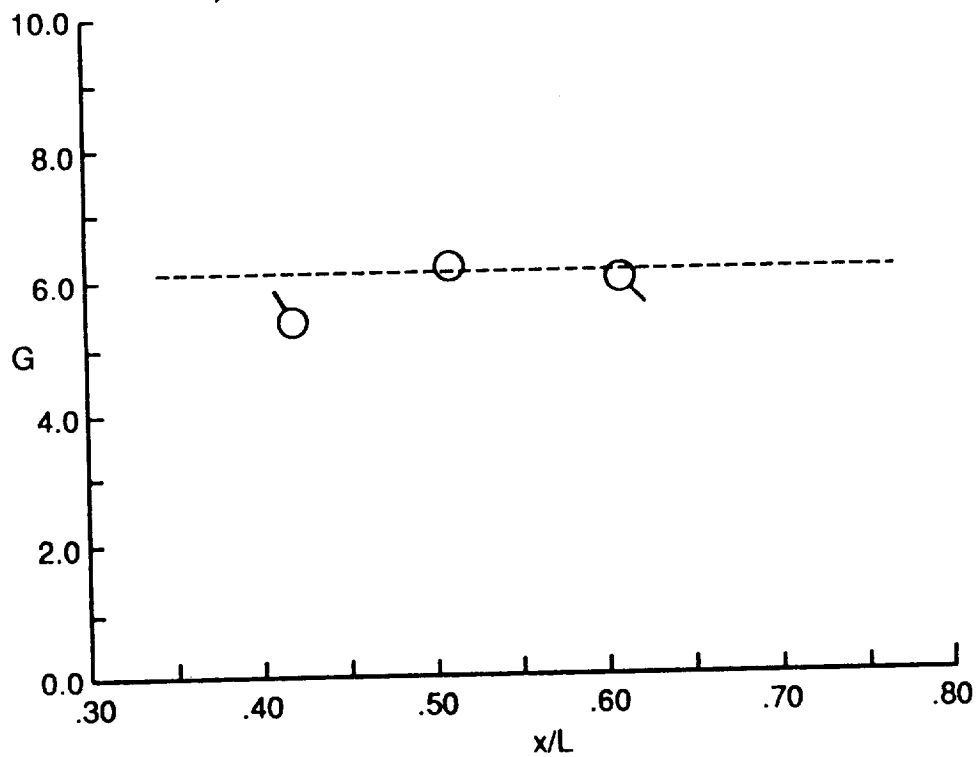


b) $Re^* = 0.92 \times 10^6 \text{ ft.}^{-1}$, $Me = 4.9$, $T_{aw}/T_w = 5.6$

Fig. 53. Effect of location on Clauser's shape factor.

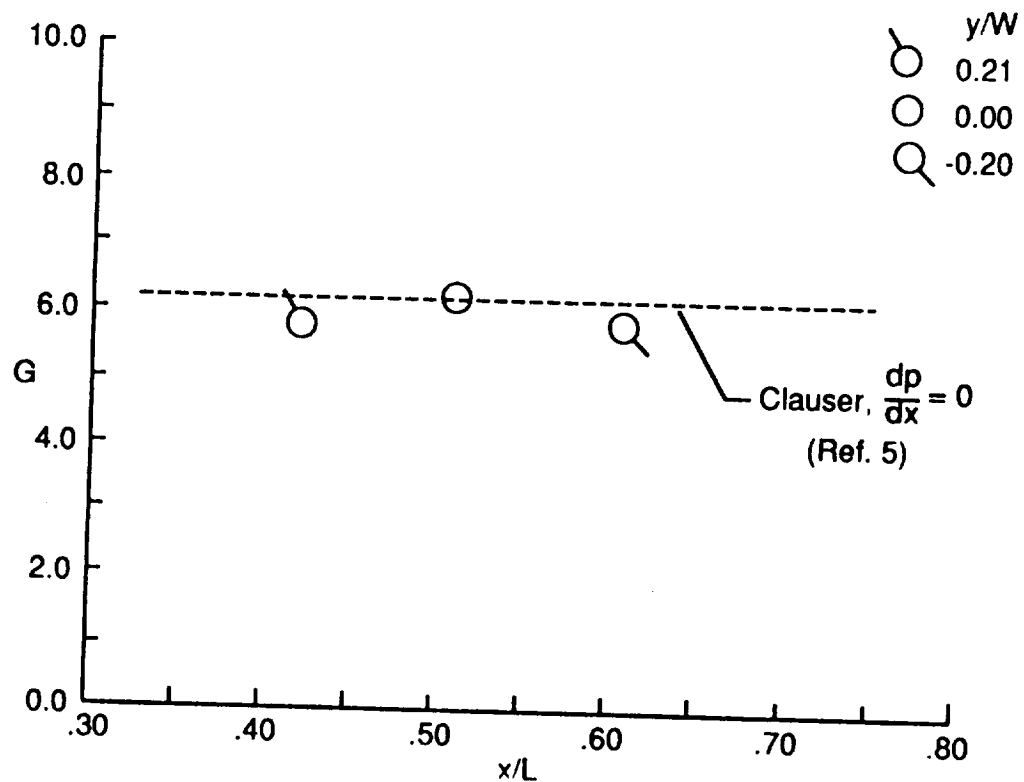


c) $Re^* = 1.17 \times 10^6 \text{ ft.}^{-1}$, $Me = 4.9$, $T_{aw}/T_w = 5.3$

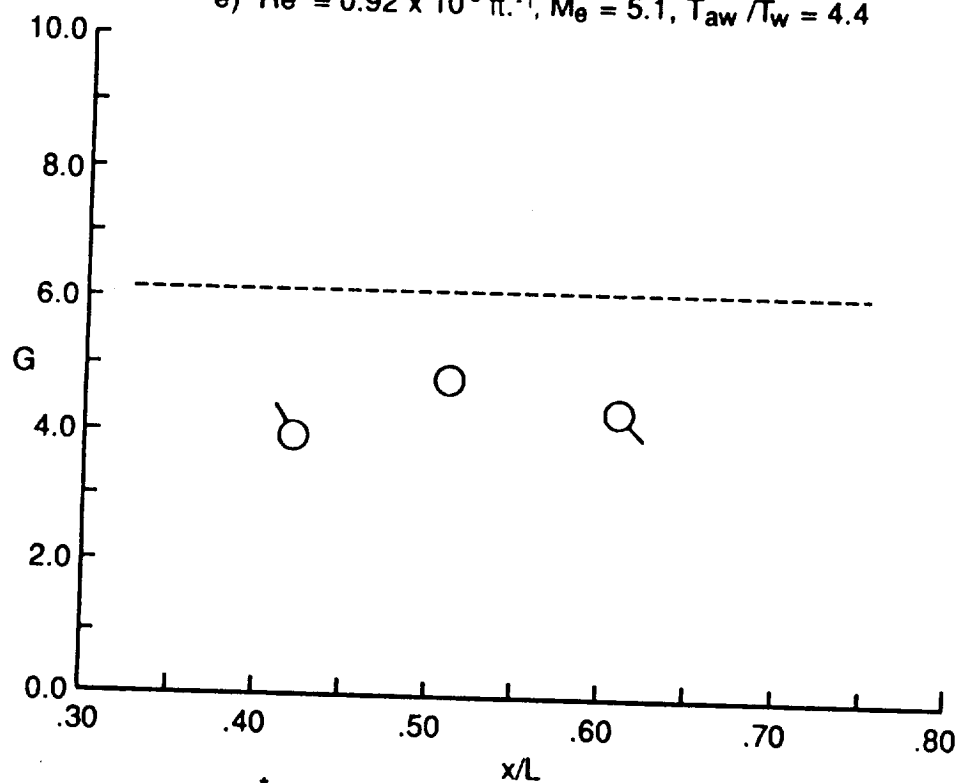


d) $Re^* = 0.69 \times 10^6 \text{ ft.}^{-1}$, $Me = 5.1$, $T_{aw}/T_w = 4.4$

Fig. 53. Continued.



e) $Re^* = 0.92 \times 10^6 \text{ ft.}^{-1}$, $Me = 5.1$, $T_{aw}/T_w = 4.4$



f) $Re^* = 0.21 \times 10^6 \text{ ft.}^{-1}$, $Me = 6.2$, $T_{aw}/T_w = 5.3$

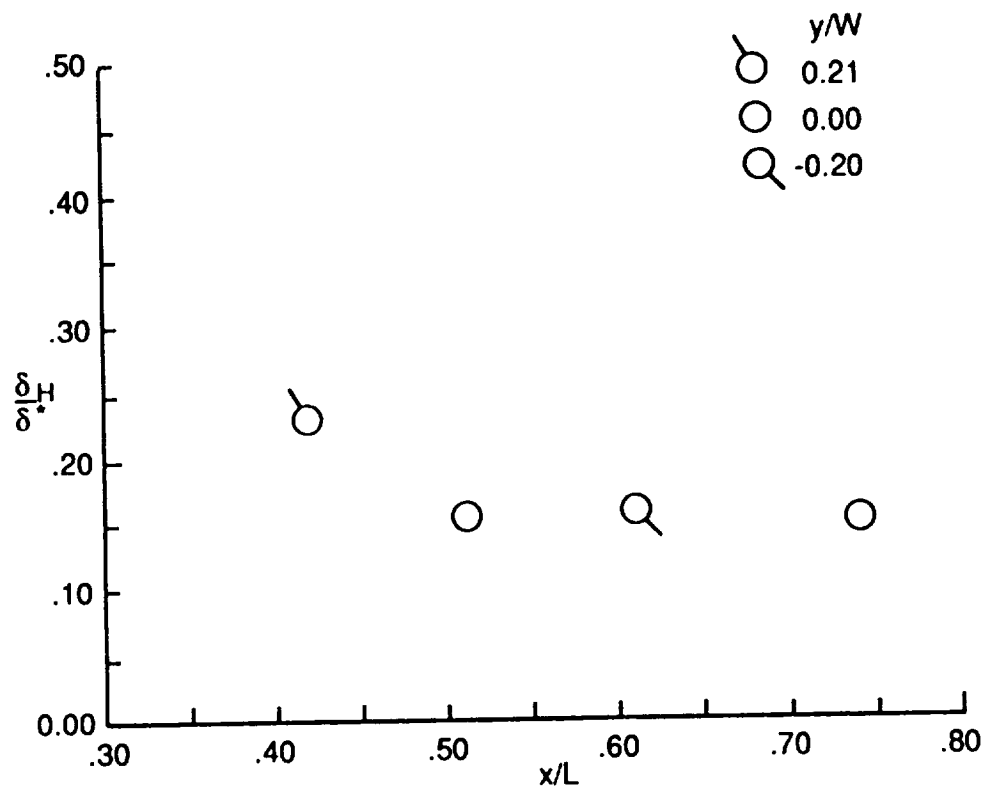
Fig. 53. Concluded.

factors agree reasonably well with Clauser's level of 6.1, except for the lowest Reynolds number data (Fig. 53f).

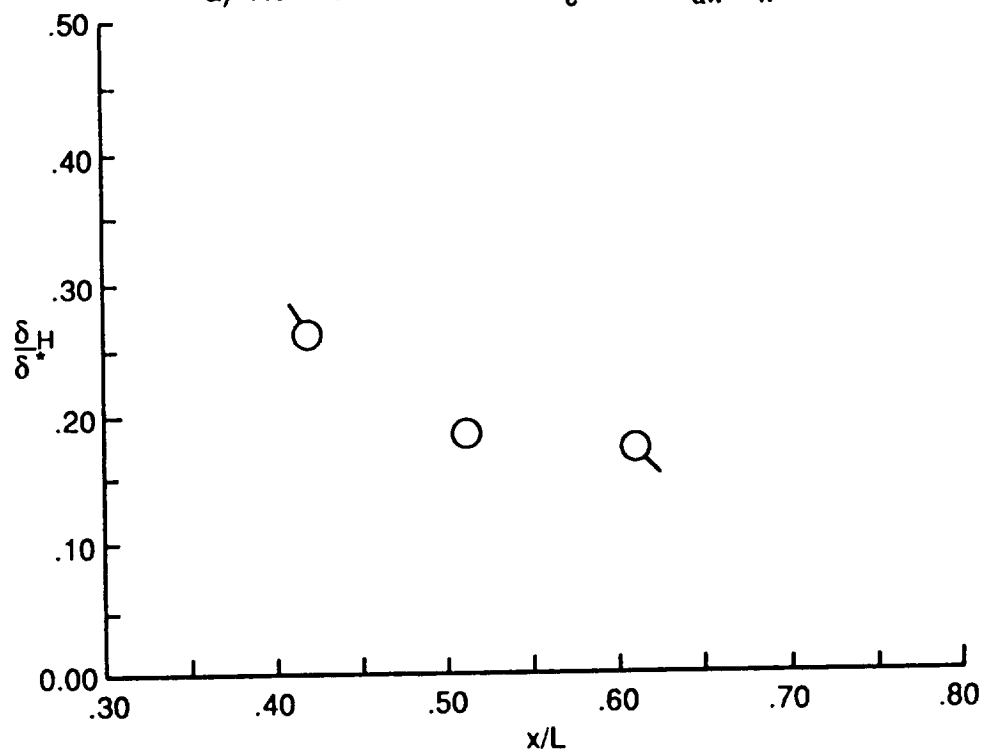
The effect of location on thermal shape factor 1, δ_H/δ^* , is shown for various test conditions in Fig. 54. The shape factors obtained at unit Reynolds numbers ranging from 0.69×10^6 to 1.17×10^6 /ft. and at a nominal temperature ratio of 5.4 appear uniform between $0.51 \leq x/L \leq 0.74$ (Figs. 54a through 54c). However, as with the shape factor δ^*/θ , the thermal shape factor corresponding to $x/L = 0.42$ is not at the same level as those between $0.51 \leq x/L \leq 0.74$, particularly for local unit Reynolds numbers of 0.69×10^6 and 0.92×10^6 /ft. At the highest unit Reynolds number condition of 1.17×10^6 /ft (Fig. 54c) the level of the shape factor at $x/L=0.42$ appears to be approaching that of the shape factors obtained between $x/L=0.51$ and 0.74 . The shape factor distributions obtained at the lower temperature ratio of 4.4 (Figs. 54d and 54e) also show a nonuniformity at $x/L=0.42$. The shape factors obtained at the lowest Reynolds number condition (Fig 54f) show the largest nonuniformity at $x/L= 0.42$. Note that in Figs. 54a through 54f, the trends in the thermal shape factor 1, δ_H/δ^* , are reversed from that of the shape factor δ^*/θ .

The effect of location on the thermal shape factor 2, δ_H/θ , is shown for various test conditions in Fig. 55. The data generally show the same trends as those shown by thermal shape factor 1, δ_H/δ^* , but are generally more uniform. The shape factors obtained at $Re^* = 1.17 \times 10^6$ /ft, (Fig. 55c) for example, vary only 11% as compared to 17% for thermal shape factor 1 (Fig. 54c). As mentioned in the discussion on the spanwise distributions, this probably indicates that thermal shape factor 2, δ_H/θ , is less sensitive to flow variations.

In Figs. 56 through 59, the effect of momentum thickness Reynolds number on the various shape factors are shown. The shape factors are shown

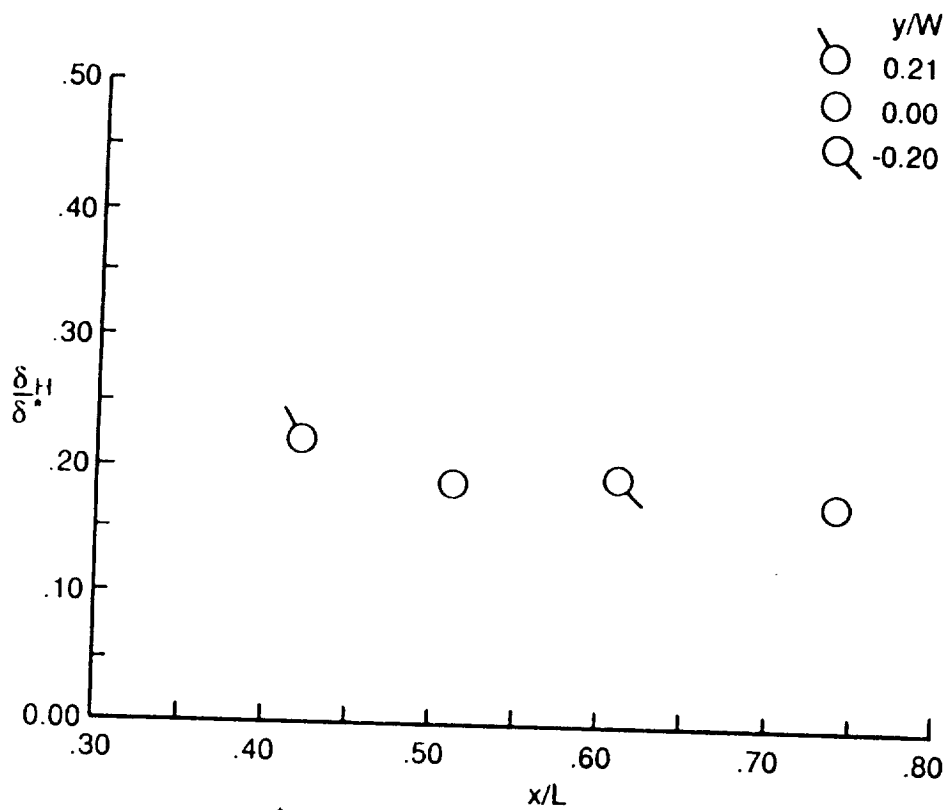


a) $Re^* = 0.69 \times 10^6 \text{ ft.}^{-1}$, $M_e = 5.0$, $T_{aw}/T_w = 5.3$

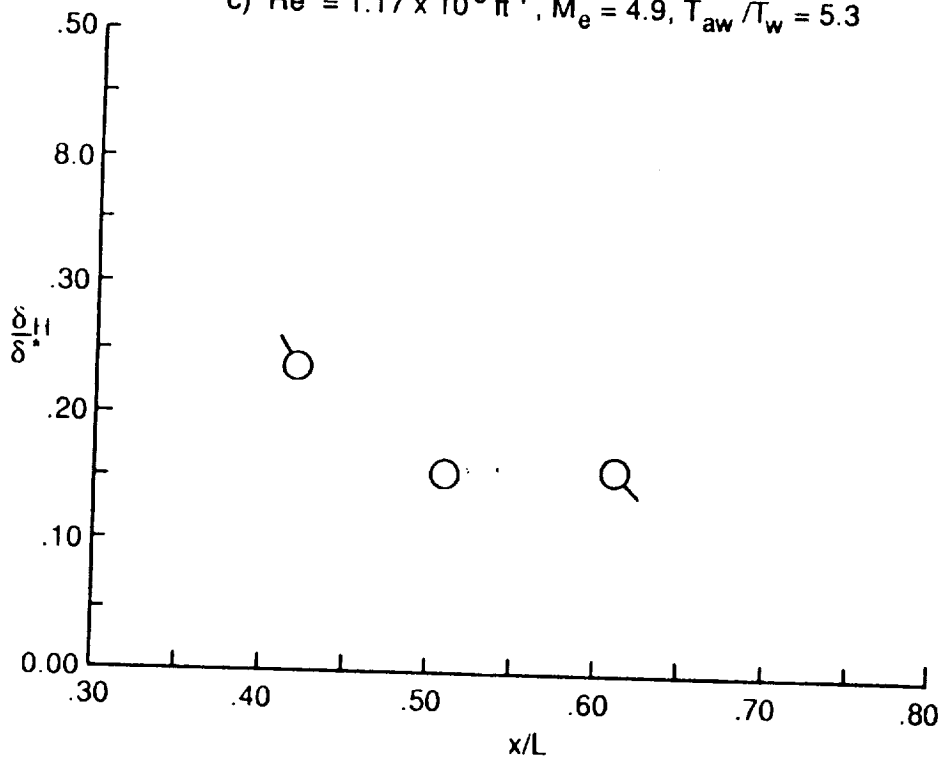


b) $Re^* = 0.92 \times 10^6 \text{ ft.}^{-1}$, $M_e = 4.9$, $T_{aw}/T_w = 5.6$

Fig. 54. Effect of location on thermal shape factor, δ_H/δ^* .

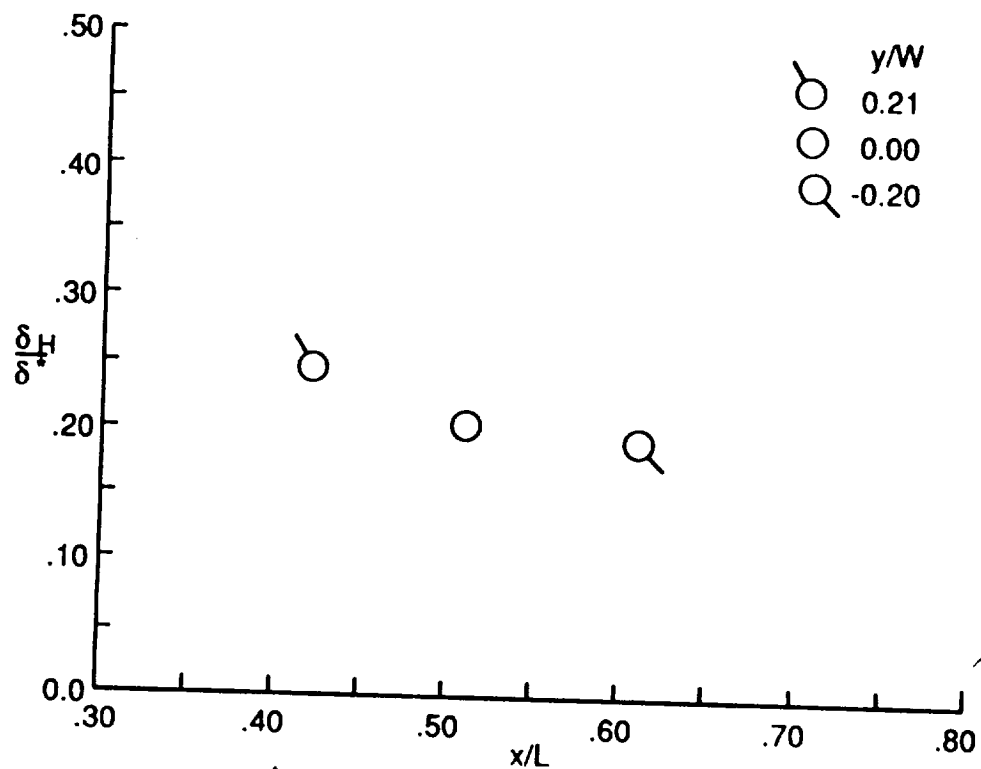


c) $Re^* = 1.17 \times 10^6 ft^{-1}$, $M_e = 4.9$, $T_{aw}/T_w = 5.3$

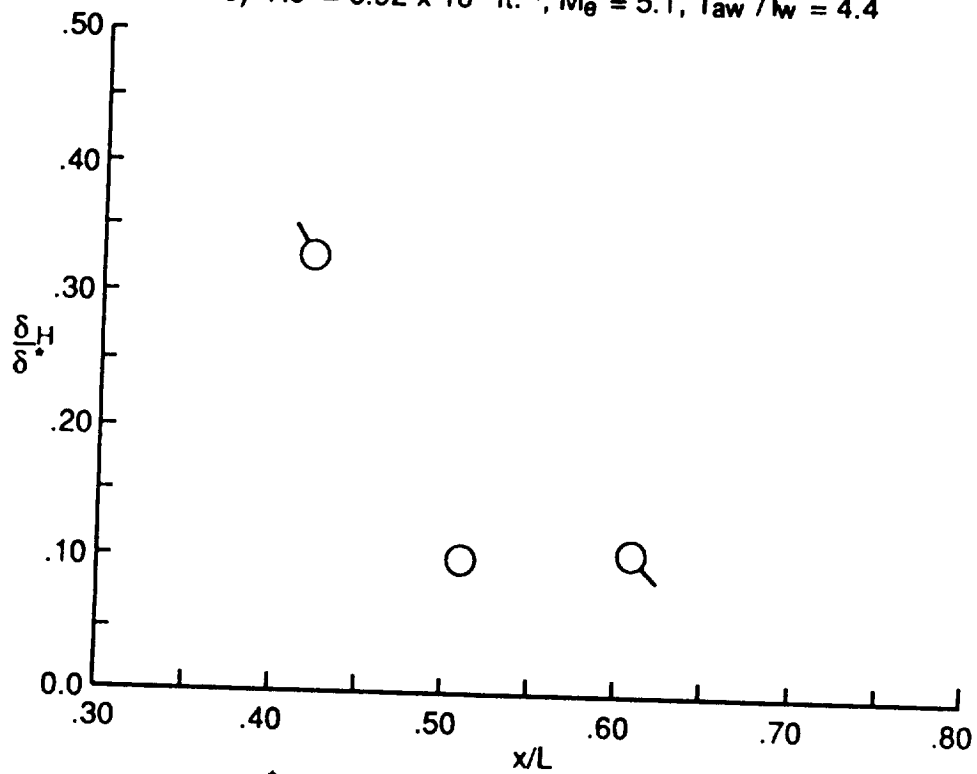


d) $Re^* = 0.69 \times 10^6 ft^{-1}$, $M_e = 5.1$, $T_{aw}/T_w = 4.4$

Fig. 54. Continued.

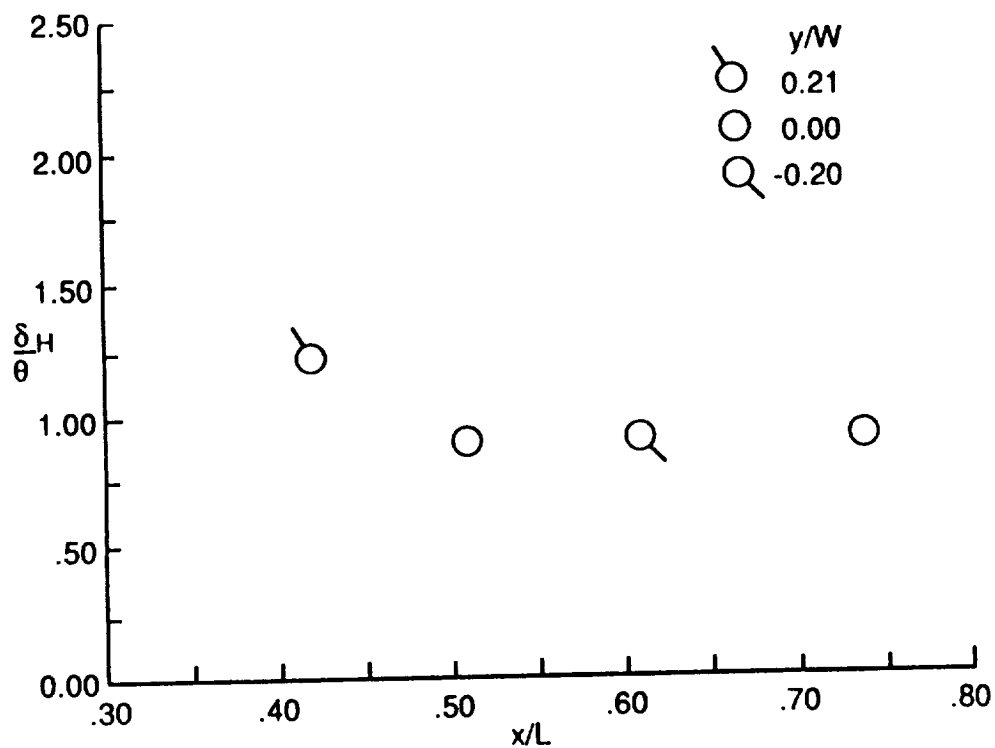


e) $Re^* = 0.92 \times 10^6 \text{ ft}^{-1}$, $Me = 5.1$, $T_{aw}/T_w = 4.4$

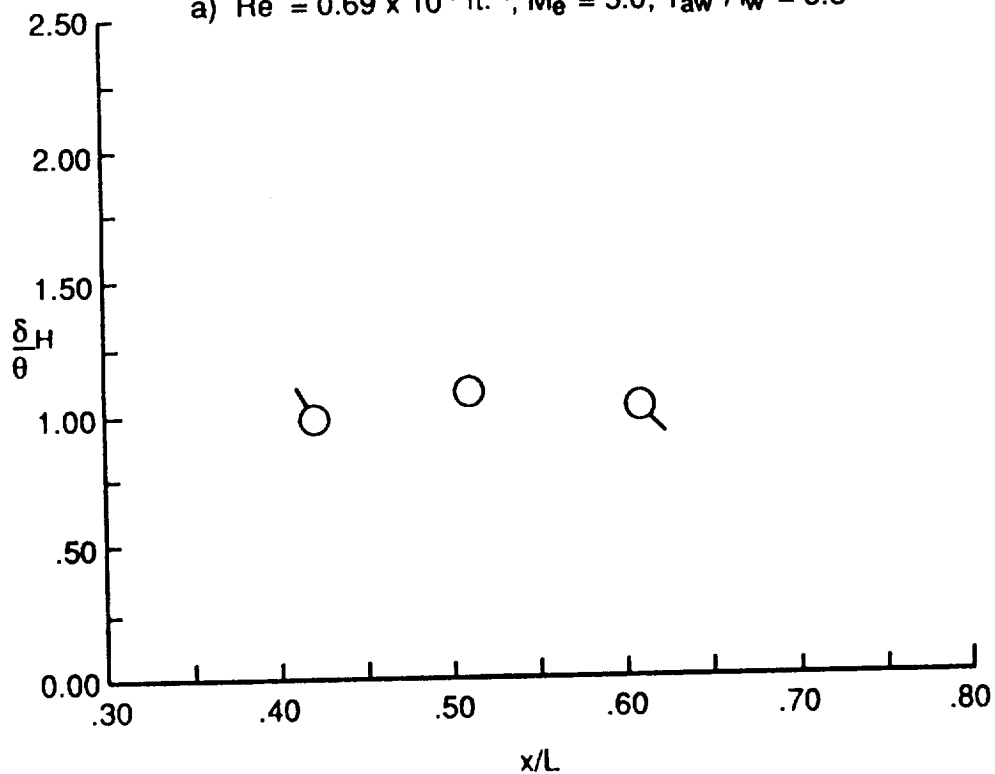


f) $Re^* = 0.21 \times 10^6 \text{ ft}^{-1}$, $Me = 6.2$, $T_{aw}/T_w = 5.3$

Fig. 54. Concluded.

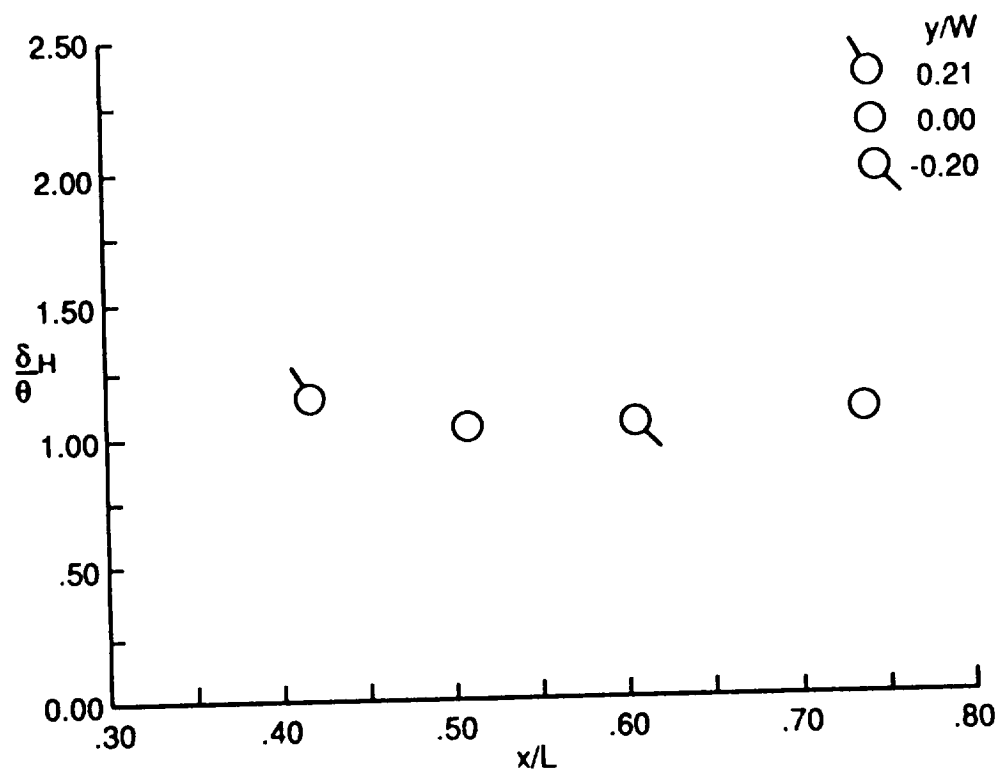


a) $Re = 0.69 \times 10^6 \text{ ft.}^{-1}$, $M_e = 5.0$, $T_{aw}/T_w = 5.3$

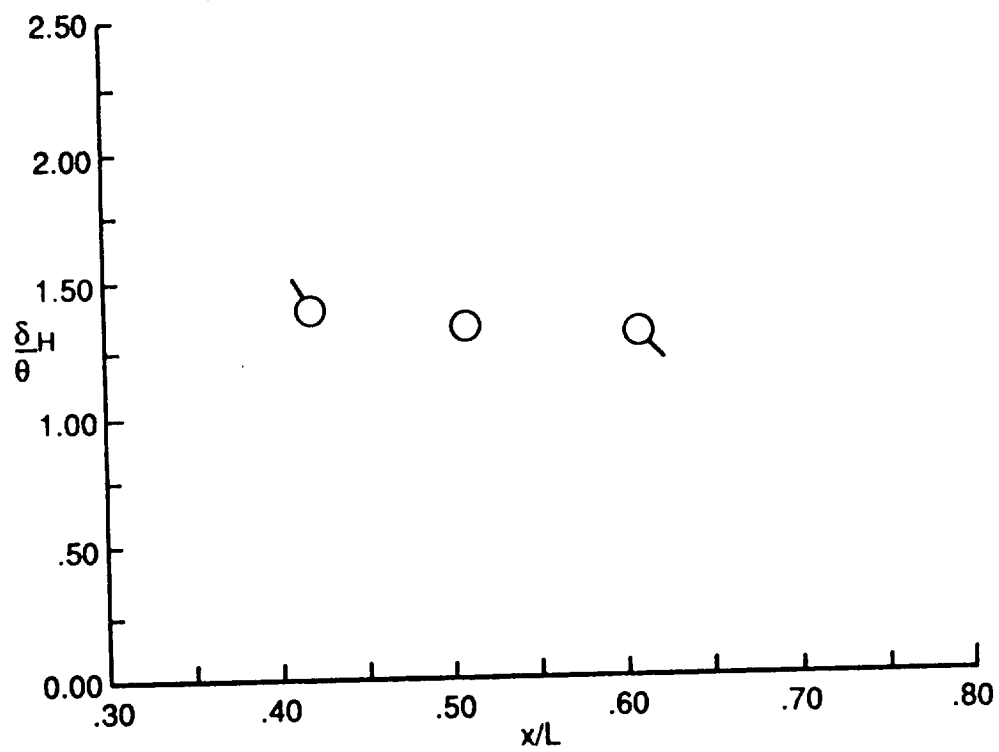


b) $Re = 0.92 \times 10^6 \text{ ft.}^{-1}$, $M_e = 4.9$, $T_{aw}/T_w = 5.6$

Fig. 55. Effect of location on thermal shape factor, δ_H/θ .

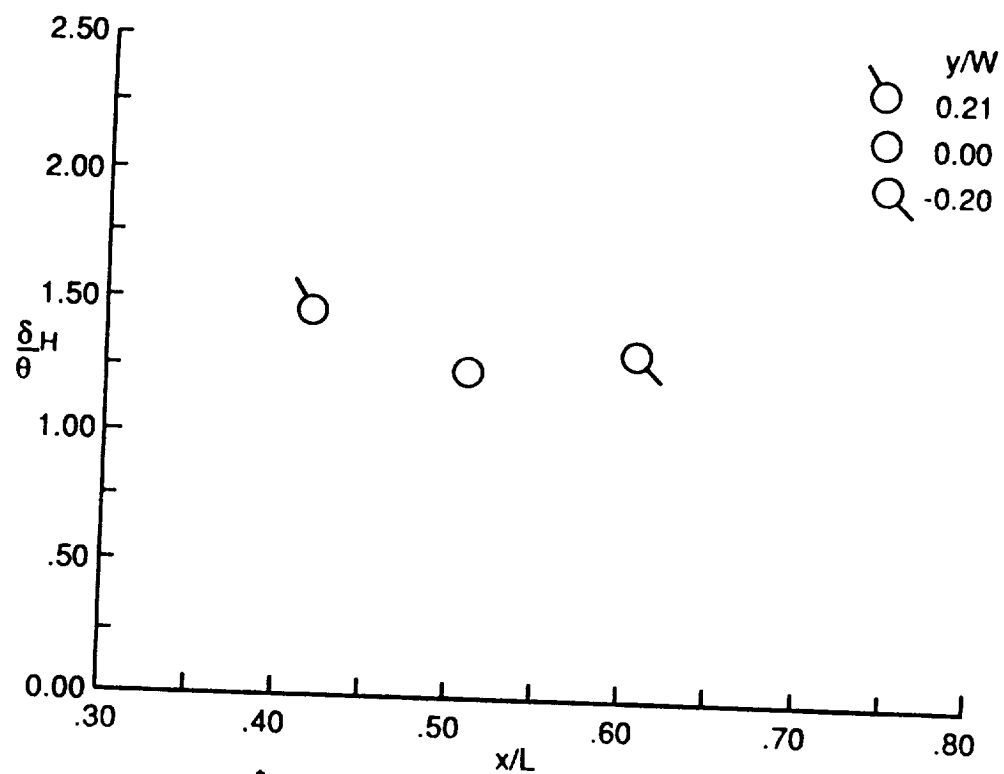


c) $Re_\theta = 1.17 \times 10^6 \text{ ft.}^{-1}$, $M_\theta = 4.9$, $T_{aw}/T_w = 5.3$

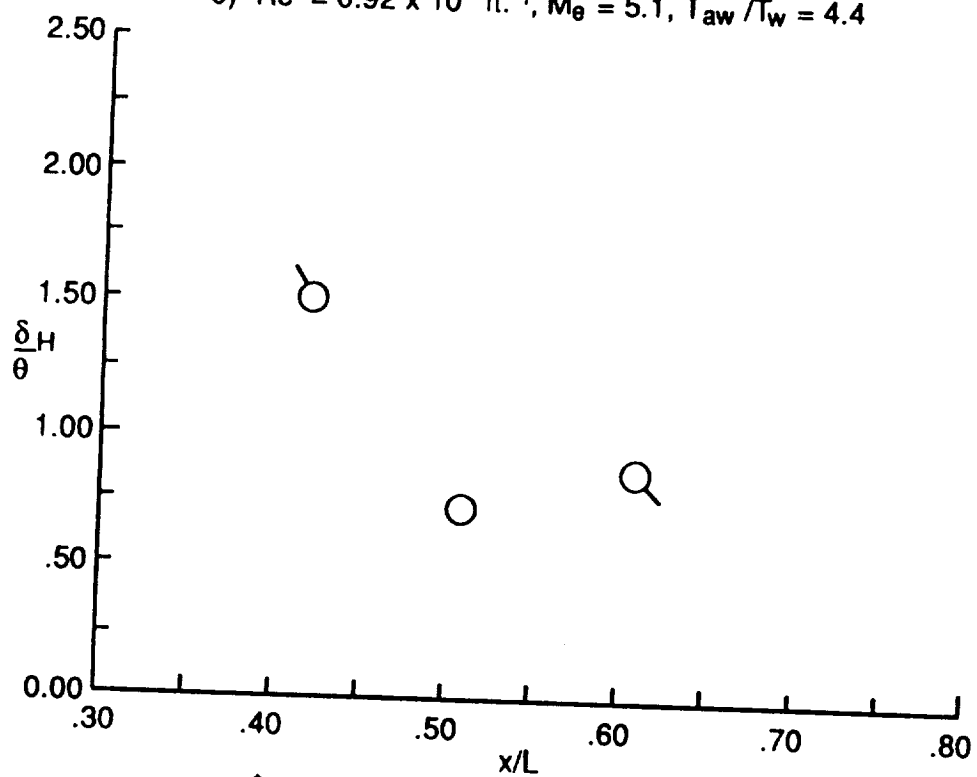


d) $Re_\theta = 0.69 \times 10^6 \text{ ft.}^{-1}$, $M_\theta = 5.1$, $T_{aw}/T_w = 4.4$

Fig. 55. Continued.



e) $Re^* = 0.92 \times 10^6 \text{ ft}^{-1}$, $M_e = 5.1$, $T_{aw}/T_w = 4.4$



f) $Re^* = 0.21 \times 10^6 \text{ ft}^{-1}$, $M_e = 6.2$, $T_{aw}/T_w = 5.3$

Fig. 55. Concluded.

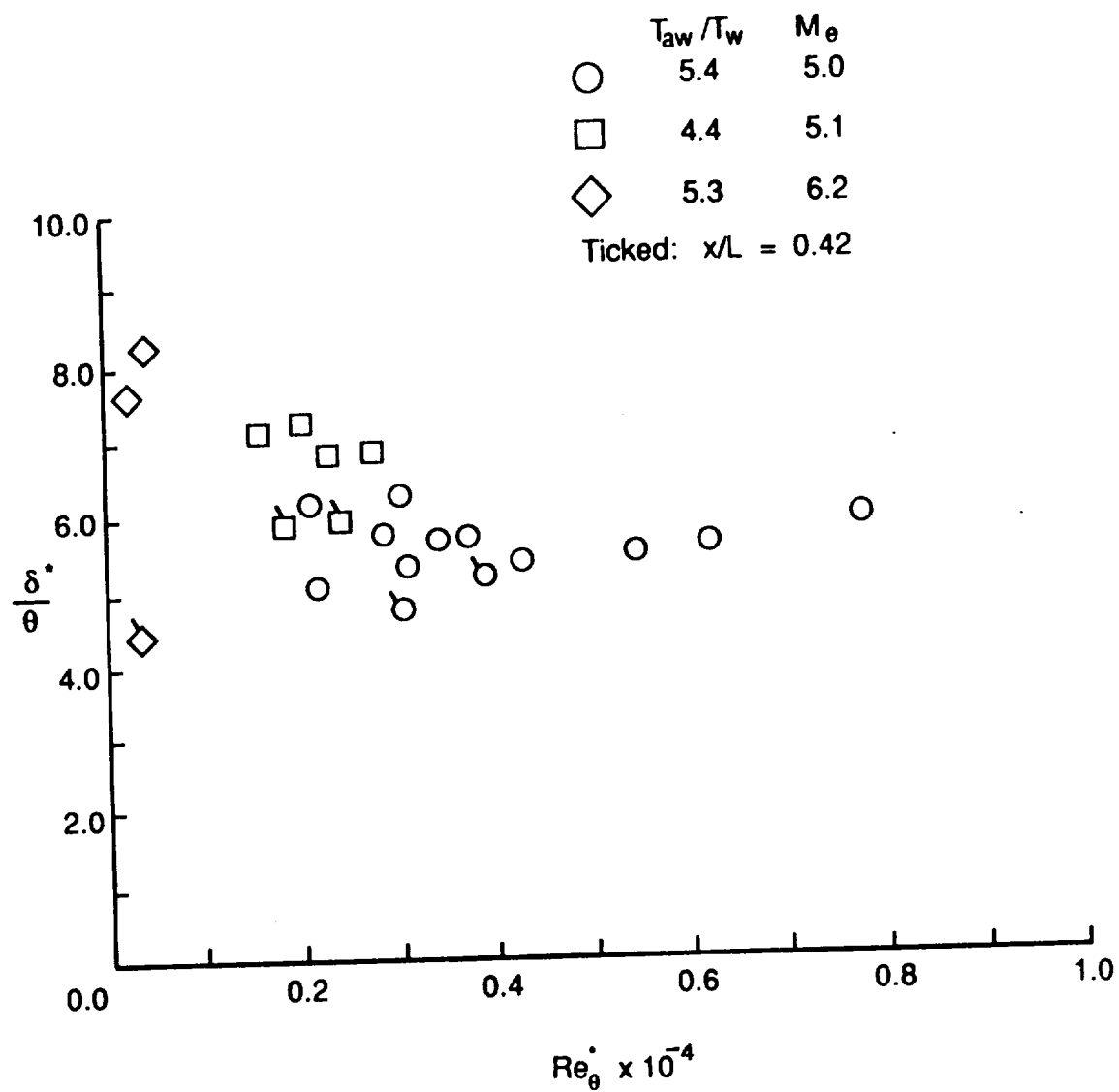


Fig. 56. Effect of momentum thickness Reynolds number on shape factor, δ^* / θ .

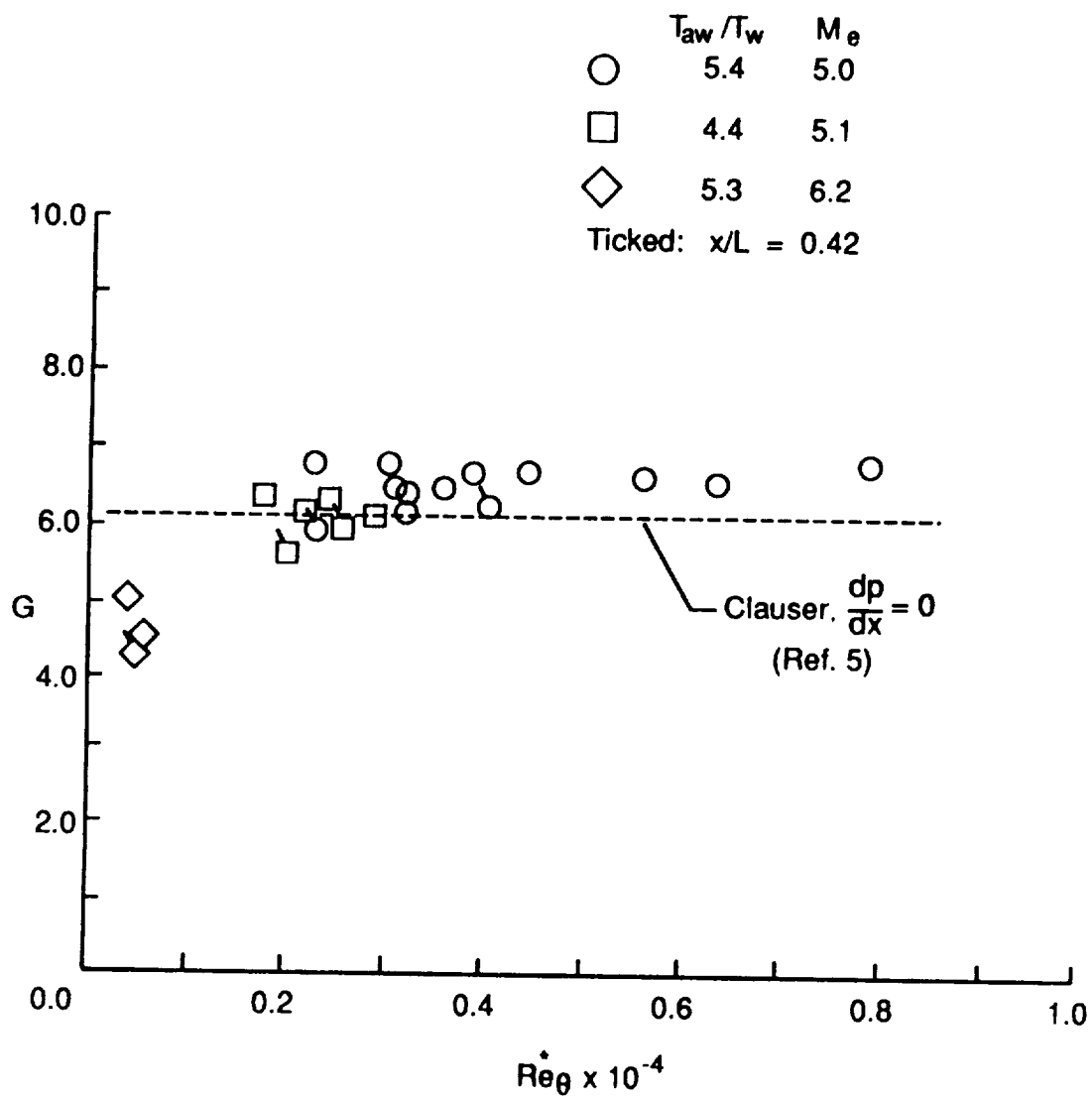


Fig. 57. Effect of momentum thickness Reynolds number on Clauser's shape factor.

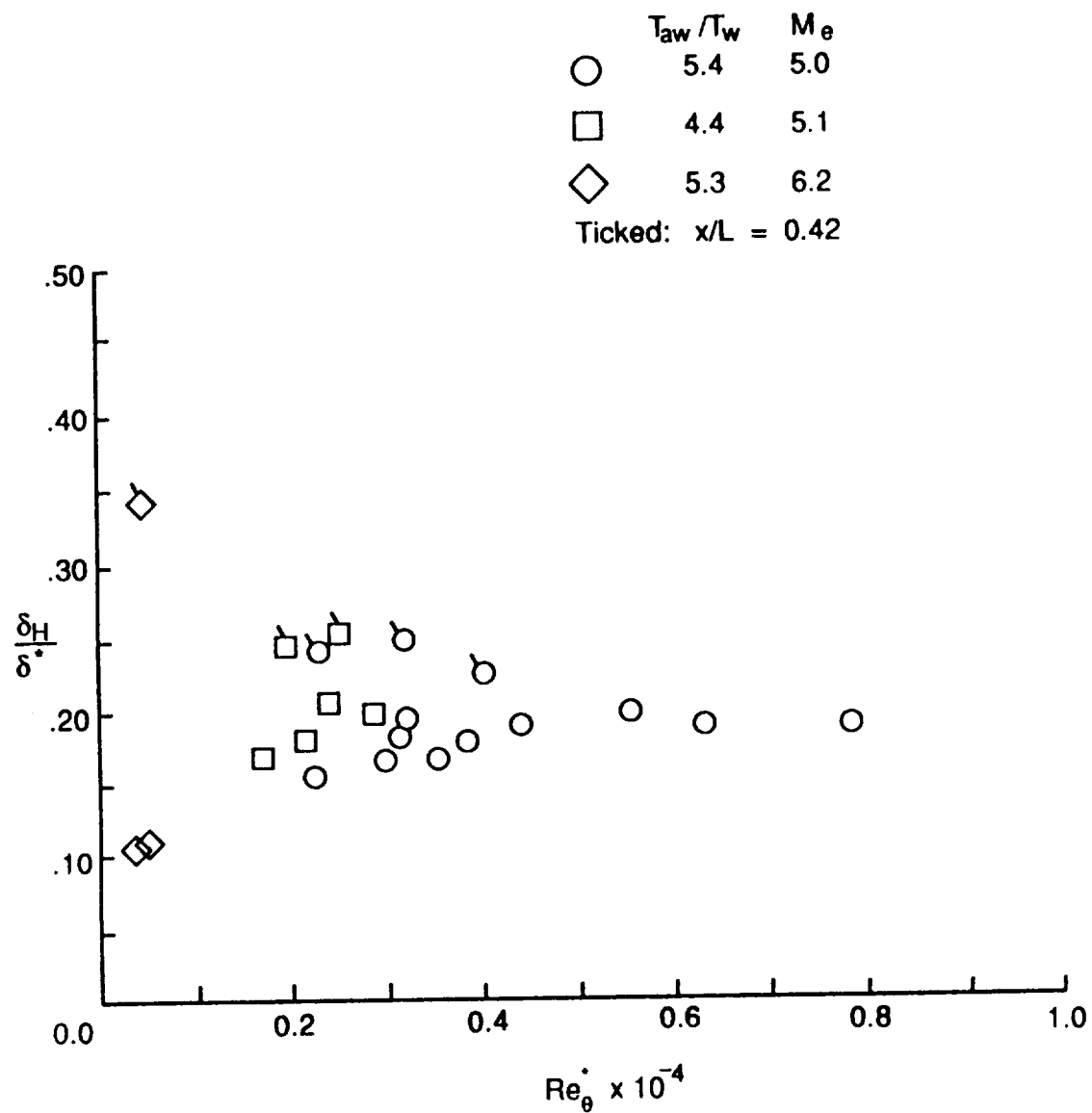


Fig. 58. Effect of momentum thickness Reynolds number on shape factor, δ_H/δ^* .

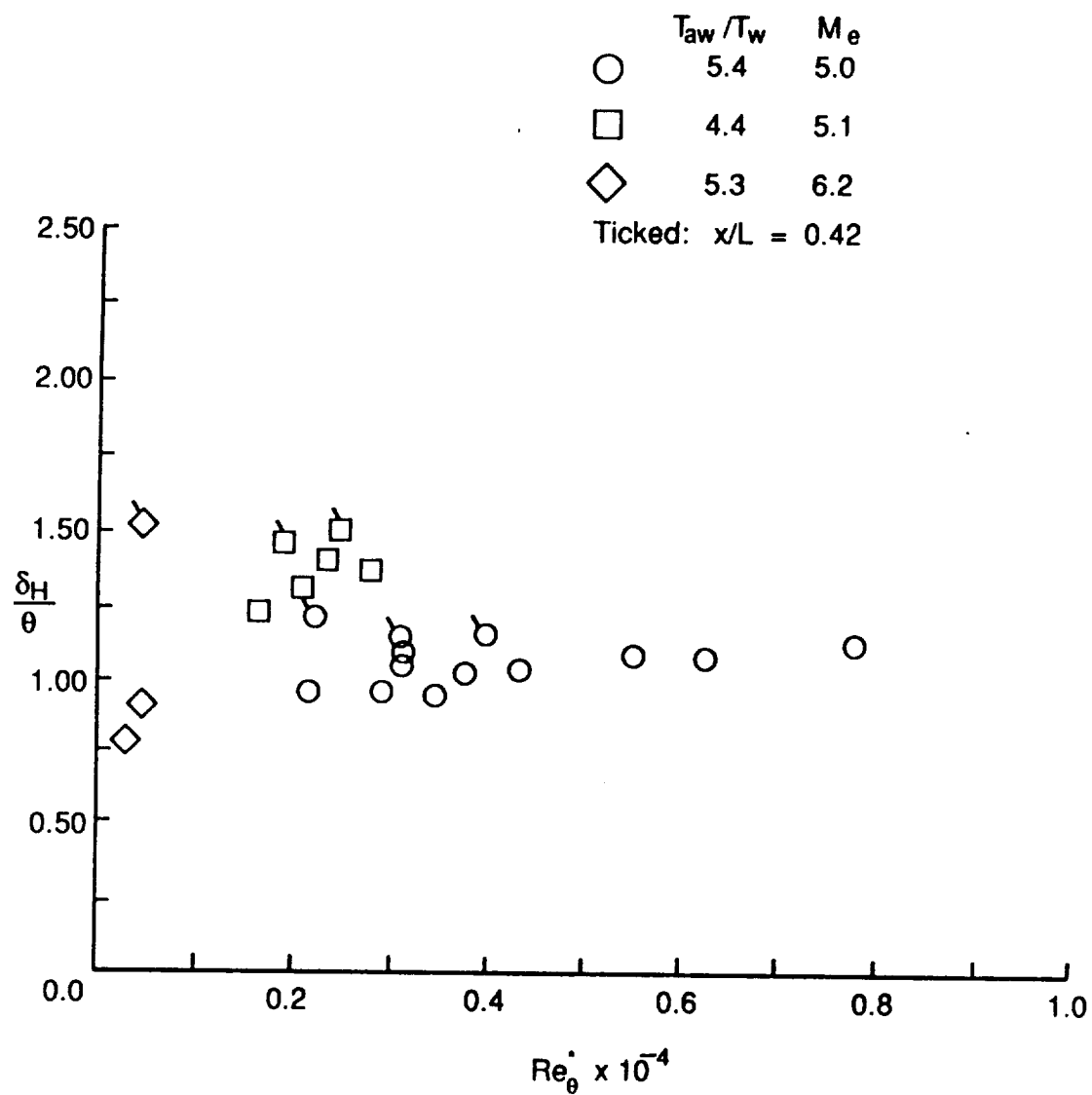


Fig. 59. Effect of momentum thickness Reynolds number on shape factor, δ_H/δ^* .

for all locations and test conditions. The shape factors obtained at $x/L = 0.42$ are distinguished by tick marks because of their inconsistency with those obtained between $0.51 \leq x/L \leq 0.74$. Note that the shape factor variations with momentum thickness Reynolds number are very similar to the power law exponents (Fig. 38). In Fig. 56, the shape factor δ^*/θ is uniform for $Re^*_\theta \geq 4000$. Below an Re^*_θ of 4000, all the data display scatter, similar to the power law exponents. Similar results are shown for thermal shape factor 1 (δ_H/δ^*) and for thermal shape factor 2 (δ_H/θ) in Figs. 58 and 59, respectively. Clauser's shape factor (Fig. 57) levels off to a constant value of approximately 6.8 for $Re^*_\theta \geq 4000$. Below an Re^*_θ of 4000, the Clauser shape factor distributions show less scatter than the other shape factors and a general downward trend with decreasing Re^*_θ . Overall, the data indicate that a minimum Re^*_θ of 4000 is necessary of equilibrium turbulence in the 8-foot High Temperature Tunnel.

4.3 Correlation of Test Conditions with Momentum Thickness Reynolds Number

To provide guidelines for future turbulent studies in the 8-Foot High Temperature Tunnel, the results of the preceding turbulent assessment are summarized in Figs. 60 and 61.

The effect of total pressure in the combustor on momentum thickness Reynolds number is shown for various locations on the plate in Fig. 60. The nominal temperature ratio, T_{aw}/T_w , for the data is 5.4. This corresponds to a total temperature in the combustor of 3300 °R for a nominal wall temperature of 600 °R. The data are not shown for $x/L = 0.42$ because the shape factor distributions, discussed in section 4.2, indicate that the boundary layer at this

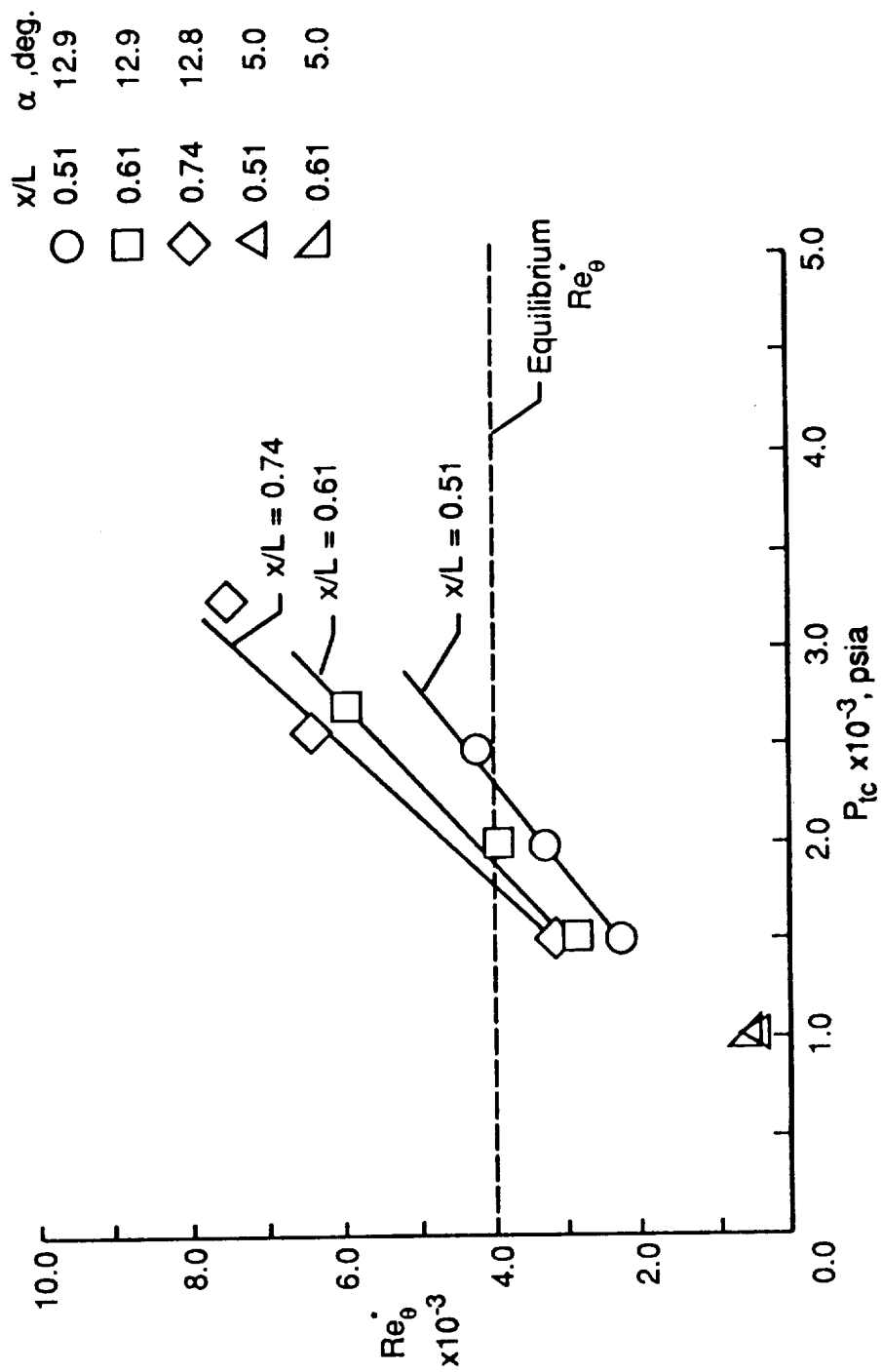


Fig. 60. Effect of total pressure in the combustor on Re_θ for various locations on the plate. ($T_{tc} = 3300^\circ R$)

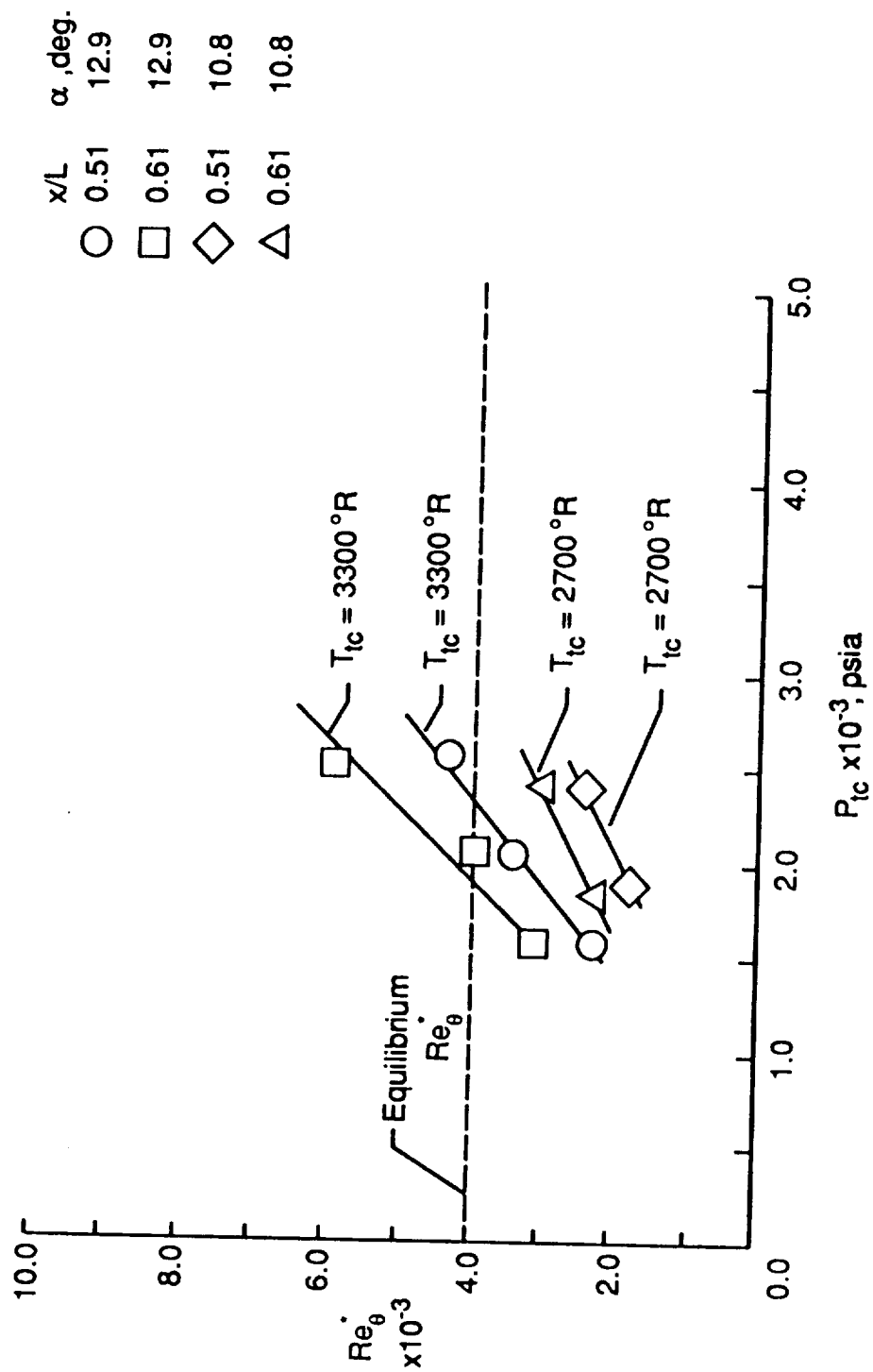


Fig. 61. Effect of total pressure in the combustor on Re_{θ} for various total temperatures.

location is not in equilibrium, possibly due to pressure gradients imposed by the test section core, as discussed in section 4.2. Also shown with the data is a dashed line corresponding to $Re^*_\theta = 4000$. This value was determined from the plots of shape factor distributions with Re^*_θ as the minimum Re^*_θ in which the boundary layer is in equilibrium. The results indicate that a minimum combustor total pressure of 2300 psia is required for equilibrium turbulence at an angle of attack of 13° and a combustor total temperature of 3300 °R. This statement is valid at least for $0.51 \leq x/L \leq 0.74$.

In Fig. 61, the effect of total pressure in the combustor on momentum thickness Reynolds number is shown for nominal combustor total temperatures of 3300 and 2700 °R. The lower temperature condition corresponds to the lower temperature ratio of 4.4 for a nominal wall temperature of 580 °R. The momentum thickness Reynolds numbers for the low temperature data are below that of the higher temperature data and the equilibrium momentum thickness Reynolds number of 4000. An extrapolation of the low temperature results indicates that a combustor total pressure of 3500 psia is required for equilibrium turbulence between x/L of 0.51 and 0.74 at the low temperature condition.

Chapter 5

CONCLUDING REMARKS

5.1 Recapitulation

This paper presents an experimental study to characterize the compressible turbulent boundary layer produced along a flat plate in the NASA Langley 8-foot High Temperature Tunnel and determine the test conditions necessary to achieve equilibrium turbulence. In addition, the present study extends the current data base for equilibrium compressible turbulent boundary layers over quasi-isothermal walls which are far from the adiabatic wall temperature. The measurements consist of pitot pressure, static pressure, and total temperature distributions in the boundary layer. A flat plate measuring 9.7 feet long by 4.3 feet wide was used for the study to provide a naturally turbulent boundary layer which was suitably thick for probing. In addition, surface measurements consisting of heat transfer and pressure distributions were obtained. Skin friction measurements were attempted; however, the signal conditioner used with the skin friction balance failed and could not be repaired prior to a major facility shutdown for modifications. The tests were conducted at a nominal free-stream Mach number of 6.5, total temperatures of 2700 and 3300 °R, and angles of attack of 5 and 13 degrees. The corresponding nominal boundary-layer edge Mach numbers were 6.2 and 5.0. The nominal ratios of adiabatic wall temperature to cold wall

temperature were 4.4 and 5.4 and the momentum thickness Reynolds numbers at the boundary-layer probe locations ranged from 400 to 7800.

5.2 Conclusions

The results of this study indicate that a momentum thickness Reynolds number of at least 4000 is required to obtain an equilibrium turbulent boundary layer along a flat plate in the Langley 8-foot High Temperature Tunnel. This statement is valid for normalized distances from the leading edge between 0.51 and 0.74. The boundary-layer measurements obtained at a normalized distance of 0.42 indicate that the boundary layer is not in equilibrium, up to a momentum thickness Reynolds number of 4000, the maximum value obtained at this location. However, spanwise pressure distributions obtained at a nearby location ($x/L = 0.46$) indicate pressure gradients were present which may have adversely affected the boundary layer at this location. The assessment of equilibrium turbulence is based primarily on the behavior of shape factors calculated from the velocity and density distributions inferred from the pressure and temperature measurements in the boundary layer. These results are generally supported by comparisons made with the standard incompressible velocity distributions of Coles [6] using the compressible transformation of van Driest [17].

The results indicate that for a combustor total temperature of 3300 °R and a model angle of attack of 13°, a minimum combustor total pressure of 2300 psia is required to achieve equilibrium turbulence over a normalized distance between 0.51 and 0.74. The results also indicate that higher combustor total pressures are needed to obtain equilibrium turbulence at

lower combustor total temperatures and lower model angles of attack. The results obtained at a total temperature of 2700 °R, indicate that a minimum combustor total pressure of 3500 psia is necessary to achieve equilibrium turbulence for normalized distances between 0.51 and 0.74. There was not enough information obtained at an angle of attack of 5 degrees to determine the minimum tunnel operation conditions required equilibrium turbulence. However, assessing equilibrium turbulence at lower angles of attack may be of future interest because the surface pressure distributions obtained at an angle of attack of 5 degrees were more uniform than those obtained at 13 degrees.

5.3 Recommendations

The present study has answered many questions concerning the behavior of a turbulent boundary layer in the Langley 8-foot High Temperature Tunnel, but has raised other questions. Based on this study, the following recommendations are made:

(1) Because the surface pressure distributions are more uniform at an angle of attack of 5 degrees than at 13 degrees, a future study is proposed to assess equilibrium turbulence at an angle of attack of 5 degrees. In addition, spanwise boundary-layer variations should be assessed at local unit Reynolds numbers greater than 0.69×10^6 /ft for angles of attack of 5 and 13 degrees.

(2) The modifications to the 8-foot High Temperature Tunnel mentioned in section 4.2 include an alternate free-stream Mach number capability. To

extend the present data base, equilibrium turbulence should also be assessed at the alternate Mach numbers.

(3) To avoid the pitot probe interference problems encountered during the present investigation, it is proposed that an evaluation study be conducted using two separate rakes with the probes spaced further apart and the probe heights staggered between the rakes.

(4) Although the total temperature measurements measured outside the boundary layer agreed well with the measurements obtained in the combustor, an accurate means of calibrating total temperature probes should be pursued for future studies.

REFERENCES

1. Holden, M. S.: "A Review of Aerothermal Problems Associated with Hypersonic Flight," AIAA Paper No. 86-0267, January 1986.
2. Graves, R., Jr.; and Hunt, J. L.: "NASA's Hypersonic Fluid and Thermal Physics Programs," AIAA Paper No. 85-0922, June 1985.
3. Settles, G. S.; and Dolling, D. S.: "Swept Shock Wave/Boundary-Layer Interactions," *Progress in Astronautics and Aeronautics*, Vol. 104, 1986, pp. 297-379.
4. Schlichting, H.: *Boundary Layer Theory*, seventh edition, McGraw- Hill Book Company, 1979, pp. 354, 659-660, 680.
5. Clauser, F. H.: "Turbulent Boundary Layers in Adverse Pressure Gradients," *Journal of the Aeronautical Sciences*, Vol. 21, 1954, pp. 91-108.
6. Coles, D. E.: "The Law of the Wake in the Turbulent Boundary Layer," *Journal of Fluid Mechanics*, Vol. 1, part 2, July 1956.
7. Coles, D. E.; and Hirst, E. A., editors.: "Computation of Turbulent Boundary Layers - 1968 AFOSR-IFP-Stanford Conference," Volume II, Compiled Data, Stanford University, August 1968.
8. Kline, S. J.; Morkovin, M. V.; Sovran, G.; and Cockrell, D. J, editors.: "Computation of Turbulent Boundary Layers - 1968 AFOSR-IFP-Stanford Conference," Volume I, Methods, Predictions, Evaluation and Flow Structure, Stanford University, August 1968.
9. White, F. M.: *Viscous Fluid Flow*, McGraw-Hill, Inc., 1974, pp. 480-481.
10. Fernholz, H. H.; and Finley, P. J.: "A Critical Compilation of Compressible Turbulent Boundary Layer Data," AGARD-AG-223, June 1977.
11. Fernholz, H. H.; and Finley, P. J.: "A Critical Commentary on Mean Flow Data for Two-Dimensional Compressible Turbulent Boundary Layers," AGARD-AG-253, May 1980.
12. Holden, M. S.: "An Experimental Investigation of Turbulent Boundary Layers at High Mach Numbers and Reynolds Numbers," CAL Report No. AB-5072-A-1, Cornell Aeronautical Laboratory, Inc., November 1972.

13. Holloway, P. F.; and Sterrett, J. R.: "Effect of Controlled Surface Roughness on Boundary-Layer Transition and Heat Transfer at Mach Numbers of 4.8 and 6.0," NASA TN D-2054, 1964.
14. Morrisette, E. L.; Stone, D. R.; and Cary, A. M.: "Downstream Effects of Boundary Layer Trips in Hypersonic Flow," *Proceedings of the Langley Symposium on Compressible Turbulent Boundary Layers*, NASA SP 216, December 1968.
15. Morkovin, M. V.; and Kline, S. L.: "Calculation of Incompressible Turbulent Boundary Layers - A Review of the AFOSR-IFP- Stanford Conference," *Proceedings of the Langley Symposium on Compressible Turbulent Boundary Layers*, NASA SP 216, December 1968.
16. Fernholz, H. H.; and Finley, P. J.: "A Further Compilation of Compressible Boundary Layer Data with a Survey of Turbulence Data," AGARD-AG-263, November 1981.
17. van Driest, E. R.: "Turbulent Boundary Layer in Compressible Fluids," *Journal of the Aeronautical Sciences*, Vol. 18, No. 5, 1951, pp. 145-160.
18. Bertram, M. H. and Neal, L., Jr.: "Recent Experiments in Hypersonic Turbulent Boundary Layers," Presented at the AGARD Specialists Meeting on Recent Developments in Boundary-Layer Research, Naples, Italy, AGARDograph 97, May 10-14, 1965.
19. Maise, G.; and McDonald, H.: "Mixing Length and Kinematic Eddy Viscosity in a Compressible Boundary Layer," *AIAA Journal*, Vol. 6, No. 1, January 1968.
20. Bradshaw, P.; and Ferris, D. H.: "Calculation of Boundary Layer Development Using the Turbulent Energy Equation: Compressible Flow on Adiabatic Walls," *Journal of Fluid Mechanics*, Vol. 46, 1971, pp. 83-110.
21. Morkovin, M. V.: "Effects of Compressibility on Turbulent Flows," Colloques Int. CNRS No. 108, *Mecanique de la turbulence*, Marseille, 1962, pp. 367-380.
22. Crocco, L.: "Sulla trasmissione del calore da una lamina piana a un fluido scorrente ad alta velocita," *L'Aerotecnica*, Vol. 12, 1932, pp. 181-197.
23. Busemann, A.: "Gasstromung mit laminarer Grenzschicht entlang einer Platte," *Zeitschrift fur Angewandte Mathematik und Mechanik*, Vol. 15, 1935, pp. 23-25.
24. Sandborn, V. A.: "A Review of Turbulence Measurements in Compressible Flow," NASA TM X-62 337, 1974.

25. Klebanoff, P. S.: "Characteristics of Turbulence in a Boundary Layer with Zero Pressure Gradient," NACA Rep. 1247, 1955.
26. Watson, R. D.: "Characteristics of Mach 10 Transitional and Turbulent Boundary Layers," NASA TP-1243, 1978.
27. Sinclair, A. R.; and Robins, A. W.: "A Method for the Determination of the Time Lag in Pressure Measuring Systems Incorporating Capillaries," NACA TN 2793, September 1952.
28. Keener, E. R.; and Hopkins, E. J.: "Accuracy of Pitot Pressure Rakes for Turbulent Boundary Layer Measurements in Supersonic Flow," NASA TN D-6229, March 1971.
29. Behrens, W.: "Viscous Interaction Effects on a Static Pressure Probe at $M = 6$," *AIAA Journal*, Vol. 1, No. 12, December 1963, pp. 2864-2866.
30. Ames Research Staff: "Equations, Tables, and Charts for Compressible Flow," NACA Report 1135, 1953.
31. Nowak, R. J.; Albertson, C. W.; and Hunt, L. R.: "Aerothermal Tests of a 12.5 Degree Cone at Mach 6.7 for Various Reynolds Numbers, Angles of Attack, and Nose Shapes," NASA TP-2345, January 1985.
32. Marlowe, M. E.; Moore, R. A.; and Whetstone, W. D.: "Spar Thermal Analysis Processors Reference Manual, System Level 16," NASA CR-159162, October 1979.
33. Leyhe, E. W.; and Howell, R. R.: "Calculation Procedure for Thermodynamic, Transport, and Flow Properties of the Combustion Products of a Hydrocarbon Fuel Mixture Burned in Air with Results for Ethylene-Air and Methane-Air Mixtures," NASA TN D-914, January 1962.
34. Bushnell, D. M.; Cary, A. M.; and Harris, J. E.: "Calculation Methods for Compressible Turbulent Boundary Layers - 1976," NASA SP-422, 1977.
35. Bushnell, D. M.; Johnson, C. B.; Harvey, W. D.; and Feller, W. V.: "Comparison of Prediction Methods and Studies of Relaxation in Hypersonic Turbulent Nozzle-Wall Boundary Layers," NASA TN D-5433, September, 1969.
36. Bertram, M. H.; and Blackstock, T. A.: "Some Simple Solutions to the Problem of Predicting Boundary-Layer Self-Induced Pressures," NASA TN D-798, April 1961.

37. Eckert, E. R. G.: "Engineering Relations for Heat Transfer and Friction in High-Velocity Laminar and Turbulent Boundary-Layer Flow Over Surfaces With Constant Pressure and Temperature," *Transactions of the ASME*, Vol. 78, No. 6, August 1956, pp. 1273-1283.
38. Kays, W. M.; and Crawford, M. E.: *Convective Heat and Mass Transfer*, McGraw-Hill, Inc., 1980, pp. 138, 213.
39. Hopkins, E. J.; Keener, E. R.; Polek, T. E.; and Dwyer, H. A.: "Hypersonic Turbulent Skin-Friction and Boundary-Layer Profiles on Nonadiabatic Flat Plates," *AIAA Journal*, Vol. 10, No. 12, January 1972, pp. 40-48.
40. Fenter, F. W.: "A New Analytical Method for the Prediction of Turbulent Boundary Layer Characteristics on a Thermally-Insulated Flat Plate at Supersonic Speeds," Report DRL-343, CF-2095, Defense Research Lab, University of Texas, June 1954.
41. Roark, R. J.: *Formulas for Stress and Strain*, McGraw-Hill Book Company, Inc., c. 1954.
42. Winkler, E. M.: "Stagnation Temperature Probes for Use at High Supersonic Speeds and Elevated Temperatures," NAVORD Report 3834, October, 1954.
43. Keener, E. R.; and Hopkins, E. J.: "Turbulent Boundary-Layer Velocity Profiles on a Nonadiabatic Flat Plate at Mach Number 6.5," NASA TN D-6907, August, 1972.

APPENDIX A

MODEL THERMAL DISTORTION ESTIMATES

Thermal distortion of the model was minimized to an extent by the sliding attachments which allowed for in-plane thermal expansion. However, because the convective heat load to the upper surface of the plate produced a temperature difference between the upper and lower surfaces, some thermal distortion to the plate was present. A worst case thermal distortion estimate was obtained using the highest measured heat load of 38.5 Btu/ft²-s. Additionally, it was assumed that the plate was unrestrained, the temperature over the upper and lower surfaces was uniform, and the temperature difference, ΔT , between the two surfaces was linear. Under these conditions, the plate should assume a spherical shape of radius R (See Fig. 62.), as discussed by Roark [41]. The equation for this radius is:

$$R = t / (\Delta T E) \quad (21)$$

For Nickel 200, the thermal expansion coefficient, E , is 7.4×10^{-6} in/in °R and the plate thickness, t , was 0.375 inches. The temperature difference between the upper and lower surfaces was obtained by using the finite element thermal analysis program discussed in Ref. 32. For the maximum measured heating condition of $q_w = 38.5$ Btu/ft² sec., the maximum ΔT calculated was 23°R. This resulted in a maximum bowing radius of 1320 in.

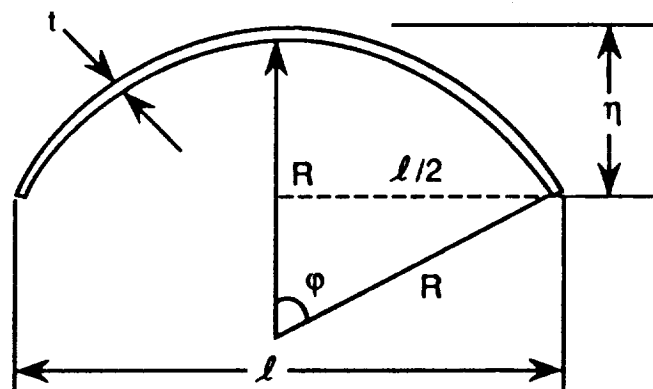


Fig. 62. Thermal bowing illustration.

The maximum bowing height, η , was then calculated as follows:

$$\eta = R (1. - \cos \varphi) \quad (22)$$

where:

$$\cos \varphi = (R - \eta) / R \quad (23)$$

and:

$$\varphi = \sin (0.5 \ell \cdot R) \quad (24)$$

For $\ell = 15.4$ inches, the maximum distance between attachments, the plate should bow no more than 0.014 inches. This is a conservative estimate because the plate was restrained by the attachments normal to the surface.

APPENDIX B

SURFACE ROUGHNESS CALCULATIONS

For a hydraulically smooth wall, in which the roughness height, r , is contained within the laminar sublayer of a turbulent boundary layer, Schlichting [4] gives:

$$r \leq 100/Re^* \quad (25)$$

Here Re^* is a unit Reynolds number defined as:

$$Re^* = U_e / \nu^* \quad (26)$$

The $*$ denotes that the property was evaluated at a temperature corresponding to Eckert's reference enthalpy, as discussed in section 3.2.

The worst case, or smallest r , corresponds to the largest unit Reynolds number. Prior to model fabrication, this was estimated to be 778μ inches, which is on the order of rough sandpaper. This is well above the surface smoothness of the plate (32μ inches). Therefore the plate smoothness was well within the criteria given by Schlichting for a hydraulically smooth wall.

APPENDIX C

BOUNDARY-LAYER THERMAL DISTORTION ESTIMATES

Because the thermal properties of chromel and nickel are different, the wall temperature along the surface of the plate was not constant. As illustrated in Fig. 63, this will produce an inflection in the thermal boundary layer which dissipates as the boundary layer propagates downstream. To evaluate this effect on the boundary layer, one can run a boundary-layer code to determine how far downstream the resulting thermal inflection travels prior to dissipating. This requires selecting a code which incorporates the thermal and transport properties of methane-air combustion products as well as an appropriate turbulence model. A much simpler method is to examine the effect of the temperature discontinuity on the surface heating rates. This method is outlined in Kayes and Crawford [38] in which the surface heating rate is given as:

$$q_w = \sum_{i=1}^n h(\epsilon_i, x) \Delta T_{w,i} \quad (27)$$

In Eq. (27), n is the number of temperature jumps, h is the heat transfer coefficient, x is the location of the temperature jump, and ϵ_i is the distance between the leading edge, or virtual origin, and the temperature jump. A worst case wall temperature jump corresponds to the highest heat load exposure for the model. Using the highest measured heat load of 38.5 Btu/ft²s, the finite element thermal analysis program mentioned in Appendix A and described in Ref. 32 was used to obtain temperature-time histories for both the nickel and

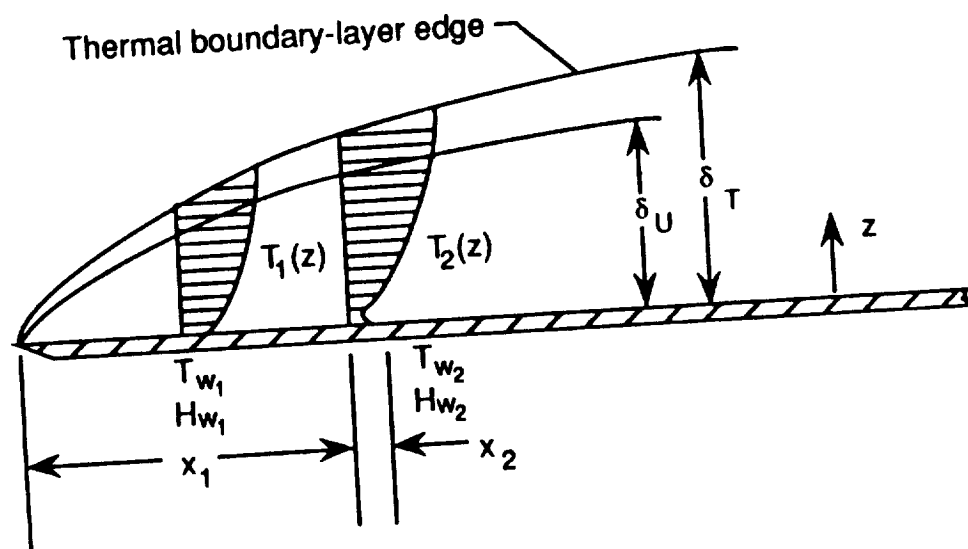


Fig. 63. Illustration of boundary-layer thermal distortion due to wall temperature discontinuity.

chromel. The wall temperatures were selected after two seconds, yielding a conservative estimate because the heating rate data for the model were typically obtained within 1.0 to 2.0 seconds of exposure. The highest heat load is produced by a turbulent boundary layer, for which q_w is given as:

$$q_w = 0.0287 U_e (x - x_v)^{-0.2} \sum_{i=1}^n \{ (\Delta H)_i Pr_i^*^{-0.4} Re_i^*^{-0.2} [1 - (\frac{\epsilon_i}{x - x_v})^{0.9}]^{-1/9} \} \quad (28)$$

In Eq. (28), ΔH is the difference in total enthalpy. Using the thermocouple location closest to the leading edge, where the maximum heating occurs, and expanding Eq. (28) gives:

$$q_w = 0.0287 U_e (x - x_v)^{-0.2} \{ \{ Pr_1^*^{-0.4} Re_1^*^{-0.2} (H_{aw} - H_{w1}) \{ 1 - [\epsilon_1 / (x - x_v)]^{0.9} \}^{-1/9} \\ + \{ Pr_2^*^{-0.4} Re_2^*^{-0.2} (H_{aw} - H_{w2}) \{ 1 - [\epsilon_2 / (x - x_v)]^{0.9} \}^{-1/9} \} \quad (29)$$

In Eq. (29), x_1 is the distance to the edge of the chromel plug, x_2 is the distance from the edge of the chromel plug to the centerline of the coaxial thermocouple, $\epsilon_1 = 0$, and $\epsilon_2 = x_1 - x_v$ where x_v is the distance from the leading edge to the origin of turbulence. Also the * denotes that the property was evaluated at a temperature corresponding to Eckert's reference enthalpy, as discussed in section 3.2. Solving Eq. (29) gives $q_w = 39.7 \text{ Btu/ft}^2 \text{ sec}$ and $h = .0166 \text{ Btu/ft}^2 \text{ sec } ^\circ\text{R}$.

For an all nickel plate, q_w is given as:

$$q_w = 0.0287 U_e x^{-0.2} \rho^* Pr^{*-0.4} Re^{*-0.2} (H_{aw} - H_w) \quad (30)$$

Solving Eq. (30) gives $q_w = 41.4$ Btu/ft sec and $h = .0167$ Btu/ft² sec °R. The resulting error in h is approximately 0.6%. Therefore, any wall temperature discontinuity is estimated to have a minimal effect on the boundary layer and resulting measurements.

APPENDIX D

SURFACE HEATING RATE ERROR ESTIMATES

As discussed in section 2.3, the heat transfer data were calculated from the measured surface temperatures using a finite difference program which models a one-dimensional, semi-infinite slab with temperature dependent properties. However, because of the finite thickness of the chromel plugs, a temperature gradient will exist on the surface exposed to the interior of the panel holder. Also circumferential conduction errors will exist, even though a polyester insulation was used between the chromel and nickel. This circumferential conduction error results from temperature gradients produced by thermal property differences between the two metals, as illustrated in Fig. 64. Because the diffusivity of nickel is higher than that of chromel, the surface of the nickel remains cooler than the chromel and the chromel will lose heat to the nickel near the surface. At some depth below the surface, the heat flow will reverse direction, again because of the difference in diffusivity between the two metals.

To estimate the errors in the heating rate data, an axisymmetric section of a chromel plug and the surrounding nickel were modeled using the finite element program discussed in Ref. 32. The insulation was not included in the thermal model due to the small elements necessary to represent the temperature gradient across the 0.002 inch thick film. These small elements require very small time steps to obtain a stable solution. The temperature history at the thermocouple location was calculated by the finite element program using the maximum measured heating rate of 38.5 Btu/ft-sec. This

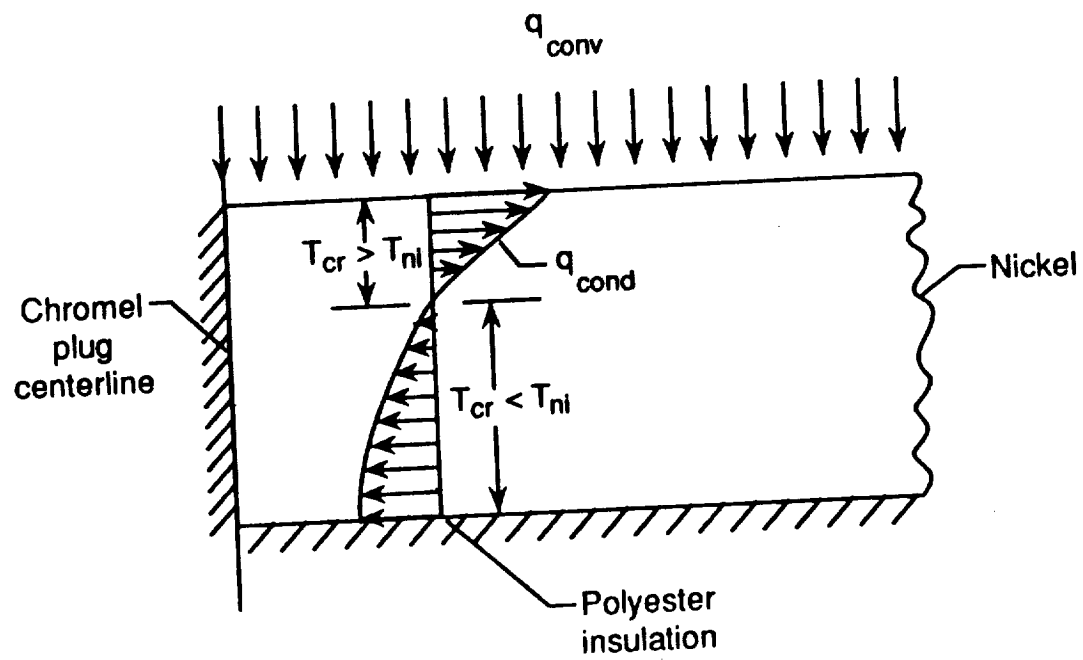


Fig. 64. Illustration of heat transfer between a chromel plug and the surrounding nickel.

temperature history was then converted to heating rates using the semi-infinite slab program described in section 2.3. The calculated heating rate was 6.5% below the applied convective heating rate. The actual conduction errors in the bulk of the heating rate data are much less because the chromel was insulated and the applied heat load to the thermal model represents a worse case situation.

To bracket the conduction error, a second thermal model was constructed in which the heat transfer was assumed to be one-dimensional, representing perfect insulation between the chromel and nickel. The calculated heating rate, obtained under the same maximum heat load and at the same time of 2 seconds, was only 0.3% below the applied convective heat load. Because of the uncertainty in the actual conduction error and because the error is believed to be much less than the 6.5% calculated for the uninsulated case, the data were not corrected for conduction errors.

The radiation leaving the surface was estimated using the maximum measured temperature of 690 °R, obtained after two seconds exposure, and using the following equation:

$$q_w = \sigma e \tau_{w-p} (T_w^4 - T_p^4) \quad (31)$$

In Eq. (31), σ is the Stefan-Boltzmann constant, τ_{w-p} is the radiation view factor, and e is the emissivity. A view factor of 1.0, representing a plate radiating to space, was used in the calculation. The emissivity was 0.053, representing polished nickel. (Chromel is 90% nickel.) The plate was assumed to be radiating to the test section pod wall which was estimated to be at 540 °R. The resulting radiation heat loss was 3.73×10^{-3} Btu/ft² sec, which represents less

than 0.01% of the convective heating to the plate. Therefore, there was no need to correct the data for radiation losses.

APPENDIX E

TOTAL TEMPERATURE PROBE ERROR ESTIMATES

In Ref. 42, Winkler showed that the recovery factor for a total temperature probe, $(T_{ti} - T_e)/(T_t - T_e)$, correlates with a parameter based on the Nusselt number of the flow inside the probe. This parameter, given as $p_{t2} \times T_t^{-1.75}$, was shown to be independent of Mach number. Winkler's correlation was later used by Keener and Hopkins [43] to calibrate their total temperature probes from measurements outside the boundary layer assuming that the upstream reservoir temperature is the correct temperature. This correlation method was used for the present data and the results are shown in Fig. 65. Note that the recovery factors obtained with the rakes located at $y/W = -0.20$ are consistently lower than those obtained at the centerline at $y/W = 0.00$ and off the centerline at $y/W = 0.20$. This indicates that the core is probably cooler at $y/W = -0.20$. Free-stream total temperature measurements made across the height of 8' HTT test core indicate variations in total temperature, as discussed in Appendix F. Unfortunately, spanwise distributions of total temperature are not available. Therefore the total temperature at the probe location can not be accurately inferred from the combustor and free-stream measurements. For this reason, the total temperatures measured through the boundary layer were not corrected to the combustor total temperature. However, the recovery factors are high and range from 0.94 to 1.03. The resulting error in total temperature is estimated to be no worse than -6.0%.

$T_{tc} \text{ } ^\circ R$
(nominal)

y/W Probe type

3240

A

0.21

○

3240

A

0.00

□

3240

A

-0.20

◇

2600

-

Filled

B

Ticked

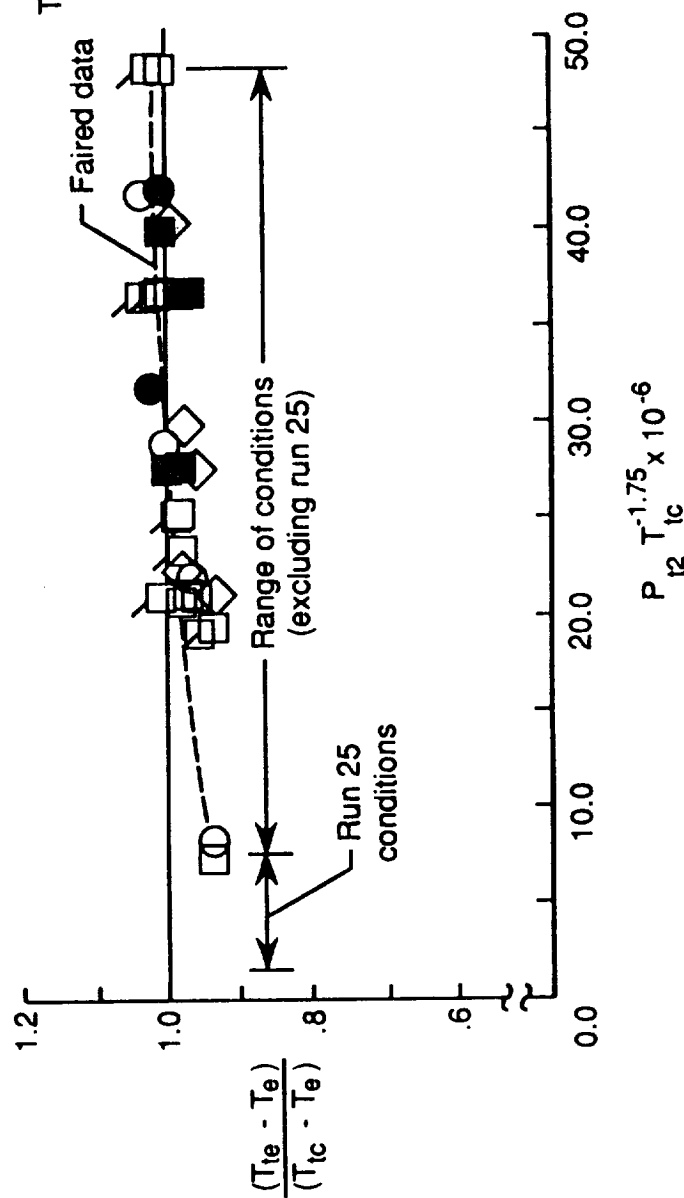


Fig. 65. Total temperature probe recovery factor correlation with total temperature measured in the combustor.

APPENDIX F

FREE-STREAM FLOW SURVEYS

Free-stream flow surveys were obtained during the present test series across the height of the test core at tunnel stations 630.0 and 703.5, as indicated in Fig. 66. (Station measurements are referenced from the nozzle throat and are in inches.) These tunnel stations correspond to $x/L = 0.0$ and 0.62 on the model. The measurements consisted of pitot pressure, static pressure and total temperature obtained at a nominal combustor total temperature of 3300°R and for nominal combustor total pressures of 1500 and 2500 psia. The resulting distributions are shown in Figs. 67 through 71. In each figure, the height of the test core, \bar{H} , is normalized by the width of the plate, W . Also indicated is the position of the model in the test core at $\alpha = 13^{\circ}$ and 5.6° . The pitot pressure normalized by combustor total pressure, p_{t2}/p_{tc} , (Fig. 67) varies not only across the height of the test core, but also from tunnel station 630.0 to station 703.5. The static pressure distributions normalized by combustor total pressure, p_1/p_{tc} , (Fig. 68) show similar trends. The ratio of static pressure to pitot pressure, p_1/p_{t2} , (Fig. 69) shows much less variation than p_{t2}/p_{tc} and p_1/p_{tc} across both the test core height and from station 630.0 to 703.5. The Mach number (Fig. 70), which tends to follow p_1/p_{t2} , also shows much less of a variation than p_{t2}/p_{tc} and p_1/p_{tc} . The ratio of total temperature measured in the test section to the total temperature measured in the combustor (Fig. 71) varies predominately across the height of the test core. The overall profile does not vary much from station 630 to 703.5.

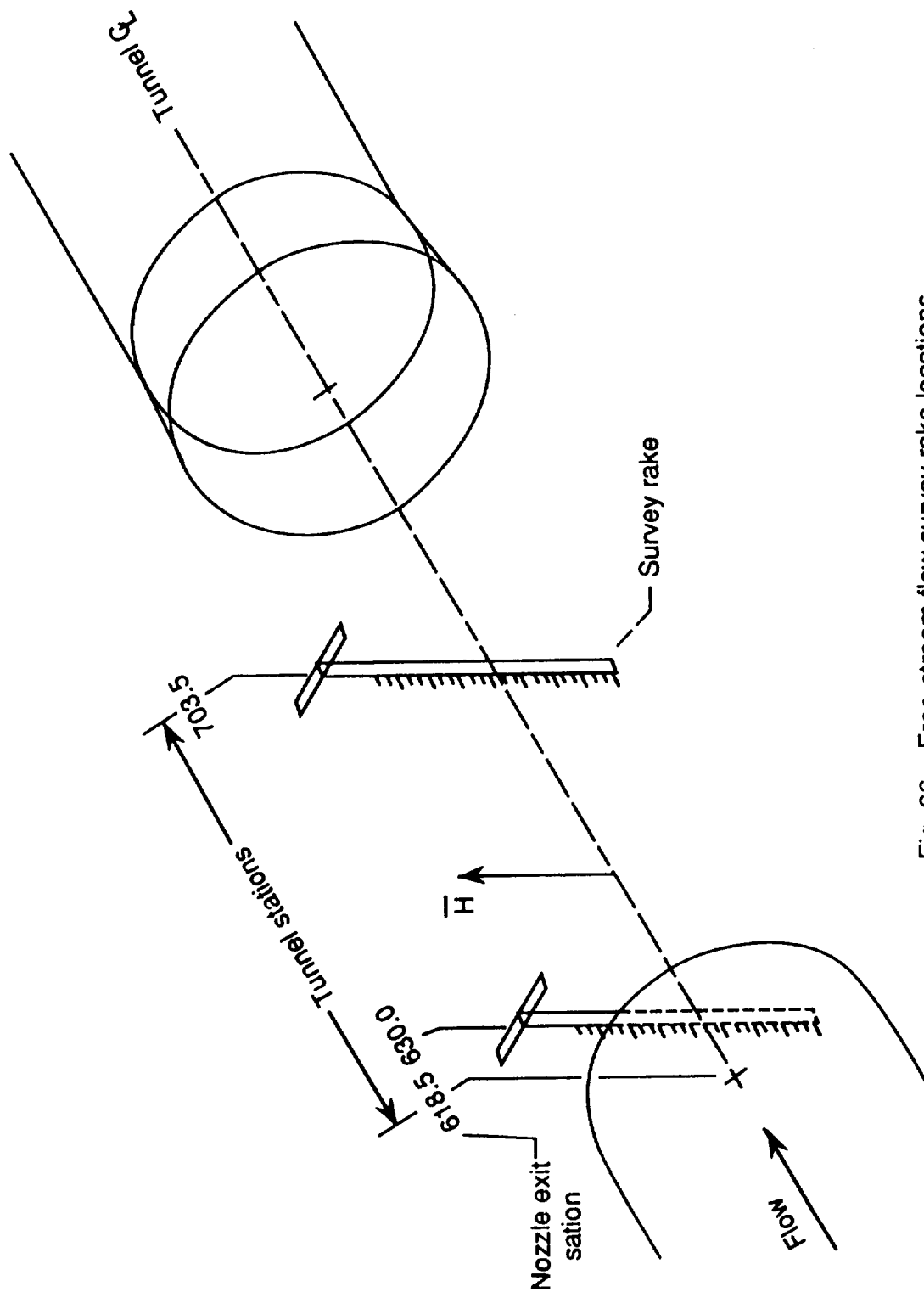
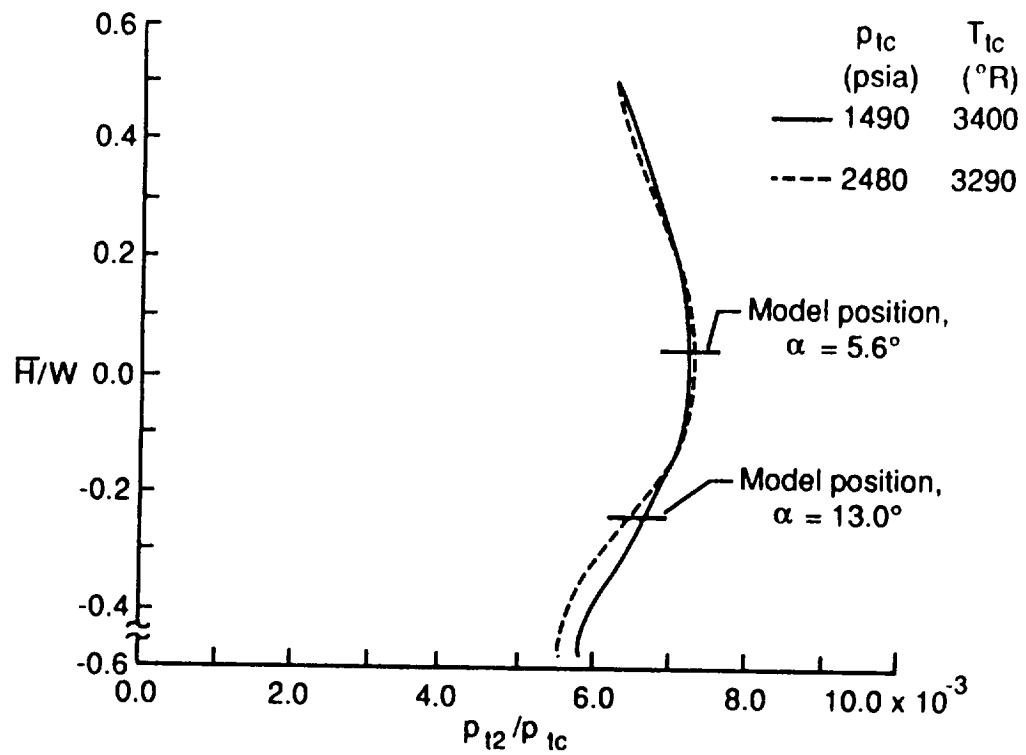
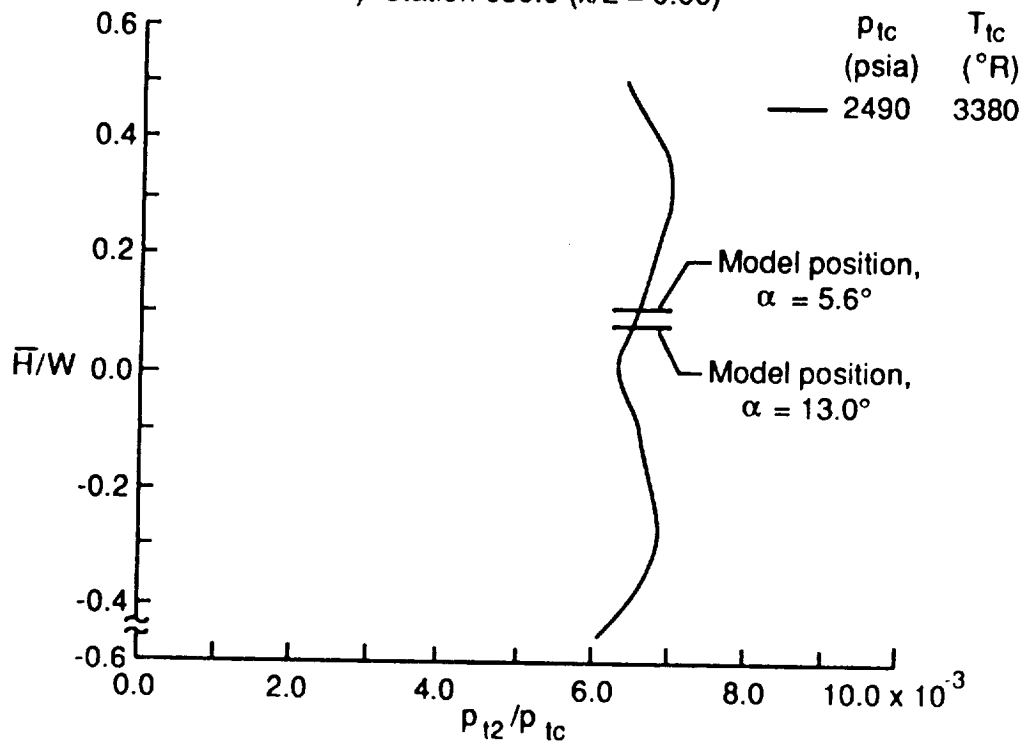


Fig. 66. Free-stream flow survey rake locations.

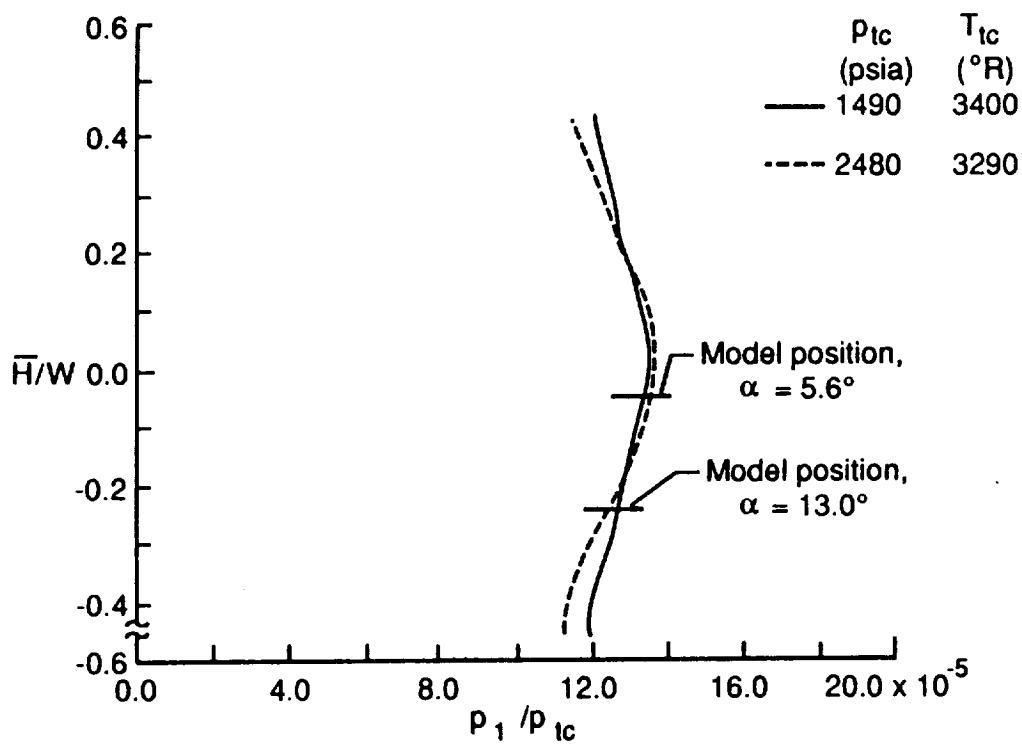


a) Station 630.0 ($x/L = 0.00$)

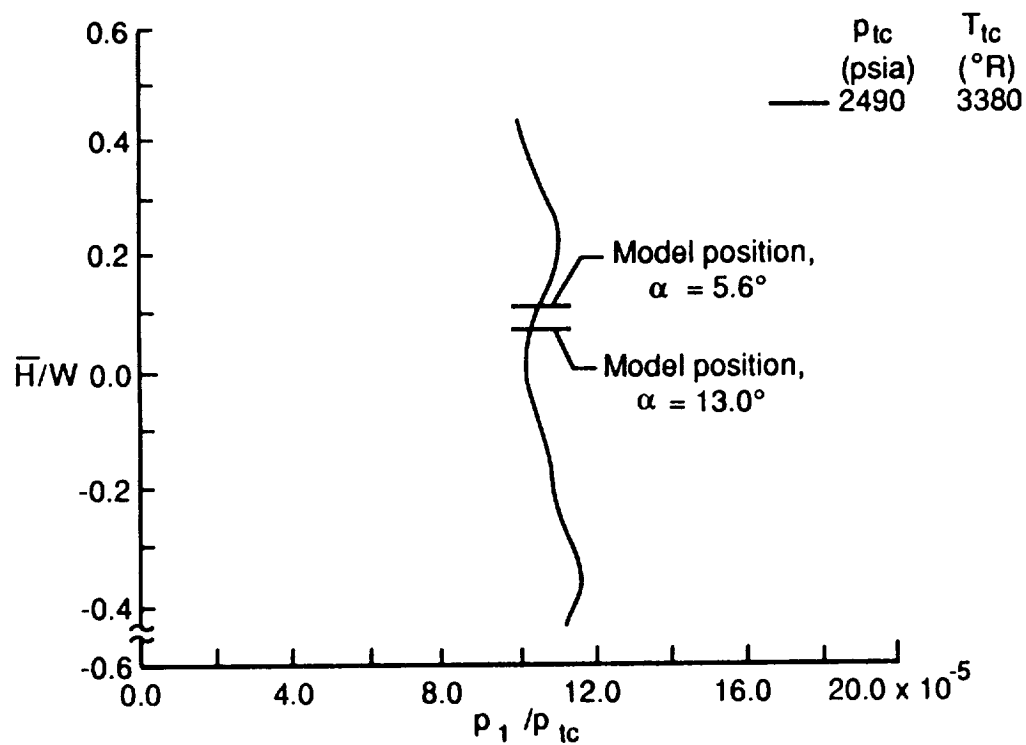


b) Station 703.5 ($x/L = 0.62$)

Fig. 67. Free-stream pitot pressure distributions normalized by combustor total pressure.

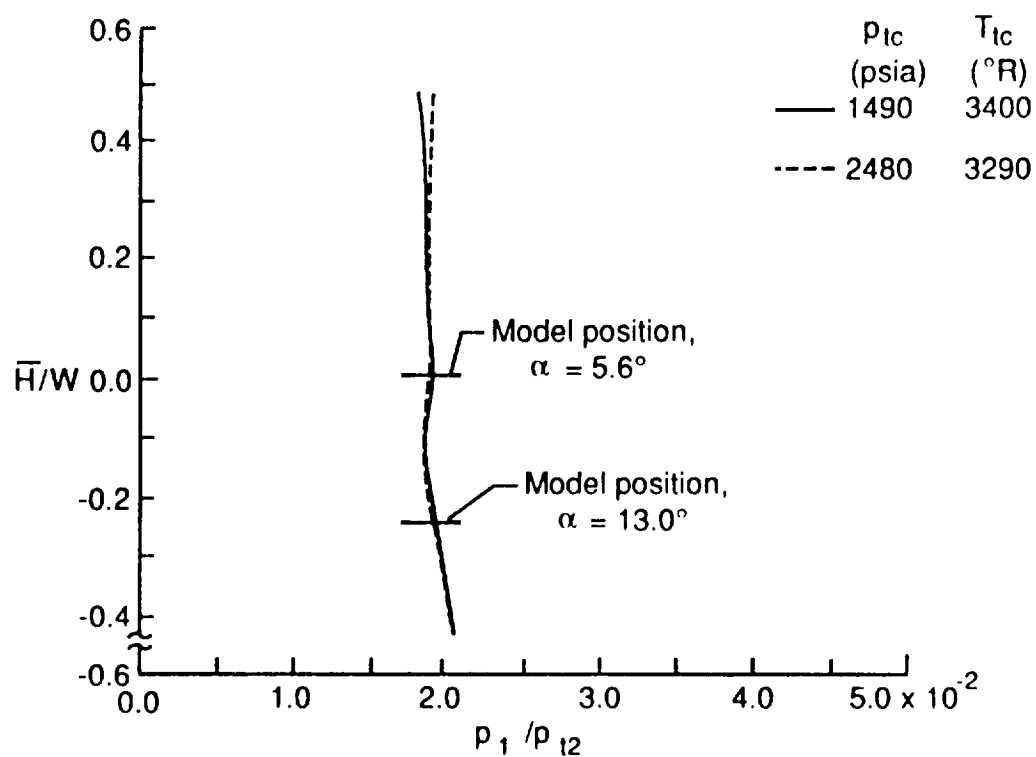


a) Station 630.0 ($x/L = 0.00$)

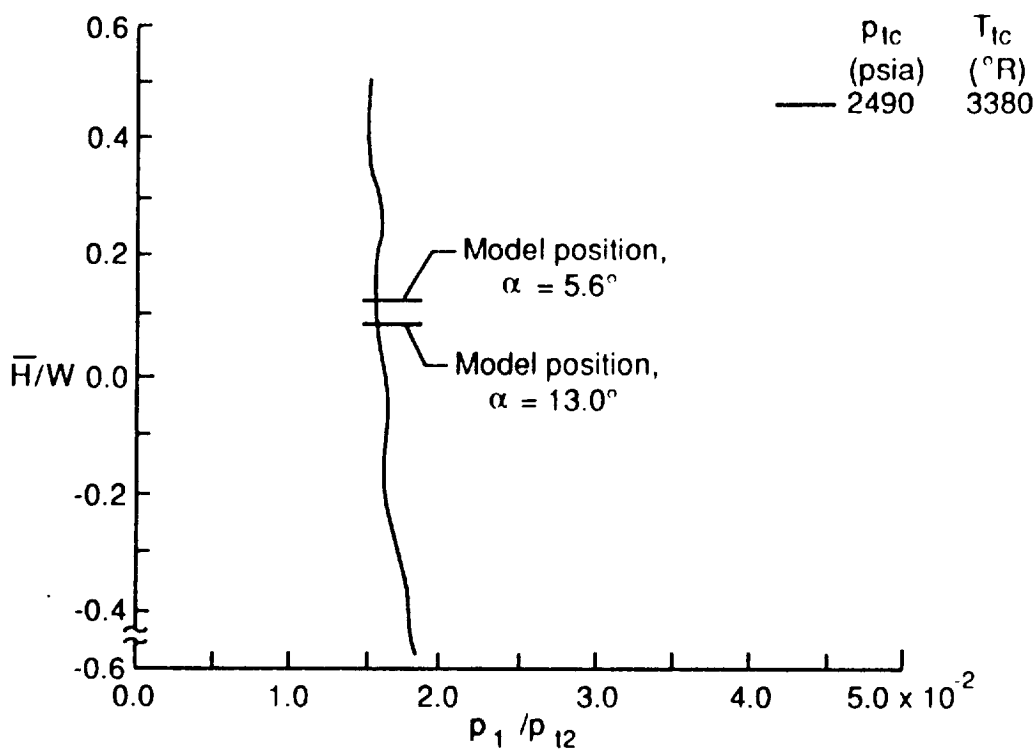


b) Station 703.5 ($x/L = 0.62$)

Fig. 68. Free-stream static pressure distributions normalized by combustor total pressure.

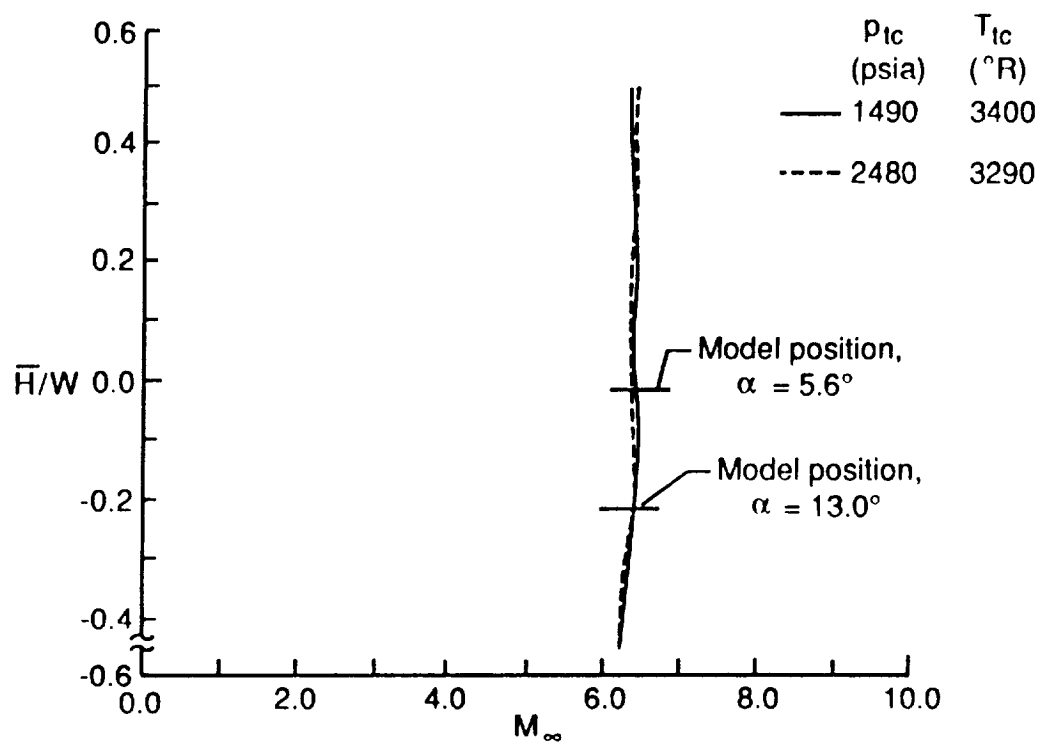


a) Station 630.0 ($x/L = 0.00$)

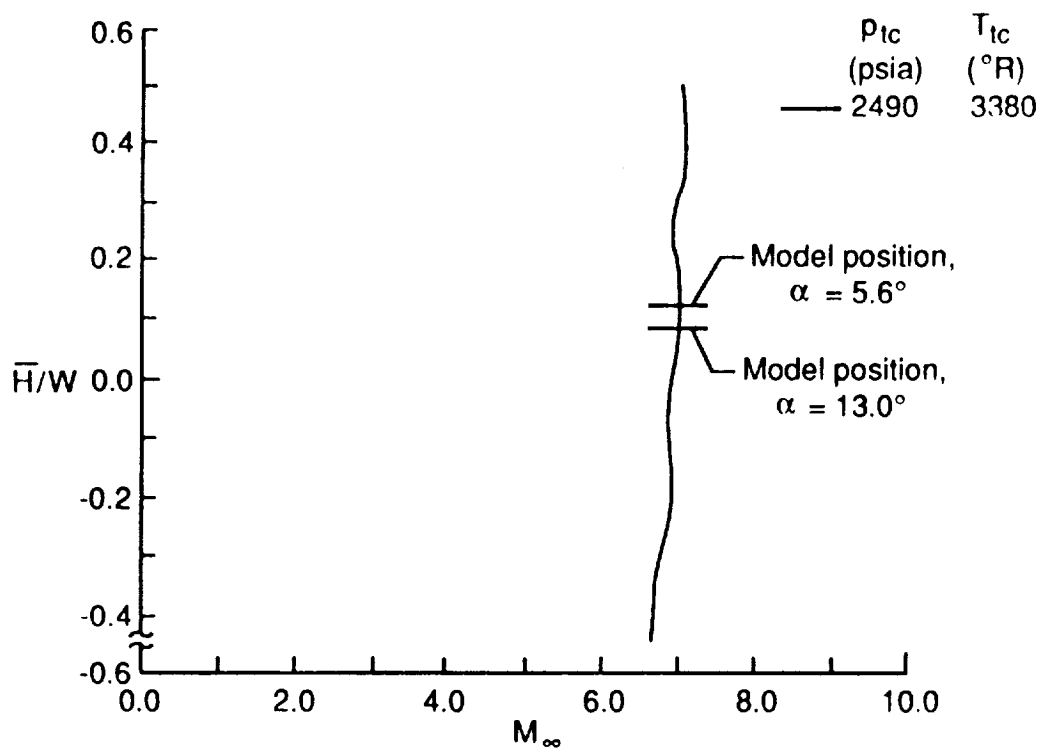


b) Station 703.5 ($x/L = 0.62$)

Fig. 69. Free-stream static pressure distributions normalized by free-stream pitot pressure.

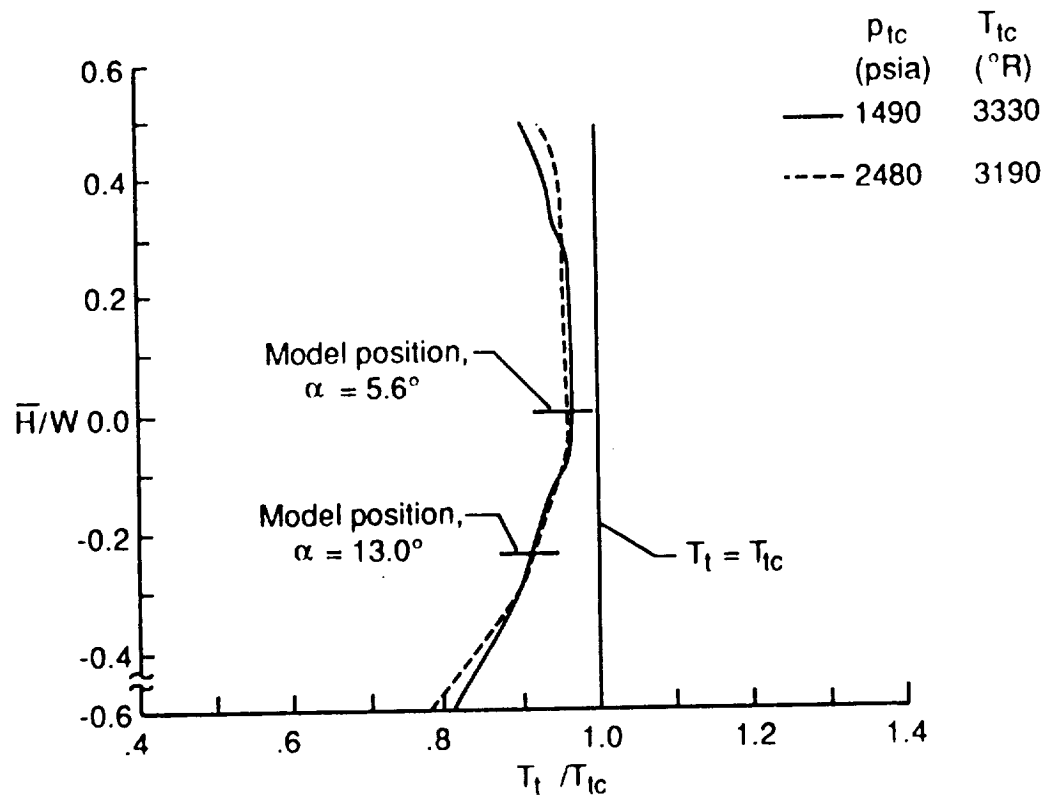


a) Station 630.0 ($x/L = 0.00$)

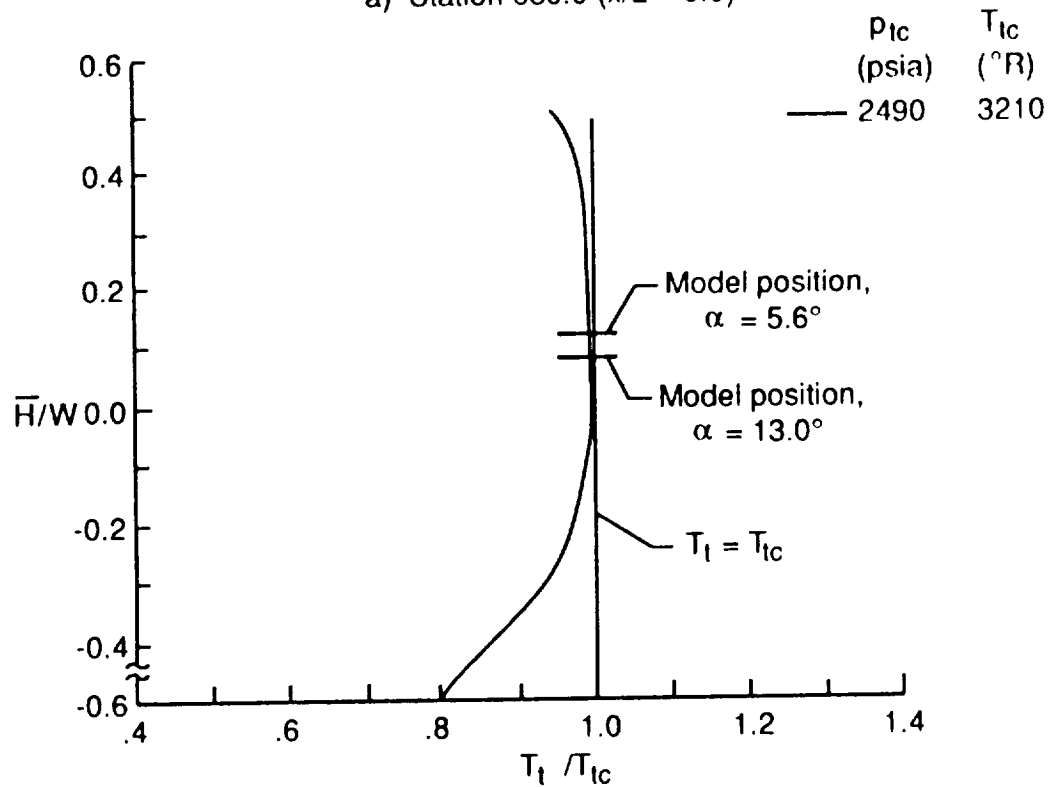


b) Station 703.5 ($x/L = 0.62$)

Fig. 70. Free-stream Mach number distributions.



a) Station 630.0 ($x/L = 0.0$)



b) Station 703.5 ($x/L = 0.62$)

Fig. 71. Free-stream total temperature distributions normalized to combustor total temperature.

APPENDIX G
SURFACE PRESSURE AND HEAT TRANSFER
DATA TABULATION

The surface pressure and heat transfer data are tabulated in this appendix by tunnel run number. The first column of the tabulated data is the gage designation for the test series, the location of which is given in Table 1. The second column of the tabulated data is the measured pressure normalized by the free-stream static pressure. The free-stream static pressure was obtained by flow surveys. The third, fourth, fifth, and sixth columns of the tabulated data are the measured wall temperature, the heat transfer rate at the measured wall temperature, the corrected heat transfer rate for a uniform wall temperature of 530 °R, and the Stanton number corresponding to the measured heat transfer rate, respectively. Stanton numbers were calculated using a turbulent recovery factor of $Pr^{1/3}$ and the thermodynamic and transport properties of methane-air combustion products given in by Leyhe and Howell [33].

RUN 6

Gage	PRESSURE ($p_{\infty} = .300$ psia)	Tw (°R)	HEAT TRANSFER Btu/ft ² -s		
	p/ p_{∞}		q[hw]	q[cw]	St*
1	5.139	634.21	25.41	26.42	.153E-02
2	5.360	629.13	24.33	25.24	.146E-02
3	5.222	618.17	21.18	21.87	.126E-02
4	5.763	645.37	29.30	30.60	.177E-02
5	5.773	640.39	28.04	29.22	.169E-02
6	5.899	663.21	32.31	34.00	.196E-02
7	5.906	624.08	23.24	24.05	.139E-02
8	5.903	634.16	25.03	26.02	.150E-02
9	5.623	616.08	20.93	21.59	.125E-02
10	5.463	619.11	21.32	22.02	.127E-02
11	5.323	612.74	20.14	20.75	.120E-02
12	5.345	613.62	20.37	21.00	.121E-02
13	6.344	650.43	30.50	31.92	.184E-02
14	5.873	640.97	26.67	27.80	.161E-02
15	5.543	603.91	18.52	19.01	.110E-02
16	6.662	649.63	30.66	32.08	.185E-02
17	-----	647.78	30.31	31.68	.183E-02
18	6.642	640.55	28.17	29.36	.170E-02
19	-----	630.15	25.32	26.28	.152E-02
20	6.016	636.28	26.13	27.19	.157E-02
21	-----	606.36	20.40	20.96	.121E-02
22	5.806	630.65	24.93	25.88	.149E-02
23	-----	617.57	21.75	22.45	.130E-02
24	5.673	645.59	27.59	28.82	.166E-02
25	-----	612.71	20.64	21.26	.123E-02
26	5.491	620.50	22.03	22.77	.131E-02
27	-----	615.99	21.13	21.80	.126E-02
28	5.325	609.23	19.81	20.38	.118E-02
29	-----	627.79	23.05	23.90	.138E-02
30	5.405	599.11	17.56	17.99	.104E-02
31	-----	602.62	18.09	18.56	.107E-02
32	5.371	616.64	21.07	21.74	.126E-02
33	-----	614.36	20.56	21.19	.122E-02
34	5.420	613.50	20.14	20.76	.120E-02
35	-----	625.29	22.05	22.83	.132E-02
36	5.470	600.33	17.91	18.36	.106E-02
37	-----	596.04	16.98	17.38	.100E-02
38	5.608	606.97	19.24	19.77	.114E-02
39	5.746	610.92	20.37	20.96	.121E-02
40	5.857	629.26	24.16	25.06	.145E-02
41	5.612	603.73	19.56	20.08	.116E-02
42	5.921	586.70	15.62	15.92	.919E-03

RUN 6

Gage	PRESSURE ($p_{\infty} = .300$ psia)		HEAT TRANSFER Btu/ft ² -s		
	p/p_{∞}	T_w (°R)	$q[hw]$	$q[cw]$	St^*
43	5.718	610.89	19.63	20.21	.117E-02
44	5.644	609.13	19.15	19.70	.114E-02
45	5.278	607.76	18.34	18.86	.109E-02
46	6.690	640.99	27.80	28.98	.167E-02
47	5.934	641.26	27.22	28.38	.164E-02
48	5.998	644.48	26.54	27.71	.160E-02
49	5.728	620.27	22.25	22.99	.133E-02
50	5.915	592.69	17.40	17.77	.103E-02
51	6.393	623.54	22.71	23.50	.136E-02
52	6.423	636.85	27.69	28.82	.166E-02
53	6.310	643.64	29.09	30.36	.175E-02
54	6.090	633.10	26.05	27.07	.156E-02
55	6.019	628.49	24.35	25.25	.146E-02
56	5.822	621.83	23.04	23.82	.138E-02
57	5.764	619.34	21.90	22.63	.131E-02
58	5.457	607.70	19.75	20.31	.117E-02
59	5.801	629.53	23.37	24.24	.140E-02
60	6.240	660.47	32.60	34.27	.198E-02
61	6.118	652.61	29.68	31.10	.180E-02
62	5.395	612.13	20.76	21.38	.123E-02
63	5.025	611.13	20.46	21.06	.122E-02

RUN 7

Gage	PRESSURE ($p_{\infty} = .299$ psia)		HEAT TRANSFER Btu/ft ² -s		
	p/p_{∞}	T_w (°R)	$q[hw]$	$q[cw]$	St^*
1	2.200	558.73	8.90	8.96	.111E-02
2	2.239	578.80	14.50	14.73	.182E-02
3	2.166	569.41	11.41	11.54	.143E-02
4	2.315	580.21	14.04	14.28	.176E-02
5	2.320	585.61	16.64	16.95	.210E-02
6	2.335	592.04	18.01	18.40	.227E-02
7	2.315	571.93	12.59	12.75	.158E-02
8	2.323	574.46	12.91	13.09	.162E-02
9	2.271	567.33	11.14	11.27	.139E-02
10	2.236	568.64	11.23	11.36	.140E-02
11	2.203	565.93	10.56	10.67	.132E-02
12	2.261	566.50	10.83	10.95	.135E-02
13	2.286	560.21	8.44	8.50	.105E-02
14	2.223	582.19	15.36	15.63	.193E-02
15	2.233	562.51	9.88	9.97	.123E-02
16	2.315	551.76	6.09	6.12	.756E-03
17	-----	556.33	7.52	7.57	.935E-03
18	3.060	561.03	8.77	8.84	.109E-02
19	-----	565.00	10.05	10.15	.125E-02
20	2.166	573.38	12.13	12.29	.152E-02
21	-----	563.36	10.83	10.93	.135E-02
22	2.164	576.16	13.62	13.82	.171E-02
23	-----	570.70	12.26	12.41	.153E-02
24	2.178	584.52	15.69	15.97	.197E-02
25	-----	568.52	12.10	12.24	.151E-02
26	2.141	571.78	12.53	12.69	.157E-02
27	-----	570.19	12.20	12.35	.153E-02
28	2.109	565.30	10.98	11.09	.137E-02
29	-----	575.14	12.73	12.91	.160E-02
30	2.151	561.19	9.89	9.98	.123E-02
31	-----	563.56	10.21	10.30	.127E-02
32	2.154	569.78	11.48	11.62	.144E-02
33	-----	568.37	11.43	11.56	.143E-02
34	2.180	567.79	10.97	11.10	.137E-02
35	-----	572.38	11.79	11.94	.148E-02
36	2.247	560.69	9.59	9.67	.120E-02
37	-----	559.18	9.08	9.15	.113E-02
38	2.305	563.17	10.41	10.50	.130E-02
39	2.321	564.52	10.85	10.95	.135E-02
40	2.329	571.35	12.66	12.82	.158E-02
41	2.246	559.62	10.67	10.75	.133E-02
42	2.389	553.01	8.13	8.17	.101E-02

RUN 7

Gage	PRESSURE ($p_{\infty} = .299$ psia)		HEAT TRANSFER Btu/ft ² -s		
	p/p_{∞}	T_w (°R)	$q[hw]$	$q[cw]$	St^*
43	2.360	564.59	10.13	10.23	.127E-02
44	2.383	565.06	11.02	11.13	.138E-02
45	2.221	564.77	9.75	9.85	.122E-02
46	2.369	551.26	6.59	6.62	.819E-03
47	2.175	583.30	16.11	16.40	.203E-02
48	2.035	581.79	14.08	14.32	.177E-02
49	2.288	568.04	11.96	12.10	.150E-02
50	2.417	555.84	9.58	9.64	.119E-02
51	2.372	549.12	5.40	5.42	.670E-03
52	2.355	564.29	11.10	11.21	.139E-02
53	2.338	584.68	16.06	16.36	.202E-02
54	2.319	576.74	14.58	14.80	.183E-02
55	2.336	574.73	14.16	14.36	.178E-02
56	2.322	570.29	11.30	11.44	.141E-02
57	2.338	567.72	11.97	12.11	.150E-02
58	2.337	563.10	11.03	11.14	.138E-02
59	2.336	550.37	5.53	5.55	.686E-03
60	2.386	587.03	17.31	17.64	.218E-02
61	2.383	585.76	16.35	16.65	.206E-02
62	2.231	562.95	11.20	11.30	.140E-02
63	2.221	565.24	11.71	11.83	.146E-02

RUN 9

Gage	PRESSURE ($p_{\infty} = .180$ psia)		HEAT TRANSFER Btu/ft ² -s		
	p/p_{∞}	T_w (°R)	$q[hw]$	$q[cw]$	St^*
1	5.321	580.34	12.62	12.84	.124E-02
2	5.547	594.51	16.85	17.23	.167E-02
3	5.013	578.57	13.19	13.40	.130E-02
4	6.064	610.38	19.28	19.85	.192E-02
5	5.876	602.04	18.30	18.78	.182E-02
6	5.832	612.42	19.93	20.54	.199E-02
7	5.772	583.17	14.84	15.11	.146E-02
8	5.734	587.85	15.31	15.61	.151E-02
9	5.494	577.04	13.01	13.21	.128E-02
10	5.269	578.44	13.27	13.48	.130E-02
11	5.074	573.49	12.36	12.53	.121E-02
12	5.085	573.24	12.48	12.65	.122E-02
13	6.060	565.85	9.14	9.24	.893E-03
14	5.808	598.71	17.42	17.85	.173E-02
15	5.426	568.79	11.56	11.70	.113E-02
16	6.193	555.45	6.65	6.69	.647E-03
17	-----	558.52	7.63	7.69	.744E-03
18	5.967	563.13	8.97	9.06	.876E-03
19	-----	568.40	10.47	10.60	.102E-02
20	5.838	580.30	12.81	13.02	.126E-02
21	-----	569.58	12.00	12.15	.118E-02
22	5.650	587.66	15.11	15.40	.149E-02
23	-----	581.08	14.02	14.26	.138E-02
24	5.588	599.84	17.58	18.02	.174E-02
25	-----	577.56	13.57	13.78	.133E-02
26	5.413	582.50	14.61	14.87	.144E-02
27	-----	579.35	14.04	14.27	.138E-02
28	5.311	573.92	13.08	13.27	.128E-02
29	-----	586.82	14.92	15.21	.147E-02
30	5.366	568.33	11.77	11.91	.115E-02
31	-----	570.11	11.67	11.81	.114E-02
32	5.304	578.40	13.52	13.73	.133E-02
33	-----	576.86	13.17	13.37	.129E-02
34	5.335	576.16	12.76	12.95	.125E-02
35	-----	583.13	13.84	14.09	.136E-02
36	5.335	566.85	11.28	11.40	.110E-02
37	-----	564.24	10.90	11.01	.106E-02
38	5.522	569.59	11.96	12.10	.117E-02
39	5.519	571.38	12.63	12.80	.124E-02
40	5.564	580.89	14.41	14.66	.142E-02
41	5.320	564.69	11.71	11.83	.114E-02
42	5.633	554.38	9.76	9.82	.949E-03

RUN 9

Gage	PRESSURE	HEAT TRANSFER			
	($p_{\infty} = .180$ psia)		Btu/ft ² -s		
	p/p_{∞}	T_w (°R)	$q[hw]$	$q[cw]$	St^*
42	5.633	552.38	9.76	9.81	.948E-03
43	5.469	569.18	11.52	11.66	.113E-02
44	5.394	568.59	11.96	12.10	.117E-02
45	5.107	567.70	10.72	10.84	.105E-02
46	6.270	555.07	7.21	7.25	.701E-03
47	5.726	596.47	16.78	17.17	.166E-02
48	1.157	592.77	16.41	16.77	.162E-02
49	5.539	574.43	12.89	13.08	.126E-02
50	5.651	556.97	10.62	10.69	.103E-02
51	6.022	551.22	6.51	6.54	.632E-03
52	6.022	563.00	9.22	9.30	.900E-03
53	5.880	600.17	18.63	19.10	.185E-02
54	5.727	586.64	15.18	15.47	.150E-02
55	5.639	581.05	14.95	15.21	.147E-02
56	5.482	576.63	12.92	13.11	.127E-02
57	5.513	573.39	13.16	13.34	.129E-02
58	5.254	563.61	11.36	11.47	.111E-02
59	5.528	554.72	7.07	7.11	.687E-03
60	5.806	604.35	18.99	19.50	.189E-02
61	5.690	595.67	16.68	17.06	.165E-02
62	5.098	566.97	12.88	13.03	.126E-02
63	4.924	565.23	11.30	11.42	.110E-02

RUN 10

Gage	PRESSURE ($p_{\infty} = .179$ psia)		HEAT TRANSFER Btu/ft ² -s		
	p/p_{∞}	T_w (°R)	$q[hw]$	$q[cw]$	St^*
4	5.742	607.81	20.39	20.94	.188E-02
5	-----	606.58	19.95	20.48	.184E-02
6	5.680	-----	-----	-----	-----
7	-----	598.60	16.33	16.71	.150E-02
8	6.742	644.24	27.95	29.13	.262E-02
9	4.433	574.79	10.38	10.52	.947E-03
10	4.862	586.21	12.37	12.59	.113E-02
11	5.027	581.89	11.42	11.61	.104E-02
15	4.915	580.16	11.09	11.27	.101E-02
16	5.891	569.76	8.21	8.31	.747E-03
18	-----	576.85	10.21	10.36	.932E-03
20	5.562	-----	-----	-----	-----
21	-----	577.17	11.14	11.30	.102E-02
25	-----	589.95	13.58	13.84	.125E-02
26	5.149	596.47	15.20	15.54	.140E-02
27	-----	595.06	14.78	15.10	.136E-02
30	7.239	576.66	9.92	10.06	.905E-03
31	-----	586.33	12.87	13.11	.118E-02
34	3.836	581.67	11.05	11.23	.101E-02
35	-----	599.39	15.64	16.01	.144E-02
38	5.581	585.90	12.68	12.91	.116E-02
39	-----	587.89	13.16	13.41	.121E-02
49	4.772	588.89	12.92	13.17	.119E-02
51	5.792	566.07	7.16	7.23	.651E-03
53	5.652	-----	-----	-----	-----
54	-----	601.05	16.84	17.24	.155E-02
55	5.157	588.59	13.28	13.53	.122E-02
56	3.778	579.11	10.35	10.51	.945E-03
57	5.564	587.71	12.95	13.19	.119E-02

RUN 11

Gage	PRESSURE ($p_{\infty} = .239$ psia)	Tw (°R)	HEAT TRANSFER Btu/ft ² -s		St*
	p/ p_{∞}		q[hw]	q[cw]	
4	1.910	578.20	6.68	6.79	.111E-02
5	-----	595.54	11.11	11.35	.186E-02
6	1.914	-----	-----	-----	-----
7	-----	589.65	10.25	10.45	.171E-02
9	1.732	567.89	5.22	5.28	.863E-03
10	1.734	577.52	7.19	7.29	.119E-02
11	1.837	577.13	7.24	7.34	.120E-02
15	1.908	577.93	7.73	7.84	.128E-02
16	1.900	563.58	4.05	4.09	.669E-03
18	-----	565.81	4.41	4.45	.728E-03
20	1.750	-----	-----	-----	-----
21	-----	573.36	6.74	6.83	.112E-02
25	-----	584.40	9.30	9.46	.155E-02
26	1.739	588.27	10.06	10.26	.168E-02
27	-----	587.82	10.02	10.21	.167E-02
30	2.360	582.38	9.25	9.40	.154E-02
31	-----	591.92	11.14	11.37	.186E-02
34	1.479	573.78	6.59	6.68	.109E-02
35	-----	577.62	7.26	7.37	.120E-02
38	2.007	579.15	7.87	8.00	.131E-02
39	-----	582.34	8.57	8.71	.142E-02
49	2.087	586.87	9.43	9.60	.157E-02
51	1.941	561.72	3.46	3.49	.571E-03
53	1.918	-----	-----	-----	-----
54	-----	593.88	11.24	11.48	.188E-02
55	2.178	597.16	12.14	12.42	.203E-02
56	1.405	571.68	6.18	6.26	.102E-02
57	1.888	580.18	7.85	7.97	.130E-02

RUN 12

Gage	PRESSURE ($p_{\infty} = .179$ psia)		HEAT TRANSFER Btu/ft ² -s		
	p/p_{∞}	T_w (°R)	$q[hw]$	$q[cw]$	St^*
4	5.717	620.37	19.68	20.31	.185E-02
5	-----	608.97	15.53	15.96	.145E-02
6	5.663	-----	-----	-----	-----
7	-----	606.83	15.23	15.63	.142E-02
8	5.622	611.56	15.88	16.34	.149E-02
9	5.384	601.88	13.48	13.82	.126E-02
10	6.728	626.43	19.07	19.74	.180E-02
11	4.235	586.75	9.85	10.03	.914E-03
15	7.317	598.93	13.06	13.37	.122E-02
16	6.114	575.13	7.05	7.15	.651E-03
18	-----	582.37	8.75	8.90	.811E-03
20	5.710	-----	-----	-----	-----
21	-----	587.70	11.32	11.53	.105E-02
25	-----	600.80	14.14	14.48	.132E-02
26	5.317	606.65	15.23	15.64	.142E-02
27	-----	605.08	14.86	15.25	.139E-02
30	5.213	596.57	13.06	13.36	.122E-02
31	-----	595.20	12.54	12.82	.117E-02
34	7.310	592.90	11.19	11.43	.104E-02
35	-----	608.69	14.61	15.01	.137E-02
38	4.293	588.68	10.44	10.64	.969E-03
39	-----	597.96	12.76	13.05	.119E-02
49	6.241	604.05	13.95	14.31	.130E-02
51	5.948	572.13	6.74	6.83	.622E-03
53	5.789	620.27	19.19	19.81	.180E-02
54	-----	611.22	16.57	17.04	.155E-02
55	5.245	595.35	12.51	12.79	.116E-02
56	4.007	588.50	10.43	10.63	.968E-03
57	5.315	598.85	12.94	13.25	.121E-02

RUN 16

Gage	PRESSURE ($p_{\infty} = .234$ psia)		HEAT TRANSFER Btu/ft ² -s		
	p/p_{∞}	T_w (°R)	$q[hw]$	$q[cw]$	St^*
4	5.829	667.11	22.45	23.56	.153E-02
5	-----	611.88	9.57	10.20	.663E-03
6	5.834	-----	-----	-----	-----
7	-----	643.47	16.53	17.19	.112E-02
8	5.813	650.99	17.05	17.79	.116E-02
9	5.739	635.26	14.40	14.93	.969E-03
10	6.988	667.69	19.75	20.73	.135E-02
11	4.296	611.37	9.86	10.12	.658E-03
15	7.573	631.00	14.03	14.52	.943E-03
16	6.466	641.90	18.60	19.33	.126E-02
18	-----	656.41	20.72	21.66	.141E-02
20	6.052	-----	-----	-----	-----
21	-----	635.32	17.31	17.95	.117E-02
25	-----	636.33	15.77	16.35	.106E-02
26	5.498	641.65	15.96	16.59	.108E-02
27	-----	638.01	15.30	15.88	.103E-02
30	5.351	627.42	13.86	14.33	.931E-03
31	-----	625.17	13.17	13.60	.883E-03
34	7.448	629.68	13.08	13.53	.879E-03
35	-----	645.80	15.00	15.62	.101E-02
38	4.394	613.08	10.37	10.66	.692E-03
39	-----	630.87	13.53	14.00	.909E-03
49	6.364	639.69	14.53	15.09	.980E-03
51	6.235	621.28	12.62	13.02	.845E-03
53	6.040	660.95	20.13	21.08	.137E-02
54	-----	648.41	17.44	18.17	.118E-02
55	5.431	629.20	14.06	14.54	.944E-03
56	4.107	617.04	11.17	11.50	.747E-03
57	5.450	630.27	13.48	13.94	.906E-03

RUN 18

Gage	PRESSURE ($p_{\infty} = .297$ psia)		HEAT TRANSFER Btu/ft ² -s		
	p/p_{∞}	T_w (°R)	$q[hw]$	$q[cw]$	St^*
4	5.772	640.54	26.86	27.99	.159E-02
5	-----	-----	-----	-----	-----
6	5.723	-----	-----	-----	-----
7	-----	626.93	21.28	22.05	.125E-02
8	5.785	636.42	23.09	24.02	.137E-02
9	5.794	621.73	19.29	19.94	.113E-02
10	7.115	651.29	26.56	27.80	.158E-02
11	4.396	599.52	13.45	13.78	.784E-03
15	7.702	617.61	18.64	19.24	.109E-02
16	6.332	651.27	29.81	31.19	.177E-02
18	-----	635.26	24.86	25.84	.147E-02
20	5.718	-----	-----	-----	-----
21	-----	608.80	18.41	18.93	.108E-02
25	-----	616.76	18.94	19.54	.111E-02
26	5.323	623.18	20.12	20.81	.118E-02
27	-----	620.70	19.33	19.98	.114E-02
30	5.304	610.93	17.16	17.66	.100E-02
31	-----	610.01	16.84	17.33	.986E-03
34	7.486	624.16	19.92	20.61	.117E-02
35	-----	637.79	22.59	23.50	.134E-02
38	4.468	600.58	13.93	14.28	.812E-03
39	-----	619.48	19.38	20.02	.114E-02
49	6.457	627.68	20.83	21.58	.123E-02
51	6.191	635.42	25.64	26.65	.152E-02
53	5.928	-----	-----	-----	-----
54	-----	631.36	23.02	23.89	.136E-02
55	5.461	618.02	19.36	19.98	.114E-02
56	4.057	606.61	15.82	16.26	.925E-03
57	5.460	619.37	19.55	20.19	.115E-02

RUN 19

Gage	PRESSURE ($p_{\infty} = .178$ psia)		HEAT TRANSFER Btu/ft ² -s		
	p/p_{∞}	T_w (°R)	$q[hw]$	$q[cw]$	St^*
4	5.752	619.41	18.48	19.06	.176E-02
5	-----	-----	-----	-----	-----
6	5.609	-----	-----	-----	-----
7	-----	604.04	14.11	14.47	.134E-02
8	5.523	608.38	14.87	15.28	.141E-02
9	5.477	599.13	12.68	12.98	.120E-02
10	6.648	622.73	17.76	18.35	.169E-02
11	4.225	585.14	9.33	9.49	.876E-03
15	7.250	595.80	12.19	12.46	.115E-02
16	5.839	590.77	9.78	9.98	.921E-03
18	-----	596.47	11.69	11.95	.110E-02
20	5.521	-----	-----	-----	-----
21	-----	590.45	11.66	11.89	.110E-02
25	-----	596.76	12.83	13.11	.121E-02
26	5.241	601.42	13.44	13.77	.127E-02
27	-----	599.74	13.26	13.58	.125E-02
30	5.182	592.55	11.76	12.00	.111E-02
31	-----	591.08	11.29	11.52	.106E-02
34	7.285	591.32	10.74	10.96	.101E-02
35	-----	603.88	13.34	13.68	.126E-02
38	4.356	585.54	9.50	9.67	.893E-03
39	-----	594.38	11.65	11.90	.110E-02
49	6.120	601.92	13.17	13.50	.125E-02
51	5.825	587.30	9.18	9.35	.863E-03
53	5.647	-----	-----	-----	-----
54	-----	605.99	14.66	15.05	.139E-02
55	5.181	592.67	11.60	11.85	.109E-02
56	3.920	586.05	9.65	9.83	.907E-03
57	5.251	594.90	11.75	12.01	.111E-02

RUN 22

Gage	PRESSURE ($p_{\infty} = .279$ psia)		HEAT TRANSFER Btu/ft ² -s		
	p/p_{∞}	T_w (°R)	$q[hw]$	$q[cw]$	St^*
4	4.644	627.78	16.48	17.25	.184E-02
5	-----	-----	-----	-----	-----
6	4.251	-----	-----	-----	-----
7	-----	605.40	12.04	12.46	.133E-02
8	4.050	608.69	12.54	12.99	.138E-02
9	4.043	598.78	10.80	11.14	.119E-02
10	4.730	620.57	14.74	15.37	.164E-02
11	3.128	576.66	6.72	6.85	.730E-03
15	5.059	597.13	10.92	11.25	.120E-02
16	4.409	630.02	16.89	17.70	.189E-02
18	-----	615.99	14.28	14.86	.158E-02
20	4.012	-----	-----	-----	-----
21	-----	596.83	11.45	11.79	.126E-02
25	-----	599.32	11.31	11.66	.124E-02
26	3.768	603.04	11.67	12.06	.128E-02
27	-----	601.25	11.41	11.78	.125E-02
30	3.756	594.96	10.53	10.83	.115E-02
31	-----	592.83	10.00	10.28	.110E-02
34	5.097	594.81	10.09	10.38	.111E-02
35	-----	607.18	11.71	12.13	.129E-02
38	3.184	583.05	7.91	8.09	.861E-03
39	-----	593.31	9.76	10.03	.107E-02
49	4.453	604.62	11.69	12.09	.129E-02
51	4.598	629.12	16.87	17.67	.188E-02
53	4.193	-----	-----	-----	-----
54	-----	609.84	12.88	13.36	.142E-02
55	3.698	597.02	10.55	10.86	.116E-02
56	2.727	584.08	8.00	8.18	.872E-03

RUN 24

Gage	PRESSURE ($p_{\infty} = .210$ psia)		HEAT TRANSFER Btu/ft ² -s		
	p/p_{∞}	T_w (°R)	$q[hw]$	$q[cw]$	St^*
4	4.633	597.66	14.76	15.21	.216E-02
5	-----	-----	-----	-----	-----
6	4.219	-----	-----	-----	-----
7	-----	582.90	10.08	10.31	.147E-02
8	3.974	584.92	10.42	10.67	.152E-02
9	3.945	578.83	8.93	9.11	.130E-02
10	4.599	594.24	12.58	12.94	.184E-02
11	3.010	565.22	5.50	5.57	.793E-03
15	4.973	576.05	8.64	8.80	.125E-02
16	4.331	570.19	6.09	6.19	.880E-03
18	-----	584.85	10.76	11.01	.157E-02
20	3.982	-----	-----	-----	-----
21	-----	576.37	9.71	9.89	.141E-02
25	-----	578.30	9.48	9.67	.138E-02
26	3.735	581.59	10.00	10.22	.145E-02
27	-----	580.13	9.69	9.89	.141E-02
30	3.684	574.77	8.45	8.60	.122E-02
31	-----	573.82	8.20	8.35	.119E-02
34	5.027	572.29	7.35	7.48	.106E-02
35	-----	582.20	9.60	9.81	.140E-02
38	3.000	568.56	6.50	6.60	.939E-03
39	-----	573.48	7.84	7.98	.114E-02
49	4.335	580.28	9.43	9.63	.137E-02
51	4.407	568.49	6.38	6.48	.922E-03
53	4.089	-----	-----	-----	-----
54	-----	584.20	10.85	11.10	.158E-02
55	3.570	575.24	8.54	8.69	.124E-02
56	2.609	567.65	6.28	6.37	.906E-03
57	3.600	576.90	8.94	9.11	.130E-02

RUN 25

Gage	PRESSURE ($p_{\infty} = .119$ psia)		HEAT TRANSFER Btu/ft ² -s		
	p/p_{∞}	T_w (°R)	$q[hw]$	$q[cw]$	St^*
4	2.065	560.96	2.72	2.75	.900E-03
5	-----	-----	-----	-----	-----
6	1.988	-----	-----	-----	-----
7	-----	575.12	5.61	5.69	.186E-02
8	1.951	575.87	5.92	6.00	.197E-02
9	1.919	571.85	5.13	5.20	.170E-02
10	2.350	608.19	11.96	12.28	.403E-02
11	1.609	553.41	1.81	1.82	.595E-03
15	2.542	571.15	5.25	5.32	.174E-02
16	1.911	559.29	2.32	2.34	.766E-03
18	-----	557.21	1.91	1.92	.631E-03
20	1.823	-----	-----	-----	-----
21	-----	557.01	2.13	2.14	.703E-03
25	-----	561.45	3.11	3.13	.103E-02
26	1.762	563.27	3.25	3.28	.107E-02
27	-----	564.24	3.52	3.55	.116E-02
30	1.783	565.20	3.85	3.89	.127E-02
31	-----	564.94	3.88	3.92	.129E-02
34	2.567	574.51	5.66	5.74	.188E-02
35	-----	583.15	7.26	7.38	.242E-02
38	1.568	562.46	3.40	3.43	.112E-02
39	-----	570.04	4.85	4.90	.161E-02
49	2.603	575.89	5.89	5.97	.196E-02
51	1.971	558.44	2.26	2.28	.746E-03
53	1.894	-----	-----	-----	-----
54	-----	570.73	4.99	5.05	.166E-02
55	2.204	580.27	6.81	6.92	.227E-02
56	1.329	562.78	3.43	3.46	.113E-02
57	1.698	566.91	4.32	4.37	.143E-02

RUN 30

Gage	PRESSURE ($p_{\infty} = .180$ psia)		HEAT TRANSFER Btu/ft ² -s		
	p/p_{∞}	T_w (°R)	$q[hw]$	$q[cw]$	St^*
4	5.607	615.74	18.05	18.62	.177E-02
5	-----	610.99	16.48	16.96	.162E-02
6	5.377	-----	-----	-----	-----
7	-----	601.00	13.52	13.86	.132E-02
8	5.289	605.16	14.25	14.64	.140E-02
9	5.263	597.19	12.31	12.60	.120E-02
10	4.924	596.68	12.06	12.34	.118E-02
11	4.734	595.60	11.65	11.91	.114E-02
15	5.018	590.33	10.89	11.12	.106E-02
16	5.594	586.17	8.79	8.95	.853E-03
18	-----	592.34	11.00	11.24	.107E-02
20	5.255	-----	-----	-----	-----
21	-----	588.19	11.42	11.64	.111E-02
25	-----	594.27	12.40	12.68	.121E-02
26	4.938	598.63	13.14	13.45	.128E-02
27	-----	596.80	12.68	12.98	.124E-02
30	4.955	585.86	10.29	10.48	.999E-03
31	-----	588.82	10.81	11.03	.105E-02
34	4.948	595.39	11.91	12.18	.116E-02
35	-----	600.75	12.80	13.12	.125E-02
38	5.147	592.08	11.12	11.36	.108E-02
39	-----	593.43	11.46	11.71	.112E-02
49	5.167	596.52	12.15	12.43	.119E-02
51	5.594	595.20	12.24	12.52	.119E-02
53	5.393	608.54	16.00	16.46	.157E-02
54	-----	601.62	14.05	14.41	.137E-02
55	5.216	599.47	13.20	13.53	.129E-02
56	5.079	596.94	12.50	12.79	.122E-02
57	5.157	595.21	12.01	12.28	.117E-02

RUN 31

Gage	PRESSURE ($p_{\infty} = .298$ psia)		HEAT TRANSFER Btu/ft ² -s		
	p/p_{∞}	T_w (°R)	$q[hw]$	$q[cw]$	St^*
4	5.683	670.13	28.13	29.62	.158E-02
5	-----	665.25	26.28	27.61	.148E-02
6	5.710	-----	-----	-----	-----
7	-----	651.62	22.04	23.03	.123E-02
8	5.685	661.42	23.91	25.08	.134E-02
9	5.639	644.43	20.12	20.97	.112E-02
10	5.222	642.80	19.89	20.70	.111E-02
11	5.075	639.15	19.22	19.98	.107E-02
15	5.335	632.70	18.14	18.81	.101E-02
16	6.503	690.80	32.93	34.96	.187E-02
18	-----	669.30	27.05	28.46	.152E-02
20	5.869	-----	-----	-----	-----
21	-----	636.75	20.08	20.86	.111E-02
25	-----	642.58	20.10	20.93	.112E-02
26	5.334	648.86	20.90	21.82	.117E-02
27	-----	645.47	20.20	21.06	.113E-02
30	5.259	627.74	16.96	17.55	.938E-03
31	-----	632.09	17.56	18.20	.973E-03
34	5.232	642.73	19.54	20.34	.109E-02
35	-----	652.44	21.05	22.00	.118E-02
38	5.441	634.53	18.40	19.09	.102E-02
39	-----	635.16	19.01	19.74	.105E-02
49	5.494	643.89	20.49	21.34	.114E-02
51	6.268	675.00	29.16	30.76	.164E-02
53	6.022	666.84	25.67	26.99	.144E-02
54	-----	658.15	23.44	24.55	.131E-02
55	5.762	654.73	22.36	23.40	.125E-02
56	5.527	648.91	21.17	22.09	.118E-02
57	5.485	642.32	20.47	21.31	.114E-02

RUN 32

Gage	PRESSURE ($p_{\infty} = .179$ psia)		HEAT TRANSFER Btu/ft ² -s		
	p/p_{∞}	Tw (°R)	$q[hw]$	$q[cw]$	St^*
4	5.585	609.32	19.07	19.59	.181E-02
5	-----	605.45	17.69	18.15	.168E-02
6	5.401	-----	-----	-----	-----
7	-----	597.84	14.52	14.85	.137E-02
8	5.325	602.57	15.50	15.88	.147E-02
9	5.278	593.64	13.03	13.30	.123E-02
10	4.954	593.73	12.89	13.16	.122E-02
11	4.730	592.84	12.61	12.88	.119E-02
15	5.058	587.65	11.80	12.02	.111E-02
16	5.706	559.86	8.17	8.23	.761E-03
18	-----	576.67	8.13	8.25	.763E-03
20	5.346	-----	-----	-----	-----
21	-----	581.88	10.91	11.09	.103E-02
25	-----	593.98	13.96	14.26	.132E-02
26	5.048	599.51	15.13	15.48	.143E-02
27	-----	597.32	14.52	14.85	.137E-02
30	4.982	585.28	11.53	11.73	.108E-02
31	-----	587.56	11.98	12.20	.113E-02
34	4.998	594.30	13.23	13.51	.125E-02
35	-----	599.71	14.22	14.56	.135E-02
38	5.261	589.72	12.20	12.44	.115E-02
39	-----	591.00	12.44	12.69	.117E-02
49	5.208	593.21	13.11	13.39	.124E-02
51	5.731	576.49	8.30	8.42	.778E-03
53	5.500	609.08	18.31	18.81	.174E-02
54	-----	601.96	15.97	16.36	.151E-02
55	5.319	597.92	14.68	15.02	.139E-02
56	5.140	594.94	13.88	14.18	.131E-02
57	5.179	593.95	13.26	13.54	.125E-02

RUN 33

Gage	PRESSURE ($p_{\infty} = .393$ psia)		HEAT TRANSFER Btu/ft ² -s		
	p/p_{∞}	T_w (°R)	$q[hw]$	$q[cw]$	St^*
4	6.005	676.52	32.58	34.47	.154E-02
5	-----	671.34	30.36	32.05	.143E-02
6	5.777	-----	-----	-----	-----
7	-----	655.86	25.08	26.30	.117E-02
8	5.618	669.61	27.34	28.84	.129E-02
9	5.542	648.90	22.83	23.88	.107E-02
10	5.152	646.72	22.48	23.48	.105E-02
11	5.004	642.67	21.63	22.56	.101E-02
15	5.210	635.36	20.62	21.44	.956E-03
16	6.581	692.19	36.11	38.46	.172E-02
18	-----	671.23	30.47	32.17	.143E-02
20	5.754	-----	-----	-----	-----
21	-----	637.33	22.94	23.87	.106E-02
25	-----	645.93	23.15	24.18	.108E-02
26	5.232	653.07	24.18	25.33	.113E-02
27	-----	649.66	23.29	24.36	.109E-02
30	5.152	630.73	19.74	20.49	.914E-03
31	-----	635.49	20.35	21.16	.944E-03
34	5.100	647.17	22.52	23.53	.105E-02
35	-----	660.93	24.66	25.92	.116E-02
38	5.355	639.26	21.47	22.36	.997E-03
39	-----	639.98	22.10	23.03	.103E-02
49	5.312	649.80	24.15	25.27	.113E-02
51	6.374	678.64	34.41	36.44	.163E-02
53	5.945	674.37	31.52	33.32	.149E-02
54	-----	665.54	28.52	30.03	.134E-02
55	5.622	662.50	27.11	28.51	.127E-02
56	5.385	655.39	25.42	26.66	.119E-02
57	5.302	647.68	24.37	25.47	.114E-02

APPENDIX H

BOUNDARY-LAYER DATA TABULATION

The boundary layer data from the measured total temperature, static pressure, and pitot pressure are tabulated in this appendix by tunnel run number and rake assembly number. The x and y coordinates for the rake assembly, as defined in Fig. 4, are also given. The first column of the tabulated data is the gage designation for the test series. The second and third columns of the tabulated data are the total temperature probe distance from the wall, z , and measured total temperature. This pattern is repeated for the static pressure and pitot pressure probes in the fourth through seventh columns of the tabulated data. In addition, Mach number and velocity distributions corresponding to the pitot probe locations are given in the eighth and ninth columns of the tabulated data.

RUN 10

Rake Assembly #1
(x/L= 0.42, y/W=0.21)

Probe	z (in)	T _t (°R)	z (in)	p (psia)	z (in)	p _t (psia)	M	U (ft/s)
1	0.060	2320.	0.000	1.000	0.023	7.26	2.57	3054.
2	0.180	2678.	0.500	0.785	0.073	14.45	3.27	4668.
3	0.300	2941.	1.500	0.905	0.106	15.53	3.39	4824.
4	0.420	3030.	2.500	0.757	0.152	15.52	3.40	4966.
5	0.540	3142.	-----	-----	0.200	16.91	3.56	5176.
6	0.660	3151.	-----	-----	0.300	21.21	4.08	5631.
7	0.800	3192.	-----	-----	0.400	26.72	4.56	5855.
8	1.000	3185.	-----	-----	-----	-----	-----	-----
9	1.400	3179.	-----	-----	0.600	31.21	4.91	6119.
10	1.900	3208.	-----	-----	0.700	31.79	4.95	6153.
11	2.500	3203.	-----	-----	0.800	32.02	4.97	6196.
12	-----	-----	-----	-----	1.000	32.20	4.98	6190.
13	-----	-----	-----	-----	1.250	31.97	4.96	6181.
14	-----	-----	-----	-----	1.500	32.41	5.00	6194.
15	-----	-----	-----	-----	1.750	32.60	5.01	6217.
16	-----	-----	-----	-----	2.000	32.05	4.97	6216.
17	-----	-----	-----	-----	2.500	32.09	4.97	6212.

RUN 10

Rake Assembly #2
(x/L= 0.42, y/W=0.00)

Probe	z (in)	T _t (°R)	z (in)	p (psia)	z (in)	p _t (psia)	M	U (ft/s)
1	0.035	2395.	0.000	0.920	0.020	5.15	2.14	3220.
2	0.100	2683.	0.500	-----	0.074	12.75	3.21	4843.
3	0.165	2868.	1.500	0.691	0.113	14.97	3.49	5141.
4	0.230	-----	2.500	0.790	0.143	14.30	3.42	5198.
5	0.295	3070.	-----	-----	0.218	17.18	3.78	5530.
6	0.360	3111.	-----	-----	0.308	21.54	4.31	5852.
7	0.425	3165.	-----	-----	0.384	24.64	4.57	6000.
8	0.540	3202.	-----	-----	0.486	27.33	4.79	6138.
9	0.660	3204.	-----	-----	0.600	29.14	4.94	6203.
10	0.800	3165.	-----	-----	0.700	29.65	4.98	6201.
11	1.000	3211.	-----	-----	0.800	29.88	5.00	6170.
12	1.400	3229.	-----	-----	1.000	30.00	5.01	6233.
13	1.900	3187.	-----	-----	1.250	30.20	5.03	6252.
14	2.200	3236.	-----	-----	1.500	30.36	5.04	6253.
15	2.500	3198.	-----	-----	1.750	29.34	4.96	6203.
16	-----	-----	-----	-----	2.000	-----	-----	-----
17	-----	-----	-----	-----	2.500	29.06	4.93	6194.

RUN 10

Rake Assembly #3
(x/L= 0.42, y/W= -0.20)

Probe	z (in)	T _t (°R)	z (in)	p (psia)	z (in)	p _t (psia)	M	U (ft/s)
1	0.060	2441.	0.000	1.000	0.020	5.87	2.39	2922.
2	0.180	2745.	0.500	0.607	0.063	10.94	2.86	4505.
3	0.300	2849.	1.500	-----	0.097	14.53	3.28	4849.
4	0.420	3124.	2.500	0.828	0.130	14.56	3.29	4938.
5	0.540	2948.	-----	-----	0.200	14.97	3.35	5117.
6	0.660	3078.	-----	-----	0.300	19.19	3.82	5433.
7	0.800	3180.	-----	-----	0.400	-----	-----	-----
8	1.000	3071.	-----	-----	0.500	27.39	4.61	5859.
9	1.400	3151.	-----	-----	0.600	29.42	4.77	5912.
10	1.900	3094.	-----	-----	0.700	30.68	4.87	6058.
11	2.500	3191.	-----	-----	0.800	31.00	4.89	6159.
12	-----	-----	-----	-----	1.000	31.55	4.93	6029.
13	-----	-----	-----	-----	1.250	31.68	4.94	6096.
14	-----	-----	-----	-----	1.500	31.82	4.95	6123.
15	-----	-----	-----	-----	1.750	31.56	4.93	6081.
16	-----	-----	-----	-----	2.000	-----	-----	-----
17	-----	-----	-----	-----	2.500	31.19	4.90	6178.

RUN 11

Rake Assembly #1
(x/L= 0.42, y/W=0.21)

Probe	z (in)	T _t (°R)	z (in)	p (psia)	z (in)	p _t (psia)	M	U (ft/s)
1	0.060	2303.	0.000	0.450	0.023	4.29	2.27	2905.
2	0.180	2693.	0.500	0.314	0.073	8.95	3.87	4911.
3	0.300	3008.	1.500	0.442	0.106	10.16	4.17	5153.
4	0.420	3073.	2.500	0.456	0.152	11.36	4.43	5387.
5	0.540	3198.	-----	-----	0.200	11.59	4.48	5536.
6	0.660	3184.	-----	-----	0.300	14.94	5.05	5976.
7	0.800	3246.	-----	-----	0.400	19.41	5.78	6197.
8	1.000	3255.	-----	-----	0.500	-----	-----	-----
9	1.400	3228.	-----	-----	0.600	22.92	6.25	6417.
10	1.900	3293.	-----	-----	0.700	23.42	6.31	6439.
11	2.500	3291.	-----	-----	0.800	23.65	6.35	6506.
12	-----	-----	-----	-----	1.000	23.70	6.36	6520.
13	-----	-----	-----	-----	1.250	23.66	6.35	6495.
14	-----	-----	-----	-----	1.500	23.84	6.37	6502.
15	-----	-----	-----	-----	1.750	24.09	6.41	6569.
16	-----	-----	-----	-----	2.000	23.75	6.37	6576.
17	-----	-----	-----	-----	2.500	23.90	6.39	6591.

RUN 12

Rake Assembly #1
(x/L= 0.42, y/W=0.21)

Probe	z (in)	T _t (°R)	z (in)	p (psia)	z (in)	p _t (psia)	M	U (ft/s)
1	0.060	2315.	0.000	0.925	0.027	7.06	2.54	3182.
2	0.180	2678.	0.500	0.855	0.063	14.05	3.35	4675.
3	0.300	2952.	1.500	1.010	0.094	14.58	3.41	4796.
4	0.420	3040.	2.500	0.876	0.138	15.05	3.47	4957.
5	0.540	3159.	-----	-----	0.202	16.29	3.63	5219.
6	0.660	3164.	-----	-----	0.300	20.47	4.17	5663.
7	0.800	3205.	-----	-----	0.400	25.98	4.67	5900.
8	1.000	3216.	-----	-----	0.500	29.29	4.94	6094.
9	1.400	3215.	-----	-----	0.600	30.44	5.04	6173.
10	1.900	3243.	-----	-----	0.700	31.00	5.08	6204.
11	2.500	3251.	-----	-----	0.800	31.28	5.10	6249.
12	-----	-----	-----	-----	1.000	31.33	5.11	6265.
13	-----	-----	-----	-----	1.250	31.02	5.08	6257.
14	-----	-----	-----	-----	1.500	31.72	5.14	6278.
15	-----	-----	-----	-----	1.750	31.85	5.15	6300.
16	-----	-----	-----	-----	2.000	31.08	5.09	6296.
17	-----	-----	-----	-----	2.500	31.22	5.10	6308.

RUN 16

Rake Assembly #1
(x/L= 0.42, y/W=0.21)

Probe	z (in)	T _t (°R)	z (in)	p (psia)	z (in)	p _t (psia)	M	U (ft/s)
1	0.060	2409.	0.000	1.354	0.027	9.27	2.47	3206.
2	0.180	2765.	0.500	1.304	0.063	19.48	3.27	4725.
3	0.300	3024.	1.500	1.643	0.094	18.70	3.20	4784.
4	0.420	3120.	2.500	1.305	0.138	19.42	3.27	4951.
5	0.540	3233.	----	----	0.202	21.52	3.46	5226.
6	0.660	3242.	----	----	0.300	26.74	3.91	5667.
7	0.800	3254.	----	----	0.400	33.88	4.46	5933.
8	1.000	3292.	----	----	0.500	38.90	4.73	6132.
9	1.400	3298.	----	----	0.600	41.27	4.85	6225.
10	1.900	3322.	----	----	0.700	42.27	4.91	6251.
11	2.500	3335.	----	----	0.800	42.84	4.94	6271.
12	----	----	----	----	1.000	42.95	4.94	6322.
13	----	----	----	----	1.250	42.91	4.94	6326.
14	----	----	----	----	1.500	43.23	4.96	6340.
15	----	----	----	----	1.750	43.22	4.96	6355.
16	----	----	----	----	2.000	42.63	4.92	6358.
17	----	----	----	----	2.500	42.41	4.91	6369.

RUN 16

Rake Assembly #2
(x/L= 0.51, y/W=0.00)

Probe	z (in)	T _t (°R)	z (in)	p (psia)	z (in)	p _t (psia)	M	U (ft/s)
1	0.035	2345.	0.000	1.214	0.023	6.26	2.01	3193.
2	0.100	2583.	0.500	1.178	0.075	15.45	3.06	4687.
3	0.165	2735.	1.500	1.297	0.101	16.59	3.18	4846.
4	0.230	-----	2.500	1.253	0.133	15.48	3.08	4857.
5	0.295	2944.	-----	-----	0.212	18.33	3.36	5173.
6	0.360	3006.	-----	-----	0.308	22.32	3.73	5520.
7	0.425	3097.	-----	-----	0.384	25.84	4.09	5747.
8	0.540	3180.	-----	-----	0.486	30.13	4.43	5968.
9	0.660	3226.	-----	-----	0.600	26.83	4.19	5963.
10	0.800	3217.	-----	-----	0.700	37.33	4.86	6207.
11	1.000	3269.	-----	-----	0.800	38.65	4.94	6222.
12	1.400	3284.	-----	-----	1.000	39.54	4.99	6305.
13	1.900	3200.	-----	-----	1.250	39.21	4.97	6311.
14	2.200	3245.	-----	-----	1.500	40.18	5.03	6313.
15	2.500	3279.	-----	-----	1.750	37.69	4.88	6216.
16	-----	-----	-----	-----	2.000	-----	-----	-----
17	-----	-----	-----	-----	2.500	36.99	4.83	6274.

RUN 16

Rake Assembly #3
(x/L= 0.61, y/W= -0.20)

Probe	z (in)	T _t (°R)	z (in)	p (psia)	z (in)	p _t (psia)	M	U (ft/s)
1	0.060	2402.	0.000	1.278	0.023	7.72	2.40	3016.
2	0.180	2683.	0.500	1.116	0.055	14.08	2.85	4322.
3	0.300	2759.	1.500	1.490	0.090	17.08	3.14	4713.
4	0.420	2983.	2.500	1.362	0.153	16.34	3.09	4820.
5	0.540	2995.	----	----	0.228	18.31	3.27	5024.
6	0.660	3045.	----	----	0.300	21.07	3.51	5194.
7	0.800	3112.	----	----	0.400	24.76	3.85	5554.
8	1.000	3059.	----	----	0.500	28.35	4.18	5709.
9	1.400	3153.	----	----	0.600	31.10	4.38	5807.
10	1.900	3119.	----	----	0.700	34.48	4.58	5920.
11	2.500	3204.	----	----	0.800	37.01	4.73	6027.
12	----	----	----	----	1.000	40.08	4.91	6008.
13	----	----	----	----	1.250	40.72	4.95	6095.
14	----	----	----	----	1.500	41.01	4.97	6136.
15	----	----	----	----	1.750	40.60	4.95	6108.
16	----	----	----	----	2.000	40.54	4.94	6112.
17	----	----	----	----	2.500	40.43	4.93	6203.

RUN 18

Rake Assembly #1
(x/L= 0.42, y/W=0.21)

Probe	z (in)	T _t (°R)	z (in)	p (psia)	z (in)	p _t (psia)	M	U (ft/s)
1	0.060	2264.	0.000	1.706	0.027	12.37	2.53	3139.
2	0.180	2572.	0.500	1.619	0.063	26.32	3.36	4626.
3	0.300	2810.	1.500	1.940	0.094	23.13	3.14	4592.
4	0.420	2883.	2.500	1.548	0.138	24.66	3.25	4761.
5	0.540	2988.	-----	-----	0.202	27.87	3.46	5018.
6	0.660	2994.	-----	-----	0.300	34.20	3.88	5412.
7	0.800	3022.	-----	-----	0.400	42.64	4.40	5644.
8	1.000	3081.	-----	-----	0.500	48.50	4.66	5810.
9	1.400	3113.	-----	-----	0.600	52.00	4.82	5897.
10	1.900	3159.	-----	-----	0.700	53.66	4.89	5929.
11	2.500	3200.	-----	-----	0.800	54.65	4.93	5965.
12	-----	-----	-----	-----	1.000	55.12	4.96	6047.
13	-----	-----	-----	-----	1.250	55.01	4.95	6072.
14	-----	-----	-----	-----	1.500	55.47	4.97	6105.
15	-----	-----	-----	-----	1.750	55.80	4.99	6139.
16	-----	-----	-----	-----	2.000	54.71	4.94	6153.
17	-----	-----	-----	-----	2.500	54.54	4.93	6196.

RUN 18

Rake Assembly #2
(x/L= 0.51, y/W=0.00)

Probe	z (in)	T _t (°R)	z (in)	p (psia)	z (in)	p _t (psia)	M	U (ft/s)
1	0.035	2187.	0.000	1.560	0.023	8.29	2.07	3135.
2	0.100	2412.	0.500	1.472	0.075	20.63	3.12	4557.
3	0.165	2538.	1.500	1.671	0.101	20.02	3.08	4619.
4	0.230	2609.	2.500	1.580	0.133	19.16	3.02	4643.
5	0.295	2722.	-----	-----	0.212	23.36	3.34	4931.
6	0.360	2767.	-----	-----	0.308	28.11	3.68	5241.
7	0.425	2850.	-----	-----	0.384	32.40	4.02	5449.
8	0.540	2931.	-----	-----	0.486	37.36	4.33	5650.
9	0.660	2995.	-----	-----	0.600	-----	-----	-----
10	0.800	2984.	-----	-----	0.700	46.84	4.81	5897.
11	1.000	3051.	-----	-----	0.800	49.05	4.92	5913.
12	1.400	3077.	-----	-----	1.000	50.62	5.00	6019.
13	1.900	3036.	-----	-----	1.250	50.93	5.01	6045.
14	2.200	3097.	-----	-----	1.500	51.77	5.06	6057.
15	2.500	3121.	-----	-----	1.750	48.46	4.89	5990.
16	-----	-----	-----	-----	2.000	-----	-----	-----
17	-----	-----	-----	-----	2.500	47.40	4.84	6070.

RUN 18

Rake Assembly #3
(x/L= 0.61, y/W= -0.20)

Probe	z (in)	T _t (°R)	z (in)	p (psia)	z (in)	p _t (psia)	M	U (ft/s)
1	0.060	2302.	0.000	1.713	0.023	9.99	2.37	2948.
2	0.180	2567.	0.500	1.478	0.055	19.82	2.92	4276.
3	0.300	2634.	1.500	2.009	0.090	22.89	3.14	4611.
4	0.420	2836.	2.500	1.801	0.153	21.26	3.04	4687.
5	0.540	2852.	-----	-----	0.228	24.29	3.25	4892.
6	0.660	2894.	-----	-----	0.300	27.85	3.48	5047.
7	0.800	2958.	-----	-----	0.400	32.96	3.82	5381.
8	1.000	2905.	-----	-----	0.500	37.74	4.15	5545.
9	1.400	3008.	-----	-----	0.600	41.40	4.36	5635.
10	1.900	2977.	-----	-----	0.700	45.91	4.56	5735.
11	2.500	3087.	-----	-----	0.800	49.14	4.71	5830.
12	-----	-----	-----	-----	1.000	52.79	4.87	5803.
13	-----	-----	-----	-----	1.250	53.41	4.90	5891.
14	-----	-----	-----	-----	1.500	53.63	4.91	5935.
15	-----	-----	-----	-----	1.750	53.10	4.89	5909.
16	-----	-----	-----	-----	2.000	52.73	4.87	5917.
17	-----	-----	-----	-----	2.500	52.53	4.87	6033.

RUN 19

Rake Assembly #1
(x/L= 0.42, y/W=0.21)

Probe	z (in)	T _t (°R)	z (in)	p (psia)	z (in)	p _t (psia)	M	U (ft/s)
1	0.060	2247.	0.000	0.969	0.027	6.88	2.53	3128.
2	0.180	2594.	0.500	0.944	0.063	13.35	3.19	4525.
3	0.300	2855.	1.500	1.021	0.094	13.71	3.23	4636.
4	0.420	2963.	2.500	0.827	0.138	14.41	3.32	4805.
5	0.540	3054.	-----	-----	0.202	15.34	3.43	5031.
6	0.660	3058.	-----	-----	0.300	19.10	3.87	5461.
7	0.800	3094.	-----	-----	0.400	24.34	4.44	5739.
8	1.000	3122.	-----	-----	0.500	27.56	4.69	5905.
9	1.400	3129.	-----	-----	0.600	29.44	4.84	5986.
10	1.900	3171.	-----	-----	0.700	30.12	4.89	6015.
11	2.500	3186.	-----	-----	0.800	30.56	4.93	6057.
12	-----	-----	-----	-----	1.000	30.59	4.93	6095.
13	-----	-----	-----	-----	1.250	28.87	4.80	6064.
14	-----	-----	-----	-----	1.500	31.07	4.97	6125.
15	-----	-----	-----	-----	1.750	31.32	4.99	6157.
16	-----	-----	-----	-----	2.000	30.58	4.93	6162.
17	-----	-----	-----	-----	2.500	30.78	4.94	6182.

RUN 19

Rake Assembly #2
(x/L= 0.51, y/W=0.00)

Probe	z (in)	T _t (°R)	z (in)	p (psia)	z (in)	p _t (psia)	M	U (ft/s)
1	0.035	2250.	0.000	0.903	0.023	4.87	2.07	3186.
2	0.100	2479.	0.500	0.884	0.075	10.83	2.97	4526.
3	0.165	2636.	1.500	0.890	0.101	12.35	3.17	4737.
4	0.230	2719.	2.500	0.923	0.133	11.82	3.11	4778.
5	0.295	2842.	-----	-----	0.212	13.51	3.33	5038.
6	0.360	2893.	-----	-----	0.308	16.30	3.68	5378.
7	0.425	2979.	-----	-----	0.384	18.97	4.04	5599.
8	0.540	3048.	-----	-----	0.486	22.21	4.39	5805.
9	0.660	3081.	-----	-----	0.600	-----	-----	-----
10	0.800	3061.	-----	-----	0.700	26.92	4.78	5994.
11	1.000	3128.	-----	-----	0.800	27.96	4.87	5999.
12	1.400	3140.	-----	-----	1.000	29.03	4.96	6110.
13	1.900	3046.	-----	-----	1.250	28.51	4.92	6108.
14	2.200	3102.	-----	-----	1.500	29.42	4.99	6110.
15	2.500	3136.	-----	-----	1.750	27.72	4.85	6011.
16	-----	-----	-----	-----	2.000	-----	-----	-----
17	-----	-----	-----	-----	2.500	27.40	4.82	6083.

RUN 19

Rake Assembly #3
(x/L= 0.61, y/W= -0.20)

Probe	z (in)	T _t (°R)	z (in)	p (psia)	z (in)	p _t (psia)	M	U (ft/s)
1	0.060	2292.	0.000	0.974	0.023	5.66	2.37	2943.
2	0.180	2568.	0.500	0.771	0.055	9.70	2.68	4088.
3	0.300	2573.	1.500	0.971	0.090	11.84	3.00	4518.
4	0.420	2889.	2.500	0.968	0.153	11.82	3.01	4661.
5	0.540	2836.	-----	-----	0.228	13.00	3.16	4817.
6	0.660	2893.	-----	-----	0.300	14.85	3.37	4932.
7	0.800	2960.	-----	-----	0.400	17.60	3.70	5370.
8	1.000	2886.	-----	-----	0.500	20.29	4.04	5518.
9	1.400	3045.	-----	-----	0.600	22.44	4.26	5597.
10	1.900	2982.	-----	-----	0.700	24.90	4.49	5715.
11	2.500	3119.	-----	-----	0.800	26.80	4.63	5810.
12	-----	-----	-----	-----	1.000	29.18	4.81	5766.
13	-----	-----	-----	-----	1.250	29.55	4.85	5897.
14	-----	-----	-----	-----	1.500	30.04	4.89	5967.
15	-----	-----	-----	-----	1.750	29.55	4.85	5917.
16	-----	-----	-----	-----	2.000	29.78	4.86	5927.
17	-----	-----	-----	-----	2.500	29.75	4.87	6073.

RUN 22

Rake Assembly #1
(x/L= 0.42, y/W=0.21)

Probe	z (in)	T _t (°R)	z (in)	p (psia)	z (in)	p _t (psia)	M	U (ft/s)
1	0.060	1920.	0.000	1.104	0.027	8.03	2.61	2939.
2	0.180	2191.	0.500	1.064	0.063	17.35	3.44	4349.
3	0.300	2387.	1.500	1.433	0.094	16.53	3.34	4363.
4	0.420	2473.	2.500	1.111	0.138	17.14	3.39	4477.
5	0.540	2539.	-----	-----	0.202	19.31	3.60	4671.
6	0.660	2532.	-----	-----	0.300	24.19	4.10	5056.
7	0.800	2554.	-----	-----	0.400	30.69	4.57	5295.
8	1.000	2587.	-----	-----	0.500	35.11	4.85	5357.
9	1.400	2591.	-----	-----	0.600	37.35	4.99	5393.
10	1.900	2617.	-----	-----	0.700	38.20	5.04	5402.
11	2.500	2624.	-----	-----	0.800	38.50	5.06	5422.
12	-----	-----	-----	-----	1.000	38.72	5.09	5463.
13	-----	-----	-----	-----	1.250	37.11	4.99	5452.
14	-----	-----	-----	-----	1.500	39.07	5.12	5476.
15	-----	-----	-----	-----	1.750	39.72	5.16	5497.
16	-----	-----	-----	-----	2.000	39.09	5.13	5503.
17	-----	-----	-----	-----	2.500	39.53	5.16	5515.

RUN 22

Rake Assembly #2
(x/L= 0.51, y/W=0.00)

Probe	z (in)	T _t (°R)	z (in)	p (psia)	z (in)	p _t (psia)	M	U (ft/s)
1	0.035	1862.	0.000	1.034	0.023	5.53	2.11	2919.
2	0.100	2048.	0.500	0.984	0.075	14.05	3.17	4244.
3	0.165	2155.	1.500	1.237	0.101	14.90	3.26	4372.
4	0.230	2216.	2.500	1.227	0.133	13.89	3.14	4348.
5	0.295	2307.	-----	-----	0.212	16.85	3.47	4605.
6	0.360	2344.	-----	-----	0.308	20.58	3.86	4875.
7	0.425	2410.	-----	-----	0.384	23.93	4.22	5094.
8	0.540	2467.	-----	-----	0.486	27.83	4.51	5269.
9	0.660	2515.	-----	-----	0.600	-----	-----	-----
10	0.800	2498.	-----	-----	0.700	34.19	4.93	5359.
11	1.000	2543.	-----	-----	0.800	35.36	5.00	5353.
12	1.400	2554.	-----	-----	1.000	36.16	5.07	5409.
13	1.900	2486.	-----	-----	1.250	35.82	5.05	5415.
14	2.200	2510.	-----	-----	1.500	36.80	5.11	5412.
15	2.500	2555.	-----	-----	1.750	34.73	4.96	5358.
16	-----	-----	-----	-----	2.000	-----	-----	-----
17	-----	-----	-----	-----	2.500	34.70	4.97	5412.

RUN 22

Rake Assembly #3
(x/L= 0.61, y/W= -0.20)

Probe	z (in)	T _t (°R)	z (in)	p (psia)	z (in)	p _t (psia)	M	U (ft/s)
1	0.060	1890.	0.000	1.100	0.023	6.59	2.52	2760.
2	0.180	2099.	0.500	0.921	0.055	12.93	2.94	3825.
3	0.300	2156.	1.500	1.377	0.090	15.69	3.27	4276.
4	0.420	2320.	2.500	1.278	0.153	14.82	3.16	4310.
5	0.540	2336.	-----	-----	0.228	16.95	3.39	4498.
6	0.660	2372.	-----	-----	0.300	19.73	3.66	4630.
7	0.800	2403.	-----	-----	0.400	23.54	4.06	4950.
8	1.000	2356.	-----	-----	0.500	27.08	4.37	5155.
9	1.400	2452.	-----	-----	0.600	29.62	4.51	5204.
10	1.900	2409.	-----	-----	0.700	32.73	4.69	5253.
11	2.500	2466.	-----	-----	0.800	34.73	4.81	5242.
12	-----	-----	-----	-----	1.000	36.78	4.91	5202.
13	-----	-----	-----	-----	1.250	37.02	4.95	5263.
14	-----	-----	-----	-----	1.500	37.37	4.98	5293.
15	-----	-----	-----	-----	1.750	37.19	4.96	5270.
16	-----	-----	-----	-----	2.000	37.25	4.96	5267.
17	-----	-----	-----	-----	2.500	37.64	5.00	5319.

RUN 24

Rake Assembly #1
(x/L= 0.42, y/W=0.21)

Probe	z (in)	T _t (°R)	z (in)	p (psia)	z (in)	p _t (psia)	M	U (ft/s)
1	0.060	1916.	0.000	0.839	0.027	6.12	2.61	2938.
2	0.180	2210.	0.500	0.807	0.063	12.49	3.35	4303.
3	0.300	2422.	1.500	1.029	0.094	12.76	3.37	4382.
4	0.420	2517.	2.500	0.819	0.138	13.24	3.43	4503.
5	0.540	2589.	-----	-----	0.202	14.75	3.61	4701.
6	0.660	2587.	-----	-----	0.300	18.69	4.14	5109.
7	0.800	2601.	-----	-----	0.400	23.98	4.64	5343.
8	1.000	2630.	-----	-----	0.500	27.29	4.92	5416.
9	1.400	2631.	-----	-----	0.600	28.76	5.04	5458.
10	1.900	2655.	-----	-----	0.700	29.19	5.08	5466.
11	2.500	2657.	-----	-----	0.800	29.43	5.11	5481.
12	-----	-----	-----	-----	1.000	29.57	5.13	5518.
13	-----	-----	-----	-----	1.250	28.58	5.04	5507.
14	-----	-----	-----	-----	1.500	-----	-----	-----
15	-----	-----	-----	-----	1.750	30.45	5.21	5550.
16	-----	-----	-----	-----	2.000	29.65	5.14	5550.
17	-----	-----	-----	-----	2.500	30.24	5.19	5559.

RUN 24

Rake Assembly #2
(x/L= 0.51, y/W=0.00)

Probe	z (in)	T _t (°R)	z (in)	p (psia)	z (in)	p _t (psia)	M	U (ft/s)
1	0.035	1903.	0.000	0.763	0.023	4.30	2.20	3029.
2	0.100	2092.	0.500	0.735	0.075	9.99	3.12	4251.
3	0.165	2216.	1.500	0.851	0.101	11.38	3.34	4450.
4	0.230	2286.	2.500	0.879	0.133	10.68	3.22	4448.
5	0.295	2388.	-----	-----	0.212	12.83	3.54	4687.
6	0.360	2433.	-----	-----	0.308	15.82	3.99	5020.
7	0.425	2505.	-----	-----	0.384	18.58	4.36	5247.
8	0.540	2560.	-----	-----	0.486	21.88	4.66	5376.
9	0.660	2590.	-----	-----	0.600	-----	-----	-----
10	0.800	2566.	-----	-----	0.700	26.50	5.09	5459.
11	1.000	2607.	-----	-----	0.800	27.11	5.14	5445.
12	1.400	2610.	-----	-----	1.000	27.57	5.20	5499.
13	1.900	2528.	-----	-----	1.250	27.04	5.15	5495.
14	2.200	2560.	-----	-----	1.500	28.01	5.23	5487.
15	2.500	2585.	-----	-----	1.750	26.47	5.07	5421.
16	-----	-----	-----	-----	2.000	-----	-----	-----
17	-----	-----	-----	-----	2.500	26.38	5.08	5459.

RUN 24

Rake Assembly #3
(x/L= 0.61, y/W= -0.20)

Probe	z (in)	T _t (°R)	z (in)	p (psia)	z (in)	P _t (psia)	M	U (ft/s)
1	0.060	1911.	0.000	0.824	0.023	4.94	2.52	2773.
2	0.180	2133.	0.500	0.613	0.055	8.81	2.75	3710.
3	0.300	2169.	1.500	1.039	0.090	10.97	3.15	4222.
4	0.420	2386.	2.500	0.934	0.153	10.72	3.11	4306.
5	0.540	2382.	-----	-----	0.228	12.14	3.31	4488.
6	0.660	2426.	-----	-----	0.300	14.19	3.59	4612.
7	0.800	2462.	-----	-----	0.400	17.08	4.00	4976.
8	1.000	2398.	-----	-----	0.500	19.89	4.34	5184.
9	1.400	2497.	-----	-----	0.600	22.05	4.51	5242.
10	1.900	2443.	-----	-----	0.700	24.75	4.74	5302.
11	2.500	2499.	-----	-----	0.800	26.43	4.87	5304.
12	-----	-----	-----	-----	1.000	28.17	4.99	5247.
13	-----	-----	-----	-----	1.250	28.23	5.01	5313.
14	-----	-----	-----	-----	1.500	28.46	5.04	5344.
15	-----	-----	-----	-----	1.750	28.21	5.01	5313.
16	-----	-----	-----	-----	2.000	28.42	5.03	5307.
17	-----	-----	-----	-----	2.500	28.55	5.05	5359.

RUN 25

Rake Assembly #1
(x/L= 0.42, y/W=0.21)

Probe	z (in)	T _t (°R)	z (in)	p (psia)	z (in)	p _t (psia)	M	U (ft/s)
1	0.060	2154.	0.000	0.222	0.027	1.52	2.53	3065.
2	0.180	2566.	0.500	0.213	0.063	4.04	3.69	4652.
3	0.300	2880.	1.500	----	0.094	4.40	3.86	4835.
4	0.420	2960.	2.500	----	0.138	5.56	4.41	5231.
5	0.540	3034.	----	----	0.202	6.36	4.67	5459.
6	0.660	2997.	----	----	0.300	8.19	5.31	5864.
7	0.800	3040.	----	----	0.400	9.66	5.77	6035.
8	1.000	3118.	----	----	0.500	10.27	5.94	6141.
9	1.400	3045.	----	----	0.600	10.94	6.12	6166.
10	1.900	3174.	----	----	0.700	11.26	6.20	6166.
11	2.500	3146.	----	----	0.800	11.43	6.24	6212.
12	----	----	----	----	1.000	11.52	6.28	6322.
13	----	----	----	----	1.250	11.28	6.21	6252.
14	----	----	----	----	1.500	----	----	----
15	----	----	----	----	1.750	11.73	6.34	6351.
16	----	----	----	----	2.000	11.18	6.21	6383.
17	----	----	----	----	2.500	11.56	6.30	6361.

RUN 25

Rake Assembly #2
(x/L= 0.51, y/W=0.00)

Probe	z (in)	T _t (°R)	z (in)	p (psia)	z (in)	p _t (psia)	M	U (ft/s)
1	0.035	1901.	0.000	0.211	0.023	1.07	2.04	2882.
2	0.100	2260.	0.500	0.210	0.075	3.06	3.28	4448.
3	0.165	2509.	1.500	0.188	0.101	4.13	3.83	4814.
4	0.230	2670.	2.500	0.198	0.133	4.33	3.96	4996.
5	0.295	2879.	-----	-----	0.212	5.32	4.42	5407.
6	0.360	2914.	-----	-----	0.308	6.88	5.00	5808.
7	0.425	3018.	-----	-----	0.384	8.10	5.44	5988.
8	0.540	3064.	-----	-----	0.486	9.28	5.83	6176.
9	0.660	3081.	-----	-----	0.600	-----	-----	-----
10	0.800	3005.	-----	-----	0.700	10.32	6.10	6224.
11	1.000	3127.	-----	-----	0.800	10.62	6.17	6159.
12	1.400	3102.	-----	-----	1.000	11.05	6.31	6337.
13	1.900	2914.	-----	-----	1.250	-----	-----	-----
14	2.200	3025.	-----	-----	1.500	11.26	6.35	6256.
15	2.500	3016.	-----	-----	1.750	10.54	6.14	6110.
16	-----	-----	-----	-----	2.000	-----	-----	-----
17	-----	-----	-----	-----	2.500	10.54	6.14	6102.

RUN 25

Rake Assembly #3
(x/L= 0.61, y/W= -0.20)

Probe	z (in)	T _t (°R)	z (in)	p (psia)	z (in)	p _t (psia)	M	U (ft/s)
1	0.060	2125.	0.000	0.222	0.023	1.40	2.52	2911.
2	0.180	2385.	0.500	-----	0.055	3.03	3.18	4297.
3	0.300	2203.	1.500	-----	0.090	3.90	3.62	4645.
4	0.420	2802.	2.500	0.209	0.153	4.22	3.77	4848.
5	0.540	2526.	-----	-----	0.228	4.51	3.91	4900.
6	0.660	2582.	-----	-----	0.300	5.33	4.34	5061.
7	0.800	2661.	-----	-----	0.400	6.41	4.69	5530.
8	1.000	2484.	-----	-----	0.500	7.46	5.01	5488.
9	1.400	2795.	-----	-----	0.600	8.30	5.25	5443.
10	1.900	2639.	-----	-----	0.700	9.25	5.53	5523.
11	2.500	2934.	-----	-----	0.800	9.99	5.75	5633.
12	-----	-----	-----	-----	1.000	11.06	5.95	5429.
13	-----	-----	-----	-----	1.250	11.24	6.09	5723.
14	-----	-----	-----	-----	1.500	11.49	6.18	5847.
15	-----	-----	-----	-----	1.750	11.27	6.10	5735.
16	-----	-----	-----	-----	2.000	11.43	6.15	5746.
17	-----	-----	-----	-----	2.500	11.51	6.24	6072.

RUN 30

Rake Assembly #2
(x/L= 0.74, y/W=0.00)

Probe	z (in)	T _t (°R)	z (in)	p (psia)	z (in)	p _t (psia)	M	U (ft/s)
1	0.035	2128.	0.000	0.933	0.023	4.97	2.08	3098.
2	0.100	2329.	0.500	0.906	0.075	10.44	2.88	4311.
3	0.165	-----	1.500	0.987	0.104	11.34	2.99	4487.
4	0.230	2519.	2.500	0.984	0.146	10.87	2.94	4511.
5	0.295	2631.	-----	-----	0.233	12.19	3.11	4748.
6	0.360	2664.	-----	-----	0.314	14.04	3.35	4989.
7	0.425	2737.	-----	-----	0.390	15.95	3.57	5158.
8	0.540	2825.	-----	-----	0.508	18.18	3.85	5389.
9	0.660	2908.	-----	-----	0.612	20.34	4.13	5572.
10	0.800	2919.	-----	-----	0.704	22.88	4.39	5686.
11	1.000	3008.	-----	-----	0.808	25.07	4.57	5748.
12	1.400	3025.	-----	-----	1.005	28.50	4.85	5928.
13	1.900	2940.	-----	-----	1.250	29.46	4.93	5960.
14	2.200	2967.	-----	-----	1.475	30.79	5.04	5978.
15	2.500	2991.	-----	-----	1.753	29.39	4.92	5891.
16	-----	-----	-----	-----	2.016	29.49	4.93	5874.
17	-----	-----	-----	-----	2.487	29.20	4.91	5919.

RUN 31

Rake Assembly #2
(x/L= 0.74, y/W=0.00)

Probe	z (in)	T _t (°R)	z (in)	p (psia)	z (in)	p _t (psia)	M	U (ft/s)
1	0.035	2276.	0.000	1.655	0.023	8.37	2.00	3130.
2	0.100	2502.	0.500	1.563	0.075	19.50	2.95	4538.
3	0.165	-----	1.500	1.851	0.104	18.90	2.91	4601.
4	0.230	2680.	2.500	1.686	0.146	18.08	2.86	4627.
5	0.295	2786.	-----	-----	0.233	21.47	3.11	4899.
6	0.360	2815.	-----	-----	0.314	24.56	3.33	5142.
7	0.425	2887.	-----	-----	0.390	27.47	3.53	5303.
8	0.540	2979.	-----	-----	0.508	30.78	3.76	5528.
9	0.660	3077.	-----	-----	0.612	34.16	4.03	5725.
10	0.800	3096.	-----	-----	0.704	38.27	4.27	5847.
11	1.000	3218.	-----	-----	0.808	41.00	4.43	5918.
12	1.400	3255.	-----	-----	1.005	47.65	4.72	6160.
13	1.900	3181.	-----	-----	1.250	50.63	4.85	6228.
14	2.200	3197.	-----	-----	1.475	52.32	4.93	6253.
15	2.500	3240.	-----	-----	1.753	49.85	4.82	6168.
16	-----	-----	-----	-----	2.016	49.72	4.81	6146.
17	-----	-----	-----	-----	2.487	49.04	4.78	6203.

RUN 32

Rake Assembly #2
(x/L= 0.74, y/W=0.00)

Probe	z (in)	T _t (°R)	z (in)	p (psia)	z (in)	p _t (psia)	M	U (ft/s)
1	0.035	2157.	0.000	0.936	0.023	4.72	2.01	3056.
2	0.100	2361.	0.500	0.897	0.075	10.03	2.81	4299.
3	0.165	-----	1.500	0.969	0.104	11.39	3.00	4521.
4	0.230	2547.	2.500	0.964	0.146	11.03	2.95	4553.
5	0.295	2685.	-----	-----	0.233	12.00	3.09	4761.
6	0.360	2706.	-----	-----	0.314	13.96	3.34	5036.
7	0.425	2795.	-----	-----	0.390	15.95	3.57	5212.
8	0.540	2899.	-----	-----	0.508	18.38	3.87	5477.
9	0.660	2993.	-----	-----	0.612	20.89	4.19	5673.
10	0.800	3014.	-----	-----	0.704	23.69	4.47	5809.
11	1.000	3121.	-----	-----	0.808	26.00	4.64	5884.
12	1.400	3143.	-----	-----	1.005	29.53	4.93	6094.
13	1.900	3057.	-----	-----	1.250	30.08	4.98	6123.
14	2.200	3080.	-----	-----	1.475	31.11	5.06	6138.
15	2.500	3109.	-----	-----	1.753	29.52	4.93	6043.
16	-----	-----	-----	-----	2.016	29.37	4.92	6018.
17	-----	-----	-----	-----	2.487	29.07	4.89	6066.

RUN 33

Rake Assembly #2
(x/L= 0.74, y/W=0.00)

Probe	z (in)	T _t (°R)	z (in)	p (psia)	z (in)	p _t (psia)	M	U (ft/s)
1	0.035	2242.	0.000	2.119	0.023	10.82	2.01	3120.
2	0.100	2467.	0.500	1.980	0.075	25.87	3.00	4538.
3	0.165	-----	1.500	2.389	0.104	24.13	2.91	4564.
4	0.230	2628.	2.500	2.050	0.146	23.63	2.89	4606.
5	0.295	2729.	-----	-----	0.233	28.06	3.14	4866.
6	0.360	2753.	-----	-----	0.314	32.21	3.37	5101.
7	0.425	2818.	-----	-----	0.390	36.10	3.57	5252.
8	0.540	2899.	-----	-----	0.508	40.59	3.82	5463.
9	0.660	2988.	-----	-----	0.612	45.52	4.11	5652.
10	0.800	3034.	-----	-----	0.704	51.02	4.36	5779.
11	1.000	3127.	-----	-----	0.808	55.44	4.52	5870.
12	1.400	3167.	-----	-----	1.005	63.65	4.82	6071.
13	1.900	3107.	-----	-----	1.250	67.15	4.94	6136.
14	2.200	3133.	-----	-----	1.475	68.32	4.98	6155.
15	2.500	3161.	-----	-----	1.753	64.68	4.85	6077.
16	-----	-----	-----	-----	2.016	64.41	4.84	6065.
17	-----	-----	-----	-----	2.487	63.35	4.81	6109.



Report Documentation Page

1. Report No. NASA TM-101663	2. Government Accession No.	3. Recipient's Catalog No.	
4. Title and Subtitle Evaluation of Equilibrium Turbulence for a Hypersonic Boundary Layer at Nonadiabatic Wall Conditions		5. Report Date November 1989	
		6. Performing Organization Code	
7. Author(s) Cindy W. Albertson		8. Performing Organization Report No.	
		10. Work Unit No. 506-40-21-01	
9. Performing Organization Name and Address NASA Langley Research Center Hampton, VA 23665-5225		11. Contract or Grant No.	
		13. Type of Report and Period Covered Technical Memorandum	
12. Sponsoring Agency Name and Address National Aeronautics and Space Administration Washington, D. C. 20546-0001		14. Sponsoring Agency Code	
15. Supplementary Notes A Thesis submitted to the faculty of Old Dominion University in partial fulfillment of the requirements for the Degree of Master of Science in Mechanical Engineering			
16. Abstract THIS paper presents an experimental study to characterize the naturally developing compressible turbulent boundary layer produced along a flat plate measuring 9.7 feet long in the NASA Langley 8-Foot High Temperature Tunnel and to determine the test conditions necessary to achieve equilibrium turbulence. The measurements consist of pitot pressure, static pressure, and total temperature distributions in the boundary layer. In addition, surface measurements consisting of heat transfer and pressure distributions were obtained. The tests were conducted at a nominal free-stream Mach number of 6.5, total temperatures of 2700 and 3300°R, and angles of attack of 5 and 13 degrees. The corresponding nominal boundary-layer edge Mach numbers were 6.2 and 5.0. The nominal ratios of adiabatic wall temperature to cold wall temperature were 4.4 and 5.4 and the momentum thickness Reynolds numbers at the boundary layer probe locations ranged from 400 to 7800. The results of this study indicate that momentum thickness Reynolds numbers of at least 4000 are required to obtain an equilibrium turbulent boundary layer in the Langley 8-Foot High Temperature Tunnel. This evaluation is based primarily on the behavior of shape factors inferred from the boundary-layer measurements.			
17. Key Words (Suggested by Author(s)) Hypersonic Turbulent Boundary Layer Equilibrium Turbulence Heat Transfer Pitot and Total Temperature Data		18. Distribution Statement Unclassified - Unlimited Subject Category - 34	
19. Security Classif. (of this report) Unclassified	20. Security Classif. (of this page) Unclassified	21. No. of pages 264	22. Price A12